Synchronisation in Signed Complex Networks Motivated by Neural Population Networks

Saeed Ahmadizadeh

Submitted in total fulfilment of the requirements of the degree of

Doctor of Philosophy

Department of Electrical and Electronic Engineering
THE UNIVERSITY OF MELBOURNE

March 2017

Abstract

Synchronisation is a ubiquitous phenomenon which is observed in a wide range of network applications. The absence or presence of synchronisation depends on network features which are characterised by two factors: (i) dynamics of each subsystem and (ii) network topology. This thesis develops tools for analysing synchronisation via the aforementioned two factors. Our results concerning the network topology are quite general, and, the rest of results are tailored for networks of neural populations. Nevertheless, they can be adopted for other classes of networks. Neural mass populations describe the averaged activity of cortical ensembles which, from the modelling perspective, is particularly important for epilepsy, as this is the scale observed through clinical electroencephalographic (EEG) and intracranial EEG recordings. From the analysis point of view, these networks pose new challenges in studying synchronisation, as their models are non-linear and their interconnections are directed with both positive and negative weights which, in network science, are known as directed signed graph networks.

First, bifurcation analyses are conducted to explore various ranges of behaviours that can be generated by a simple network of neural populations by initialising it around equilibrium points. The underlying network contains two neural populations; each of them is modelled by a well-known Jansen-Rit model. For different values of interconnection gains, bifurcation diagrams are presented, where the input to the neural regions is the bifurcation parameter. The bifurcation analyses reveal that this network can generate various unexpected oscillatory activities, such as delta wave. Surprisingly, by changing the value of the input in one neural population, another neural population shows spike-wave output observed during epilepsy. Using human clinical data, we also investigated the suitability of these models for monitoring seizures.

To analyse a larger network of neural populations, we use mathematical tools from control theory and graph theory to study synchronisation in Wilson-Cowan oscillators. This class of oscillators describes the activity of both excitatory and inhibitory populations of neurons and reproduces self-sustained oscillations observed in EEG signals. Since the interest is to investigate synchronisation with respect to a specific limit-cycle, that is responsible for producing oscillatory output, we linearise the model of the whole network around that limit-cycle, leading to a periodic linear time-varying system. By applying an appropriate change of coordinates, we transform the linearised system to a new system that itself contains a number of subsystems. We then observe that stability (instability) of those subsystems, excluding one of them, implies the presence (absence) of synchronous behaviour in the original network. The stability/instability of aforementioned subsystems depends on parameters of the models, as well as eigenvalues of a so-called "Laplacian matrix" which solely depends on interconnection gains (network structure). We propose a combination of numerical and theoretical approaches to check the stability/instability of those subsystems in terms of their eigenvalues. To prove the stability and instability results, we use Floquet theory along with Lyapunov stability and Chetaev instability theorems. For the numerical approach, we use a tool from robust control theory. We also investigate how changes in the network can affect the presence/absence of synchronisation. These results are developed using Weyl's inequality and results from the first part of analysis.

Eigenvalues of the Laplacian matrix play a crucial role in reaching objectives such as synchronisation, formation control and etc in all network applications. For directed signed networks, it is still challenging to characterise eigenvalues of Laplacian matrix in terms of network structure. To this end, we consider a class of directed signed networks that have a specific property : the real parts of the non-zero eigenvalues of its Laplacian matrix are positive. This property, called a "nice property", and ensures that this class of network achieves synchronisation for applications such as the decision-making in social networks. The absence of this nice property leads to the absence of synchronous behaviour in applications such as in neural populations. Under a mild assumption, we provide a necessary and sufficient condition under which the following statement holds:

"if edges between an arbitrary pair of nodes are perturbed with negative weights that satisfy an easily computed bound, the perturbed network has also the nice property. Furthermore, under certain conditions, we identify "sensitive pairs of nodes", which if connected by infinitesimal negative weights, the network cannot have the nice property. Our proof techniques for these results are novel and based on tools from linear algebra.

Declaration

This is to certify that

1. the thesis comprises only my original work towards the PhD,
2. due acknowledgement has been made in the text to all other material used,
3. the thesis is less than 100,000 words in length, exclusive of tables, maps, bibliographies and appendices.

Saeed Ahmadizadeh, March 2017

Acknowledgements

First and foremost, the biggest thanks to God for bestowing me the power to press on and finish my PhD study.

I would like to express my sincere appreciation to my principle supervisor Prof. Dragan Nešić. Due to family issues and lack of interest in my topic, I underwent several personal crises during which I have fully been exposed by his emotional supports. Dragan taught me quite invaluable lessons from life perspective; those that I should have been taught by others. I remember very few joyful moments in my research journey among which the most memorable ones happened on May 8, 2014 when Dragan offered me an opportunity to meet my superhero Prof. Andrew Teel. I am thankful to Dragan for organising the meeting in his office.

I would like to thank my co-supervisors Prof. David Grayden and Dr. Dean Freestone for being patient and endlessly kind to me.

I would also like to thank my committee members, A/Prof. Ying Tan and Dr. Tatiana Kameneva, for all useful advice.

I am indebted to Dr. Iman Shames for co-supervising me in the last year. For the last part of my thesis, I found the right direction of solving questions through a series of one-to-one discussions with him. Apart from my research, he organised several meetings during which I was injected a hope to pursue my study toward finishing it, while I lacked motivation and interest. During those periods, I have also been boosted up by Dr. Romain Postoyan through some emails. I would like to take this opportunity to thank him for his advice.

I have cooperated with A/Prof. Samuel Martin from CNRS and CRAN lab, Université de Lorraine. He provided me constructive comments to improve the results of the last

part of my thesis. I am grateful for his effort to organise a visit for me, however, I couldn't manage to use this opportunity.

A great deal of the work on clinical data has been carried out by Philippa Jane Karoly. I would like to thank her for working on this part before her visiting trip. I would also thank Prof. Mark Cook from St. Vincents Hospital for providing the clinical data.

I gratefully acknowledge an "Australian Government Research Training Program Scholarship" for supporting my research financially.

I am grateful to all my friends Sasan, Omid, Adel, Amir, Laven, Roghieh, Ahvand, Amin, Ehsan, Amir hossein, Keith, Hasan, Merid, Alejandro and Luis. My special thanks go to Navid who, after being graduated from the master, encouraged me to do research, pointing out that it is a joyful task if the topics are close to your heart. I perfectly understand this point now! I will never forget those moments that we both were excited by reading our superhero's papers.

In the last year of my study, I met my special friend A/Prof. Emre Tuna. I enjoyed my time discussing with him about different aspects of research and life, and also discovering different places. I would like to thank Emre for being an amazing and globally attractive friend in the highly nonlinear domain.

Finally, this journey would not have been possible without supports of my parents, sister and close relatives. They are the most precious things in my life and I express my deepest gratitude to them.

To my parents, sister and close relatives.

Contents

Preliminaries and Graph Notation **xvii**
0.1 Preliminaries . . . xvii
0.2 Graph Notation . . . xviii

1 Introduction **1**
1.1 Neurons and Neural Mass Models . . . 4
1.2 Synchronisation in Dynamical Systems . . . 6
1.2.1 Dynamical Properties for Analysing Synchronisation . . . 6
1.2.2 Synchronisation, Network Structure and Signed Graphs . . . 9
1.2.3 Various Versions of Synchronisation . . . 11
1.2.4 Mechanisms of Synchronising, Global Synchronisation Versus Local Synchronisation . . . 13
1.3 Thesis Outline and Contributions . . . 15

2 Bifurcation Analysis of Two Coupled Jansen-Rit Neural Mass Models **19**
2.1 Introduction . . . 19
2.2 Model Description . . . 21
2.3 Equilibria . . . 26
2.4 Case I: Bifurcation Analysis with a Common Input . . . 27
2.4.1 Bifurcation Analysis with Weak Coupling ($K = 25$) . . . 28
2.4.2 Bifurcation Analysis with Intermediate Coupling ($K = 50$) . . . 35
2.4.3 Bifurcation Analysis with Strong Coupling ($K = 100$ and 150) . . . 35
2.5 Case II: Bifurcation Analysis of Two Coupled Neural Mass Model with a Single Input . . . 38
2.5.1 Bifurcation analysis with coupling gain $K = 250$ . . . 42
2.6 Case III: Bifurcation Analysis of Two Coupled Neural Mass Model with a Single Input and Feed-Forward Structure . . . 46
2.7 Relationship to Clinical Data . . . 50
2.7.1 Seizure one . . . 52
2.7.2 Seizure two . . . 53
2.8 Discussion . . . 55

3 Local Synchronisation of Networks of Wilson-Cowan Oscillators With Diffusive Coupling **61**
3.1 Introduction . . . 61

3.2 Wilson-Cowan Model . . . 62
3.3 Problem Formulation . . . 64
3.4 Stability Analysis of the Linearised Model . . . 68
3.4.1 Synchronisation in Set Ω_β^1 . . . 69
3.4.2 Synchronisation in Set Ω_β^3 . . . 72
3.4.3 Synchronisation in Ω_β^2 . . . 74
3.5 Network Topology and Synchronisation . . . 76
3.6 Simulation Results . . . 78
3.7 Conclusions . . . 83

4 On Eigenvalues of Laplacian Matrix for a Class of Directed Signed Graphs 85
4.1 Introduction . . . 85
4.2 Preliminaries . . . 87
4.3 Problem Formulation and Results . . . 93
4.3.1 Adding a (un)directed negative edge to directed signed graphs . . . 93
4.3.2 Directed graphs with multiple negative weights . . . 105
4.4 Application in Consensus Protocol . . . 109
4.5 Conclusion and Remark on applicability of results on Synchronisation . . . 111

5 Summary and Future Work 113
5.1 Summary of Thesis . . . 113
5.2 Future Work . . . 114

A Supplementary Materials For Chapter 2 117
A.1 Jacobian matrix of the network of Jansen-Rit in (2.4) . . . 117
A.2 Detection of a saddle-node homoclinic bifurcation . . . 118
A.3 Notes on Equilibria for Case II . . . 118
A.4 Estimation Method . . . 123
A.4.1 Augmented Model of a Cortical Region . . . 123
A.4.2 Re-parametrization for Model for Inversion . . . 125
A.4.3 Augmentation for Model for Inversion . . . 126
A.4.4 A Filter for the Population Model . . . 127

B Instability Lemma in the Proof of Proposition 3.1 131
B.1 Instability Using Two-Time Averaging . . . 131

C Supplementary Lemmas in Chapter 4. 137
C.1 Lemmas in Proof of Theorems 4.1 and 4.3 . . . 137
C.2 Lemmas in Proof of Theorem 4.4 . . . 139

List of Figures

2.1 The schematic diagram of network of Jansen's model studied in Chapter 2 26
2.2 Bifurcation diagram for the symmetric solution for Case I with coupling gain $K = 25$. 31
2.3 Equilibria curves for asymmetric solutions of case I with coupling gain $K = 25$. 32
2.4 Bifurcation diagrams arising from the asymmetric equilibria for Case I with coupling gain $K = 25$. 33
2.5 Magnified parts from bifurcation diagrams in Figure 2.4 34
2.6 Bifurcation diagram of Case I with coupling gain $K = 100$. 36
2.7 Bifurcation diagrams arising from the first branch of equilibria in Case I with coupling gain $K = 150$. 37
2.8 Equilibria and bifurcation diagrams for Case II with coupling gain $K = 50$. 40
2.9 Magnified parts from the bifurcation diagram of the third branch of equilibria in Figure 2.8C and Figure 2.8F. 41
2.10 Magnified parts from the bifurcation diagram of the third branch of equilibria in Figure 2.9C_1. 42
2.11 Bifurcation diagrams for case II with coupling gain $K = 250$. 44
2.12 Magnified parts from the bifurcation diagram of the third branch of equilibria in Figure 2.11C and F. 45
2.13 Bifurcation diagrams for Case III with coupling gain $K = 50$. 47
2.14 Magnified parts from the bifurcation diagram of the third branch of equilibria in Figure 2.13C and Figure 2.13F. 48
2.15 Bifurcation diagrams for Case II with coupling gain $K = 250$ 49
2.16 Recorded ECoG from two channels for seizure one and the bifurcation diagrams. 53
2.17 Recorded ECoG from two channels for seizure two and the bifurcation diagrams. 54

3.1 Schematic diagram of two interconnected Wilson-Cowan models [129] . . 65
3.2 The stability and instability regions of the system (3.16) for the example in Section 3.6. 80
3.3 Five diffusively coupled Wilson-Cowan oscillators for the example in Section 3.6 80
3.4 The trajectories of heterogeneous Wilson-Cowan network depicted in Figure 3.3 (a). 81

3.5 The trajectories of heterogeneous Wilson-Cowan network depicted in Figure 3.3 (b) and coupling gain $k = 1.2$. 82
3.6 The trajectories of heterogeneous Wilson-Cowan network depicted in Figure 3.3 (b) and coupling gain $k = 1.8$. 82

4.1 A directed graph with 12 nodes in Example 1 in Chapter 3. 88
4.2 A directed graph studied in Example 2. The solid arrows represent the positive weight edges while the dashed arrows show the edges with negative weights. All positive and negative weights are set equal to 2 and -1, respectively. 99
4.3 The Nyquist diagram in Example 2. 100
4.4 A directed graph studied in Example 3. The solid arrows represent the positive weight edges while the dashed arrows show the edges with negative weights. All positive and negative weights are set equal to 2 and -1, respectively. 101
4.5 The Nyquist diagrams in Example 3. The left Nyquist diagram corresponds to the first scenario with the graph in Figure 4.4(a), while the right Nyquist diagram corresponds to the second scenario with the graph in Figure 4.4(b). 102
4.6 An equivalent electrical circuit for a connected undirected graph with non-negative weights. 105
4.7 An equivalent electrical circuit for a connected undirected graph with single negative wieght and non-negative weights. 105
4.8 A schematic diagram of the connections between the nodes in a graph whose negative edges meet conditions in Theorem 4.4. 107
4.9 A directed signed graph studied in Example 3 in Chapter 3. 109
4.10 Evolution of node states over time for a network with the graph in Example 1. The perturbation between two nodes 3 and 8 set equal to $\delta_{38} = 1.5$. . 110
4.11 Evolution of node states over time for a network with the graph in Example 1. The perturbation between two nodes 3 and 8 set equal to $\delta_{38} = 1.95$. 110

A.1 Detecting a saddle-node homoclinic bifurcation. 119
A.2 The values of $\Upsilon(y^b, K)$ defined in A.7 121
A.3 Equilibria of second region for case II and for different values of coupling gain K. 122

Preliminaries and Graph Notation

0.1 Preliminaries

Throughout this thesis, $I_N \in \mathbb{R}^{N\times N}$, $\mathbf{1}_N \in \mathbb{R}^N$, and $\mathbf{0}_N \in \mathbb{R}^N$ denote the $N \times N$ identity matrix, the N-dimensional vectors containing 1, and 0 in every entry, respectively. The standard bases in $\mathbb{R}^N$ are represented by $\{\mathbf{e}_1, \ldots, \mathbf{e}_N\}$ where $\mathbf{e}_i$ is the i^{th} column of I_N. The 2-norm of a vector $x \in \mathbb{R}^N$ is shown by $\|x\|$. The entry in the i^{th} row and j^{th} column of a matrix A is represented by $[A]_{ij}$. $[A]_i$ denotes the i-th row of matrix $A \in \mathbb{R}^{N\times M}$, while the i^{th} entry of a vector x is denoted by $[x]_i$. The Kronecker product of two matrices $A \in \mathbb{R}^{N\times M}$ and $B \in \mathbb{R}^{P\times Q}$ is a matrix $C \in \mathbb{R}^{NP\times MQ}$ that is defined as,

$$C = A \otimes B = \begin{bmatrix} [A]_{11}B & \ldots & [A]_{1M}B \\ \vdots & \ddots & \vdots \\ [A]_{N1}B & \ldots & [A]_{NM}B \end{bmatrix}.$$

For a complex variable, vector or matrix, $\Re(\cdot)$ and $\Im(\cdot)$ stand for their real and imaginary parts. For a matrix $A \in \mathbb{R}^{N\times N}$, $\mathrm{Spec}(A) = \{\lambda_i(A)\}_{i=1}^N$ denotes the set of eigenvalues of A where $\Re(\lambda_1) \le \Re(\lambda_2) \le \cdots \le \Re(\lambda_N)$. An eigenvalue $\lambda_i(A)$ is called semisimple if its algebraic and geometric multiplicities are equal (see [19, Definitions 4.4.4 and 4.5.1]). The operator $\mathrm{diag}(\cdot)$ constructs a block diagonal matrix from its arguments. For a set $\mathcal{A}$, its cardinality is denoted by $|\mathcal{A}|$.

0.2 Graph Notation

A weighted directed signed graph $\mathcal{G}$ is represented by the triple $\mathcal{G}(\mathcal{V}, \mathcal{E}, \mathcal{W})$ where $\mathcal{V} = \{1, \ldots, N\}$ is the nodes set, $\mathcal{E} \subset \mathcal{V} \times \mathcal{V}$ is the edge set, and $\mathcal{W} : \mathcal{V} \times \mathcal{V} \to \mathbb{R}$ is a weight function that maps each $(i, j) \in \mathcal{E}$ to a nonzero scalar a_{ij} and returns 0 for all other $(i, j) \notin \mathcal{E}$. The adjacency matrix $A \in \mathbb{R}^{N \times N}$ captures the interconnection between the nodes in the graph where $[A]_{ij} = a_{ij} \neq 0$ iff $(i, j) \in \mathcal{E}$. For the edge (i, j), we follow the definition corresponding to a sensing convention which indicates that node i receives information form node j or equivalently, the node j influences the node i; see [137] for more information. For each node $i \in \mathcal{V}$, $\mathcal{N}_i$ denotes the set of its neighbours, i.e., $\mathcal{N}(i) = \{j \mid a_{ij} \neq 0\}$.

For a given graph $\mathcal{G}(\mathcal{V}, \mathcal{E}, \mathcal{W})$ and a set $\overline{\mathcal{V}} \subseteq \mathcal{V}$, the induced subgraph is defined as follow.

Definition 0.1. *(Induced subgraph) For a given graph $\mathcal{G}(\mathcal{V}, \mathcal{E}, \mathcal{W})$ and a set $\overline{\mathcal{V}} \subseteq \mathcal{V}$, the corresponding induced subgraph is denoted by $\mathcal{G}(\overline{\mathcal{V}}, \overline{\mathcal{E}}, \overline{\mathcal{W}})$, where the set $\overline{\mathcal{E}}$ is defined as $\overline{\mathcal{E}} = \{(i, j) \in \mathcal{E} \mid i, j \in \overline{\mathcal{V}}\}$, and $\overline{\mathcal{W}} : \overline{\mathcal{V}} \times \overline{\mathcal{V}} \to \mathbb{R}$ is defined as $\overline{\mathcal{W}}(i, j) = \mathcal{W}(i, j)$.*

In order to categorize edges in terms of the sign of their values, we define the sets $\mathcal{E}^+ = \{(i, j) \mid a_{ij} > 0\}$, and $\mathcal{E}^- = \mathcal{E} \backslash \mathcal{E}^+ = \{(i, j) \mid a_{ij} < 0\}$. We call the edges in $\mathcal{E}^+$ and $\mathcal{E}^-$ positive edges and negative edges, respectively. Subsequently, for a signed graph $\mathcal{G}(\mathcal{V}, \mathcal{E}, \mathcal{W})$, we denote the subgraph with non-negative weights by $\mathcal{G}(\mathcal{V}, \mathcal{E}^+, \mathcal{W}^+)$ where $\mathcal{W}^+ : \mathcal{V} \times \mathcal{V} \to \mathbb{R}_{\geq 0}$ is defined as $\mathcal{W}^+(i, j) = \mathcal{W}(i, j)$ for all $(i, j) \in \mathcal{E}^+$ and $\mathcal{W}^+(i, j) = 0$ for all $(i, j) \notin \mathcal{E}^+$. Similarly, for a signed graph $\mathcal{G}(\mathcal{V}, \mathcal{E}, \mathcal{W})$, we denote the subgraph with non-positive weights by $\mathcal{G}(\mathcal{V}, \mathcal{E}^-, \mathcal{W}^-)$. The superposition of two weighted graphs is defined as follow.

Definition 0.2. *The superposition of two signed directed graphs $\mathcal{G}_1(\mathcal{V}, \mathcal{E}_1, \mathcal{W}_1) \oplus \mathcal{G}_2(\mathcal{V}, \mathcal{E}_2, \mathcal{W}_2)$ is a new graph $\mathcal{G}(\mathcal{V}, \mathcal{E}, \mathcal{W})$ where $\mathcal{E} = \mathcal{E}_1 \cup \mathcal{E}_2$ and, $\mathcal{W}(i, j) = \mathcal{W}_1(i, j) + \mathcal{W}_2(i, j)$ for every $(i, j) \in \{\mathcal{V} \times \mathcal{V}\}$.*

The Laplacian matrix is defined as follows.

Definition 0.3. *The Laplacian matrix $L \in \mathbb{R}^{N \times N}$ is defined by*

$$L = D - A, \tag{1}$$

where $D = diag\{d_1^{out}, \dots, d_N^{out}\}$. $d_i^{out} = \sum_j a_{ij}$ *is the out degree of node* i.

Since the rows of the Laplacian matrix add to zero, $\mathbf{1}_N$ is always one of its eigenvectors that corresponds to the eigenvalue 0. This eigenvalue is called the trivial eigenvalue while the rest of eigenvalues is called non-trivial eigenvalues.

Let $\Pi = I_N - \frac{1}{N}\mathbf{1}_N\mathbf{1}_N^T$ denote the orthogonal projection matrix onto the subspace of $\mathbb{R}^N$ perpendicular to $\mathbf{1}_N$. The matrix Π is symmetric and since $L\mathbf{1}_N = \mathbf{0}$, $L\Pi = L$ and $\Pi L^T = L^T$ for any graph. We define a matrix $Q \in \mathbb{R}^{(N-1)\times N}$ whose rows are the orthonormal bases for $\text{span}\{\mathbf{1}_N\}^\perp$ where $\perp$ denotes the orthogonal complement of the space. Hence, Q^T is a full column rank matrix. On $\text{span}\{\mathbf{1}_N\}^\perp$, the Laplacian matrix is equivalent to the so-called *reduced Laplacian* $\bar{L} \in \mathbb{R}^{(N-1)\times(N-1)}$ which is defined by [137],

$$\bar{L} := QLQ^T. \tag{2}$$

A *path* of length r from $i_1 \in \mathcal{V}$ to $i_r \in \mathcal{V}$ in graph $\mathcal{G}$ is a sequence $(i_1, i_2, \dots, i_r)$ of distinct nodes in $\mathcal{V}$ where i_{j+1} is a neighbour of i_j for all $j = 1, \dots, r-1$. If there exists a path (no path) from the node j to the node i, then the node i is (not) reachable from node j. We use $j \nrightarrow i$ ($j \nrightarrow i$) to show the existence (absence) of path from j to i. A node i is a globally reachable node if it is reachable from all other nodes of the graph. Similar to [137], we say that two nodes i and j are connected if the graph contains two paths $i \nrightarrow k$ and $j \nrightarrow k$ with $k \in \mathcal{V}$[1]. The graph $\mathcal{G}$ is connected if every pair of nodes is connected. This notion of a connected graph corresponds to the scrambling matrices [111]. It has been shown that the graph is connected if and only if there exists at least one *globally reachable node*; the node, to which, there exists at least one path from every node in the graph [137]. A graph $\mathcal{G}$ is strongly connected if for every $i \in \mathcal{V}$ and $j \in \mathcal{V}$, $i \nrightarrow j$. Hence, the graph $\mathcal{G}$ is strongly connected if and only if every node of the graph is a globally reachable node.

[1] Note that k can be any node (including i and j) of the graph.

Chapter 1
Introduction

Complex networks arise in a wide range of applications where many subsystems interact with each other . Examples are numerous. The Internet is one of the largest complex networks in which a large number of devices are linked. A social network is another example of a complex network that contains many interacting people. Perhaps the most complicated natural network is the brain which consists of many neurons. Despite their diversity, complex networks have a common feature: they consist of many interconnected subsystems.

Instead of talking about behaviours of each subsystem individually, we can talk about collective behaviours in complex networks; the behaviours which are observed among a group of subsystems. Synchronisation is regarded as a collective behaviour that occurs when the states or outputs of subsystems converge to the same behaviour. Synchronisation can also be considered as the asymptotic stability of error vectors between the state (or output) vectors of two or more subsystems. Synchronisation is a ubiquitous phenomenon observed in diverse networks of interconnected subsystems that arise in neuroscience, physics, biology, social networks, and so on. In order to synchronise a group of subsystems[1], information is transferred between the subsystems. Hence, both the dynamics of each subsystem and the structure of the network affect the presence or absence of synchronous behaviour.

Mathematical models are crucial for analysing complex networks. Rigorous analysis of such networks is sophisticated due to large numbers of subsystems. Hence, the network analysis is often carried out by splitting it into two parts to reduce the complexity.

[1]It is also called a group of individuals, group of compartments or group of species in the literature.

In the first part, the dynamical properties of each subsystem are investigated from an input-output perspective. These properties generally facilitate the analysis in the second part in which every subsystem is treated as a node in a graph, and their interconnections are modelled as the edges. When it comes to the analysis of synchronisation (and also stability), there are some important factors which simplify or complicate the analysis and, lead to different types of synchronisation. These factors include, but are not limited to:

- **Heterogeneity or homogeneity of subsystems**
  In almost all applications, underlying networks contain non-identical subsystems, meaning that different mathematical models are used to describe each subsystem. For example, the brain consists of different types of neurons, i.e. excitatory and inhibitory[2] ones, which have different working mechanisms and are described by different mathematical models. Even the same type of neurons may have different parameters in their models leading to a heterogeneous network. While heterogeneous networks are more realistic, their analyses involve more complexity than homogeneous networks [91, 92, 100, 128, 141].

- **Presence of delay between subsystems interactions**
  The presence of a delay is a common feature in all networks. As mentioned earlier, the exchange of information is necessary to synchronise subsystems in a network. In synchronisation of multi-agent systems, outputs of each agent are measured with sensors and transmitted to neighbour agents that have communication delay [98]. The time needed to transmit the information is a source of delay in the network of neurons [87].

- **Existence of positive and negative coupling between subsystems**
  Interaction between subsystems in a network is usually modelled by coupling weights that can be either positive or negative. In the context of social science, a positive/negative weight models friendship/enmity relation between two members in

[2]Neurons are connected to each other in a synaptic network. Signals exchanged by neurons are spike trains. Spike trains coming from pre-synaptic neurons generate a post-synaptic potential (PSP). PSP can be either positive or negative. For excitatory neurons, Spikes coming from pre-synaptic neuron increase the membrane potential of the post-synaptic neuron which more likely leads to generating spike trains. For inhibitory neurons, PSP can be negative. The spike train response of the post-synaptic neuron propagates to other neurons [32].

a network [6, 140]. In networks of neurons, one possible way to model interaction between inhibitory and excitatory neurons is to use negative weights, indicating the differences between synapses [129]. Generally, networks with both positive and negative interconnections are called "signed networks" in the context of network science.

The main objective of this thesis is to establish tools to rigorously study synchronisation in complex networks. This thesis is motivated by synchronisation in neural networks as it contributes to different mechanisms in the body. Circadian rhythms in the mammals is an example in which synchronisation of neurons plays a crucial role in body regulation [83]. Furthermore, it is thought to play a key role in information integration and processing. Synchronisation of distributed brain regions has been speculated to play an important role in cognition [105]. On the other hand, synchronising between neurons can lead to some brain disorders such as epilepsy which is regarded as the most common neurological disease after stroke.

It is widely reported that a group of neurons becomes synchronised during seizure, although the main mechanism that leads to epilepsy is still unknown. Synchronisation results in spike-like waveform observed in electroencephalogram (EEG) signals, while the neurons are more asynchronous during the normal brain activity. The hallmark of epilepsy is recurrent unprovoked seizures, during which the brain is "hyperexcitable" [16]. Medication is the main method for controlling epilepsy. Surgery is another option for some patients whose problems continue despite taking medicine; however, surgery may cause memory problems for patients [74]. Hence, much research has been carried out on neurostimulation as an alternative method to suppress seizures. In this regard, understanding the mechanisms of seizures is an important step.

The analysis of complex networks requires mathematical models of the network that can be determined by knowing (i) a mathematical model of each subsystem, and (ii) a mathematical description of interconnections between subsystems. Hence, both the dynamics of each subsystem and the structure of the network (coupling configuration) affect the presence or absence of synchronisation in the network.

Considering the description above, in what follows, we overview the mathematical

models of neurons and neural populations that have been reported in the literature in Section 1.1. Section 1.2 presents different notions of synchronisation and different approaches which have been used to study synchronisation in complex networks. This section also includes the literature overview on the relation between network structures and synchronisation. In Section 1.3, the outline of the thesis is presented.

1.1 Neurons and Neural Mass Models

In the context of computational neuroscience, the main goal is developing a computational model that can describe the brain activity and structure. Mathematical models can be classified into two general groups: microscopic models and macroscopic models.

At the microscopic level, neurons communicate through synapses by spontaneous variations of membrane potential which is known as action potential or nerve impulses. These mechanisms of communication have been studied in models of firing neurons. The Hodgkin-Huxley model [73] and its simplified model [56], enable us to understand and simulate mechanisms that reproduce the neuronal behaviour in the generating action potential. The well-known Hindmarsh-Rose model of neuronal activity is aimed at studying the spiking-bursting behaviour of the membrane potential observed in experiments made with a single neuron [72]. It is also possible to study the overall behaviour of a neuronal population using networks of microscopic models [27, 122]. Since microscopic models of the brain are computationally expensive, macroscopic models are often utilised to study large-scale brain behaviours.

A macroscopic model of the brain that produces the average behaviour of the brain was first developed by Wilson and Cowan [135], and was generalized by Da Silva et al. [39]. This type of model has been used by other researchers to study brain activity. Jansen and Rit discovered that this model was able to simulate evoked potentials by adding mathematical expression of excitatory and inhibitory populations along with pyramidal model [76]. Wendling et al. [133] showed that Jansen and Rit's model can repli-

cate the alpha-activity [3] and spike-activity [4] of brain that are observed in the EEG signal. They also extended a single population to multiple populations by interconnecting each population. They observed that for high values of interconnection gains, all passive populations are synchronised to a reference population that has been previously activated by exerting an external input. They concluded that the alpha activity and spike wave activity can be obtained by changing either the model parameters or the external input of the population, which captures the effect of the neighbouring populations. The effect of parameter changes on responses of Jansen and Rit's model has been investigated in [127]. This model can show other brain activities such as theta [5]. Using bifurcation analysis, it was also showed that the functional connectivity is increased during epilepsy [20]. Behaviour of Jansen and Rit's model with respect to the input has been investigated through bifurcation analysis [65]. It was observed that Jansen and Rit's model undergoes two bifurcations, *Hopf bifurcation* and *Homoclinic bifurcation*, by changing the input, which results in the appearance of two different limit cycles in the phase space of the system. The system shows periodic output resembling alpha-like signals when the system undergoes a Hopf limit cycle. The Homoclinic cycle determines periodic spike-like behaviour of systems.

An approach to study oscillatory behaviour of neural populations is to approximate them by nonlinear oscillators. One class of nonlinear oscillators is the *Kuramoto oscillator*, which has been frequently adopted in diverse applications such as stability of power networks [51] and flocking models [66]. This approximation has been applied to a network of the *Wilson-Cowan* models to investigate the effect of connectivity gains in phase synchronisation of populations [40, 135]. To this end, each neural population was approximated with a Kuramoto Oscillator, characterised by natural frequency and phase, around its limit cycle. Consequently, the relation between interconnection gains of these two networks was obtained; however, the phase synchronisation was not investigated

[3] Alpha waves are neural oscillations in the frequency range of 7.5 – 12.5 Hz that are detected by EEG during wakeful relaxation with closed eyes. See [62] for more information.

[4] Spike-and-wave is the term that describes a particular pattern of EEG typically observed during epileptic seizures. The frequency of the signal is about 3 Hz. See [2] for more information.

[5] Theta waves are neural oscillations in the frequency range of 4 – 7 Hz that are detected by EEG during meditative, drowsy, hypnotic or sleeping states. See [130] for more information.

analytically. The problem of desynchronisation for general networks of interconnected Kuramoto oscillators was studied in a rigorous manner in [57]. In [38], the generalised network of Kuramoto models has been utilised for the study of synchronisation in the brain. The authors considered different types of distribution for natural frequencies and connection gains and then analysed phase synchronisation through simulation results. A more general case of the Kuramoto model, which is known as the *Canonical model* of coupled limit-cycle oscillators, can be taken to analyse the oscillatory behaviour of dynamical systems. This model is obtained by calculating the phase response curve of the system around the limit cycle [53]. Therefore, it serves as an analysis tool for general limit cycles [52]. The Canonical models of different types of neurons have been presented in [25]; however, only uncoupled neurons were considered.

1.2 Synchronisation in Dynamical Systems

Analysis of complex networks usually follows a "divide and conquer approach". First, each subsystem is considered as a node in a graph and input-output properties of each node are investigated. Then, properties of the graph along with input-output properties are combined to analyse the network. Different input-output properties can be investigated in the first step that with considering graph properties and mechanisms of interconnections may lead to different types of synchronisation. We present an overview of the available results on these topics.

1.2.1 Dynamical Properties for Analysing Synchronisation

Generally, synchronisation is achieved if the difference between states (outputs) of subsystems converges to zero. This means that the study of synchronisation can be seen as a stability study of a "synchronisation subspace" in which all states (outputs) are equal. Hence, the presence/absence of synchronisation can be studied by using approaches which are utilised to study the stability of dynamical systems with respect to sets [69,121]. A well-known notion of input to state stability (ISS) is utilised to study robust stability of nonlinear dynamic systems. This concept, which was first introduced in [117], is a

useful tool for studying the stability of interconnected systems [77]. Comparing the difference between responses of a system resulted in the concept of incremental-ISS (δ-ISS) that determines how the system trajectories converge to another, while being attracted toward some equilibrium points [7]. On the other hand, the convergence property is defined based on the convergence of all trajectories of a system to a specific solution of the system [101]. Although it seems that these two concepts are the same, they are in fact different and some conditions must hold to imply one notion from the other [106]. These two concepts have been applied to synchronisation applications. In [7], δ-ISS has been applied to provide the condition for synchronisation of two coupled chaotic systems. This notion has been applied to synchronise the network of identical nodes in which each subsystem has been assumed to be δ-ISS [29]. To the best of our knowledge, it is still a challenge to study application of these two notions for more complex networks.

The dissipativity property of dynamical systems, introduced by Willems [134] and extended in [71], is regarded as a useful tool in stability analysis of complex networks. Due to the input-output property of dissipativity and its special case, passivity, the analysis of complex networks can be carried out at two levels: the component level and the network level [12]. At the component level, each subsystem is analysed using a state space model to check whether it possesses a particular input-output property. At the network level, the subsystems are represented as vertices of a network graph, and then the stability of the underlying network is analysed. Stability of interconnected passive systems was investigated for some simple feedback configurations in [119]. Stability of these configurations was determined from the diagonal stability of a so-called dissipativity matrix. Motivated by a class of biochemical reaction networks, this approach was extended to stability analysis of other interconnected systems [11, 15]. Diagonal stability of a dissipativity matrix for cyclic systems can be examined by the secant criterion [14,118]. Although the dissipativity-based approach can be also utilised to determine stability of more complex networks, it is still an open problem to obtain necessary and sufficient conditions for checking the diagonal stability for general networks. However, some results were recently proposed for interconnected systems whose digraphs are cactus structure [13] and the graphs with connected circles in which two different loops can have a common

edge [131].

The notion of dissipativity and its incremental version was utilised to study global synchronisation of networks of oscillators in cyclic feedback systems. Motivated by the cellular network, the problem of output feedback synchronisation was considered using the notion of incremental output-feedback passivity [121]. This notion was extended to the so called cocoercive property in order to study synchronisation in networks of identical nodes [109]. To deal with the network with non-identical nodes, mutual relaxed co-coercivity was proposed, which is a generalisation of cocercivity for a network with mild heterogeneity [57].

Passivity and incremental passivity can be applied to cyclic interconnected systems with negative feedback; however, these notions are not suitable for the analysis of systems with positive feedback since it is impossible to show positive feedback of some passive or incrementally passive systems remains passive or incrementally passive. To study a system with positive feedback using the input-output approach, the notion of counterclockwise (CCW) property was recently introduced [8]. It was utilised to study stability analysis of biological systems and neural networks [9,10]. The cascade and positive feedback interconnections of CCW systems are CCW. It is worth noting that the CCW property is a property different from passivity. Semi-passivity is another dynamic property that has been exploited to study synchronisation in coupled neurons [123]. Similar to the passivity property, this property guarantees the boundedness of solutions, even when the system evolves in the network. Semi-passivity is milder than passivity, however it is not possible to show that the positive feedback of two semi-passive systems remains semi-passive.

Contraction of nonlinear dynamical systems is another property which is useful to study of synchronisation [47, 116, 132]. Contracting systems have the following property; for every input, all trajectories converge to a unique trajectory that implies that the contracting network reaches complete synchronisation or consensus at the end. This property of dynamical system has been utilised to study synchronisation in the network of coupled oscillators and the network of FitzHugh-Nagumo neural models [116, 132].

Synchronisation was also studied by assuming that a quadratic type inequality, called

QUAD conditions[6], holds for each subsystem. It was proven that this condition is sufficient for synchronisation of identical systems [44, 45]. The QUAD condition is the weakest condition compared to global Lipschitzness or contraction. It was shown that if a dynamical systems is contacting or globally Lipschitz, then it is also QUAD [44]. Many well-known systems possess this property such as Lorenz system, Van der Pol oscillator. This property was used to study practical synchronisation for hetregenous networks [93]. For the sake of completeness, we summarise the dynamical properties of neural populations models in Table 1.1.

Table 1.1: Dynamical properties of neuron/neural population models.

Model	Dynamical property
Hodgkin-Huxley	Semi-passive [123]
FitzHugh-Nagumo	Semi-passive [123]
Hindmarsh-Rose model	Semi-passive [123], relaxed co-coercive [57]
Wilson-Cowan	Globally Lipschitz and therefore QUAD, Contracting for some values of parameters [33]
Jansen and Rit	Globally Lipschitz [35] and therefore QUAD

1.2.2 Synchronisation, Network Structure and Signed Graphs

As mentioned earlier, two factors have a significant impact on presence or absence of synchronisation in complex networks: dynamical models of network nodes and network topology. In particular, investigating the effect of the latter has attracted much research in the systems and control community, and it is still an ongoing problem [18, 103]. More recently, this point has been explored in neuroscience using a computational model of the brain [125]. It has been observed that, in the network of oscillators, removing or adding interconnections between nodes can lead to the disappearance or persistence of

[6] Assume that the dynamic of each subsystem is represented by $\dot{x}_i = f_i(x_i, t) + u_i$, where $x_i \in \mathbb{R}^{n_i}$ and $u_i \in \mathbb{R}^{n_i}$ are the state and the input of the subsystem i. A function $f : \mathbb{R}^{n_i} \times \mathbb{R}^+$ is QUAD(Δ, ω) if and only if, for any $z, y \in \mathbb{R}^{n_i}$,

$$(z-y)^T[f(z,t) - f(y,t)] - (z-y)^T\Delta(z-y) \leq -\omega(z-y)^T(z-y),$$

where $\Delta\mathbb{R}^{n_i \times n_i}$ is a diagonal matrix and ω is a real positive scalar.

synchronous activity in the system. However, all these observations have been obtained only by simulations.

To investigate how the network structure affects the presence/absence of synchronisation, first, the network model should be derived by considering the type of interconnection between all subsystems. For some neural/neural population (and many applications in control), the evolution of the states of each subsystem (neural population or neuron) is primarily influenced by the relative information from its neighbours. This type of interconnection is mathematically described by the Laplacian matrix that captures the structure of the network graph. In general, this graph can be directed with both positive and negative weights. For example, in the network of neurons, the connections between presynaptic neurons and postsynaptic neurons are directed. Furthermore, the coupling weights between excitatory neurons to other neurons are positive while the coupling weights between inhibitory neurons to other neurons are negative [75, 105]. In the context of network science, this type of networks is called directed signed networks and the graph structures is refereed to as a directed signed graph.

In most cases, the absence or presence of synchronisation needs the eigenvalues of the Laplacian matrix to be located in some specific regions which are obtained from analysing the network. For instance, it is well-known that synchronisation in a network of integrators, known as consensus, can be reached if and only if the Laplacian matrix is allowed to have a single zero eigenvalue with all non-zero eigenvalues having positive real parts [97]. This type of network is employed to model the evaluation of opinion in social networks. Synchronisation in the network of linear and nonlinear systems highly depends on the structure of network which itself determines the eigenvalues of the Laplacian matrix [18]. In most studies such as ones in [110,113] and networks of Wilson-Cowan neural populations in Chapter 3, synchronisation cannot be guaranteed if the Laplacian matrix has an eigenvalue with negative real part [110,113]. The existence of both positive and negative weights also leads to clustering in the network that can be demonstrated in terms of eigenvectors and eigenvalues of the Laplacian matrix [114, 136].

Thus, the spectral characterisation of the Laplacian matrix has been a subject of many research activities and it is well-understood for undirected graphs with non-negative

weights [36]. For directed graphs with positive weights, there is a relation between the so-called normalized Laplacian matrix and the stochastic matrices that is employed to explore the locations of eigenvalues of the Laplacian matrix [3, 26, 31]. In the presence of negative weights, this relation is hard to establish and, consequently, the spectral characterisation of Laplacian matrix becomes more challenging. For undirected graphs, there exist powerful results that mainly provide bounds on the number of negative and positive eigenvalues [17, 22, 23]. Recently, a connection between the number of positive eigenvalues of the Laplacian matrix and negative weights has been developed for undirected graphs in [24]. More specifically, it has been proven that the number of positive eigenvalues equals the number of negative weights in the graph minus the number of positive eigenvalues of the associated cycle intersection matrix [24, Theorem 2.9]. However, no conditions on the magnitude of the negative weights has been identified to ensure the existence of eigenvalues with negative real parts.

In some applications, e.g. see [110, 113, 128], the objective is to prevent the Laplacian matrix from having eigenvalues with negative real parts. Robustness of uncertain undirected networks was recently studied where the negative weight was incorporated as uncertainty in the network. Under certain assumptions on the distribution of negative weights, robustness of network was also analysed in the presence of multiple negative weights [140]. It has been argued that these results can be interpreted using the notion of effective resistance originally introduced in electrical networks [82]. Recently, this work has been extended to undirected graphs with arbitrary distribution of negative weights [34]. Robustness of uncertain directed signed networks was studied in [95].

1.2.3 Various Versions of Synchronisation

The most common type of synchronisation in the literature is complete synchronisation which has been studied for diverse applications such as formation control [55], biochemical networks [15, 69, 109] and networks of neurons [116, 123]. The synchronisation criteria are defined with respect to the relative difference of subsystems outputs (states) which is called as output (state) synchronisation [15, 109], and it is complete since the goal is to provide conditions that guarantee the outputs (states) of all subsystems reach to a com-

mon output (state).

In almost all existing results, the most common assumption is that all subsystems of the network are identical. Under this assumption, the analysis of network can be reduced to analysis of a lower dimensional system. However, the collective behaviour of a heterogeneous networks is more complicated than a homogeneous network and, consequently, the analysis of a network with non-identical nodes is more elaborate than analysis of a homogeneous network. Although many results exist on complete synchronisation of homogeneous networks, there are few studies on this type of synchronisation for heterogeneous networks [48,141,142].

Conditions for complete synchronisation of heterogeneous networks are hard to satisfy. Moreover, complete synchronisation of a heterogeneous network is possible by solely diffusive coupling, but using infinite gains [68]. Hence, the concept of practical synchronisation has been introduced that is easier to satisfy in heterogeneous networks [93,124]. In this type of synchronisation, all subsystems reach behaviours such that the synchronisation error is ultimately bounded by some positive scalar. It was shown that it is possible to design coupling between subsystems so that the synchronisation error becomes small enough; however the crucial assumption is that all subsystems in the network should satisfy the QUAD condition [93].

Cluster or partial synchronisation is another type of synchronisation which has attracted significant attention. This type of synchronisation is associated with the emergence of different subgroups or clusters in the network such that all subsystems in the same cluster become completely synchronised or practically synchronised with respect to each other. However, subsystems in different clusters are desynchronised [43, 136]. This type of synchronisation has been observed in many applications including flocking of birds [49], opinion agreement in social science [70, 91], and networks of neurons and neural oscillators populations [1, 79]. In particular, there is empirical evidence that synchronised behaviour is observed in some regions of brain cortex (not necessarily in the whole brain) during epilepsy or Parkinson that can be regarded as cluster synchronisation [99,126]. Generally, there are three mechanisms that lead to clustering; heterogeneity of subsystems in the network, the presence of delay between subsystems interactions,

and the existence of positive and negative coupling between subsystems [136]. It is also possible to observe this phenomenon in the homogeneous network. To this end, the negative couplings should be considered beside the positive ones. Clustering in the signed network for consensus problem was studied in [114, 136]. However, characterising complete synchronisation in signed networks is still an ongoing problem.

In some applications, such as power systems or network of neurons, the synchronisation criteria are defined based on relative differences of phases between subsystems, which is known as phase synchronisation or phase-locking [42, 50]. For instance, it was observed that the phase synchrony is increased in small neighbouring cortical areas in the recording from the patient during the seizures. However, distant synchrony (phase synchrony in cortical areas) may not increase during the seizure. This implies that the phase synchronisation can be used to predict the occurrence of focal seizure [50, 143]. In order to measure phase synchronisation or phase-locking, some definitions were proposed. As far as we are aware, there is no connection between output (state) synchronisation and phase synchronisation or phase-locking in general. However, the complete output synchronisation implies phase synchronisation or phase-locking.

1.2.4 Mechanisms of Synchronising, Global Synchronisation Versus Local Synchronisation

Two fundamental mathematical models of synchronisation can be found in the literature: the diffusive model and the kick model [89]. In the diffusive model, the synchronisation happens due to a so-called diffusive coupling which uses the difference between outputs (or states) of subsystems as inputs of each subsystem. Indeed, diffusive coupling aims at reducing the difference between outputs of all subsystems in a network [112]. In contrast, in the kick model, the synchronisation occurs due to applying short and weak pulses. This type of coupling is usually considered in synchronisation of pulse-coupled oscillators which was used to model flashing fires [28] and neurons [63]. The network containing continues subsystems with the kick coupling can be seen as a hybrid model as the kick coupling has an impulsive nature [96].

While various approaches have been developed to study different types of synchro-

nisation in complex networks, they can be categorised into two groups: global and local. As mentioned at the beginning of Section 1.2, the first step of the analysis of complex network is to investigate whether subsystems of the network satisfy properties, such as passivity [11,15] and dissipativity [12], which leads to treating each subsystem in the analysis from the input-output perspective. Then synchronisation conditions can be obtained by considering the structure of the network along with the input-output behaviour of each subsystem. If those properties are satisfied globally (locally), then the obtained conditions guarantee the presence (or absence in some cases) of synchronisation for all (some) initial conditions. In this case, the network reaches global (locally) synchronisation. In some applications, it may be challenging to demonstrate that properties such as passivity or dissipativity are satisfied globally or locally.

Furthermore, the interest might be to study synchronisation with respect to an invariant set such as a limit cycle which is responsible for generating a specific behaviour among subsystems in the network. In these situations, there are a few local approaches that are useful alternatives.

One possible approach for a local study is to approximate the model by nonlinear oscillators which can be achieved by computing the phase response curve of subsystems around the limit cycle [25, 52]. Another promising local approach is to linearise the model of the whole network around an existing limit cycle in the dynamic of each subsystem. In this way, synchronisation in a network of oscillators can be analysed via the well-known master stability equation (MSE) [102]. The stability of MSE depends on the model parameters and network topology that has previously been evaluated using numerical approaches, which are computationally intensive. However, a possible way to reduce computational effort would be to combine analytical methods with numerical tools. Synchronisation of a network of oscillators with nonlinear dynamics was investigated analytically in [139]. Recently, a framework was proposed to study synchronisation in a network of oscillators by combining both analytical and numerical methods [113].

1.3 Thesis Outline and Contributions

Motivated by the importance of synchronisation in neural population, we first present the bifurcation analysis of a network of Jansen-Rit neural populations in Chapter 2 to explore a range of behaviours that are observed in this network. This study provides insight into assumptions that are needed to analyse this class of model in the network. In order to analyse the synchronisation in a network of neural population, we focus on a network of Wilson-Cowan oscillators in Chapter 3. The reason is that this model is simpler to analyse. We present a framework to locally analyse synchronisation in this class of network in which the interconnections between neural populations are both positive and negative. We overcome the difficulty in analysing the network, that is arisen due to both positive and negative interconnections, by using a trick. The trick allows us to treat the signed network as a network with only non-negative interconnections. Since this trick may not be applicable in some networks, we investigate eigenvalues of Laplacian matrix for a class of directed signed graph in Chapter 4, since eigenvalues of Laplacian matrix play a crucial role in the analysis of complex networks. Summary and future research directions are presented in Chapter 5. The contributions of this thesis are as follows.

Chapter 2:

Previous bifurcation analyses of neural mass models have enabled theoretical and computational studies to reproduce important activity of the brain, providing insights into possible mechanisms underlying transitions between different brain states. It is well known that network structure has a significant effect on cortical dynamics, such as seizure generation. Therefore, a bifurcation analysis to study the behaviour of two interconnected neural mass models is an important step towards understanding how network structure mediates seizure mechanisms.Although bifurcation analyses of networked neural mass models have been previously reported, for instance [30, 90], previous studies used different models such as a Wilson-Cowan neural population. The current study provides a bifurcation analysis of two interconnected Jansen-Rit neural populations, which each consist of three interacting neural populations. Models with three or more popula-

tions exhibit a range of dynamics that align with many different epileptic activities [127]. Furthermore, we show that a wider range of possible behaviours can be observed in the network than in a single region by changing the network configuration and external inputs. Furthermore, we show that unexpected dynamics can occur in the network, which has important implications for epilepsy related surgery. Finally, we show how our analysis is relevant for real world epileptic seizures, by relating the bifurcation diagrams to data using a parameter inference method. The results of this chapter were prepared for submission.

- Saeed Ahmadizadeh, Philippa J. Karoly, Dragan Nešić, David B. Grayden, Mark J. Cook, Daniel Soudry, Dean R. Freestone,*"Bifurcation Analysis of Two Coupled Jansen-Rit Neural Mass Models"*, Submitted to PLOS ONE.

Chapter 3:

In this chapter, we demonstrate that the framework of Shafi et al. [113] can be adapted to study local synchronisation in a network of Wilson-Cowan oscillators with arbitrary coupling strengths. As far as we are aware, this is a new result. Our contribution is fourfold. First, the Wilson-Cowan model does not fit the general model considered in [102,113,139]. As a consequence, the analysis is different. Second, the Wilson-Cowan networks do not synchronise for all coupling gains. Therefore, we had to use an instability result for the linearised model based on the Chetaev theorem to develop a novel proof. This is different from the results in Shafi et al. [113], where local synchronisation was shown for both weak and strong coupling. Furthermore, our results are also different from [139], where the authors presented a sufficient condition for synchronisation that is conservative for our network. Third, we considered the directed coupling between oscillators in the network and our results are general. Fourth, we present sufficient conditions that relate the role of perturbations in the network topology, thereby explaining robustness and absence of synchronisation. The results of this chapter were published in the following conference and journal.

[4] Saeed Ahmadizadeh, Dragan Nešić, Dean R. Freestone, David B. Grayden, *"Ana-*

lytic synchronization Conditions for a Network of Wilson and Cowan Oscillators", 54^{th} IEEE Conference on Decision and Control (CDC), 2015.

[5] Saeed Ahmadizadeh, Dragan Nešić, Dean R. Freestone, David B. Grayden, *"On synchronization of Network of Wilson and Cowan Oscillators with Diffusive Coupling"*, Automatica, 71, 169-178, 2016.

Chapter 4:

Similar to the undirected graphs, we obtain a necessary/sufficient conditions (for some cases necessary and sufficient) which provides an upper bound of negative weights between any pairs of nodes which guarantees that none of the eigenvalues of the Laplacian matrix has a negative real part. It was not possible to employ the machinery employed in [34,140] for undirected graphs to derive the results of this paper as the Laplacian matrix of the directed graphs are not generally symmetric. The employed methodology in [140] has been recently extended to deal with directed graphs [95] where sufficient conditions for the upper bound on a single negative weight has been derived via Nyquist stability criteria. The necessary result of our paper considers the case in which both edges between any arbitrary pairs of nodes are perturbed with negative weights. Our sufficiency result is more general than the main result of [95] since we also allow perturbing two edges between two nodes with the same negative weight to the signed directed graph. Our results cover a more general set of graphs as a graph with multiple negative edges might satisfy the assumption of the theorem, while [95, Theorem 1] only is applied to graphs with no negative edges. Even though the results of our paper are interpreted via Nyquist criteria, our approaches are different from [95]. We also highlight the case where the condition becomes necessary and sufficient. Furthermore, it is argued that for directed graphs, the recently proposed notion of effective resistance [137] is not applicable to interpret the obtained upper bound. By partitioning the nodes of the graph into some sets, we identify "sensitive pairs of nodes" with the following property: If there exists at least one edge with sufficiently small negative weight, the Laplacian matrix has at least one eigenvalue with negative real part. This result is different from the main result in [23, Theorem 2.10]

which established a lower bound and upper bound for the number of negative eigenvalues. The results of this chapter were published in the following journals.

- Saeed Ahmadizadeh, Iman Shames, Sameul Martin, Dragan Nešić,"*On Eigenvalues of Laplacian Matrix for a Class of Directed Signed Graphs"*, Linear Algebra and its Application, 523, 281 – 306, (2017).
- Saeed Ahmadizadeh, Iman Shames, Sameul Martin, Dragan Nešić,"*Correction to : On Eigenvalues of Laplacian Matrix for a Class of Directed Signed Graphs"*, Linear Algebra and its Application (Accepted).

Chapter 2

Bifurcation Analysis of Two Coupled Jansen-Rit Neural Mass Models

2.1 Introduction

The hallmark of epilepsy is recurrent unprovoked seizures, during which a network of the brain is hyper-excitable [16]. Medication is the main treatment for controlling epilepsy. However, approximately 30% of patients are not well treated by anti-epileptic drugs and suffer from recurring seizures. Epilepsy surgery is a treatment option for patients whose seizures continue despite pharmacological interventions. However, surgical intervention is not viable for all patients due to the risks involved in the removal of brain tissue [74]. Hence, there is a strong research effort directed towards alternative methods to control seizures. In order to develop new robust therapies, there is a need to understand the mechanisms that lead to seizures. This has proven to be a difficult problem to unravel from an experimental point of view. Therefore, computational modelling studies are an alternative to understand epilepsy at a network level and generate new hypotheses regarding the basic mechanisms that lead to seizures.

Over the past sixty years, computational neural modelling has contributed to the development of theory that explains brain dynamics at different spatiotemporal scales. Microscopic models, such as those of [73] and [56], describe single neuron dynamics. macroscopic neural mass models have also been developed in parallel to the microscopic models, with notable early contributions from [21], [135], and [86]. Macroscopic, neural mass, or neural field models describe the averaged activity of cortical ensembles. Modelling at the macroscopic scale is particularly important for epilepsy, as this is the scale observed

through clinical electroencephalographic (EEG) and intracranial EEG recordings.

There are numerous studies that have used neural mass models to study epilepsy. The models generate hypotheses regarding the mechanisms that underlie the transitions from normal brain activity to seizures. For example, Wendling et al. [133] used a model proposed in [76] to replicate alpha and epileptic-like activity by changing the model parameters. The same group also developed a multi-region model to study the effect of changing long-range connectivity [133]. They observed that, for high interconnection gains, all regions showed synchronous behaviour that mimicked electrographic seizure recordings. These results motivated other researchers to further develop and investigate neural mass models to reproduce a wider range of observable brain dynamics (see [41,42,120,127] for more information).

Recently, [125] investigated the effects of network structure on seizure spread in a four-region network through computer simulation. Their results demonstrated that seizure spread from an onset region was highly dependent on the structure of the network. Furthermore, altering the network structure by adding or removing interconnections between regions could preserve or annihilate seizures. They also presented a network structure in which some regions show seizure behaviour while the other regions show normal behaviour These results highlight that the configuration of populations in the network significantly affects the initiation and propagation of epileptic seizures. These analyses, based on computer simulations, can be studied more rigorously by tools from control theory [4,5] or by a bifurcation analysis.

Bifurcation analysis enables visualisation of the dynamical repertoire of a computational model undergoing parameter variations. For example, a bifurcation analysis will show where a model that is undergoing parameter changes transitions into different types of oscillations. Bifurcation analysis was used to show how changes in the external input to neural mass models led to alpha-like signals and seizure-like output [65]. More recently, a bifurcation analysis of a neural mass model with variations in a time delay revealed a possible mechanism for the transition from alpha to seizure activity [60]. Understanding how such bifurcations occur is critical in interpreting many high-level brain functions. Using bifurcation analysis, [20] provided evidence that functional connectivity

may be increased during seizures.

In this chapter, we conduct bifurcation analyses for a network of two interconnected neural mass models. This is an important step towards understanding how changes in the network structure and inputs lead to different behaviour some of which are observed during seizure. The results detail the rich repertoire of dynamics that the network can generate including,

1. multiple alpha-like rhythms for all the scenarios considered in this chapter (see Figures 2.2, 2.4, 2.6, 2.7, 2.8, 2.11, 2.13, 2.15);

2. remote spiking in both regions (see Figures 2.2 2.4, 2.6, 2.7, 2.11) or one of them (see Figure 2.15);

3. remote spiking in one region and delta wave in another region (see Figures 2.8, 2.13);

4. remote spiking in one region and transient bursting in another region (see Figures 2.14, 2.15).

This chapter is organised as follows. In Section 2.2, we introduce the multi-region neural mass model that is used in this study. Sections 2.3 to 2.6 present bifurcation analyses for three different settings of inter-connectivity. Section 2.7 relates the estimation results to the bifurcation analyses. Finally, we demonstrate how clinical insights are gained from our new analyses, and discuss future work in Section 2.8.

2.2 Model Description

In this section, we briefly present the mathematical representation of a neural mass model that describes a cortical area. We start from a model proposed by [58] that is used for the estimation result. We explain how this model can be reduced to achieve the well-known model described in previous work [76, 133]. The [58] model contains three parts: pyramidal neurons, excitatory (spiny stellate) neurons, and inhibitory neurons. A pyramidal unit receives input from three sources: distant regions u, an excitatory unit v_e, and an

inhibitory unit v_i. The dynamics of the neural mass model are described by the following set of ordinary differential equations [58],

$$\begin{aligned}
\dot{v}_e &= z_e, \\
\dot{z}_e &= \alpha_{pe} c_{pe} \zeta_{pe} g\left(v_p\right) - 2\zeta_{pe} z_e - \zeta_{pe}^2 v_e, \\
\dot{v}_i &= z_i, \\
\dot{z}_i &= \alpha_{pi} c_{pi} \zeta_{pi} g\left(v_p\right) - 2\zeta_{pi} z_i - \zeta_{pi}^2 v_i, \\
\dot{v}_{p1} &= z_{p1}, \\
\dot{z}_{p1} &= \alpha_{ep} c_{ep} \zeta_{ep} g\left(v_e\right) - 2\zeta_{ep} z_{p1} - \zeta_{ep}^2 v_{p1}, \\
\dot{v}_{p2} &= z_{p2}, \\
\dot{z}_{p2} &= \alpha_{ip} c_{ip} \zeta_{ip} g\left(v_i\right) - 2\zeta_{ip} z_{p2} - \zeta_{ip}^2 v_{p2}, \\
\dot{v}_{p3} &= z_{p3}, \\
\dot{z}_{p3} &= \alpha_{up} c_{up} \zeta_{up} u - 2\zeta_{up} z_{p3} - \zeta_{up}^2 v_{p3},
\end{aligned} \tag{2.1}$$

where the post-synaptic potential, denoted by v_n, is the deviation of the membrane from the resting potential, α_{mn} is the gain for the post-synaptic response kernel, c_{mn} is the number of connections between populations, and ζ_{mn} is the reciprocal of the synaptic/membrane time constant. The index n (post-synaptic) may represent the pyramidal (p), excitatory interneuron (spiny stellate) (e), or inhibitory interneuron (i) populations. The parameter u describes the external input firing rate. v_{p1}, v_{p2}, v_{p3} are post-synaptic potential on the pyramidal cell induced by excitatory feedback, inhibitory feedback and external input, respectively. The post-synaptic potential of the pyramidal cell is then defined as $v_p = v_{p1} - v_{p2} + v_{p3}$. The sigmoid function, $g(v_m)$, characterises internal firing rates as a function of the pre-synaptic (subscript m) membrane potential, defined by

$$g(v) = \frac{2e_0}{1 + \exp\left(r(v_{th} - v)\right)}, \tag{2.2}$$

where r defines the slope of the sigmoid, v_{th} is the mean firing threshold, and $2e_0$ is the maximum firing rate.

In order to achieve the model in [76, 133], it is first assumed that the following set

of equalities holds on excitatory gains and time constants, $\alpha_{pe} = \alpha_{pi} = \alpha_{ep} = \alpha_{up} \triangleq \alpha_e$, $\zeta_{pe} = \zeta_{pi} = \zeta_{ep} = \zeta_{up} \triangleq \zeta_e$, $\alpha_{ip} \triangleq \alpha_i$, $\zeta_{ip} \triangleq \zeta_i$. These assumptions imply that the internal mathematical models of excitatory and inhibitory neurons are the same; however, their influence on post-synaptic potential of the pyramidal cell are different. Furthermore, the same mathematical formulation is used to model the influence of input u and excitatory feedback v_{p1} on the pyramidal cell. Therefore, we can define a new variable that incorporates the influence of u and v_{p1}, leading to

$$v_1 \triangleq v_{p1} + v_{p3}, \quad v_2 \triangleq v_{p2}, \quad z_1 \triangleq z_{p1} + z_{p3}, \quad z_2 \triangleq z_{p2}.$$

Given the above definition, the post-synaptic potential of the pyramidal cell can be written as $v_p = v_1 - v_2$. Furthermore, it is supposed that the co-activation of spiny stellate and inhibitory cells are proportional and mathematically described as,

$$v_0 \triangleq \frac{v_i}{c_{pi}} = \frac{v_e}{c_{pe}}, \quad z_0 \triangleq \frac{z_i}{c_{pi}} = \frac{z_e}{c_{pe}}.$$

It is also assumed[1] that the number of connections between the input and the pyramidal cells is equal to one, i.e. $c_{up} = 1$. Considering all aforementioned assumptions, the tenth-order system in (2.1) is reduced to the sixth-order state-space model,

$$\begin{aligned}
\dot{v}_0 &= z_0, \\
\dot{z}_0 &= \alpha_e \zeta_e g(v_1 - v_2) - 2\zeta_e z_0 - {\zeta_e}^2 v_0, \\
\dot{v}_1 &= z_1, \\
\dot{z}_1 &= \alpha_e \zeta_e \Big(u + c_{ep} g(c_{pe} v_0) \Big) - 2\zeta_e z_1 - {\zeta_e}^2 v_1, \\
\dot{v}_2 &= z_2, \\
\dot{z}_2 &= \alpha_i \zeta_i c_{ip} g(c_{pi} v_0) - 2\zeta_i z_2 - {\zeta_i}^2 v_2.
\end{aligned} \tag{2.3}$$

The state space representation in (2.3) describes the reduced model of single neural mass model. In order to interconnect the reduced neural mass models and construct a

[1] It should be pointed out that this assumption is not conservative mathematically since we consider $\tilde{u} \triangleq c_{up} u$ as a new input for (2.1).

network, it is assumed that the pyramidal unit also receives input from neighbouring regions that is added to the external input u. In this case, the neural mass model network with N regions is described by

$$\begin{aligned}
\dot{v}_0^j &= z_0^j, \\
\dot{z}_0^j &= \alpha_e^j \zeta_e^j g(v_1^j - v_2^j) - 2\zeta_e^j z_0^j - {\zeta_e^j}^2 v_0^j, \\
\dot{v}_1^j &= z_1^j, \\
\dot{z}_1^j &= \alpha_e^j \zeta_e^j \Big(u^j + c_{ep}^j g(c_{pe}^j v_0^j) + \sum_{l=1, l\neq j}^{N} K^{j,l} v_3^l \Big) - 2\zeta_e^j z_1^j - {\zeta_e^j}^2 v_1^j, \\
\dot{v}_2^j &= z_2^j, \\
\dot{z}_2^j &= \alpha_i^j \zeta_i^j c_{ip}^j g(c_{pi}^j v_0^j) - 2\zeta_i^j z_2^j - {\zeta_i^j}^2 v_2^j, \\
\dot{v}_3^j &= z_3^j, \\
\dot{z}_3^j &= \alpha_e^j \zeta_d^j g(v_1^j - v_2^j) - 2\zeta_d^j z_3^j - {\zeta_d^j}^2 v_3^j,
\end{aligned} \tag{2.4}$$

where superscript $j = 1, \ldots, N$ indexes the neural mass in region j. The parameters $\alpha_e^j, \alpha_i^j, \zeta_e^j, \zeta_i^j, \zeta_d^j$ are considered known. The two state variables v_3 and z_3 are used to interconnect region j to the other regions in the network. The effect of external regions on local dynamics is parametrised by the coupling gain $K^{j,l} \geq 0$ and coupling outputs v_3^l. Note that $K^{i,i} = 0$, $i = 1, \ldots, n$. A schematic diagram of a two-region network is depicted in Figure 2.1.

The model (2.4) implies that each region j shows different behaviours depending on the region parameters, external inputs ($u^j(t)$) and coupling gains. The complexity of the model is increased dramatically for a network with a large number of regions. Even for a network with two regions, it is difficult to analyse the effects of variations of parameters and coupling gains. In this chapter, we consider a network with $N = 2$ regions, region a and region b, and provide a rigorous analysis. The model parameters and their interpretation are given in Table 2.1 (also see [133]).

We now state the assumptions that are required for further analysis. The first assumption is that the local parameters of the two regions are identical, and changes in the network behaviour result from a varying input. This assumption implies that these

Table 2.1: The parameters of model (2.4) from [133]

Parameter	Description	Value
α_e, α_i	Average gain of excitatory (e) and inhibitory (i) synaptic gains	$\alpha_e = 3.25$, $\alpha_i = 22$
$\frac{1}{\zeta_e}, \frac{1}{\zeta_i}, \frac{1}{\zeta_d}$	Average time constant of post-synaptic potential. d is the connection between regions.	$\zeta_e = 100\ \mathrm{s}^{-1}$, $\zeta_i = 50\ \mathrm{s}^{-1}$, $\zeta_d = 33\ \mathrm{s}^{-1}$
$c_{pe}, c_{ep}, c_{pi}, c_{ip}$	Average number of synaptic contacts of excitatory and inhibitory connection	$c_{pe} = c$, $c_{ep} = 0.8c$, $c_{pi} = 0.25c$, $c_{ip} = 0.25c$ with $c = 135$
v_{th}, e_0, r	Threshold, half of the maximum output, and slope of sigmoid function $g(v)$	$v_{th} = 6$ mV, $e_0 = 2.5\ \mathrm{s}^{-1}$, $r = 0.56\ \mathrm{mV}^{-1}$

two regions belong to the same cortical area. For Sections 2.4 and 2.5, we will make a second assumption that the coupling gains between the two regions are symmetric; i.e., $K^{1,2} = K^{2,1} = K$. The second assumption is relaxed in Section 2.6. Although the assumptions limit the generality of the results, the networks shows very complicated behaviour when the coupling gain is varied and valuable insights are gained. The assumptions are required to gain these insights and similar approaches have been used in previous studies [125, 133].

Three cases are analysed (see Figure 2.1). In case I, the same input is applied to both regions. This structure can be seen as a network of two regions that are located near each other and receive common input. These two regions are involved in the same function; i.e., the same input and the same hierarchical level. In case II, we assume that only region a receives input, representing two regions that could be in same area with the same parameters, but with different levels of hierarchy. In case III, region a receives input and the feedback from region b is removed. In Section 2.5 and 2.6, we will point out that this change in the structure of the network induces interesting changes in the dynamics.

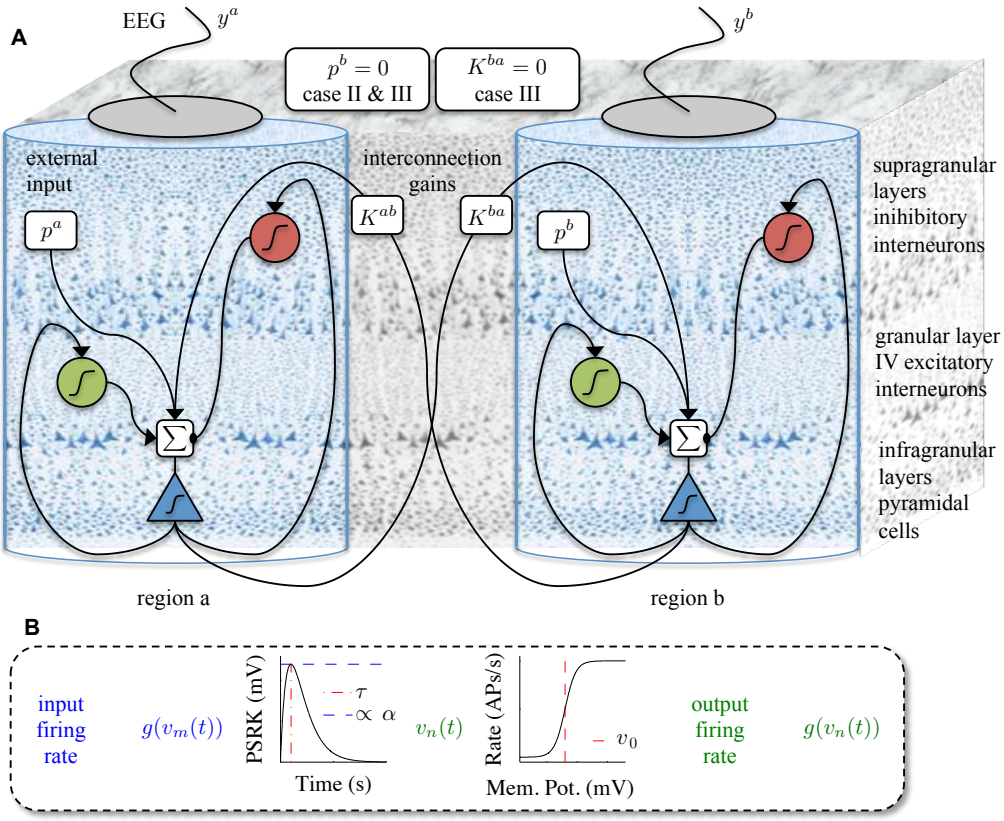

Figure 2.1: The schematic diagram of network of Jansen's model and three underlying cases. A. The schematic diagram of the neural mass model for two cortical regions described by equation (2.4). B. Elements of a neural mass, showing the synaptic kernel on the left and the sigmoidal nonlinearity on the right.

2.3 Equilibria

In order to start the bifurcation analysis, the first step is to find the equilibria of the network by setting the left hand side of (2.4) to zero for $j = a, b$. This leads to the following set of equations:

$$\begin{aligned}
v_0^a &= \frac{\alpha_e}{\zeta_e} g\left(v_1^a - v_2^a\right), & z_0^a &= 0,\\
v_1^a &= \frac{\alpha_e}{\zeta_e}\left(u^a + c_{ep} g\left(c_{pe} v_0^a\right) + K^{ab} v_6^b\right), & z_1^a &= 0,\\
v_2^a &= \frac{\alpha_i}{\zeta_i} c_{ip} g\left(c_{pi} v_0^a\right), & z_2^a &= 0,\\
v_3^a &= \frac{\alpha_e}{\zeta_d} g\left(v_1^a - v_2^a\right), & z_3^a &= 0.
\end{aligned} \tag{2.5}$$

$$\begin{aligned}
v_0^b &= \frac{\alpha_e}{\zeta_e} g\left(v_1^b - v_2^b\right), & z_0^b &= 0,\\
v_1^b &= \frac{\alpha_e}{\zeta_e}\left(u^b + c_{ep} g\left(c_{pe} v_0^b\right) + K^{ba} v_6^a\right), & z_1^b &= 0,\\
v_2^b &= \frac{\alpha_i}{\zeta_i} c_{ip} g\left(c_{pi} v_0^b\right), & z_2^b &= 0,\\
v_3^b &= \frac{\alpha_e}{\zeta_d} g\left(v_1^b - v_2^b\right), & z_3^b &= 0.
\end{aligned} \tag{2.6}$$

We define the EEG signal corresponding to region a and region b as $y^a := v_1^a - v_2^a$ and $y^b := v_1^b - v_2^b$ [133]. Now, from (2.5) and (2.6), we can write the equations describing the EEG at equilibrium as

$$\begin{aligned}
y^a =& \frac{\alpha_e}{\zeta_e} u^a + \frac{\alpha_e}{\zeta_e} c_{ep} g\left(\frac{\alpha_e}{\zeta_e} c_{pe} g\left(y^a\right)\right) - \frac{\alpha_i}{\zeta_i} c_{ip} g\left(\frac{\alpha_e}{\zeta_e} c_{pi} g\left(y^a\right)\right) + \frac{\alpha_e^2}{\zeta_e \zeta_d} K^{ab} g\left(y^b\right)\\
y^b =& \frac{\alpha_e}{\zeta_e} u^b + \frac{\alpha_e}{\zeta_e} c_{ep} g\left(\frac{\alpha_e}{\zeta_e} c_{pe} g\left(y^b\right)\right) - \frac{\alpha_i}{\zeta_i} c_{ip} g\left(\frac{\alpha_e}{\zeta_e} c_{pi} g\left(y^b\right)\right) + \frac{\alpha_e^2}{\zeta_e \zeta_d} K^{ba} g\left(y^a\right).
\end{aligned} \tag{2.7}$$

Since (2.7) is nonlinear in terms of u^a, u^b, K^{ab}, K^{ba}, a computational approach is utilised in which the values of u^a, u^b, K^{ab}, K^{ba} are considered to be fixed, and the values of y^a and y^b are obtained subsequently. Then, the equilibria of the network corresponding to those fixed values can be determined from (2.5) and (2.6). The detailed explanations of the underlying computational approach for each case are presented in the following sections. The goal of the bifurcation analysis is to analyse the behaviour of the underlying network arising around equilibria as parameters of the network are varied.

2.4 Case I: Bifurcation Analysis with a Common Input

In case I, the applied inputs and interconnection gains are considered to be same for both regions, i.e., $u^a = u^b = u$ and $K^{ab} = K^{ba} = K$. We consider u as the bifurcation parameter that changes continuously, and consider discrete interconnection gains $K = 25, 50, 100, 150$. Considering both the input u and the interconnection gain K as continuous bifurcation parameters provides a more comprehensive analysis of the underlying networks, but is beyond the scope of this chapter.

We categorise the equilibria of the network into two groups. The first group contains

the set of equilibria, called symmetric equilibria, that are equal; i.e., $y^a = y^b = y^s$. This set of equilibria results from the symmetrical structure of the network, which can be observed from both Figure 2.1 and (2.7). The symmetry makes it possible to rewrite (2.7) to

$$y^s = \frac{\alpha_e}{\zeta_e}u + \frac{\alpha_e}{\zeta_e}c_{ep}g\left(\frac{\alpha_e}{\zeta_e}c_{pe}g\left(y^s\right)\right) - \frac{\alpha_i}{\zeta_i}c_{ip}g\left(\frac{\alpha_e}{\zeta_e}c_{pi}g\left(y^s\right)\right) + \frac{\alpha_e^2}{\zeta_e\zeta_d}Kg\left(y^s\right), \tag{2.8}$$

which is used to compute the symmetric equilibria. The second group of equilibria correspond to the asymmetric solutions, which are unequal. The asymmetric equilibria are computed using (2.7).

Note that both (2.7) and (2.8) are nonlinear, so it is not possible to find explicit expressions for y^a and y^b in terms of u and K. Therefore, we utilise a numerical approach to find the solutions by changing the value of $y^s \in (-3.5, 12)$ in (2.8) and then calculating the value of the corresponding input u. The asymmetric equilibria are computed using the feature of the CL-MATCONT package [64], that exploits the continuity of solutions with respect to the variation of u. All bifurcation analyses are performed by CL-MATCONT toolbox.

2.4.1 Bifurcation Analysis with Weak Coupling ($K = 25$)

Two separate bifurcation analyses were conducted corresponding to the symmetric and asymmetric solutions to the equilibria. The equilibria that correspond to the symmetric solution are shown in Figure 2.2. In all figures presented in this chapter, the solid black lines represent the stable equilibria; i.e, all eigenvalues of the Jacobian matrix have negative real parts) and the black dashed lines show unstable equilibria. Figure 2.2 shows two subcritical Hopf bifurcations $H_{2,1}$ and $H_{2,2}$ that occur where the input, $u = -14.46$ or $u = -21.43$. For a single region neural mass model, there is only one corresponding subcritical Hopf bifurcation [65]. These two subcritical Hopf bifurcation lead to the presence of two limit cycles $LC_{2,1}$ and $LC_{2,2}$. The simulated EEG signals corresponding to each limit cycle are shown in the upper part of Figure 2.2. Since the limit cycles are unstable, they repel nearby trajectories and, consequently, the trajectories are attracted by the stable equilibria.

Figure 2.2 also shows a saddle-node homoclinic bifurcation, indicated by $SN_{2,1}$, when the input u = 110.5. The saddle-node homoclinic bifurcation leads to the appearance of two orbits[2] $LC_{2,3}$ and $LC_{2,4}$ (see Appendix A.2 for details of Shilnikov saddle-node homoclinic bifurcation detection) that generate epileptic-like spike and wave discharges, as seen in the upper part of Figure 2.2. The two types of spike and wave discharges have the same frequency as each other, but different amplitudes. The orbit $LC_{2,3}$, which is plotted in grey, terminates when the input u exceeds 125.7. This termination occurs at $SN_{2,2}$ and $SN_{2,3}$, which is due to a collision of the stable cycle $LC_{2,3}$ with the unstable limit cycle $LC_{2,1}$ originating from the subcritical Hopf bifurcation $H_{2,1}$. Similarly, the orbit $LC_{2,4}$ plotted in red, collides at $SN_{2,4}$ and $SN_{2,5}$ (u = 136.4) with the unstable limit cycle $LC_{2,2}$ originating from the subcritical Hopf bifurcation $H_{2,2}$.

A supercritical Hopf bifurcation $H_{2,3}$ occurs when the input is increased above u = 71.56. The stable equilibrium point becomes unstable resulting from the complex eigenvalues of the Jacobian matrix crossing the imaginary axis. This Hopf bifurcation gives rise to a stable limit cycle LC_2. Another two complex eigenvalues cross the imaginary axis when the input reaches u = 93.46 resulting in another supercritical Hopf bifurcation $H_{2,4}$. It should be noted that the equilibrium point remains unstable since the Jacobian matrix has eigenvalues with positive real part[3]. These two Hopf bifurcations lead to the appearance of two stable limit cycles LC_2 and LC_3. These two limit cycles disappear when the input exceeds 298.6 and 313.4. Figure 2.2 shows the alpha rhythm-like EEG for stable limit cycles with a frequency of approximately 10Hz. The two alpha-like oscillations have slightly different amplitudes and frequencies.

During continuation, two branch points BP_1 and BP_2 were detected on the symmetric equilibria curve. At these points, other branches of equilibria arise that correspond to the asymmetric solution, and are depicted in Figures 2.3A and B for region a and re-

[2]We point out that a Shlinkov saddle-node can have more than one homoclinic orbit simultaneously if the dimension of the underlying system (number of states) is strictly larger than 2. An example of Shlinkov saddle-node with a pair of the homoclinic orbits is reported in the modified Morioka-Simizu model [115]. More information can also be found in `http://www.scholarpedia.org/article/Shilnikov_saddle-node_bifurcation`. In our study, the dimension of the system is 16.

[3]In multi-dimensional systems, Hopf bifurcation occurs if a pair of complex eigenvalues crosses the imaginary axis while the rest of eigenvalues can have positive or negative real parts. The type of bifurcation (supercritical or subcritical) is determined by computing the first Lyapunov coefficient (see [85, Chapter5]).

gion b, respectively. Figures 2.3A_1, A_2, and A_3 (Figures 2.3B_1, B_2, and B_3) correspond to the lower, middle, and upper parts of the equilibria curve in Figure 2.3A (Figure 2.3B), respectively. The pair of equilibria for y^a and y^b are shown with the same colour and linestyle. For example, if y^a is an equilibrium point located on the blue solid-line in Figure 2.3A_1, the corresponding equilibrium point y^b is also located on the blue solid-line in Figure 2.3B_3. Figure 2.3 shows that the equilibria of y^a and y^b are not necessarily identical even though the underlying network has symmetric structure. Consequently, different EEG time series can be observed at each region with a suitable initialisation.

All bifurcations found for the asymmetric equilibria are plotted in Figures 2.4 and 2.5 for both regions. Panels A and B show the bifurcation structures for regions a and b, respectively. Simultaneous bifurcation points and corresponding limit cycles in both panels are color coded. During continuation, we found four subcritical Hopf bifurcations $H_{4,1}$, $H_{4,4}$, $H_{4,5}$, and $H_{4,6}$ that are located in different parts of equilibria curve, and lead to the appearance of four unstable limit cycles (see Figure 2.5). Two limit cycles $LC_{4,1}$, $LC_{4,4}$ ($LC_{4,5}$, $LC_{4,6}$), plotted in same colour, collides via a fold bifurcation of limit cycles (or Limit Point of Cycle (LPC)) at $u = 106$, which is interesting from a technical perspective since it is a point where a limit cycle is born under other parameter variations.

We also found four supercritical Hopf bifurcations for non-symmetric equilibria that are indicated by $H_{4,2}$, $H_{4,3}$, $H_{4,7}$ and $H_{4,8}$, and are located in different parts of equilibria curve. Two supercritical Hopf bifurcations $H_{4,7}$ and $H_{4,3}$ occur at $u = 87.43$, while another two supercritical Hopf bifurcations $H_{4,8}$ and $H_{4,2}$ occur at for $u = 88.93$. As a result, four stable limit cycles appear, which generate alpha-like oscillation (10 Hz). The corresponding behaviour for $LC_{4,7}$ is show in Figure 2.4. However, similar behaviour is generated by other stable limit cycles with different amplitude. Similar to unstable limit cycles, two limit cycles $LC_{4,7}$, $LC_{4,8}$ ($LC_{4,2}$, $LC_{4,3}$), plotted in same colour, collide via LPC at $u = 106$.

By considering all limit cycles detected from the symmetric and asymmetric branches of equilibria, it is concluded that the network can generate alpha-like activity for the input ranges $87.43 \leq u \leq 106$ and $71.56 \leq u \leq 313.4$, that correspond to the asymmetric and the symmetric cases, respectively. This dynamical regime is vastly more complex than a single region model, which generates alpha activity for $89.83 \leq u \leq 315.70$ from one stable

limit cycle [65].

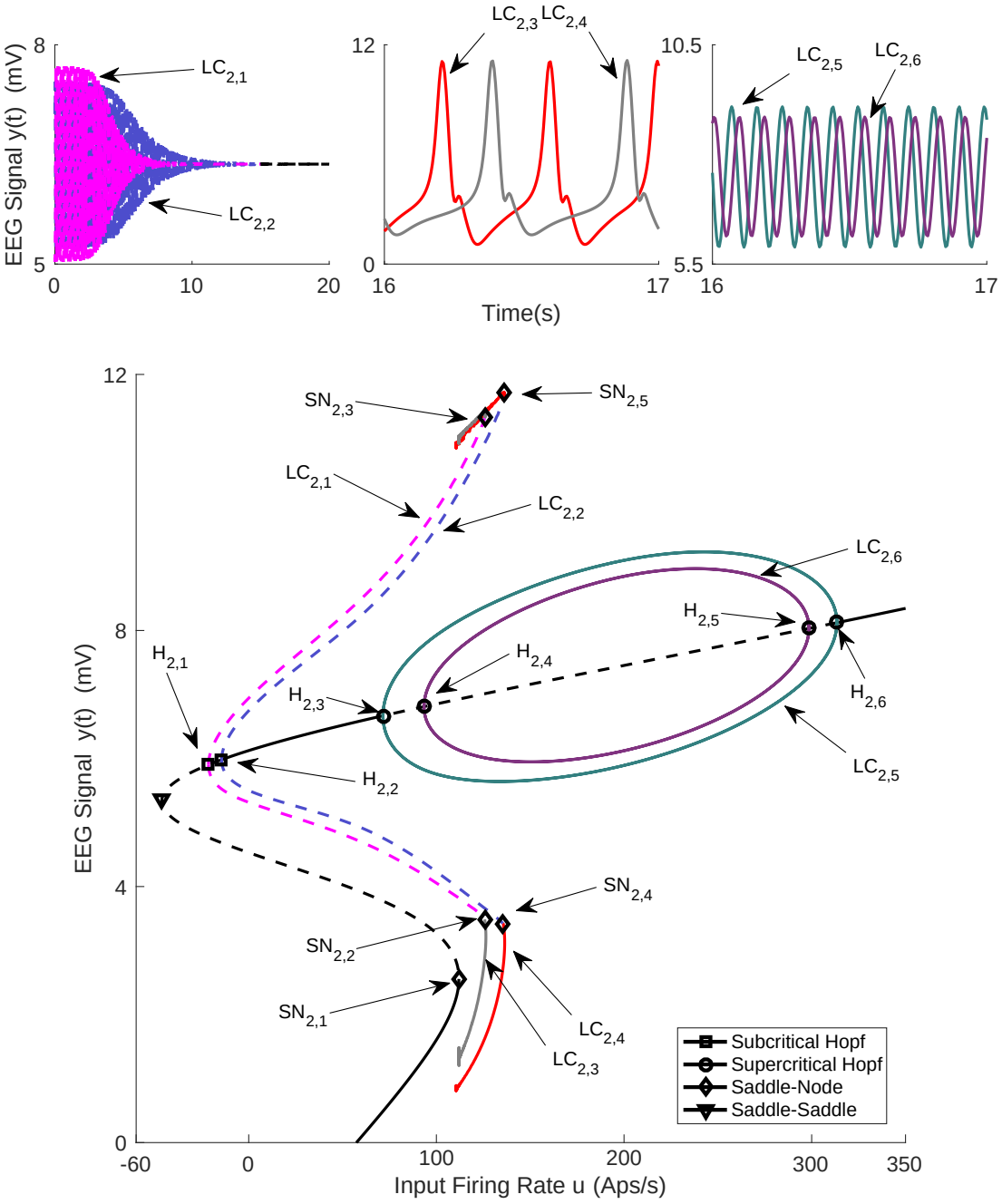

Figure 2.2: Bifurcation diagram for the symmetric solution for Case I with coupling gain $K = 25$. The time series in the upper part of the figure show the EEG associated with each bifurcation using the same colour The solid black lines show stable fixed points, the solid coloured lines show stable oscillatory behaviour and the dashed lines show unstable fixed points and unstable oscillations.

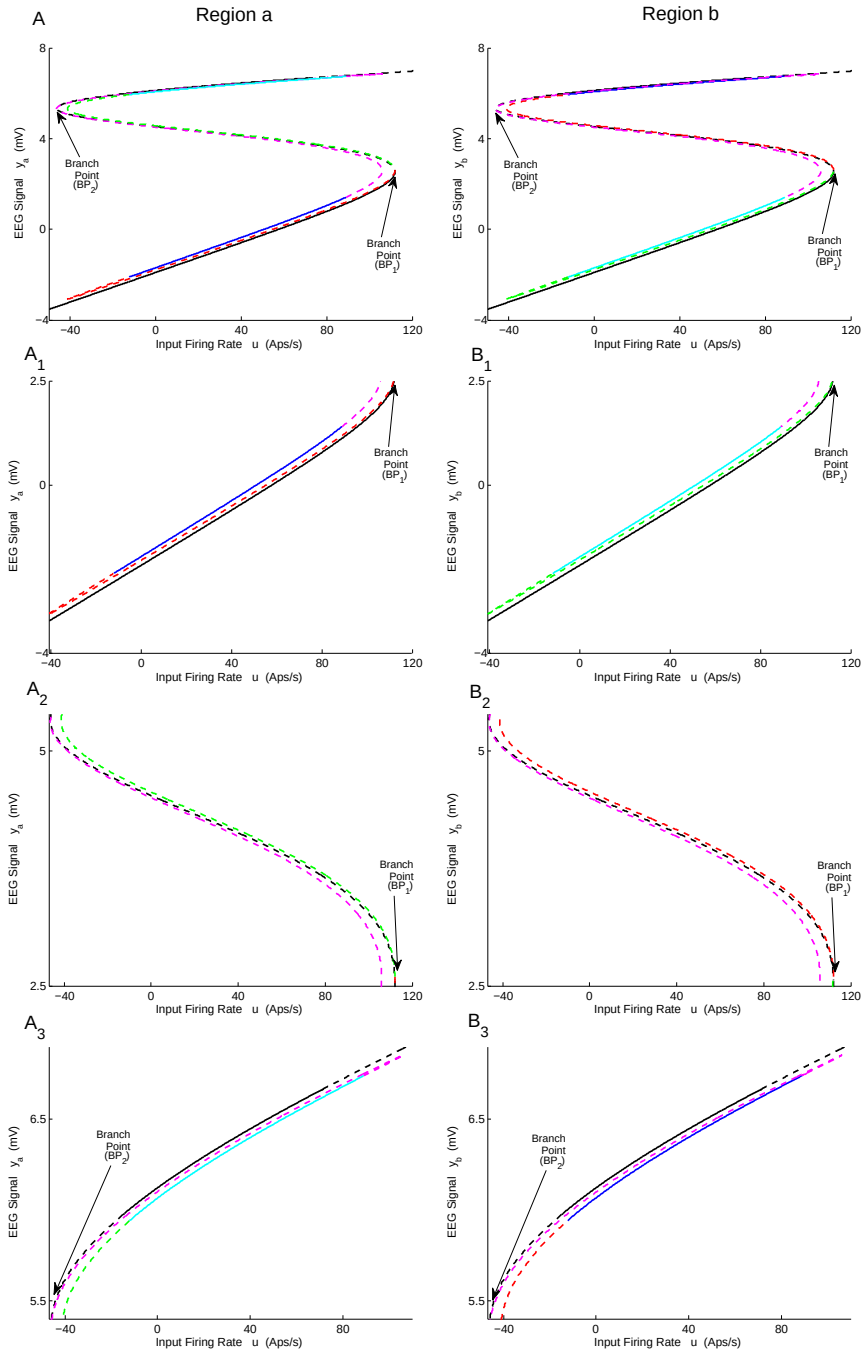

Figure 2.3: Equilibria curves for asymmetric solutions of case I with coupling gain $K = 25$. A) and B) Second branch of equilibria for regions a and b, respectively. A_1-A_3) Magnified parts from sub-panels in A) corresponding to the bottom, the middle and the upper parts. B_1-B_3) Magnified parts from sub-panels in B) corresponding to the lower, the middle and the top parts. The black lines correspond to the symmetric solutions; the red, blue, green, cyan and magenta lines correspond to asymmetric solutions. The equilibria for y^a and y^b are shown with the same color and line style. For example, an equilibrium point with blue solid-line in panel A_1 corresponds to an equilibrium point with blue solid-line in panel B_3.

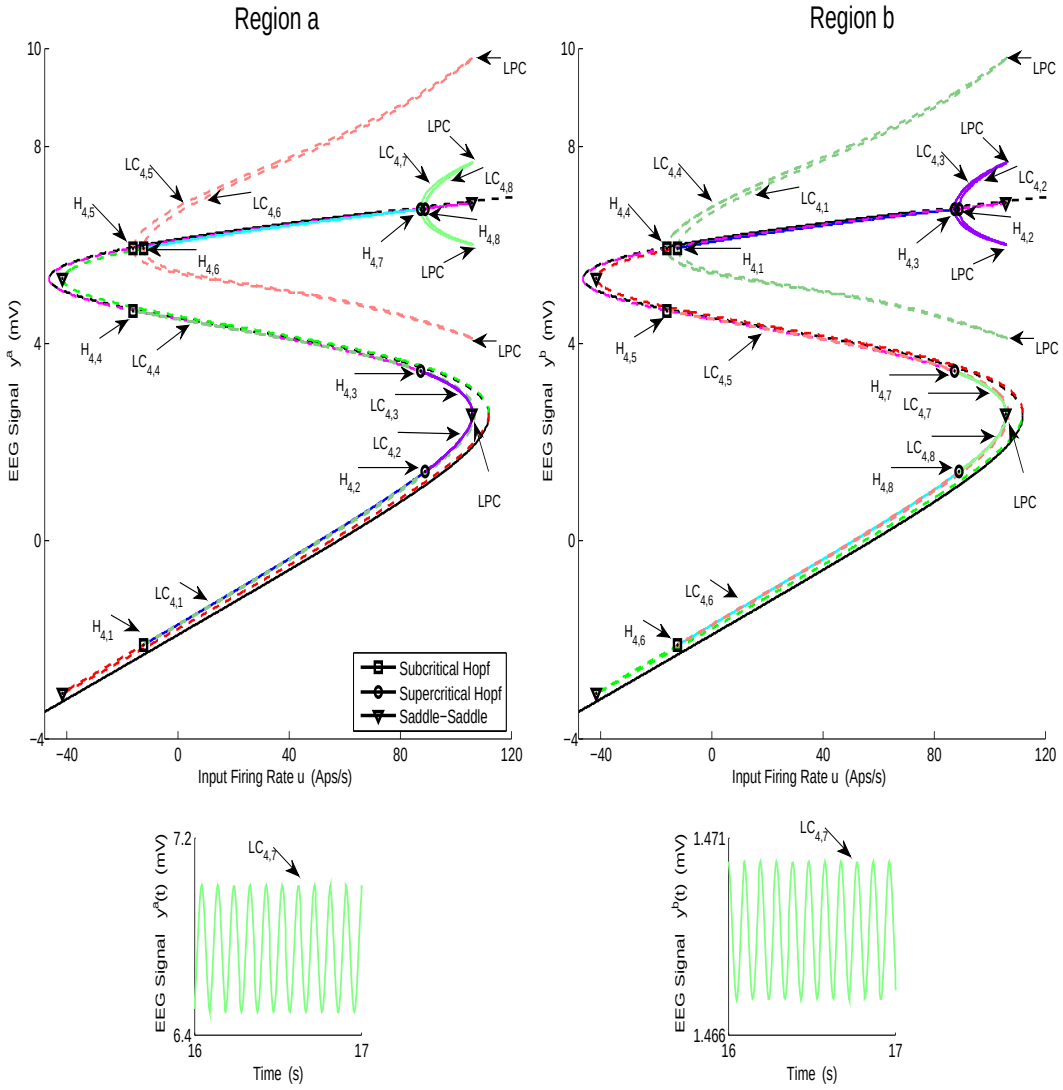

Figure 2.4: Bifurcation diagrams of A) region *a* and B) region *b* arising from the asymmetric equilibria for Case I with coupling gain $K = 25$. The time series in the upper parts of the figure show the behaviours associated with the stable limit cycle arises from supercritical Hopf bifurcation $LC_{4,7}$.

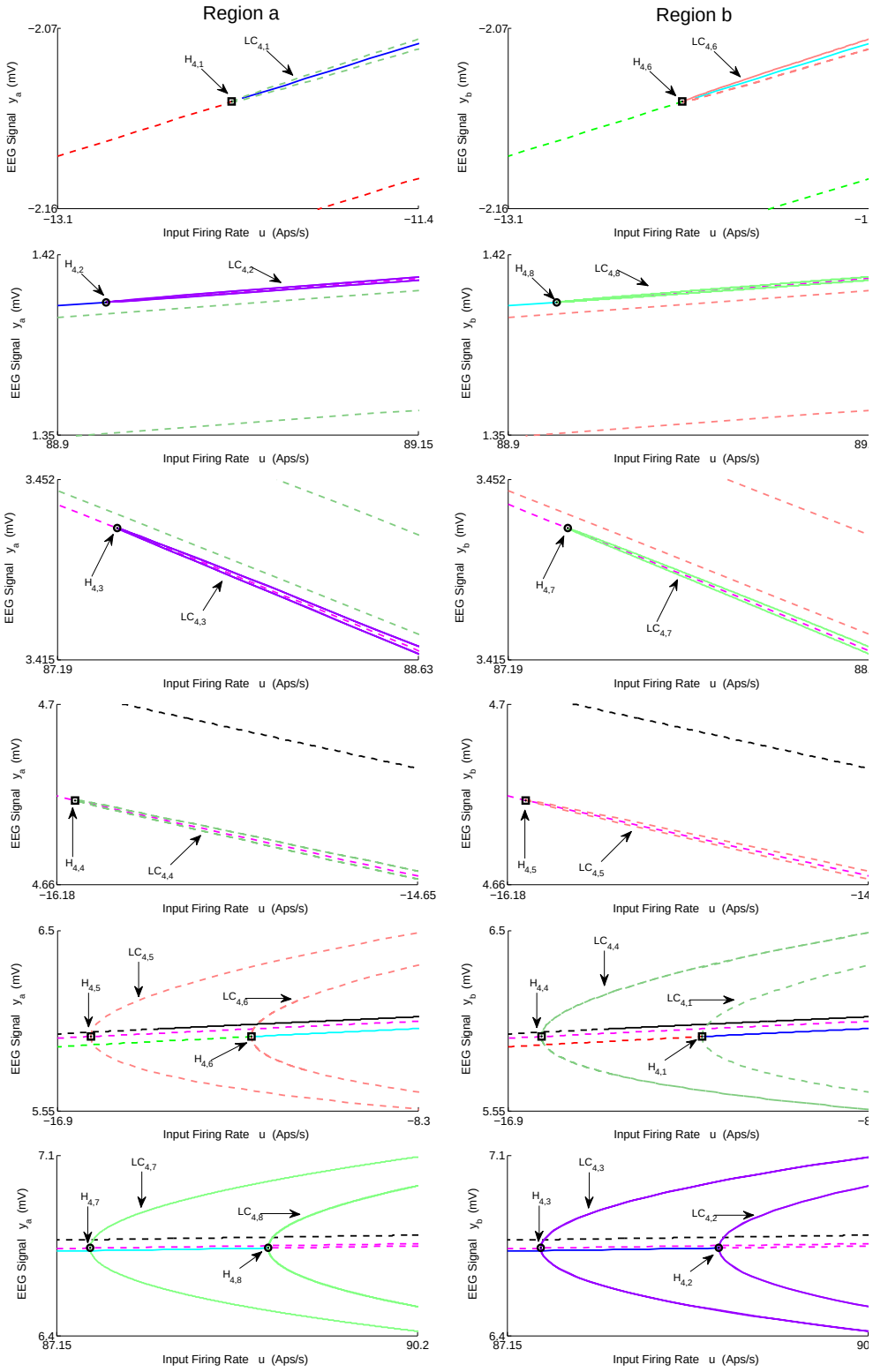

Figure 2.5: Magnified parts from bifurcation diagrams in Figure 2.4.

2.4.2 Bifurcation Analysis with Intermediate Coupling (K = *50*)

The bifurcation diagram for case I with coupling gain K = 50 is qualitatively similar to the case K = 25 in terms of types of limit cycles and shapes of equilibria branches. The differences between K = 25 and 50 are the points at which the bifurcations occur and the amplitudes of oscillations. Similar to the case K = 25, two orbits, resulting from a saddle-node homoclinic bifurcation coexist for $110.5 \leq u \leq 114.3$ and $106.2 \leq u \leq 134.4$. Two stable limit cycles emerge from supercritical Hopf bifurcations at u = 53.24 and u = 97.2 and vanish at u = 310.5 and u = 280.7, respectively. A similar situation to the case K = 25 is observed for the limit cycle corresponding to the second branch of equilibria. Due to these similarities, the bifurcation diagrams are not presented.

2.4.3 Bifurcation Analysis with Strong Coupling (K = *100* and *150*)

The symmetric solutions to the equilibria were computed and are plotted in Figure 2.6 for case I with strong inter-region coupling gain (K = 100). Figure 2.6 shows two stable limit cycles $LC_{6,4}$ and $LC_{6,5}$ that originate from supercritical Hopf bifurcations $H_{6,4}$($H_{6,5}$) and $H_{6,6}$ respectively. The first limit cycle $LC_{6,4}$ occurs for the input range $107.1 \leq u \leq 241.7$. The limit cycle $LC_{6,5}$ arises as a result of LPC with an unstable limit cycle at the indicated point $LPC_{6,1}$, and terminates at u = 303.3. The frequency of oscillations from both $LC_{6,4}$ and $LC_{6,5}$ is approximately 10 Hz, corresponding to alpha-like activity. Contrary to the network with weak coupling (K = 25), there is only one limit cycle $LC_{6,2}$ that generates spike-wave-like discharges. The limit cycle $LC_{6,2}$ arises from a saddle-node homoclinic bifurcation and collides with an unstable limit cycle through LPC at the point indicated by $LPC_{6,2}$. The frequency and amplitude of spikes for this case are approximately the same as with weak coupling.

There are two subcritical Hopf bifurcations $H_{6,1}$ and $H_{6,2}$ that generate the unstable limit cycles $LC_{6,1}$ and $LC_{6,3}$ respectively. The limit cycle $LC_{6,1}$ emerges when the input $u = -46.74$ [4]. The limit cycle $LC_{6,3}$ begins at $u = -13.28$ and ends at u = 11.92 through Hopf bifurcation $H_{6,3}$. The EEG time series in the bottom part of Figure 2.6 shows decaying

[4] We couldn't identify how $LC_{6,1}$ ends by increasing u as CL-MATCONT package was not able to proceed the continuation process further.

oscillations that settle down to constant values corresponding to stable equilibria.

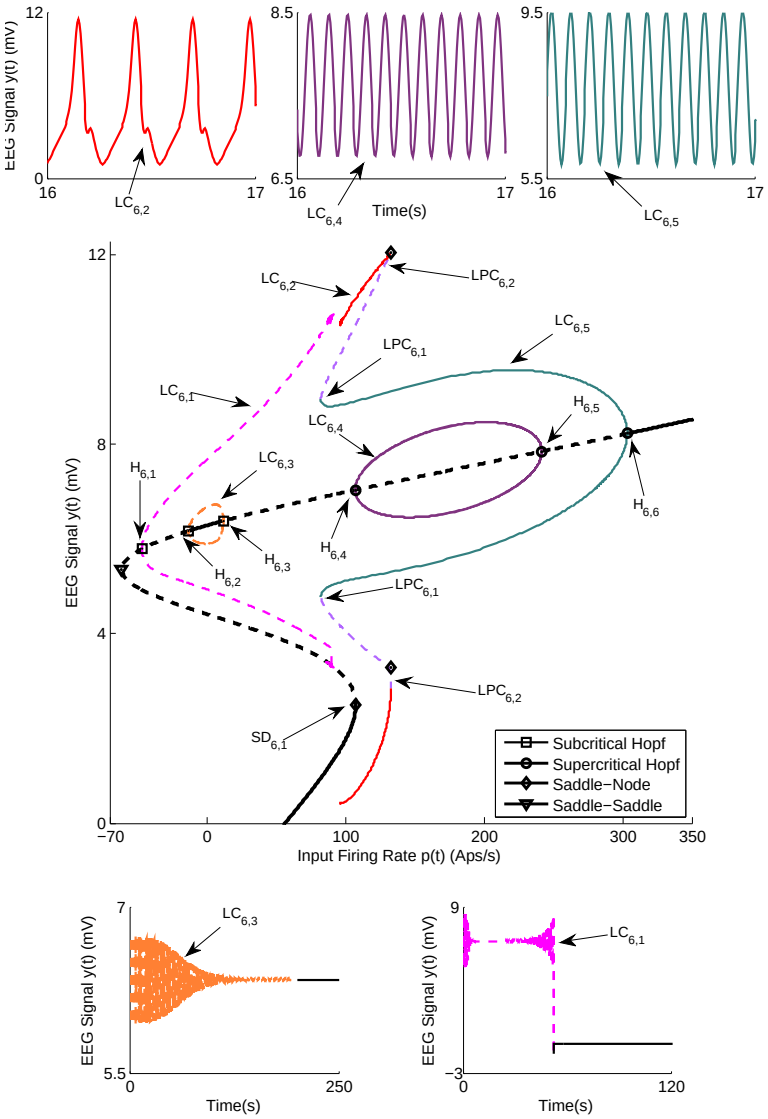

Figure 2.6: Bifurcation diagram of Case I with coupling gain $K = 100$. The time series in the insets of the figure show the simulated EEG for each bifurcation with the same colour The solid black lines show stable fixed points, the solid colored lines show stable oscillatory behaviour and the dashed lines show unstable fixed points and unstable oscillations.

For coupling gain $K = 150$, the network has two branches of equilibria. The bifurcation diagram for the symmetric equilibria for $K = 150$ is plotted in Figure 2.7. The diagram has a notable exception of the disappearance of the small unstable limit cycle $LC_{6,3}$ which results from a subcritical Hopf bifurcation for $K = 100$. The reason is that, for the corre-

sponding range of u, the Jacobian matrix for the system 2.4 has no complex eigenvalue with zero real part. There are also differences in the levels of the input at which other types of bifurcations arise. For the asymmetric case of equilibria, there are two unstable limit cycles, arising from subcritical Hopf bifurcations, that do not lead to any interesting behavior and are not discussed further.

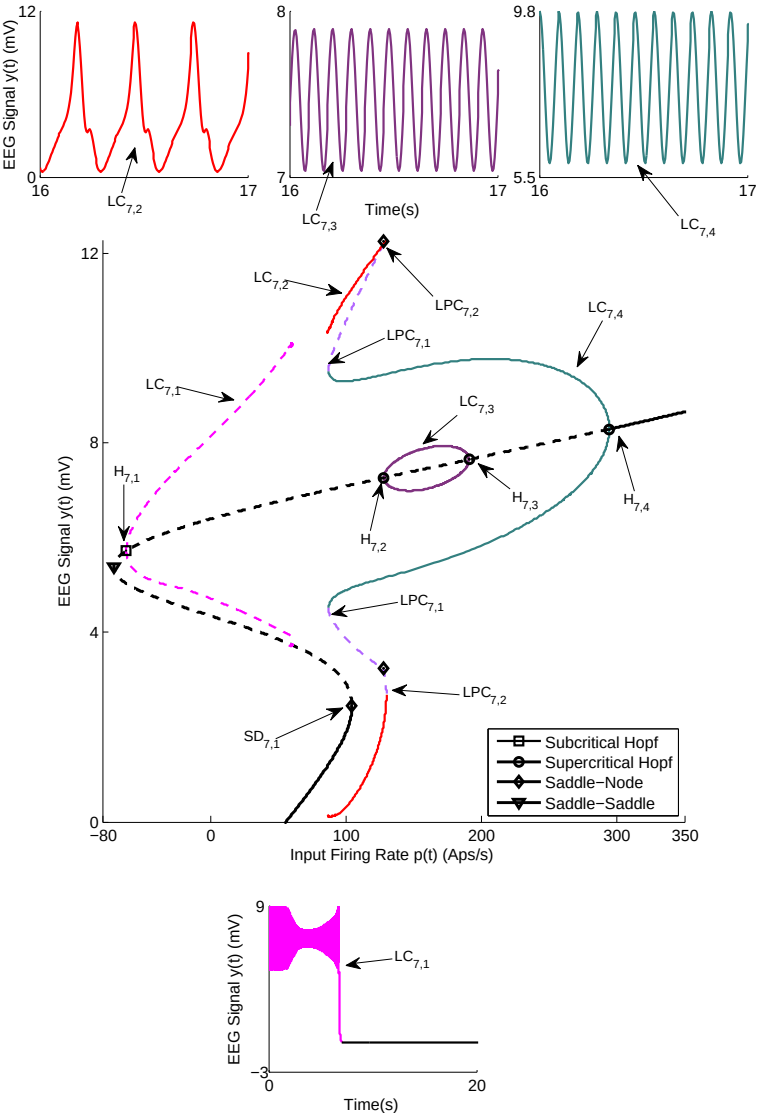

Figure 2.7: Bifurcation diagrams arising from the first branch of equilibria in Case I with coupling gain $K = 150$. The time series in the insets of the figure show the simulated EEG for each bifurcation with the same colour. The solid black lines show stable fixed points, the solid coloured lines show stable oscillatory behaviour and the dashed lines show unstable fixed points and unstable oscillations.

2.5 Case II: Bifurcation Analysis of Two Coupled Neural Mass Model with a Single Input

In this section, the bifurcation analyses of the neural mass model network are presented where the input is applied only to region a (see Figure 2.1). Similar to Section 2.4, the first step of the bifurcation analysis is finding the equilibria of the overall system. We follow the procedure in Section 2.3, setting u^b to zero. Additional notes on calculating the equilibria for this case are provided in Appendix A.3.

Bifurcation analysis with coupling gain $K = 50$

Figure 2.8 depicts three branches of equilibria and bifurcation diagrams for region a and region b. Since there is no interconnection from the second region to the first region, the equilibria of region a are very similar in all three branches. However, the equilibria for region b have a more complex structure (see Appendix A.3 for further explanation).

There are two stable limit cycles $LC_{8,3}$ and $LC_{8,18}$ on the first and the third branches of equilibria that exist between supercritical Hopf bifurcation points ($H_{8,2}$, $H_{8,3}$) and ($H_{8,8}$, $H_{8,9}$), respectively. These limit cycles exist for input values between $u = 100$ and $u = 300$. Similar to Case I, a supercritical Hopf bifurcation leads to a stable limit cycle which generates stable oscillations, depicted in Figure 2.8, that resemble alpha activity. These two limit cycles generate different types of alpha activity with the same frequency at distinctly different amplitude ranges in region b. In order to study the behaviour of the network near the stable limit cycles, we simulated the EEG signals with initial conditions close to the cycles and plotted the corresponding time series shown in the lower part of Figure 2.8. The time series associated with the stable limit cycles on the first and third branches verify that the limit cycles are stable.

We found several subcritical Hopf bifurcations on all branches of equilibria. The one for the first branch $H_{8,1}$ results in the unstable limit cycle $LC_{8,1}$. This limit cycle collides with the limit cycle $LC_{8,2}$ via a saddle-node bifurcation at the point $SN_{8,2}$. The limit cycle $LC_{8,2}$ originates from a saddle-node homoclinic bifurcation at the point $SN_{8,1}$. The stable limit cycle $LC_{8,2}$ produces spike-wave-like signals with a frequency of approximately

3 Hz, which is observed in region *a* (Figure 2.8). However, the spike-wave-like signal does not appear in region *b* as shown in Figure 2.8. Instead, region *b* shows an EEG signal similar to delta-wave activity. The occurrence of delta wave activity is interesting considering the strong links between epileptic seizures and sleep [16].

The second unstable limit cycle $LC_{8,4}$ in Figure 2.8B and E originates from subcritical Hopf bifurcation $H_{8,4}$, and appears to collide with the limit cycle $LC_{8,5}$ at $u = 129.4$. At this point indicated by $LPC_{8,1}$, LPC was detected. The limit cycle $LC_{8,5}$ originates from a homoclinic bifurcation of a saddle-saddle which was originally proposed by Shilnikov[5]. The simulated EEG for $LC_{8,4}$ shows that the trajectories that start near the limit cycle converge to the equilibria on the first branch. Furthermore, the trajectories that start from the limit cycle $LC_{8,5}$, depicted in Figure 2.8, converge to the $LC_{8,2}$ on the first branch of equilibria. Furthermore, we notice that there are two subcritical Hopf bifurcations $H_{8,5}$ and $LC_{8,6}$ for the second branch of equilibria that leads to the existence of the unstable limit cycle $LC_{8,6}$. By initialising the system near to this limit cycle, the trajectories converge to the limit cycle $LC_{8,3}$ as shown in Figure 2.8. Therefore, the analysis indicates that this second branch does not contribute to specific behaviours

Figure 2.8C and F, Figures 2.9-2.10 show the bifurcation diagram for the third branch of equilibria. In contrast to the bifurcation diagram for the first equilibria, the unstable limit cycle $LC_{8,7}$, which arises from subcritical Hopf bifurcation $H_{8,7}$, does not collide with the unstable limit cycle $LC_{8,12}$ resulted from a saddle-node homoclinic bifurcation $SN_{8,3}$. During continuation of the third limit cycle $LC_{8,7}$, we detected LPC which is plotted by a grey plus sign. At this point, the limit cycle $LC_{8,7}$ collides with the limit cycle $LC_{8,8}$ (see Figure 2.9C_1 and F_1 and Figure 2.9C_1(c)). By proceeding the continuation, we detected another LPC point. We labelled the limit cycle after this point as $LC_{8,9}$. We also noticed that the toolbox detected Neimark-Sacker bifurcation of cycles[6] at two points; (i) the intersection of limit cycles $LC_{8,9}$ and $LC_{8,10}$ (Figure 2.9F_1 and Figure 2.10c_1(d)) (ii) the intersection of limit cycles $LC_{8,10}$ and $LC_{8,11}$ (Figure 2.9C_2 and Figure 2.9F_2). To study the corresponding simulated EEG to these limit cycles, the initial value was chosen near each

[5] See `http://www.scholarpedia.org/article/Shilnikov_saddle-node_bifurcation`.

[6] Neimark-Sacker bifurcation of cycles is a co-dimension 1 bifurcation corresponds to the case when the multipliers are complex and simple and lie on the unit circle. See [85] for more details.

limit cycle. We observed that trajectories converge to either the equilibria on the third branch or the equilibrium point on the first branch.

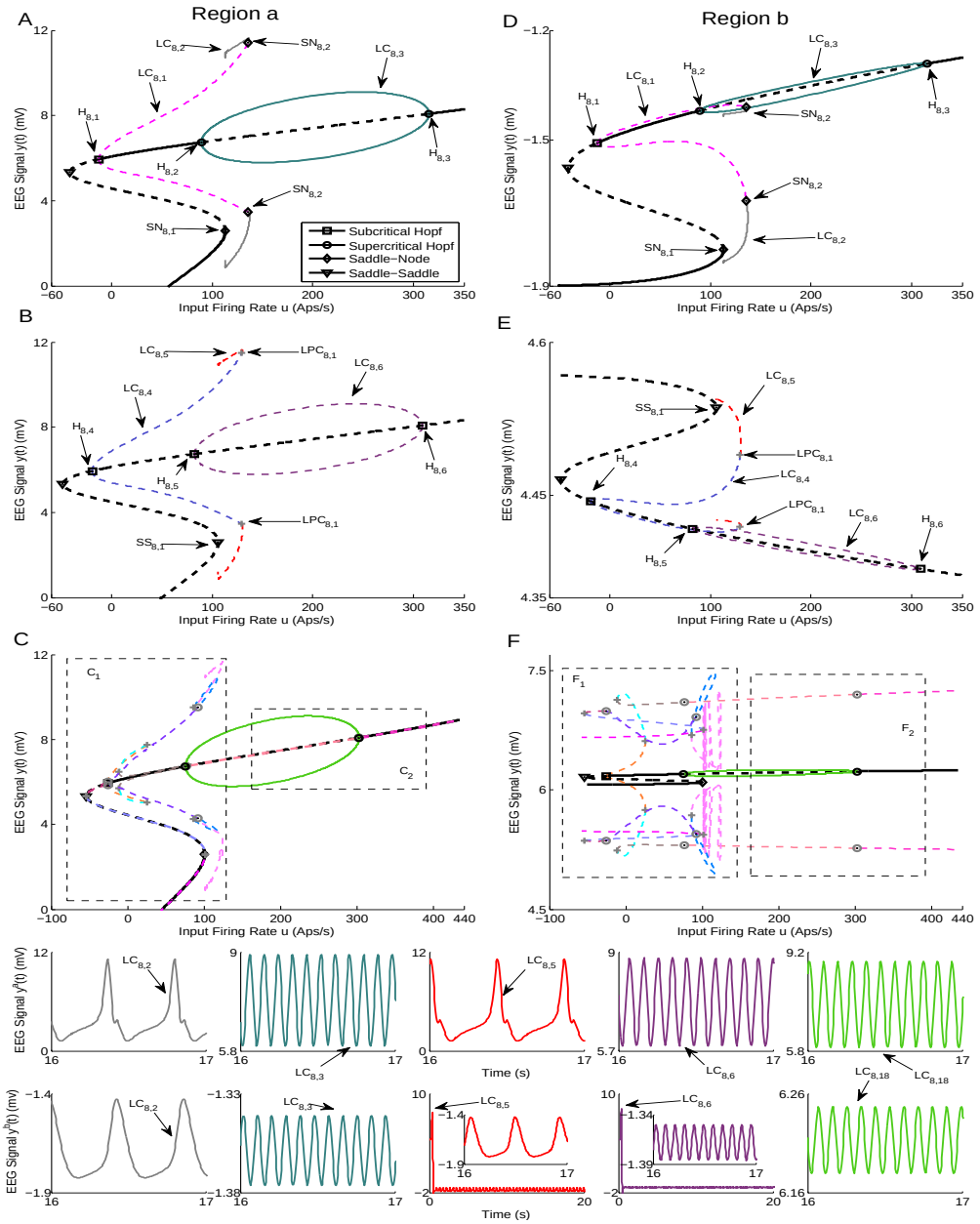

Figure 2.8: Equilibria and bifurcation diagrams for Case II with coupling gain $K = 50$. A), B), and C) are the first, second, and third branches of equilibria for region a. D), E), and F) are the first, second, and third branches of equilibria for region b. The subpanels show the EEG time series corresponding to the each part in the bifurcation diagrams. The solid black lines show stable fixed points, the solid coloured lines show stable oscillatory behaviour and the dashed lines show unstable fixed points and unstable oscillations.

Near the saddle node point $SN_{8,3}$ on the third branch, we noticed that there exists a saddle-node homoclinic bifurcation, which results in an appearance of the limit cycle $LC_{8,12}$. By initialising the system close to this limit cycle, we observed that it produces unstable spikes in region *a* and an oscillation in region *b*. These spike-wave discharges have a frequency similar to that observed during seizures in clinical EEG recordings, until the activity of each region settles to the equilibrium point. During the continuation of this cycle, three LPCs and one Neimark-Sacker bifurcation of cycles are detected (see Figure 2.9C_1 and 2.9F_1, and Figure 2.10c_1(a),(b),(c)). By selecting an initial condition near each limit cycle and simulating the EEG, we observed the solutions converge to the equilibria on either the first branch or the third branch.

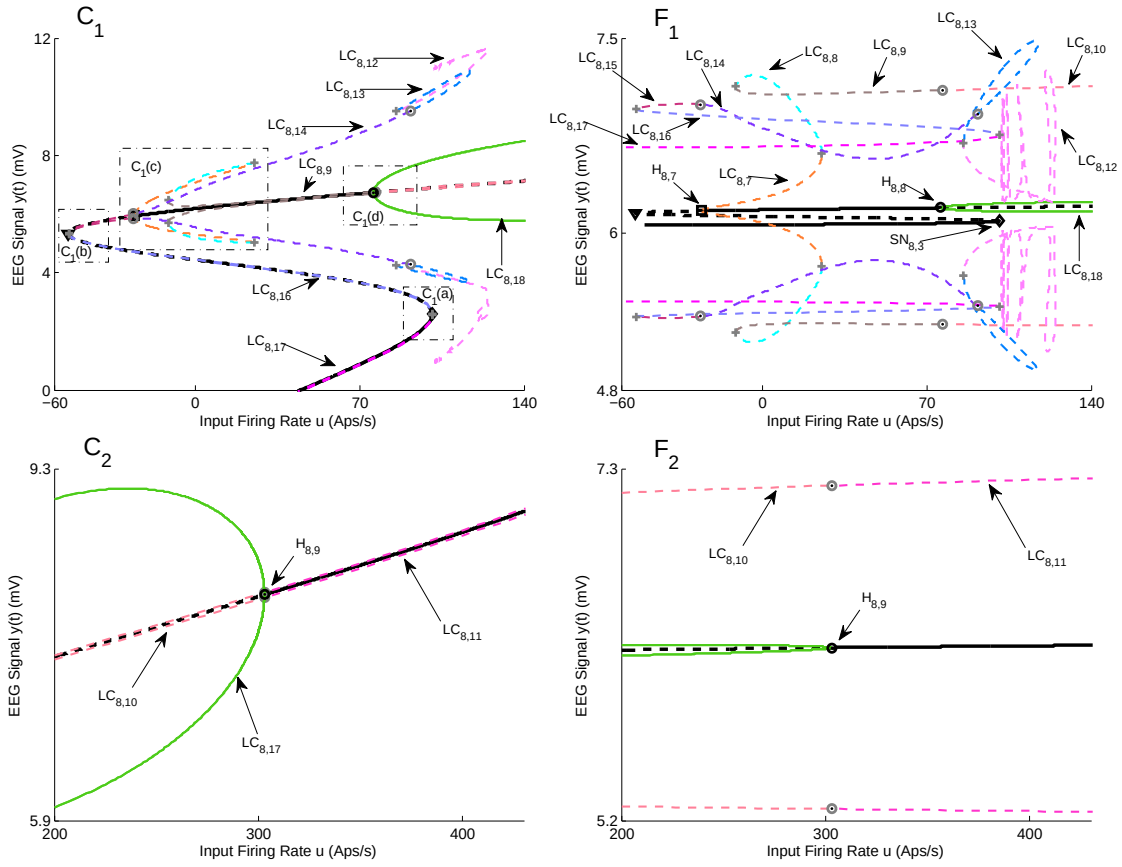

Figure 2.9: Magnified parts from the bifurcation diagram of the third branch of equilibria in Figure 2.8C and Figure 2.8F.

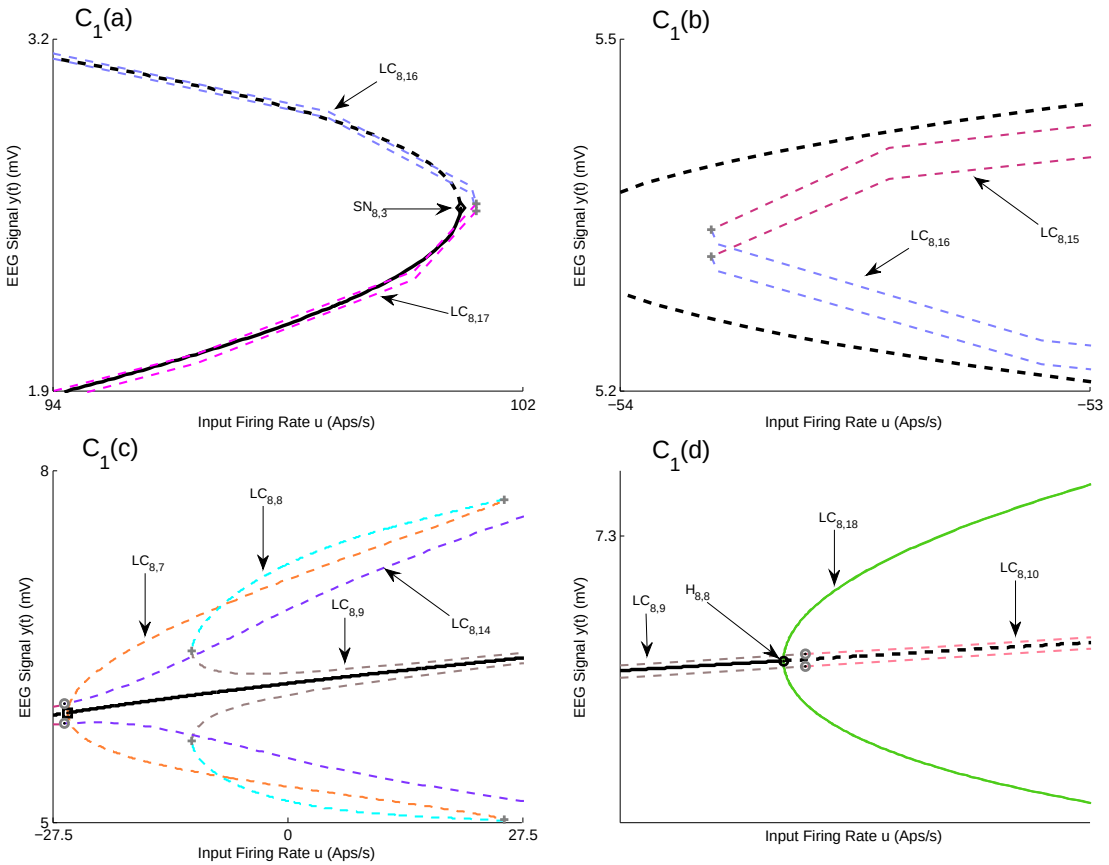

Figure 2.10: Magnified parts from the bifurcation diagram of the third branch of equilibria in Figure 2.9C_1.

2.5.1 Bifurcation analysis with coupling gain $K = 250$

By increasing the coupling gain to $K = 250$, two branches of equilibria for region b join up, which results in the appearance of a saddle node in the joint point (refer to the Appendix A.3 and Figure A.3). As a consequence, the new saddle-node homoclinic bifurcation starts that leads to new behaviour in the network, such as observing spikes in only one region or in both regions for all inputs larger than the value at which the saddle node arises. Figure 2.11 shows that all equilibria branches and bifurcations are detected in this case. In order to present this case, we split the first branch of equilibria from the saddle point and present them in two separate sub-figures (Figure 2.11A, B, D, and E).

Figure 2.11A, B, D, and E show the bifurcation diagram from the first branch of equilibria. There are six Hopf bifurcations detected on this branch ($H_{11,1}$-$H_{11,6}$) and only two

of them ($H_{11,2}$,$H_{11,3}$,) are supercritical. Figure 2.11A and D illustrate two limit cycles that arise from the bottom part of this branch. Similar to the case of $K = 50$, the unstable limit cycle $LC_{11,1}$ collides with the limit cycle $LC_{11,2}$ that appears from the saddle-node homoclinic bifurcation. The time series associated with these two limit cycles, depicted in lower part of the figures, verify that the cycle causes region a to produce spikes while region b generates delta activity. Furthermore, the stable limit cycle $LC_{11,3}$, results from supercritical Hopf bifurcation, provokes alpha activity in both regions. The bifurcation analysis of the top part of the first equilibria branch, shown in Figure 2.11B and E, is similar to the second branch of equilibria of the previous case; the trajectories of the network initialised near these two limit cycles are either attracted by the stable limit cycles or attracted by the stable equilibria on the bottom part of the first equilibrium curves.

From a topological point of view, the differences between the two cases with coupling gains $K = 50$ and $K = 250$ emerge from limit cycles that arise from the third branch of equilibria and the appearance of a limit cycle from the saddle-node homoclinic bifurcation on the first branch. The bifurcation analysis shows that the limit cycle $LC_{11,4}$ starts near the saddle-node homoclinic bifurcation on the first branch of equilibria, denoted by $SN_{11,3}$ in Figures 2.11A, B, D, and E for $u = 618$, and it exists for all values of input larger than $u = 618$, which means that the underlying network can generate spikes in both regions for large values of u in contrast to all previous cases in which spikes disappear for large values of u.

All limit cycles that emerge from the second branch of equilibria are depicted in Figure 2.11C and F and Figure 2.12. There are four Hopf bifurcations ($H_{11,7}$-$H_{11,10}$) among which three are supercritical ($H_{11,8}$-$H_{11,10}$). All limit cycles ($LC_{11,9}$, $LC_{11,16}$, $H_{11,17}$), originated from supercritical Hopf bifurcation, generate alpha activity with frequency 11 Hz. The stable limit cycle $LC_{11,16}$ starts at $u = 280$ from supercritical Hopf bifurcation and collides with $LC_{11,15}$ through LPC bifurcation at $u = 100$. We also observed that the limit cycle $LC_{11,15}$ collide with the limit cycle $LC_{11,14}$ via LPC. We were not able to proceed the continuation further to check the origin of the limit cycle $LC_{11,14}$. The time responses in lower part of Figure 2.12 shows that the trajectories of the network near these limit cycles converge to the equilibria on the first branch. The stable limit cycle $LC_{11,17}$ starts

at $u = 300$ and exists for all values of input larger that $u = 300$. As a consequence, the network can also generate alpha activity in both regions for large values of u; however, in all previous cases, alpha activity was only observed for values of u in finite intervals.

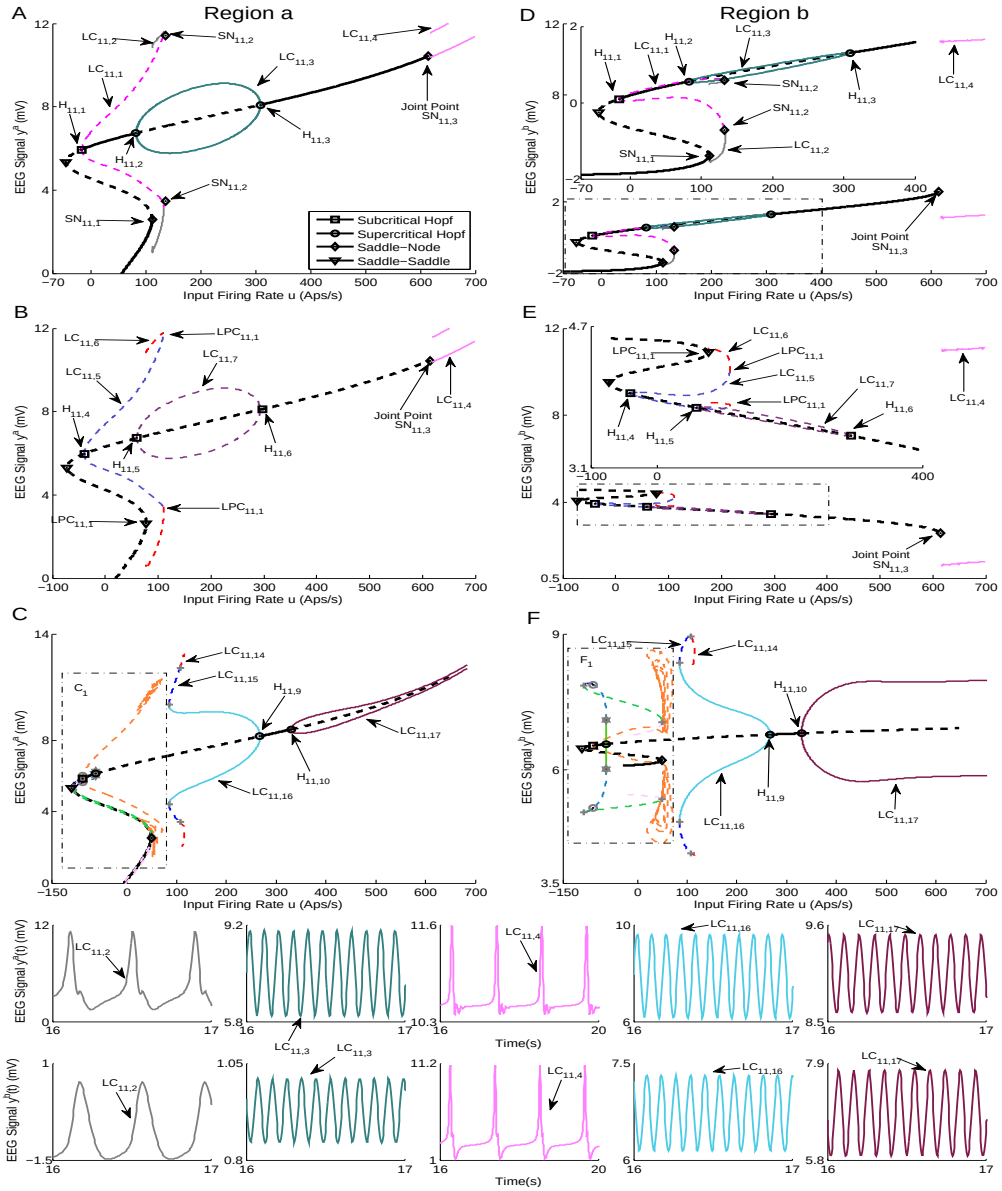

Figure 2.11: Bifurcation diagrams for case II with coupling gain $K = 250$. A), B), and C) are the first, second, and third branches of equilibria for region a. D), E), and F) are the first, second, and third branches of equilibria for region b. The lower subpanels show the EEG time series corresponding to the each part in the bifurcation diagrams. The solid black lines show stable fixed points, the solid coloured lines show stable oscillatory behaviour and the dashed lines show unstable fixed points and unstable oscillations.

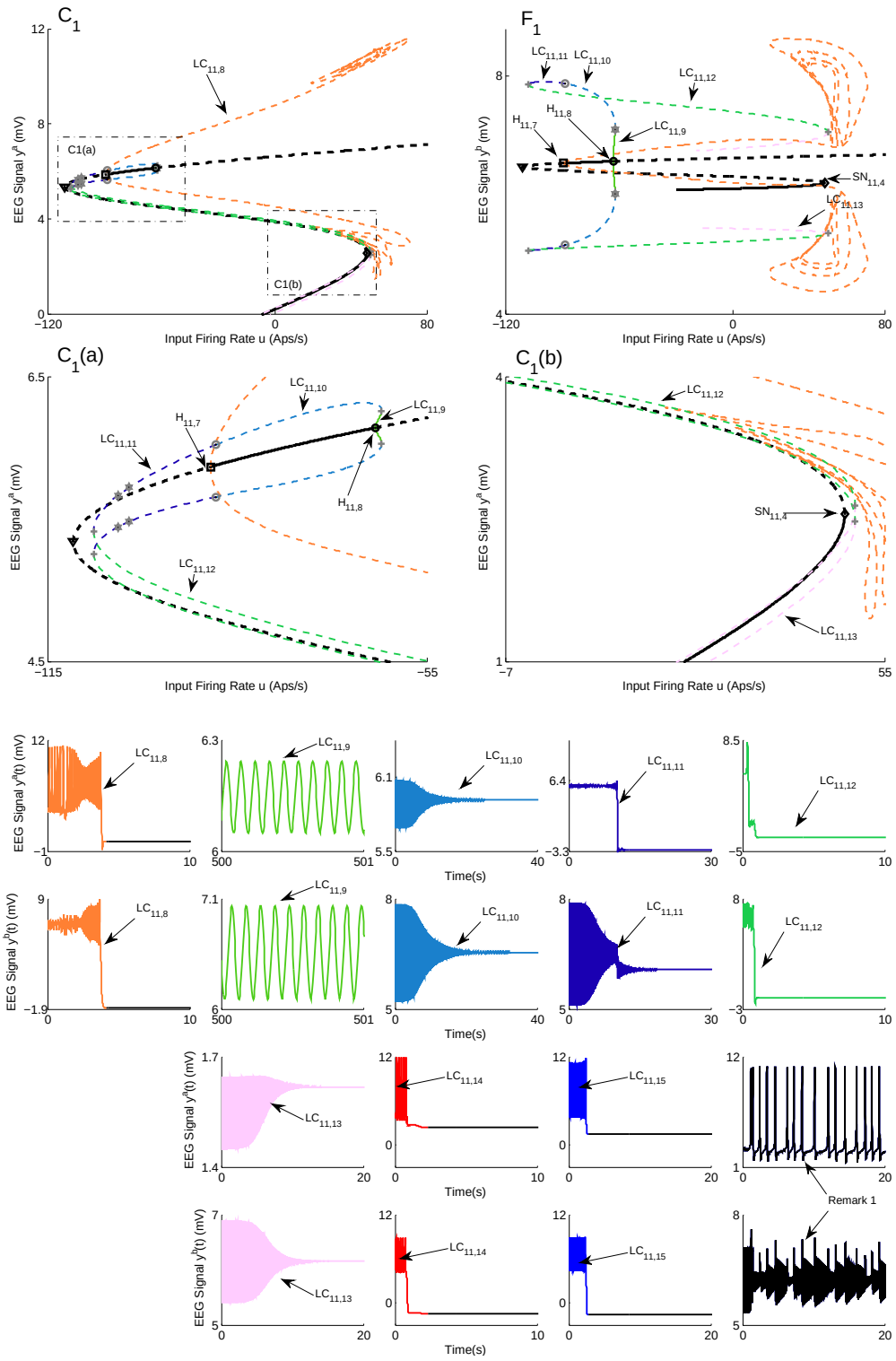

Figure 2.12: Magnified parts from the bifurcation diagram of the third branch of equilibria in Figure 2.11C and F.

The stable limit cycle $LC_{11,9}$ arises from supercritical bifurcation $H_{11,6}$. However, it collides with the limit cycle $LC_{11,10}$ via LPC as shown in Figures 2.12F_1 and C_1(a). By looking at these figures, it is possible to see how different bifurcations lead to different limit cycles. We should mention that Neimark-Sacker bifurcation of cycles (indicated by gray circle in Figure 2.12) and period-doubling bifurcations (indicated by grey hexagram in Figure 2.12) are detected during the continuation.

Remark 2.1. *We initialised the model near to the saddle node $SN_{11,4}$ in order to check the existence of a limit cycle. It seems that there exists a limit cycle which generates the output depicted in Figure 2.12. We couldn't do the continuation from this point due to software limitations.*

2.6 Case III: Bifurcation Analysis of Two Coupled Neural Mass Model with a Single Input and Feed-Forward Structure

In this section, we present the bifurcation analysis of case III, which is graphically depicted in Figure 2.1. Similar to previous cases, we start by finding equilibria of the network by solving (2.7) with u^b and K^{ba} set to zero. We observe that equilibrium curves for region b are qualitatively similar to Case II. However, the equilibrium curves for region a are slightly different. Hence, we analyse the bifurcation diagram for the network with interconnection gains $K = 50$ and 250, and explain the important differences

The bifurcation diagrams of the network with $K = 50$ are presented in Figures 2.13 and 2.14. It can be seen that the bifurcation diagram of the first and second branches of equilibria are qualitatively similar to the case in Section 2.5. For the third branch of equilibria, there is a stable limit cycle $LC_{13,7}$ that, similar to the previous cases, produces the alpha activity. There is an unstable limit cycle that emerges for $u = -12.15$ from supercritical bifurcation $H_{13,7}$. This limit cycle collides with other limit cycles through LPC as can be seen in Figures 2.13C and F. By continuing along the curve, we detected several LPC points (indicated by gray plus sign), Neimark-Sacker bifurcation of cycles (indicated by grey circle). Since there are many of them and consequently many limit cycles, we haven't labelled them. However, all limit cycles can be clearly seen in Figure can be seen in Figure 2.14. The simulated EEG for some stable limit cycles are plotted in the lower

part of Figure 2.14.

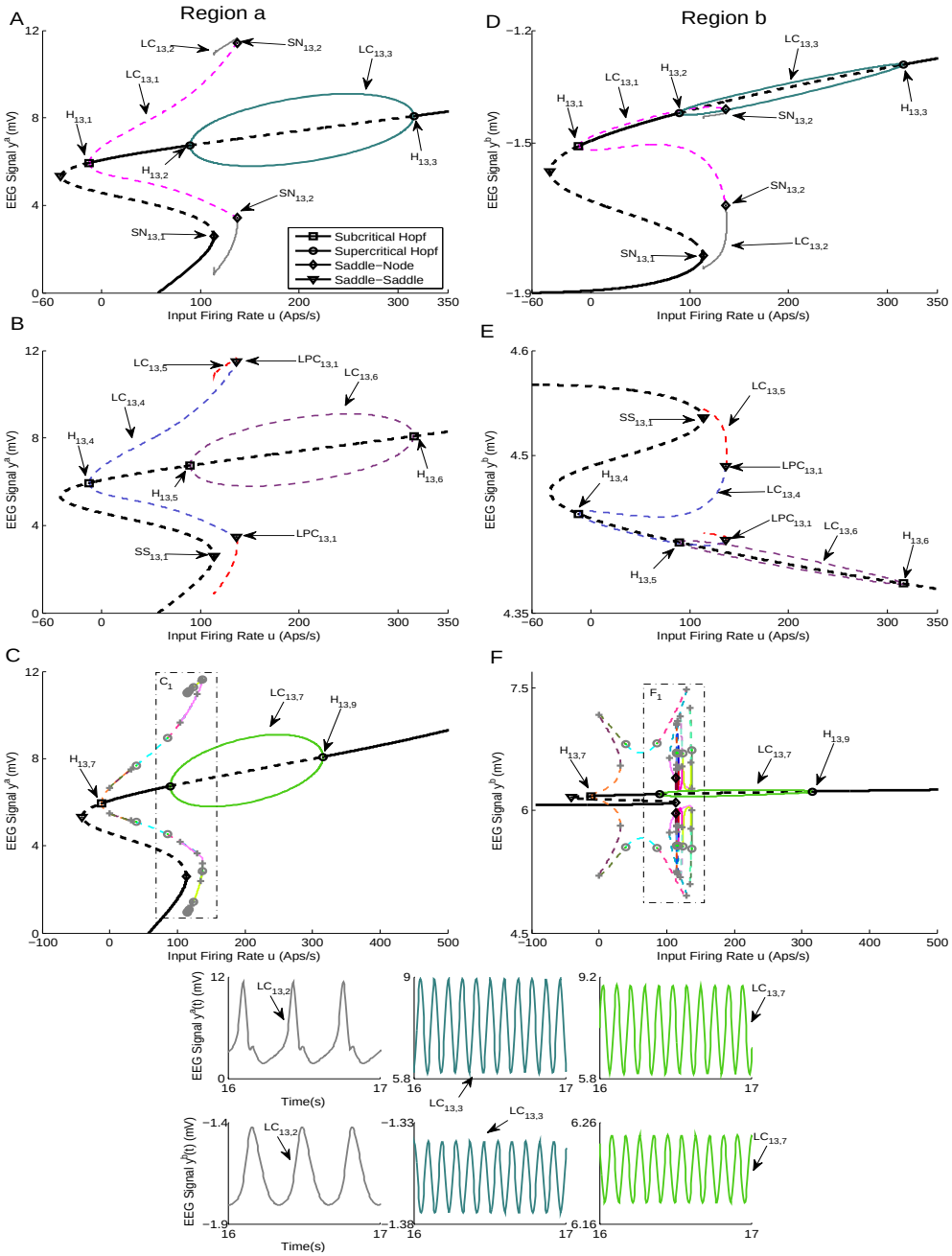

Figure 2.13: Bifurcation diagrams for Case III with coupling gain $K = 50$. A), B), and C) are the first, second, and third branches of equilibria for region a. D), E), and F) are the first, second, and third branches of equilibria for region b. The subpanels show the EEG time series corresponding to the each part in the bifurcation diagrams. The solid black lines show stable fixed points, the solid coloured lines show stable oscillatory behaviour and the dashed lines show unstable fixed points and unstable oscillations.

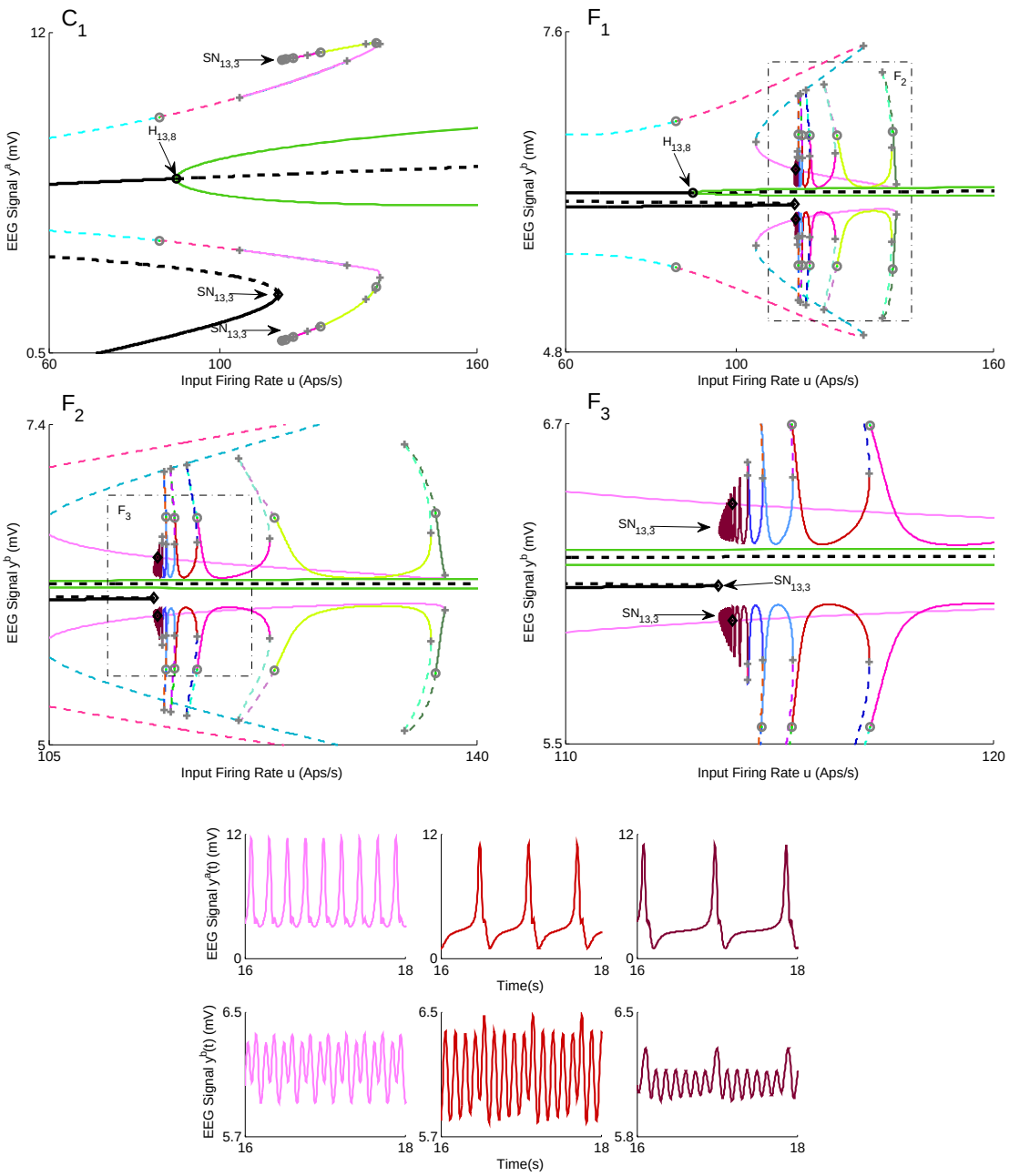

Figure 2.14: Magnified parts from the bifurcation diagram of the third branch of equilibria in A) Figure 2.13C and B) Figure 2.13F.

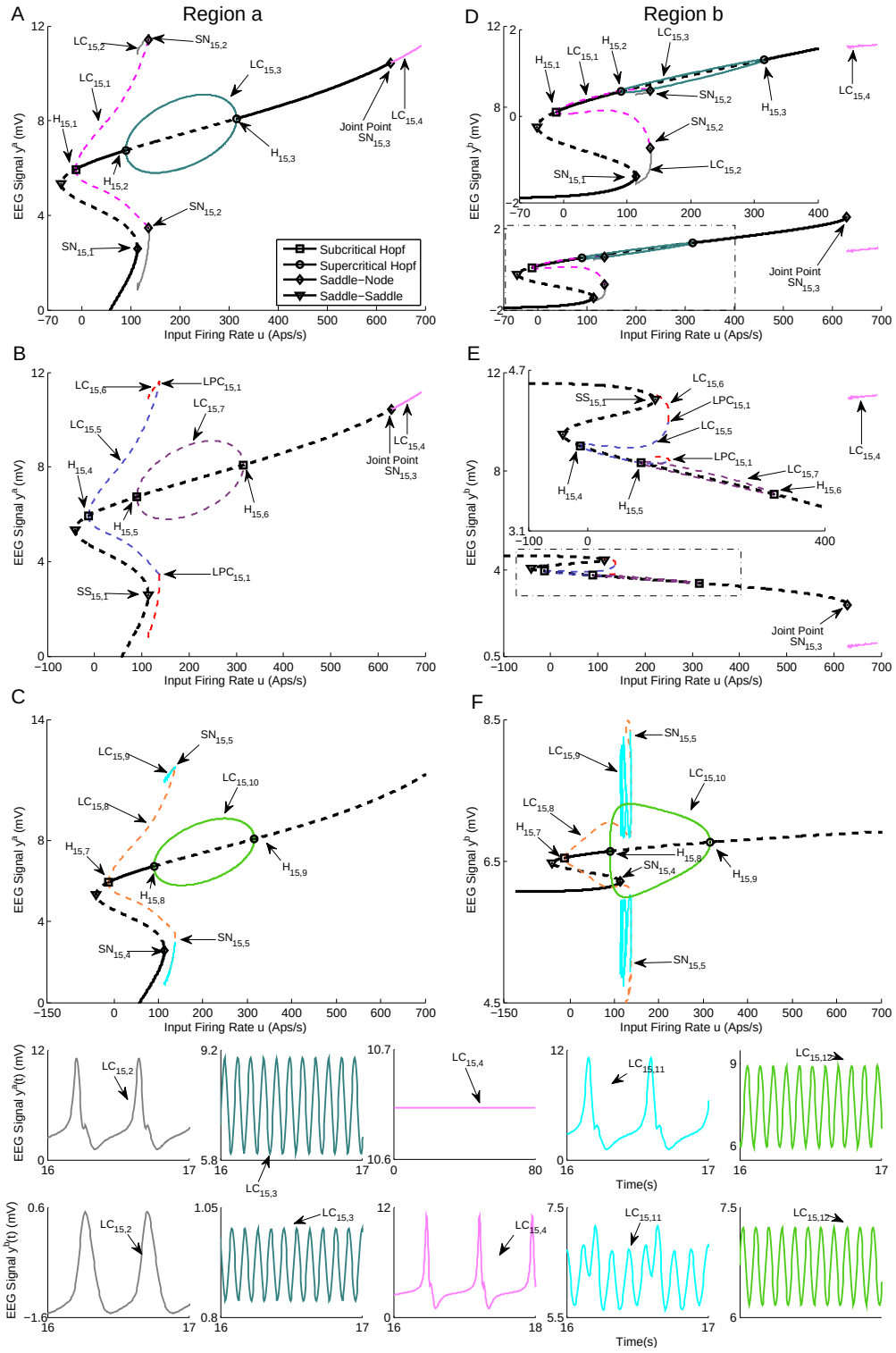

Figure 2.15: Bifurcation diagrams for Case II with coupling gain $K = 250$. A), B), and C) are the first, second, and the third branches of equilibria for region a. D), E), and F) are the first, second, and the third branches of equilibria for region b. The subpanels show the EEG time series corresponding to the each part in the bifurcation diagrams. The solid black lines show stable fixed points, the solid coloured lines show stable oscillatory behaviour and the dashed lines show unstable fixed points and unstable oscillations.

We also observed that the simulated trajectory of the network for unstable limit cycles converges to either the branch of equilibria in Figures 2.13A and D or the limit cycle $LC_{13,2}$. Furthermore, we found a limit cycle that appears from the saddle-node homoclinic bifurcation of equilibria at $SN_{13,3}$. This orbit provokes spike-wave-like discharges in region *a* and periodic output that is alpha-like with some amplitude modulation, as plotted in Figure 2.14.

The bifurcation diagrams for coupling gain $K = 250$ are plotted in Figure 2.15. Similar to case II with coupling gain $K = 250$, there is a limit cycle $LC_{15,4}$ that starts from a saddle-node homoclinic bifurcation $SN_{15,3}$ on the first branch of equilibria for $u = 631$. This limit cycle generates spike-wave-like discharges with the frequency of 1.25Hz in the region *b*. Region *a* shows constant behaviour in the time domain when the whole network evolves on the cycle. The bifurcation diagram of the second branch of equilibria in Figure 2.15C and F includes a stable limit cycle $LC_{15,10}$, results from a supercritical Hopf bifurcation, and generates alpha-like activity in both regions. The unstable limit cycle $LC_{15,5}$ collides with the limit cycle $LC_{15,9}$, resulting from the saddle-node homoclinic bifurcation, for $u = 135.4$. According to the simulated EEG, this orbit results in the appearance of spikes with the frequency of 3Hz in the region *a* and delta-like output in the region *b*.

2.7 Relationship to Clinical Data

We have presented a series of snapshot bifurcation diagrams to explore different behaviors that can be observed in interconnected neural mass models. In this section, we relate our analyses to clinical ECoG recorded from two electrode channels during seizures from a single patient with refractory temporal lobe epilepsy. Data was obtained from a previous clinical trial (see [37] for details, the current patient is subject 3). State and parameter estimation were conducted on two 6 minute recordings (sampled at 400 Hz), each containing a different epileptic seizure. The estimation approach used a method of Gaussian belief propagation (see Appendix A.4 for detail on the estimation method) to simultaneously track fast states (the membrane potentials of the population in the coupled neural mass model and their derivatives), the slowly varying bifurcation parameter u (repre-

senting the external input to each neural region), and a DC offset to compensate for drift introduced by changes in the input parameter (since the data had previously been amplified using a common average reference, removing most true DC content from the signal).

In brief, the estimation proceeded as follows, data were first pre-processed using a zero-phase bandpass (1-180 Hz) and notch filter (50Hz notch), and upsampled (lowpass interpolation) to 1200 Hz[7]. Data were also scaled to reflect the dynamic range observed in the bifurcation analysis (approximately 0 - 12 mV). The estimation algorithm has three steps; initialisation, prediction, and update. Initialisation sets the estimation prior as a multivariate Gaussian probability density function (pdf) over the estimation states and parameters. The next step is to predict the posterior pdf by propagating the Gaussian prior through the non-linear, discretised neural mass equations. The update step then adjusts the predicted posterior based on the incoming measurement. Finally, the prior is reinitialised as a Gaussian distribution with the same mean and variance as the posterior, and the process is iterated for the next time step ($dt = \frac{1}{1200}$). In the case of a linear model, this estimation scheme is known as the Kalman filter [80]; however, here we are able to use a fast, semi-analytic solution to the belief propagation step to relax the linearity assumption. Nevertheless, several simplifying assumptions are used; model and measurement errors are described by additive, white Gaussian noise, and cortical dynamics are assumed to be Markovian, or memoryless. These assumptions are certainly not ideal for modelling epileptic dynamics; however, without this simplification there is no tractable solution for tracking parameters in real time. To our knowledge this algorithm reflects the current state-of-the-art for joint state and parameter estimation in the neural mass model [58], and the best available solution for relating measured ECoG to the hidden bifurcation parameter u.

[7]The band-pass filter was to remove noise from the data (it was recorded from a noisy, real-word setting with a sampling rate of 400Hz so we expected an upper cut-off of maybe 150-180Hz. The recording device used a common average reference, so there should be no DC content, and any DC drift is considered as noise. So we set the lower cut-off to be something above 0Hz.) The upsampling is for a different reason. It is because the inference uses numerical integration and when the step-size is too large we did not get convergence. The smallest step size is about 1000Hz. So if we used 400Hz for inference it would not match the bifurcation plots that are generated. But our data was 400Hz so it's easiest to up-sample to 1200Hz.

The following sections relate the estimation results for the bifurcation parameter u in each of the three models (Case I, II, and III) for weak coupling ($K = 50$) to the dynamic snapshots that were presented in the preceding sections. The estimation is the statistically most likely evolution of the input parameter u given a distribution conditioned jointly on the model parameters and data (and subject to the assumptions outlined above). In addition to performing estimation, we also implemented a deterministic forward simulation of the coupled regions using the Runge-Kutte method on the discretised form of equation 2.1. We ran the simulation using values for the input parameter u which were estimated from data and keeping all other values fixed (according to Table 2.1). This step provided further insight into the predicted dynamics of the output ECoG based on alterations in input. All code used for estimation and simulation was implemented in MATLAB and Statistics Toolbox (release 2015a, The MathWorks Inc., MA, United States) and is available online from `https://github.com/pkaroly/Bifurcation-Estimation`.

2.7.1 Seizure one

Figures 2.16A, B show recorded ECoG from two channels for seizure one (data were sampled at 400 Hz and bandpass filtered between 1 - 180 Hz). For interconnected model in the Case I, the estimation results are plotted on the left wall panel of Figure 2.16C, D. These figures indicate that, during the early stage of the seizure, the estimated input u varies between 80 and 100 followed by a sudden increase to approximately 200. By comparing the estimated parameter to the bifurcation plot in the floor panel of Figure 2.16C, D, we see that, for the first range of the input, the system has two orbits which are associated with spike generation. However, the bifurcation diagrams show that by increasing the input, the system transitions to the limit cycle (alpha activity). There is no clear transition at the end of the seizure as the model does not transition back to a fixed point. Consequently, if the estimated input is applied to the model in forward simulation (with all other parameters fixed), it will show alpha activity at the end of seizure, as we see in the right wall panel of Figure 2.16C, D. This suggests that this model configuration may not be suitable to capture the observed behaviour for seizure one.

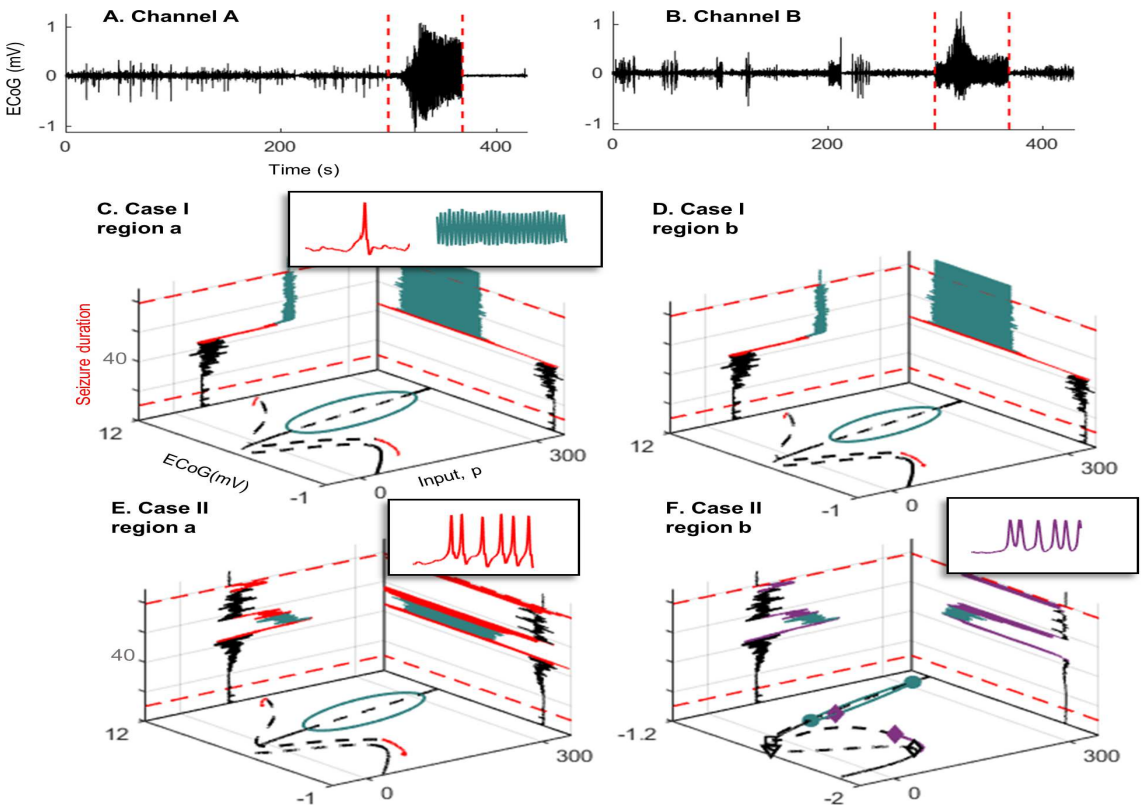

Figure 2.16: Recorded ECoG from two channels for seizure one and the bifurcation diagrams. Panels A) and B) are ECoG recordings of the same seizure (seizure one) on two different electrode channels. Recording was taken five minutes prior to seizure onset (red dashed line) and continued for 1 minute after offset (red dashed line). C) and D) show the bifurcation diagrams corresponding to case I, estimated input parameter u during the seizure and the output ECoG after forward simulation based on the estimated input. Note that the plot only shows estimation from 10s before seizure onset to 10 s after seizure offset. E) and F) show the same plots as C) and D) but correspond to case II of the coupled neural mass model.

2.7.2 Seizure two

The estimation process yielded a similar range of inputs for cases II and III, suggesting that the transition between normal behaviour and epileptic activity mainly results from the first branch of equilibria, since the bifurcation diagram associated to the first branch of equilibria for case II (Figure 2.8A, D) is the same as case III (Figure 2.13A, D). The estimation results in the left wall panel of Figure 2.16E, F show that, early in the seizure, the

input varies between 80 and 90, then briefly reaches a peak around 200, approximately 40 s into the seizure. This input peak pushes the trajectory of the system into the limit cycle after some transient spiking possibly caused by the orbit originating from the saddle-node homoclinic bifurcation. The transition in region *a* also drives region *b* to transition into a limit cycle. This transition corresponds to the seizure reaching its peak amplitude on the ECoG in Channel A (Figure 2.16E). However, as the input drops to the range of 90 to 100, the system state is attracted once more to the cycle, and returns to epileptiform spiking activity in region *a* and amplitude modulated alpha activity in region *b*.

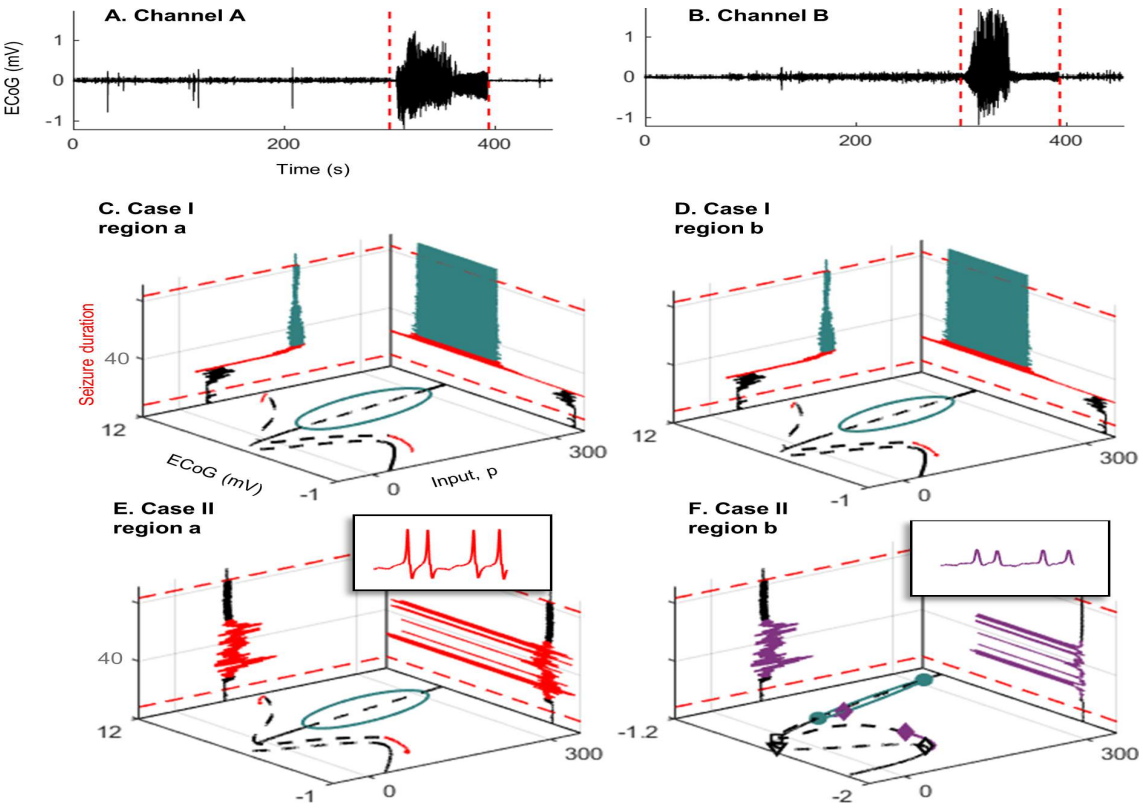

Figure 2.17: Recorded ECoG from two channels for seizure two and the bifurcation diagrams. Panels A) and B) are ECoG recordings of the same seizure (seizure two) on two different electrode channels. Recording was taken five minutes prior to seizure onset (red dashed line) and continued for 1 minute after offset (red dashed line). C) and D) show the bifurcation diagrams corresponding to case I, estimated input parameter u during the seizure and the output ECoG after forward simulation based on the estimated input. Note that the plot only shows estimation from 10s before seizure onset to 10s after seizure offset. E) and F) show the same plots as C) and D) but correspond to case II of the coupled neural mass model.

Figure 2.17A, B show recorded ECoG for seizure two. The estimation results for Case I (Figure 2.17C, D) for seizure two are very similar to the previous seizure. However, Case II (Figure 2.17E, F) shows some differences to seizure one. The estimation for Case II was the same of that for Case III. Here, for Case II, the input is higher ($u > 110$) early in the seizure and continues to vary around this level. Conversely, during seizure one, the peak did not occur until 40s into the seizure and then the input dropped approximately monotonically. The increased input variability during seizure two indicates that the states of the system experienced more transients near the homoclinic orbit. Consequently, in the simulated ECoG obtained from the estimated input u (right wall panels of Figure 2.17E, F), we see epileptic spiking during the seizure only in region a, which is consistent with simulations in Figure 2.8A, D. The difference between the results for the two data sets suggest that during some seizures region b is driven into a limit cycle, but during other seizures this state change does not occur. Interestingly, seizure two occurred in the middle of the day (around 1pm), whereas the first seizure occurred at night (approximately 10pm), so it is possible the different mechanisms were related to different states of arousal, although many more seizures would be required to investigate this hypothesis.

2.8 Discussion

This chapter presented a bifurcation analysis of a neural mass model for two cortical regions. The results detail the rich repertoire of dynamics that the network can generate and how the range of possible activity varies with changes in the external inputs and interconnectivity gains. The bifurcation plots extend previous analyses of single region neural mass models and show that the dynamics of the interconnected neural masses can generate a far broader range of oscillatory dynamics, including multiple alpha-like rhythms, transient bursting, remote spiking, and delta wave activity.

Interestingly, for all cases and all interconnectivity gains, the models were able to pro-

duce alpha-like oscillation. Furthermore, in all of the scenarios that were explored, the alpha-like rhythms occurred concurrently in both regions or not at all. Similar to earlier studies considering a single region model [65, 120], the alpha rhythms were always generated by stable limit cycles originated from supercritical Hopf bifurcations. A key difference for the multiple region model is the existence of multiple types of alpha-like rhythms, representing different limit cycles with various amplitudes ranges. It is also interesting to note that network of identical regions with symmetric coupling and balanced inputs can generate oscillations with different amplitudes across the regions. The idea of the coexistence of multiple types of a discrete number of alpha rhythms builds on existing studies and should be investigated experimentally [59].

Our analysis revealed interesting insights into the possible mechanisms of the generation of spike-wave discharges. In case I of the symmetrical network with weak inter-region coupling, our results are naturally similar to existing results for a single neural mass model [65]. However, further important insights can be gained when studying two regions. As the coupling gain is increased, we see a merger of the outer limit cycle, which is responsible for the normal alpha-like rhythm, with the pathological orbit that is responsible for the generation of spike-wave like discharges. For low inter-region connectivity gains, the only way to transition to a seizure from alpha is via a large variations in the input. However, for intermediate and high inter-region connectivity gains, a path to seizure exists by variations in the input. This merger of the respective limit cycles represents one candidate explanation for the process of epileptogenesis. It should be pointed that, for all values of connectivity gains, the model can transient from fixed points to orbit and vise versa. These transitions are also the responsible model for seizure.

For Case II with high interconnection gains, the underlying network was only able to generate spikes for all values of input larger than a specific value as seen in Figure 2.11. This new result shows the networks with this structure will always transition to an epileptiform pattern of activity given a sufficiently strong input, as the orbit, resulted from saddle-node homoclinic bifurcation, is the only stable pattern of activity. This find-

ing contrasts other cases when a perturbation from other stable cycles may also be required.

In Case III (Figure 11), we alarmingly see the occurrence of spike-wave discharges in region b due to increases in input to region a. The spikes do not occur in region a. The reason why this is alarming is that region b was set to represent healthy activity. Region b simply experienced a flow on effect from changes in the input to region a and is otherwise normal. This scenario poses a problem for planning epilepsy related surgery. The analysis shows that the presence of focal spike-wave discharges is not a sufficient condition to locate the pathology. The ideal treatment target in this scenario would be to limit to input in region a, as removal of region b would not treat the root cause.

The interconnected neural mass models are able to produce delta wave-like activity (Cases II and III). Interestingly, we observed stable delta wave-like activity in one region and spike-wave-like activity in the other region. Since the delta wave is observed during sleep, these networks can be potentially utilised to model and form a deeper understanding of nocturnal seizures in which a part of brain exhibits seizure activity while other parts do not. Our estimation results in Section 2.7 also suggested there are multiple mechanisms of seizures, which may correspond to different alertness levels. A more rigorous investigation estimating mechanisms of seizures at different times of day is the focus of ongoing work.

The estimation results showed that the model in Case I might not be representative of brain during and after the seizure. The estimated input could steer the model from spike-wave-like activity to alpha activity, however, it was not able to transition back to a resting state. As a consequence, the estimated input did not drive the system to normal behaviour at the end of seizure. In contrast, the forward simulation using the estimated input showed that Case II and III could generate non-identical spikes in both regions, and also transition between spike-like activity to the normal behaviour after the end of the seizures. These results imply that the models in Case II and III more closely cap-

ture seizure dynamics than Case I. We can speculate from this that once a seizure has spread, either an asymmetric, or possible alteration of the existing connectivity pattern is required for its termination. This is consistent with the analysis of [78], who suggest that a distinct bifurcation is required for seizure termination, compared to seizure onset.

Our estimation approach was conservative, as we estimated the input with other parameters fixed. By estimating more parameters, it may be possible to obtain a more realistic approximation of the true behaviour. However, with more free parameters, it becomes difficult or impossible to relate the estimated parameter trajectories to a bifurcation analysis. Therefore, such an extension is beyond the scope of the current work. Nevertheless, our estimation is a qualitative picture of dynamical state changes from recorded ECoG, which may provide insight into mechanisms of seizures. For instance, we found that during seizure one, both regions were driven into the limit cycle, whereas in the second seizure this was not the case. Once the system enters a limit cycle, the pathologic state may be harder to terminate, due to a hysteresis effect whereby lowering u does not immediately reverse the effects of the transient increase (as shown in Figure 2.16E,F). Identifying such differences in seizure mechanisms is important for targeting treatment.

Before closing our discussion, it should be mentioned that the computational model is a crude approximation of a real brain. Nevertheless, it is challenging to present a more comprehensive model that describes a wide range of brain activities. The authors caution the reader to interpret the results as possible behaviours that can be generated from two interconnected cortical regions, rather than behaviours that will occur. Also, we stress that the range of possible dynamics holds for the two region model. Further increasing the complexity of the model by adding neural populations or cortical regions will undoubtedly yield a more complicated bifurcation structure. Nevertheless, the work is an important contribution demonstrating the flexibility of this neural mass modelling framework.

As future work, this analysis can be extended by using co-dimension 2 bifurcation

analysis with respect to both the interconnection gain and another network parameter. From a technical perspective, it is also valuable to analyse the geometric property of the cycle that is born from the saddle-node homoclinic bifurcation in the first branch of equilibria in Cases II and III.

Chapter 3

Local Synchronisation of Networks of Wilson-Cowan Oscillators With Diffusive Coupling

3.1 Introduction

In the previous chapter, bifurcation analyses have been presented for a network with two Jansen-Rit neural populations. The bifurcation diagrams showed that oscillatory behaviours of the network result from the existence of limit cycles in the dynamic of the network. However, a single neural population can also exhibit oscillatory behaviours which emerge from limit cycles as shown through bifurcation analysis in [65,120]. Hence a possible approach to study synchronisation in the network is to consider each node as an oscillator and find the interconnection gains so that all oscillators become locally synchronised (see Subsection 1.2.4 for the overview).

In this chapter, we consider a network of Wilson-Cowan neural populations instead of a network of Jansen-Rit neural populations. The reason is that the Wilson-Cowan model is less complicated than Jansen-Rit model. The Wilson-Cowan model [135] is of great interest since it is parsimonious, as it describes the activity of both excitatory and inhibitory populations of neurons and reproduces self-sustained oscillations observed in electroencephalography (EEG) signals. In particular, local synchronisation of the Wilson-Cowan model has been investigated in the literature using the centre manifold theorem [75] and the notion of phase response curves [40]. These approaches only deal with weak couplings. However, synchronisation can be observed in Wilson-Cowan networks with in-

termediate or strong coupling if the interconnection is diffusive.

In the rest of this chapter, we use the word "node" to refer a neural population in the network. Our methodology transforms the problem of synchronisation in the original network to the stability analysis of master stability equation (MSE) which is obtained from linearisation of the network dynamic around a stable limit cycle [102,113,139]. Since we assume that the network is homogeneous, this limit cycle corresponds to a periodic solution of each node. As a consequence, the linearised system is a linear periodically time-varying system. The stability/instability of this system depends on eigenvalues of Laplacian matrix of the network. We then use a similarity transformation to show the stability/instability of linearised system can be determined by the stability/instability of some decoupled subsystems, each of which corresponds to the Jordan blocks of the Laplacian matrix. We exploit the cascade structure of each subsystem to show the equivalence between stability/instability of each subsystem and stability/instability of a reduced subsystem. At this stage, we use a combination of different tools to analyse the stability/instability of the reduced system in terms of eigenvalues of its Laplacian matrix. These tools include Floquet theory, Lyapunov stability, Chetaev instability theorem, and a numerical approach proposed in [113].

This chapter is organised as follow. In Section 3.2, we briefly introduce the Wilson-Cowan model of a single population, as well as the network of such models with non-identical nodes. In Section 3.3, we formulate the problem for a more general network with identical nodes. In Section 3.4, the synchronisation conditions are established for the network. Robustness of synchronisation is analysed in Section 3.5. Simulation results and conclusions are presented in Sections 3.6 and 3.7, respectively.

3.2 Wilson-Cowan Model

Neural mass models describe the relationships between neural populations. Lumped parameter neural mass models are constructed by interconnecting neural populations that generate some realistic EEG patterns like alpha or beta waves. In this class of model, the dynamics of each neural population can be described by a linear first-order system

coupled with a sigmoid non-linearity that converts the average membrane potential of a neural population into an average pulse density of action potentials. This model is given by

$$\dot{x}_s = -\alpha x_s + f(\rho + I), \tag{3.1}$$

where $x_s \in \mathbb{R}$ describes the average membrane potential of a single population that can be either excitatory x_E or inhibitory x_I. The parameter α is the population time constant and ρ denotes the sensory input or input from other neurons. The inputs from neighbouring or distant populations are represented by I. $f_i : \mathbb{R} \to \mathbb{R}$ is a sigmoid function given by

$$f_i(\theta_j) = \frac{1}{1 + \exp(-r_i \theta_j)} \quad , \quad r_i > 0,\ j = 1, 2. \tag{3.2}$$

The neural mass model of Wilson-Cowan [135] characterises the behaviour of spatially localised neural populations via a lumped parameter description. This model contains an excitatory and an inhibitory neural population that are coupled together and are considered as a single "node". The Wilson-Cowan model is described by

$$\dot{x}_i = -\Lambda_i x_i + F_i(\Upsilon_i + \Xi_i x_i + I_{x_i}), \tag{3.3}$$

where $x_i = [x_{E_i}, x_{I_i}]^T \in \mathbb{R}^2$ is a stack vector of the average membrane potentials of the excitatory and inhibitory populations, x_{E_i} and x_{I_i}, respectively. The vector $I_{x_i} = [I_{E_i}, I_{I_i}]^T \in \mathbb{R}^2$ represents the exogenous inputs that include the input from neighbouring populations and/or external inputs such as controller inputs. The matrices $\Lambda_i, \Upsilon_i, \Xi_i$ are determined by

$$\Lambda_i = \begin{bmatrix} \alpha_{E_i} & 0 \\ 0 & \alpha_{I_i} \end{bmatrix} \quad , \quad \Upsilon_i = \begin{bmatrix} \rho_{E_i} \\ \rho_{I_i} \end{bmatrix} \quad , \quad \Xi_i = \begin{bmatrix} a_i & -b_i \\ c_i & -d_i \end{bmatrix}, \tag{3.4}$$

where a_i, b_i, c_i, d_i are positive constants and referred to as synaptic gains. The nonlinear function $F_i(\theta) : \mathbb{R}^2 \to \mathbb{R}^2$ is described by

$$F_i(\theta) = \begin{bmatrix} f_i(\theta_1) \\ f_i(\theta_2) \end{bmatrix}. \tag{3.5}$$

In order to interconnect Wilson-Cowan oscillators, it is assumed that the excitatory neural population of one node is coupled to the excitatory neural population of another node. The same coupling configuration is assumed for connection between inhibitory populations in two distinct nodes. In other words, if a node i is coupled to a node j with coupling gain w_{ij}, then the excitatory neural population and inhibitory neural population in node i are coupled to the excitatory and inhibitory neural populations in node j with the coupling gains w_{ij} and $-w_{ij}$, respectively. We note that this assumption is somewhat restrictive as these two interconnections can have different coupling gains in general [75,129]. Figure 3.1 depicts two interconnected Wilson-Cowan models. Although the interconnection between nodes was originally considered as a direct coupling, it has been proposed that diffusive coupling can be utilised to control oscillatory behaviours and, in particular, synchrony behaviour of populations [129].

Now, consider a network with N Wilson-Cowan Oscillators interconnected with diffusive coupling. In this case, the dynamics of each node is represented by

$$\dot{x}_i = -\Lambda x_i + F_i\left(\Upsilon_i + \Xi_i x_i + D_s \sum_{j=1}^{N} w_{ij}(x_j - x_i)\right), \tag{3.6}$$

where

$$D_s = \begin{bmatrix} 1 & 0 \\ 0 & -1 \end{bmatrix}, \tag{3.7}$$

due to assuming the interconnections are restricted to being excitatory-excitatory and inhibitory-inhibitory.

3.3 Problem Formulation

In this section, we formulate the problem of synchronisation in the network of Wilson-Cowan oscillators. It is worth mentioning that the Wilson-Cowan model (3.6) differs from the general model studied in [102, 113, 139]. In the Wilson-Cowan model, the nonlinearity term acts on the diffusive term $(x_i - x_j)$; however, in [102, 113, 139], the interactions between nodes have been considered as diffusion between nonlinear terms in the form

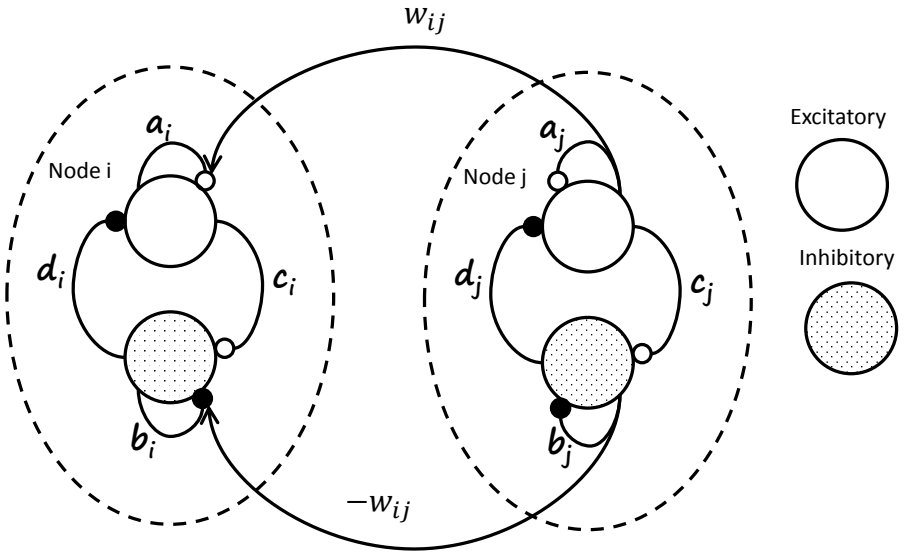

Figure 3.1: Schematic diagram of two interconnected Wilson-Cowan models [129]. Every node contains an excitatory and inhibitory populations.

of $f(x_i) - f(x_j)$. This fact leads to a different linearised model for the network of Wilson-Cowan oscillators compared to the linearised model in [102, 113, 139]. We interconnect more than two populations in (3.1) and consider a network of N homogeneous interconnected nodes in which every node is described by

$$\dot{x}_i = -\Lambda x_i + F\left(\Upsilon + \Xi x_i + D\sum_{j=1}^{N} w_{ij}(x_j - x_i)\right), \tag{3.8}$$

where $x_i \in \mathbb{R}^n$ is the state vector, $\Upsilon \in \mathbb{R}^n$ represents an external input applied to each node, and $\Xi \in \mathbb{R}^{n\times n}$ shows the internal coupling among states of the node. $F = (f, f, \ldots, f) : \mathbb{R}^n \to \mathbb{R}^n$ is a sufficiently smooth nonlinear function guaranteeing the existence of a solution. $D \in \mathbb{R}^{n\times n}$ is an arbitrary matrix, describing the inner coupling between states of all nodes. The interconnection between nodes and dynamics of each node are assumed to satisfy the following assumptions.

Assumption 1. *The interconnections among nodes are directed and there is no self loops. In this case, the interconnection topology is represented by a zero-sum row matrix $L \in \mathbb{R}^{\mathbb{N}\times\mathbb{N}}$, known as a graph Laplacian defined by $l_{ij} = -w_{ij}$ for $i \neq j$ and $l_{ii} = \sum_{j=1}^{N} w_{ij}$. We also assume that the*

interconnection graph has at least one globally reachable node, i.e. the node, to which, there exists at least one path from every node in the network. In this case, the Laplacian matrix has exactly one zero eigenvalue $\lambda_1 = 0$*, and other eigenvalues have positive real parts, i.e.* $\Re(\lambda_k) > 0$ *for* $k = 2, \ldots, N$ *[104].*

Assumption 2. *In the absence of interconnections, i.e.* $w_{ij} = 0 \ \forall i, j = 1, \ldots, N$*, each node (3.8) has a periodic solution* $\bar{x}(t) = \bar{x}(t+T)$ *produced by an asymptotically stable limit cycle that satisfies*

$$\dot{\bar{x}} = -\Lambda \bar{x} + F\left(\Upsilon + \Xi \bar{x}\right). \tag{3.9}$$

The analysis that follows is based on the master stability function approach, where we linearise (3.8) around the oscillatory trajectory $\bar{x}(t)$. The linearised trajectory is given by

$$\dot{x}_i = -\Lambda x_i + F\left(\Upsilon + \Xi \bar{x}\right) + A(t)\left(\Xi\left(x_i - \bar{x}\right) + D\sum_{j=1}^{N} l_{ij}\left(x_j - x_i\right)\right), \tag{3.10}$$

where $A(t) = \frac{\partial F}{\partial x}|_{\Upsilon + \Xi \bar{x}}$.

Define $\tilde{x}_i = x_i - \bar{x}$, the difference between trajectories of each node and the oscillatory trajectory. Considering (3.9) and (3.10), the dynamics of $\tilde{x}_i$ can be expressed as

$$\dot{\tilde{x}}_i = -\Lambda \tilde{x}_i + A(t)\left(\Xi \tilde{x}_i + D\sum_{j=1}^{N} l_{ij}\left(\tilde{x}_j - \tilde{x}_i\right)\right), \tag{3.11}$$

which leads to the aggregated linearized system form as

$$\dot{\tilde{x}} = \left(I_N \otimes \left(-\Lambda + A(t)\Xi\right) - L \otimes A(t)D\right)\tilde{x}, \tag{3.12}$$

where $\tilde{x} = \mathrm{vec}(\tilde{x}_1, \ldots, \tilde{x}_N)$.

Let Σ be the Jordan block associated with the Laplacian matrix, i.e. $L = U\Sigma U^{-1}$. Since the eigenvalues of L are complex, the matrices U and Σ are complex, i.e. $U \in \mathbb{C}^{N\times N}$, $\Sigma \in \mathbb{C}^{N\times N}$. Changing to new coordinates $\tilde{y} \in \mathbb{C}^{Nn}$, $\tilde{y} = (U^{-1} \otimes I_n)\tilde{x}$ gives

$$\dot{\tilde{y}} = \left(I_N \otimes \left(-\Lambda + A(t)\Xi\right) - \Sigma \otimes A(t)D\right)\tilde{y}. \tag{3.13}$$

Let us represent Σ as $\Sigma = \text{diag}\{\Sigma_k\}_{k=1}^{p}$, where

$$\Sigma_k = \begin{bmatrix} \lambda_k & 1 & 0 & \cdots & 0 \\ 0 & \lambda_k & 1 & \cdots & 0 \\ 0 & 0 & \lambda_k & \cdots & 0 \\ \vdots & \vdots & \ddots & \ddots & \vdots \\ 0 & 0 & 0 & \cdots & \lambda_k \end{bmatrix}_{m_k \times m_k}, \tag{3.14}$$

$\lambda_k(L) \in \mathbb{C}$ are eigenvalues of the Laplacian matrix, and $m_1 + \cdots + m_p = N$. Since Σ is a block diagonal matrix, (3.13) is decoupled into p independent systems described by

$$\dot{\tilde{y}}_k = \left(I_{m_k} \otimes (-\Lambda + A(t)\Xi) - \Sigma_k \otimes A(t)D\right)\tilde{y}_k, \quad k = 1, \ldots, p, \tag{3.15}$$

where $\tilde{y}_k \in \mathbb{C}^{m_k n}, \tilde{y}_k = [\tilde{y}_{k,1}^T, \ldots, \tilde{y}_{k,m_k}^T]^T$. Separating the real and imaginary part of $\tilde{y}_k$ in (3.15) leads to

$$\begin{aligned} \frac{d}{dt}\Re(\tilde{y}_k) &= \left(I_{m_k} \otimes (-\Lambda + A(t)\Xi) - \Re(\Sigma_k) \otimes A(t)D\right)\Re(\tilde{y}_k) \\ &\quad + (\Im(\Sigma_k) \otimes A(t)D)\,\Im(\tilde{y}_k) \\ \frac{d}{dt}\Im(\tilde{y}_k) &= \left(I_{m_k} \otimes (-\Lambda + A(t)\Xi) - \Re(\Sigma_k) \otimes A(t)D\right)\Im(\tilde{y}_k) \\ &\quad - (\Im(\Sigma_k) \otimes A(t)D)\,\Re(\tilde{y}_k). \end{aligned} \tag{3.16}$$

Under Assumption 1, $\Sigma_1 = 0$. If (3.16) is asymptotically stable for $k = 2, \ldots, p$, then, according to Lemma 3 in [139], the underlying network becomes locally completely synchronised, i.e. $x_i(t) - x_j(t) \to 0, i, j = 1, \ldots, N$ for some initial condition. Hence, in the rest of the chapter, we investigate the asymptotic stability or instability of the system (3.16). The following lemma states that this can be done by analysing the interconnected systems that have lower dimension than (3.16).

Lemma 3.1. *Consider the dynamical system described in (3.16) and the corresponding interconnected system as*

$$\begin{aligned}\dot{\zeta}_{1k} &= \big((-\Lambda + A(t)\Xi) - \beta_{R_k} A(t)D\big)\zeta_{1k} + \beta_{I_k} A(t)D\zeta_{2k} \\ \dot{\zeta}_{2k} &= \big((-\Lambda + A(t)\Xi) - \beta_{R_k} A(t)D\big)\zeta_{2k} - \beta_{I_k} A(t)D\zeta_{1k},\end{aligned} \tag{3.17}$$

where β_{R_k} and β_{I_k} are the real and imaginary parts of λ_k respectively. If (3.17) is asymptotically stable (unstable), then (3.16) is asymptotically stable (unstable).

Proof. Denote $\beta_{R_k} = \Re(\lambda_k)$ and $\beta_{I_k} = \Im(\lambda_k)$. The structure of Σ_k indicates that the dynamical system (3.16) consists of m_k subsystems described by,

$$\frac{d}{dt}\begin{bmatrix}\Re(\tilde{y}_{k,i}) \\ \Im(\tilde{y}_{k,i})\end{bmatrix} = \begin{bmatrix}\mathcal{A}_{k,1}(t) & \mathcal{A}_{k,2}(t) \\ -\mathcal{A}_{k,2}(t) & \mathcal{A}_{k,1}(t)\end{bmatrix}\begin{bmatrix}\Re(\tilde{y}_{k,i}) \\ \Im(\tilde{y}_{k,i})\end{bmatrix} + \tilde{u}_{k,i} \tag{3.18}$$

with $\mathcal{A}_{k,1}(t) = (-\Lambda + A(t)\Xi) - \beta_{R_k} A(t)D$, $\mathcal{A}_{k,2}(t) = \beta_{I_k} A(t)D$, $\hat{u}_{k,m_k} = 0$, and

$$\tilde{u}_{k,i} = \begin{bmatrix}-A(t)D & \mathbf{0} \\ \mathbf{0} & -A(t)D\end{bmatrix}\begin{bmatrix}\Re(\tilde{y}_{k,i+1}) \\ \Im(\tilde{y}_{k,i+1})\end{bmatrix}, \tag{3.19}$$

for $i = 1, \ldots, m_k - 1$. From (3.18) and (3.19), it is observed that the system (3.16) is a cascade structure of m_k identical subsystems where the states of subsystem m_k act as input for the subsystems $m_k - 1$, the states of subsystems $m_k - 1$ are input for the subsystems $m_k - 2$, and so on.

To prove the stability part, we first point out that, for linear periodic systems, asymptotic stability implies uniform asymptotic stability [88, Theorem 7] and exponential stability. If each unforced subsystem is exponentially stable, it is input to state stable (ISS) [81, Lemma 4.6], and so the cascade interconnection of subsystems $i = 1, \ldots, m_k - 1$ is also ISS. Since the subsystem m_k is exponentially stable, the cascade system (3.16) is uniformly asymptotically stable [81, Lemma 4.7]. It is straightforward to see that the instability of the subsystem m_k leads to instability of the whole system. This completes the proof. □

3.4 Stability Analysis of the Linearised Model

According to the discussion in the previous section and Lemma 3.1, presence/absence of local synchronisation is directly related to stability/instability of the linearised sys-

tem (3.17), which in turn depends on the real and imaginary parts of the eigenvalues of the Laplacian matrix L. Without loss of generality, we assume that β_{I_k} is non-negative, since stability or instability of (3.17) are invariant with respect to the sign of β_{I_k}. In order to simplify the presentation, the subscript k is dropped. We find it convenient to divide the parameter space into three regions and, for each region, we have proven different stability properties using different analysis method. Therefore, we divide the parameter space $\Omega_\beta = \{(\beta_R, \beta_I) \mid \beta_R > 0,\ \beta_I \geq 0\}$ into three regions:

1. $\Omega_\beta^1 = \{(\beta_R, \beta_I) \mid 0 < \beta_R \leq \beta_{R_{min}},\ 0 \leq \beta_I \leq \psi(\beta_R)\}$ with $\psi : [0, \beta_{R_{min}}] \to \mathbb{R}_{\geq 0}$,
2. $\Omega_\beta^2 = \{(\beta_R, \beta_I) \mid \beta_R \geq \beta_{R_{max}},\ 0 \leq \beta_I \leq \infty\}$,
3. $\Omega_\beta^3 = \{(\beta_R, \beta_I)\ \in\ \Omega_\beta - \{\Omega_1 \cup \Omega_2\}\}$.

For the first region Ω_β^1, we present Proposition 3.1 and Proposition 3.2 to check instability and stability of the linearised model (3.17). The value of $\beta_{R_{min}}$ and function $\psi(\beta_R)$ are also specified in these propositions. Proposition 3.1 is a result of Lemma B.1 in Appendix B.1. For $\beta_I = 0$, this lemma presents an instability condition using two-time scale averaging that can be used to develop a counterpart instability result of Proposition 3.1 of Shafi et al. [113]. In Proposition 3.3, we show that there exists $\beta_{R_{max}}$ such that (3.17) always becomes unstable in the region Ω_β^2. In Section 3.4.2, we present a numerical approach for parameter space Ω_β^3 that follows ideas from robust control [113].

3.4.1 Synchronisation in Set Ω_β^1

In the set Ω_β^1, we used the two-time scale averaging method following the same idea in [113]; however, our result differs due to an extra term $A(t)$ appearing in the interconnection terms in (3.17). If $\beta_R = \beta_I = 0$, (3.17) is decomposed as two independent systems with the same dynamics:

$$\dot{\zeta}_i = (-\Lambda + A(t)\Xi)\,\zeta_i, \tag{3.20}$$

for $i = 1, 2$. In this case, due to Assumption 2, (3.20) has a T-periodic solution that is associated with a stable limit cycle in the original system (3.9). We denote $\phi_i(t, t_0)$ the principle state transition matrix of periodic dynamics (3.20) for $i = 1, 2$. Since both systems

have the same dynamics, we have $\phi_1(t,t_0) = \phi_2(t,t_0) = \phi(t,t_0)$. The Floquet theory [54] indicates that the $\phi(t,t_0)$ is a T-periodic matrix that can be written as

$$\phi(t,t_0) = S(t)\exp\left(H\left(t-t_0\right)\right)R(t_0)\,, \tag{3.21}$$

where $S(t)$ is also a T-periodic matrix and $R(t) = S^{-1}(t)$. The columns of S, denoted by s_i, and rows of $R(t)$ denoted by r_j^T, are orthonormal, i.e. $r_j^T s_i = \delta_{ij}$ with $\delta_{ij} = 1$ if $i = j$, and $\delta_{ij} = 0$ otherwise. The matrix H is known as the *monodromy matrix*, which satisfies $\phi(t_0+T,t_0) = J\exp(HT)J^{-1}$, where J is a matrix that contains eigenvectors of $\phi(t_0+T,t_0)$. For a stable limit cycle, the monodromy matrix H has the structure $H = \mathrm{diag}(0,H_2)$, where H_2 is an $(n-1)\times(n-1)$ Hurwitz matrix that contains non-zero Floquet exponents. Even though computing the analytical forms of $\phi(t,t_0)$, H_2, $S(t)$, and $R(t)$ is typically impossible, there are effective approaches, for example in [46], that can be used to compute the matrices numerically. Floquet theory then implies that the change of coordinate $[s_i^T, r_i^T]^T = R(t)\zeta_i$ transforms (3.17) to the representation

$$\begin{bmatrix}\dot{s}_i\\ \dot{r}_i\end{bmatrix} = \left(H - \beta_R R(t)A(t)DS(t)\right)\begin{bmatrix}s_i\\ r_i\end{bmatrix} - (-1)^i\beta_I R(t)A(t)DS(t)\begin{bmatrix}s_{3-i}\\ r_{3-i}\end{bmatrix}, \tag{3.22}$$

for $i = 1,2$. For small values of β_R, analysis of stability of (3.22) can be conducted using a two-time scale averaging method.

Next, we present Proposition 3.1 to demonstrate an instability condition of (3.22), and then Proposition 3.2 to provide sufficient conditions for asymptotic stability of (3.22).

Proposition 3.1. *(**Instability with Weak Coupling**) Let r_1^T and s_1 be the first row and column of $R(t)$ and $S(t)$ in (3.21), respectively. For a given matrix D, if*

$$\int_0^T r_1^T(\tau)A(\tau)Ds_1(\tau)d\tau < 0, \tag{3.23}$$

there exist $\beta_{R_{min}} \neq 0$ and $\psi : [0,\beta_{R_{min}}] \to \mathbb{R}_{\geq 0}$ so that

$$\begin{aligned}\dot{\zeta_1} &= \left(\left(-\Lambda + A(t)\Xi\right) - \beta_R A(t)D\right)\zeta_1 + \beta_I A(t)D\zeta_2\\ \dot{\zeta_2} &= \left(\left(-\Lambda + A(t)\Xi\right) - \beta_R A(t)D\right)\zeta_2 - \beta_I A(t)D\zeta_1\end{aligned} \tag{3.24}$$

is unstable for every $\beta_R \in (0, \beta_{R_{min}}]$ *and the corresponding* $\beta_I \in [0, \psi(\beta_R)]$. *The value of* $\beta_{R_{min}}$ *and function* $\psi(.)$ *can be obtained from Lemma B.1.*

Proof. Proposition 3.1 is proven by applying Lemma B.1 (see Appendix B.1) to the system (3.22). □

Proposition 3.2. *(**Stability with Weak Coupling**) Let* r_1^T *and* s_1 *be the first row and column of* $R(t)$ *and* $S(t)$ *in (3.21), respectively. For a given matrix D, if*

$$\int_0^T r_1^T(\tau) A(\tau) D s_1(\tau) d\tau > 0, \tag{3.25}$$

there exist $\beta_{R_{min}} \neq 0$ *and* $\psi : [0, \beta_{R_{min}}] \to \mathbb{R}_{\geq 0}$ *so that system (3.24) is asymptotically stable for every* $\beta_R \in (0, \beta_{R_{min}}]$ *and the corresponding* $\beta_I \in [0, \psi(\beta_R)]$. *The value of* $\beta_{R_{min}}$ *and function* $\psi(.)$ *can be obtained from Lemma B.2.*

Proof. Proposition 3.2 is proven by applying Lemma B.2 (see Appendix B.1) to the system (3.22). □

Propositions 3.1 and 3.2 demonstrate that if the system is unstable (or asymptotically stable) with $\beta_I = 0$, then it stays unstable (or asymptotically stable) with sufficiently small β_I. In this case, one needs to solve the optimisation problem presented in the proof of Lemmas B.1 and B.2 in Appendix B.1 or for every $\beta_R \in (0, \beta_{R_{min}}]$, which itself is a computational approach. It is worth mentioning that this approach is not as computationally expensive as the numerical approach presented in the section 3.4.2. These two propositions are powerful tools when we know that β_I is zero; for instance, in the undirected case. We refer the interested reader to [4] for the undirected case.

Remark 3.1. *For the Wilson-Cowan model, the matrix* $A(t) \in \mathbb{R}^{2\times 2}$ *has the structure*

$$A(t) = \begin{bmatrix} \frac{\partial F}{\partial \theta}\big|_{\theta=[\Upsilon+\Xi\bar{x}]_1} & 0 \\ 0 & \frac{\partial F}{\partial \theta}\big|_{\theta=[\Upsilon+\Xi\bar{x}]_2} \end{bmatrix}. \tag{3.26}$$

Considering the structure of matrix D, condition (3.23) in Proposition 3.1 can be written as

$$\int_0^T \big(r_{11}(\tau) A_{11}(\tau) w_{11}(\tau) - r_{12}(\tau) A_{22}(\tau) w_{21}(\tau)\big) d\tau < 0, \tag{3.27}$$

and condition (3.25) of Proposition 3.2 can be written as

$$\int_0^T \big(r_{11}(\tau)A_{11}(\tau)w_{11}(\tau) - r_{12}(\tau)A_{22}(\tau)w_{21}(\tau)\big)d\tau > 0. \tag{3.28}$$

Furthermore, an alternative choice for matrix $\mathcal{Z}$ in Propositions 3.1 and 3.2 are

$$\bar{\mathcal{Z}} = \begin{bmatrix} 0 & 2|P_s|\gamma\iota_{12} \\ 2|P_r|(1+2T\bar{\epsilon}\iota_{11})\iota_{21} & 0 \end{bmatrix},$$

and

$$\bar{\mathcal{Z}} = \begin{bmatrix} 0 & \gamma\iota_{12} \\ (1+2T\bar{\epsilon}\iota_{11})\iota_{21} & 0 \end{bmatrix},$$

respectively.

3.4.2 Synchronisation in Set Ω_β^3

In this subsection, we study stability of (3.17) for $\beta_R \in [\beta_{R_{min}}, \beta_{R_{max}}]$ ($\beta_{R_{max}}$ can be chosen arbitrarily large) and $\beta_I \in [0, \infty]$ by adopting a numerical approach proposed in [113]. We represent the matrices $\beta_R D$ and $\beta_I D$ as

$$\begin{aligned} \beta_R D &= M_1 + B_1\Delta_1 C_1, \\ \beta_I D &= M_2 + B_2\Delta_2 C_2, \end{aligned} \tag{3.29}$$

where $\Delta_i \in \mathbb{R}^{m\times m}$ are diagonal matrices whose diagonal entries vary in $[-1, 1]$ for $i = 1, 2$. It should be noted that the matrices $M_i \in \mathbb{R}^{n\times n}, B_i \in \mathbb{R}^{n\times m}, C_i \in \mathbb{R}^{m\times n}$ in (3.29) are chosen in the way that, by varying the matrices Δ_1 and Δ_2, the right side of (3.29) generates all matrices $\beta_R D$ and $\beta_I D$ that are obtained by varying β_R and β_I respectively. Then, the system (3.17) can be written as a linear periodically time-varying system with block

uncertainty $\Delta = \text{diag}(\Delta_1, \Delta_1, \Delta_2, \Delta_2)$:

$$\begin{aligned} \dot{\tilde{\zeta}} &= \bar{A}(t)\tilde{\zeta} + \bar{B}(t)q, \\ z &= \bar{C}\tilde{\zeta}, \\ q &= \Delta z, \end{aligned} \tag{3.30}$$

where

$$\begin{aligned} \bar{A}(t) &= \begin{bmatrix} -\Lambda I + A(t)\Xi - A(t)M_1 & A(t)M_2 \\ -A(t)M_2 & -\Lambda I + A(t)\Xi - A(t)M_1 \end{bmatrix}, \\ \bar{B}(t) &= \begin{bmatrix} -A(t)B_1 & 0 & A(t)B_2 & 0 \\ 0 & -A(t)B_1 & 0 & -A(t)B_2 \end{bmatrix}, \\ \bar{C} &= \begin{bmatrix} C_1^T & 0 & 0 & C_2^T \\ 0 & C_1^T & C_2^T & 0 \end{bmatrix}^T \end{aligned} \tag{3.31}$$

with $\tilde{\zeta} = [\zeta_1^T, \zeta_2^T]^T \in \mathbb{R}^{2n}$, and $z \in \mathbb{R}^{2m}$ and $q \in \mathbb{R}^{4m}$ are outputs of the linear periodic time-varying system and uncertainty block. In order to check stability of (3.30), structured singular value (SSV) analysis is performed on a truncated harmonic state space model of (3.30). Under the assumption that $\bar{A}(t), \bar{B}(t)$ are continuous functions of t, using Fourier series, the state space model (3.30) can be represented in the form of a harmonic state space model

$$\begin{aligned} sY &= (\bar{\mathcal{A}} - \mathcal{N})Y + \bar{\mathcal{B}}Q, \\ Z &= \mathcal{C}Y, \\ Q &= \tilde{\Delta}Y, \end{aligned} \tag{3.32}$$

where $\bar{\mathcal{A}}, \mathcal{N}, \bar{\mathcal{B}}$ are infinite-dimensional matrices with complex entries. We refer to Shafi et al. [113] and Zhou and Hagiwara [144] for further details on such a harmonic state space model.

Although the harmonic state space model (3.32) is an infinite dimensional model, it can be approximated with a truncated model that considers the dominant harmonics in the Fourier series of $\tilde{\zeta}(t)$ [107]. Once the truncated model of (3.32) is computed, the structured singular value (SSV) μ can be calculated using a numerical approach such as *mussv*

in the Robust Control Toolbox. It is difficult to compute SSV by considering all possible combinations of β_R and β_I, since β_I varies up to infinity. However, if the number of nodes in the network is fixed, Proposition 1 in [3] states that imaginary parts of an N-dimensional Laplacian matrix satisfy $\|\beta_I\| \leq \|\beta_R\| \cot \frac{\pi}{N}$. In this case, we can split the space into several segments and run the computational approach in every segment. If $\mu \leq 1$, (3.16) is stable for all values of β_R and β_I in that segment. If $\mu > 1$, we can compute the matrix Δ with the smallest norm that leads to instability of (3.16). It is worth mentioning that the matrices in (3.29) cover all possible coupling strengths for the intermediate coupling.

Remark 3.2. *As stated in [113], the proposed numerical approach leads to less conservative results than other numerical methods such as lifting approach or computation of Lyapunov exponent. For large values of β_I, our numerical experiences show that the mussv function faces a convergence issue, which results from singularity of matrices in computing singular value decomposition. For those values of β_I, we checked the stability of (3.16) by computing the Lyapunov exponent [102].*

3.4.3 Synchronisation in Ω^2_β

As mentioned earlier, the results of this subsection are derived for the network of Wilson-Cowan oscillators. We present a property about $f(\theta)$ that turns out to be crucial in the proof of Proposition 3.3. *Fact:* The sigmoid function $f(\theta)$ (3.2) is a continuous function with positive and bounded derivative, i.e. $0 \leq f_{min} \leq f_\theta(\theta) \leq f_{max}$ for all $\theta \in \mathbb{R}$. In addition, $f_\theta(\theta) \to 0$ iff $\theta \to \pm\infty$.

Proposition 3.3. *(**Instability with Strong Coupling for the Wilson-Cowan Model**) Consider the dynamical system described by the state space model*

$$\begin{aligned} \dot{\zeta}_1 &= \left((-\Lambda + A(t)\Xi) - \beta_R A(t) D\right)\zeta_1 + \beta_I A(t) D \zeta_2, \\ \dot{\zeta}_2 &= \left((-\Lambda + A(t)\Xi) - \beta_R A(t) D\right)\zeta_2 - \beta_I A(t) D \zeta_1, \end{aligned} \tag{3.33}$$

where Λ, Ξ, D are given by (3.4) and $A(t)$ is computed from linearisation of F (3.5) around the limit cycle. Then, there exists a positive scalar $\beta_{R_{max}}$ such that (3.33) is unstable for every $\beta_R \geq \beta_R^*$

and for every $\beta_I \in \mathbb{R}$. *Furthermore,* $\beta_{R_{max}} = \max\{a, d, \beta_{R_1}\}$ *and* β_{R_1} *can be obtained from the following optimisation problem:*

$$\begin{aligned} &\beta_{R_1} = \min_{\beta>0} \beta \\ &s.t. \quad \begin{bmatrix} \alpha_E + (\beta - a)\underline{\mathfrak{A}}_{11} & -\frac{1}{2}\big(|b|\overline{\mathfrak{A}}_{11} + |c|\overline{\mathfrak{A}}_{22}\big) \\ -\frac{1}{2}\big(|b|\overline{\mathfrak{A}}_{11} + |c|\overline{\mathfrak{A}}_{22}\big) & -\alpha_I + (\beta - d)\underline{\mathfrak{A}}_{22} \end{bmatrix} > 0, \end{aligned} \tag{3.34}$$

where $0 < \underline{\mathfrak{A}}_{ii} \le A_{ii}(t) \le \overline{\mathfrak{A}}_{ii},\ i = 1, 2$ *for all* $t \ge 0$.

Proof. For the Wilson-Cowan model, the matrix $A(t) \in \mathbb{R}^{2\times 2}$ is a diagonal matrix that is given by (3.26). Due to Fact 3.4.3 and boundedness of $\bar{x}(t)$, there exists a non-zero positive scalar $\underline{\mathfrak{A}}_{ii}, \overline{\mathfrak{A}}_{ii}$ such that $0 < \underline{\mathfrak{A}}_{ii} \le A_{ii}(t) \le \overline{\mathfrak{A}}_{ii},\ i = 1, 2$ for all $t \ge 0$. Now, consider a candidate Lyapunov function $V(\zeta_1, \zeta_2) = \sum_{i=1}^{2} \frac{1}{2}(\zeta_{i,2}^2 - \zeta_{i,1}^2)$ with $\zeta_i = [\zeta_{i,1}, \zeta_{i,2}]^T$. Taking the derivative along (3.33) leads to

$$\begin{aligned} \dot{V} = \sum_{i=1}^{2} \Big(&\left(-\alpha_I + (\beta_R - d)\, A_{22}(t)\right) \zeta_{i,2}^2 + \left(cA_{22}(t) + bA_{11}(t)\right) \zeta_{i,1}\zeta_{i,2} \\ &- \left(-\alpha_E + (a - \beta_R)\, A_{11}(t)\right) \zeta_{i,1}^2 \Big). \end{aligned} \tag{3.35}$$

If $\beta_R \ge \max\{a, d\}$, then

$$\begin{aligned} \dot{V} \ge \sum_{i=1}^{2} \big(&-\alpha_I + (\beta_R - d)\underline{\mathfrak{A}}_{22}\big)|\zeta_{i,2}|^2 + \big(\alpha_E + (\beta_R - a)\underline{\mathfrak{A}}_{11}\big)|\zeta_{i,1}|^2 \\ &- \big(|c|\overline{\mathfrak{A}}_{22} + |b|\overline{\mathfrak{A}}_{11}\big)|\zeta_{i,1}||\zeta_{i,2}| \,. \end{aligned} \tag{3.36}$$

For large values of β_R, the first and second terms of (3.36) are positive and hence $\dot{V}$ is positive. If (3.34) holds, then $\dot{V} > 0$. Note that the set $\Omega \triangleq \big\{(\zeta_1, \zeta_2) \in \mathbb{R}^4 \mid V \ge 0\big\}$ is nonempty, since the candidate Lyapunov function is quadratic type. Hence, according to Chetaev's theorem for time-varying systems [67], the origin of (3.33) is unstable. This completes the proof. □

3.5 Network Topology and Synchronisation

In this section, we aim to address robustness of synchronisation with respect to the perturbation in the interconnection gains between nodes. We restrict our analysis to a network of Wilson-Cowan oscillators with N nodes and undirected interconnection. In this case, (3.17) is decomposed to two identical and independent systems and, therefore, the synchronisation of the network is determined by $\dot{\zeta}_1 = ((-\Lambda + A(t)\Xi) - \beta_R A(t) D)\,\zeta_1$. We assume the eigenvalues of Laplacian matrix L satisfy

$$\{\lambda_k(L)\}_{k=2}^{N} \in (\beta_{R_{min}}, \beta_{R_{max}}), \tag{3.37}$$

where $(\beta_{R_{min}}, \beta_{R_{max}})$ is the largest interval for which the initial network is synchronised. The interconnection gains of the original network are perturbed and the associated Laplacian matrix is denoted by L_Δ. In this case, the Laplacian matrix of the perturbed network, referred as the "perturbed Laplacian matrix", can be written as

$$L_\Delta = L + \Delta L, \tag{3.38}$$

where ΔL is a "Laplacian-like" matrix, which is symmetric and zero row sum but not necessarily positive definite. The question is to find conditions on perturbations that lead to the presence or absence of synchronous behaviour in the perturbed network.

Proposition 3.4 guarantees the persistence of synchronous behaviour for a class of perturbations that satisfies (3.39). However, it does not determine the effects of perturbations that violate the condition, since that perturbation can either maintain the eigenvalues in the interval $[\beta_{R_{min}}, \beta_{R_{max}}]$ or take at least one eigenvalue out of this interval. To the best of our knowledge, there is no available result that answers this case in general. Proposition 3.5 presents conditions that ensure absence of synchronous behaviour in the perturbed network.

Proposition 3.4. *Consider a network of Wilson-Cowan oscillators with N nodes and the corresponding Laplacian matrix L. Furthermore, assume the eigenvalues of L satisfy (3.37). This means that the network is locally completely synchronised. Define $\kappa = \max\{|\lambda_N(\Delta L)|, |\lambda_1(\Delta L)|\}$.*

If the following inequality holds,

$$\kappa \leq \min\left\{\lambda_2(L) - \beta_{R_{min}}, \beta_{R_{max}} - \lambda_n(L)\right\}, \tag{3.39}$$

the perturbed network also becomes locally completely synchronised.

Proof. Using Weyl's inequality [19], the eigenvalues of perturbed Laplacian matrix L_Δ satisfy $\lambda_1(\Delta L) \leq \lambda_k(L_\Delta) - \lambda_k(L) \leq \lambda_N(\Delta L)$ for $k = 1, \ldots, N$. Condition (3.39) ensures that $\lambda_2(L_\Delta)$, $\lambda_N(L_\Delta)$ stay in the interval $(\beta_{R_{min}}, \beta_{R_{max}})$, which implies that the synchronisation persists in the presence of perturbation. □

Proposition 3.5. *Consider a network of Wilson-Cowan oscillators with N nodes and the corresponding Laplacian matrix L. Furthermore, assume the eigenvalues of L satisfy (3.37). If one of the following inequalities holds,*

$$\min_{j=1,2}\{\lambda_{2+j}(L) + \lambda_{2-j}(\Delta L)\} < \beta_{R_{min}}, \tag{3.40}$$

$$\max_{j=1,\ldots,n}\{\lambda_{n-j+1}(L) + \lambda_j(\Delta L)\} > \beta_{R_{max}}, \tag{3.41}$$

the synchronous behaviour disappears in the perturbed network.

Proof. Considering (3.38) and Weyl's inequality [19], we have

$$\lambda_2(L_\Delta) \leq \min_{j=1,2}\{\lambda_{2+j}(L) + \lambda_{2-j}(\Delta L)\} \tag{3.42}$$

$$\lambda_n(L_\Delta) \geq \max_{j=1,\ldots,n}\{\lambda_{n-j+1}(L) + \lambda_j(\Delta L)\}. \tag{3.43}$$

If the right side of (3.42) is smaller than $\beta_{R_{min}}$, $\lambda_2(L_\Delta)$ is located outside of interval $[\beta_{R_{min}}, \beta_{R_{max}}]$, which means that synchronisation vanishes in the network. Similarly, if the right hand side of (3.43) is larger than $\beta_{R_{max}}$, the network becomes desynchronised □

Remark 3.3. *Conditions in Propositions 3.4 and 3.5 can be numerically verified if the Laplacian-like matrix ΔL is known. It is hard to express eigenvalues of ΔL in terms of perturbation terms in interconnection gains; however, for some simple cases, this is possible. As an example, consider the case where an arbitrary two nodes i and i′ with corresponding interconnection gain $l_{ii'}$ is*

perturbed by $\delta l_{ii'}$. It is straightforward to check that the Laplacian-like matrix ΔL has $n-1$ zero eigenvalues and a non-zero eigenvalues $2\delta l_{ii'}$. For this case, condition (3.39) is simplified to

$$|\delta l_{ii'}| \leq \min\left\{\frac{\lambda_2(L) - \beta_{R_{min}}}{2}, \frac{\beta_{R_{max}} - \lambda_N(L)}{2}\right\}. \tag{3.44}$$

The conditions (3.40) and (3.41) are also simplified to

$$\delta l_{ii'} < \frac{\beta_{R_{min}} - \lambda_3(L)}{2}, \tag{3.45}$$

$$\delta l_{ii'} > \frac{\beta_{R_{max}}}{2}. \tag{3.46}$$

3.6 Simulation Results

In this section, we present simulation results to validate the proposed approach to study of synchronisation in a network of Wilson-Cowan oscillators. The Wilson-Cowan model exhibits oscillatory behaviour resulting from the existence of a stable limit cycle that appears from the Andronov-Hopf-bifurcation of equilibrium point [75]. In the simulations, we choose the following set of variables that guarantees oscillatory behaviour: $a = 10,\ b = 10,\ c = 10,\ d = -2,\ \rho_x = 2,\ \rho_y = -6$.

To analyse the network, we first compute the matrix $A(t)$ in (3.16) using the oscillatory behaviour of each node. In the next step, we study the effect of weak coupling on stability of (3.16). We then check condition (3.23) in Proposition 3.1 and (3.25) in Proposition 3.2 using the numerical approach. For a Wilson-Cowan model, the instability condition holds. This means that there exists an $\beta_{R_{min}}$ such that, for every interconnection gain smaller than this value, (3.16) is unstable when $\beta_I = 0$. The value of $\beta_{R_{min}}$ is computed from the proof of Lemma B.1 in Appendix B.1. In our case, $\beta_{R_{min}} = 0.034$. We then follow the approach stated in Proposition 3.1 to find the region Ω^1_β in which the system is unstable. In the next step, we apply Proposition 3.3 to find the minimum value of $\beta_{R_{max}}$ such that, for every $\beta_R \geq \beta_{R_{max}}$, (3.16) is unstable irrespective of the value of β_I. Following the proof of the proposition, we obtain $\beta_{R_{max}} = 15$, which means that $\Omega^2_\beta = \{(\beta_R, \beta_I) \mid \beta_R \geq 15,\ 0 \leq \beta_I \leq \infty\}$. Then, the computational algorithm in Section 3.4.2 is exploited in the

space Ω^3_β . Note that the matrices $\beta_R D$ and $\beta_I D$ can be written in the form of (3.29) using $M_i = \text{diag}\left(\frac{\beta_{R_{max}}+\beta_{R_{min}}}{2}, -\frac{\beta_{R_{max}}+\beta_{R_{min}}}{2}\right)$, $B_i = \text{diag}\left(\frac{\beta_{R_{max}}-\beta_{R_{min}}}{2}, \frac{\beta_{R_{max}}-\beta_{R_{min}}}{2}\right)$, $\Delta_i = \text{diag}(\delta_i, \delta_i)$ and $C_i = \text{diag}(1, -1)$ for $i = 1, 2$.

The first fifteen harmonics of the Fourier series are sufficient to approximate the oscillatory trajectories in order to find the truncated harmonic state space model. To reduce numerical computation errors, we split the space Ω^2_β into some subspaces and follow the computational approach. As pointed out in Remark 3.2, we checked the stability or instability of the system via computing the Lyapunov exponent for large values of β_I. The computational results reveal that the system (3.16) is stable for all $\beta_R \in [5, 15]$ when $\beta_I = 0$.

The stability/instability region for the system (3.16) is depicted in Figure 3.2. This figure indicates that when the real parts of the eigenvalues are small, the system seems to be unstable irrespective of the values of imaginary parts; however, Proposition 3.1 states that for small values of real parts, there is a region in which the system is unstable. It is an open problem to analytically show whether this is true or not in general. This figure also shows that, in the interval $\beta_R \in [9.4, 15)$, the system is stable as long as β_I is very small. For the intermediate values of β_R, the stability of system behaves in different ways as β_I increases. In the intervals $\beta_R \in [2, 6.4)$, the system is unstable for small values of β_I, becomes stable and then unstable as β_I increases. For the interval $\beta_R \in [4, 6.5) \cup (7.69]$, it is stable for β_I small. Then it becomes unstable, stable (in small interval for β_I), and finally unstable by changing β_I. In the interval $\beta_R \in [6.5, 7.6]$, the system stays stable as long as the values of β_I becomes sufficiently large.

To verify this observation, we consider a network of Wilson-Cowan models with five nodes as illustrated in Figure 3.3 (a). The Laplacian matrix has five eigenvalues, $\lambda_1 = 0, \lambda_2 = 5.55, \lambda_{3,4} = -7 \pm 3.16i, \lambda_5 = 10.45$. According to Figure 3.2, the non-zero eigenvalues locate in the stability region which implies that the network becomes synchronised Figure 3.4 shows the underlying network becomes synchronised for this configuration.

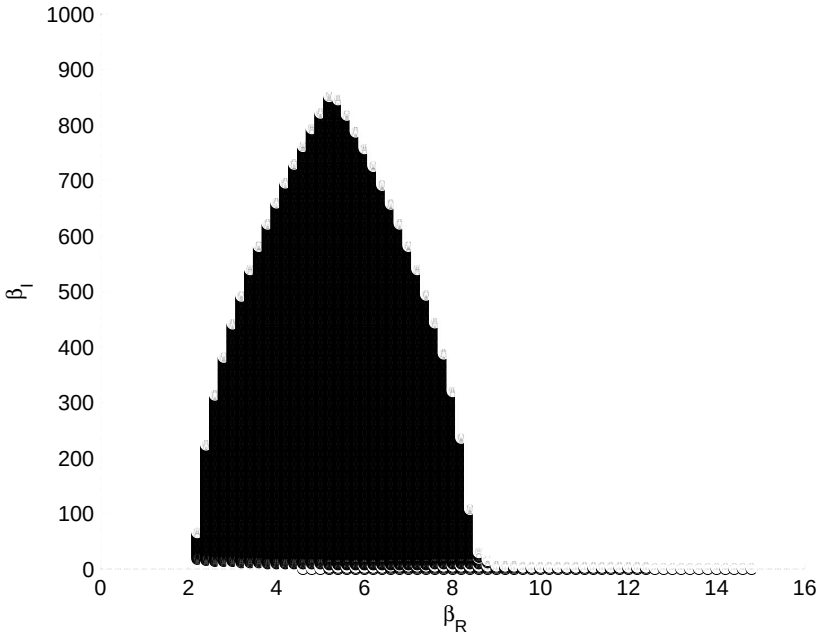

Figure 3.2: The stability (black) and instability (white) regions of the system (3.16) with parameters values $a = 10, b = 10, c = 10, d = -2, \rho_x = 2, \rho_y = -6$.

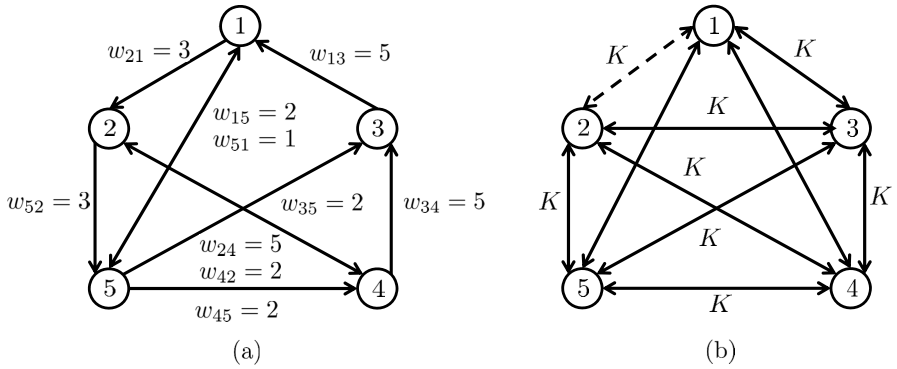

Figure 3.3: Five diffusively coupled Wilson-Cowan oscillators with (a) directed, (b) undirected interconnection and all to all interconnection with the same gain k. The dotted line indicates the perturbed edges in the network.

In order to simulate the effect of perturbation of interconnection gains on synchronisation, we consider a network depicted in Figure 3.3 (b) in which the interconnection between all nodes are assumed to be same for simplicity. In this case, the Laplacian matrix has five eigenvalues, $\lambda_1 = 0, \lambda_2 = \lambda_3 = \lambda_4 = \lambda_5 = 5K$. Based on our analysis, the

underlying network becomes synchronised if $5K \in [5;15]$. We first set $K = 1.2$. Following the simple case in Remark 3.3, the interconnection gains between node 1 and node 2 are changed. Condition (3.44) implies that $|\delta l_{12}| \leq 0.5$, which means the synchronisation persists for the range of interconnection for $l_{12} = l_{21} \in [0.7, 1.9]$. On the other hand, conditions (3.45) and (3.46) can be used to show that synchronisation vanishes for interconnection gains $l_{12} = l_{21} \in [0, 7)$ and $l_{12} = l_{21} \in [8.7, \infty)$. Indeed, these two ranges of values show that the synchronisation disappears if the interconnection gain increases or decreases significantly. Figure 3.5 shows network behaviour for the perturbed network when the interconnection between nodes 1 and 2 is removed.

This example indicates that the synchronisation disappears if the interconnection between two nodes is removed; however, this is not true in general. If the value of $K = 1.8$ is chosen, as depicted in Figure 3.6, the network becomes synchronised even if the interconnection between nodes 1 and 2 is removed. Indeed, for this choice of K, condition (3.44) leads to $|\delta l_{12}| \leq 2$, which is larger than the interconnection gain K. This means that, by removing the interconnection between these two nodes, the synchronisation may persist. These observations are consistent with the results of [125] that were obtained through only simulations.

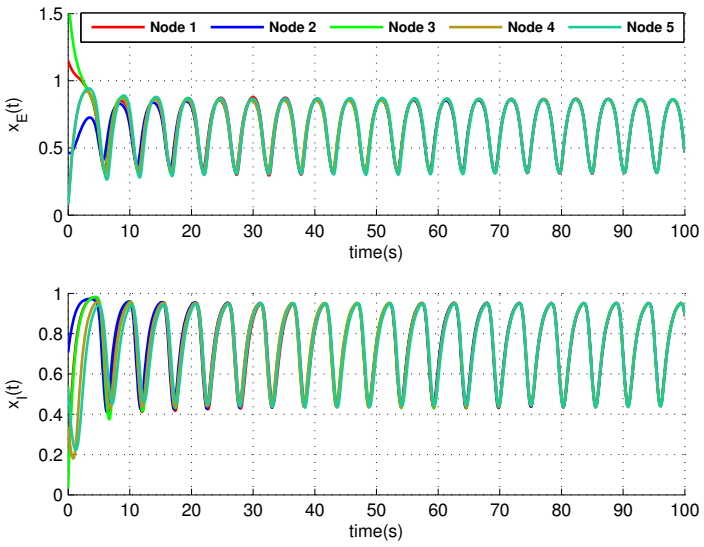

Figure 3.4: The trajectories of heterogeneous Wilson-Cowan network depicted in Figure 3.3 (a).

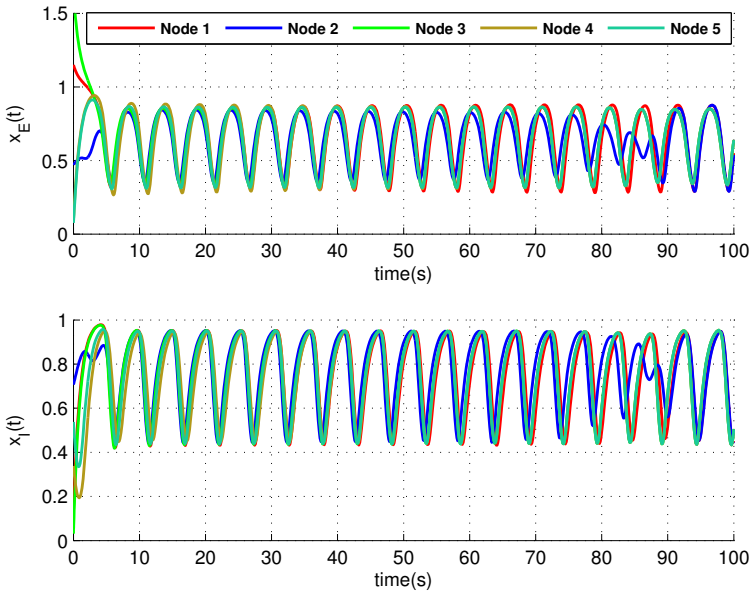

Figure 3.5: The trajectories of heterogeneous Wilson-Cowan network depicted in Figure 3.3 (b) and coupling gain $k = 1.2$. The interconnection between nodes 1 and 2 is removed.

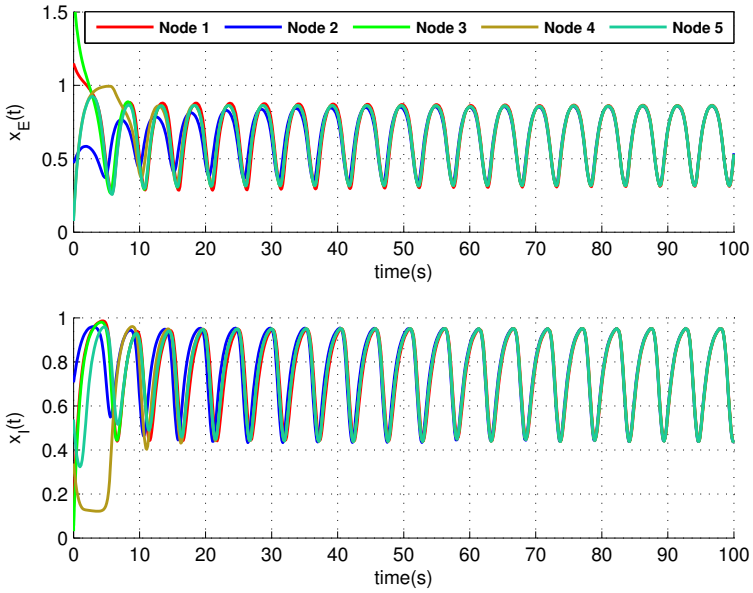

Figure 3.6: The trajectories of heterogeneous Wilson-Cowan network depicted in Figure 3.3 (b) and coupling gain $k = 1.8$. The interconnection between nodes 1 and 2 is removed.

3.7 Conclusions

A new procedure was introduced to analyse synchronisation of networks of homogeneous Wilson-Cowan models with diffusive coupling. Using the linearised model around a limit cycle, analytic results were developed that can be utilised to check for the existence or absence of synchronous behaviour. Contrary to [113], we allowed the interconnection between nodes to be directed. We proved that the network of Wilson-Cowan models always becomes desynchronised when the Laplacian matrix has some eigenvalues with large real values. A computational approach was presented for those eigenvalues of the Laplacian matrix with either intermediate values of real part or small values of real part and non-small values of imaginary part. We also addressed the presence or absence of synchronous behaviour in the case that interconnection gains are perturbed. Simulation results showed the effectiveness of our approach in determining absence or presence of synchronised behaviour.

Chapter 4

On Eigenvalues of Laplacian Matrix for a Class of Directed Signed Graphs

4.1 Introduction

In some applications, a network graph can be directed with both positive and negative weights. For instance, in a network of Wilson-Cowan oscillators described in Section 3.2, the excitatory neural population and the inhibitory neural population in one node are coupled to the excitatory and the inhibitory neural populations in other nodes with positive and negative coupling gains, respectively. This means that the network graph can be seen as a signed network. The network of Wilson-Cowan oscillators with N nodes in Section 3.2 contains $2N$ neurons where an excitatory neuron and an inhibitory in a neural population i are connected to an excitatory neuron and an inhibitory in a neural population j with the coupling weights w_{ij} and $-w_{ij}$, respectively. The Laplacian matrix of the network of neurons L_{2N} is L_{2N} =can be written as $L_{2N} = D_s \otimes L$, where L is the Laplacian matrix of the network of neural populations and D_s is defined by (3.6). We incorporated the negative sign of coupling gains into the matrix D_s. As a consequence, we ended up with the Laplacian matrix L whose off-diagonal terms are non-positive in Section 3.3.

For some signed networks, it might be possible to represent the Laplacian matrix L_1 in terms of $L_1 = D \otimes L_2$ where L_2 itself is a Laplacian of a new network with only non-negative weights, and D is a matrix with an appropriate dimension. Then, it might be possible to analyse the network using the Laplacian matrix L_2. However, this is not the case in general.

The spectral characterisation of Laplacian matrix for undirected and directed graph with non-negative weights have been reported in [36] and [3, 26, 31], respectively. For undirected signed graphs, we are aware of some work which provide a lower and upper bound on the number of negative and positive eigenvalues [17, 22, 23]. To the best of our knowledge, there is no such results for directed signed graphs.

In many applications, the objective cannot be achieved if the Laplcian matrix has at least an eigenvalue with negative real part. For some applications, the non-zero eigenvalues of the Laplacian matrix need to be positive [97, 128]. To analyse the eigenvalues of Laplacian matrix for sign graphs, one can approach the problem by starting from graphs with non-negative weights and then perturbing pairs of nodes with negative weights which are not necessarily infinitesimally small. This can be seen as robustness of uncertain networks in which the negative weights are modelled as uncertainty in the network. Following this approach, the robustness of signed undirected graphs was analysed by [140], and has recently been extended to a general case, i.e. graphs with arbitrary numbers of negative weights, using tools from electrical circuit theory [34]. Robustness of directed signed graphs was studied in [95]. However, the developed results differ from our results as highlighted in Section 1.3.

This chapter deals with robustness analysis of directed signed graphs for two different scenarios. In the first scenario, we start with a signed graph whose Laplacian matrix has a single zero eigenvalue and no eigenvalue with negative real part. We then perturb it by choosing an arbitrary pair of nodes and perturbing the edges between them with negative weights. We provide an upper bound on absolute value of those negative weights such that the perturbed graph has the required property as well. In the second scenario, we start with a graph with non-negative weights that lacks the required property. We identify "sensitive pairs of nodes" which if are connected by infinitesimally small negative weights, then the Laplacian matrix of the perturbed graph has at least one eigenvalue with negative real parts. This may lead to instability (desynchronisation) in some applications.

This chapter is organised as follows. In Section 4.2, we introduce some definitions which are used to present the main results of this chapter. Section 4.3 states the underly-

ing questions studied in the current chapter following by the main results, illustrative examples, and discussions. Section 4.4 demonstrates the applicability of this work through consensus in social networks. Conclusion and remark on applicability of the results are discussed in the section, and the proofs of some lemmas are included in Appendix C.

4.2 Preliminaries

For a given graph $\mathcal{G}(\mathcal{V}, \mathcal{E}, \mathcal{W})$, for every node $i \in \mathcal{V}$, the reachable set $\mathcal{R}(i)$ is the union of the node i and all nodes from which there exists a path to node i, i.e. $\mathcal{R}(i) = \{i\} \cup \{j \in \mathcal{V} \mid j \nrightarrow i\}$. Next the reachable, exclusive and common sets associated with a graph $\mathcal{G}$ are defined.

Definition 4.1. *For a given graph $\mathcal{G}(\mathcal{V}, \mathcal{E}, \mathcal{W})$, a set of nodes $\mathcal{R} \subseteq \mathcal{V}$ is called a reach set if (a) there exists at least one node $i \in \mathcal{V}$ such that $\mathcal{R}(i) = \mathcal{R}$, and (b) it is maximal, i.e. there is no $j \in \mathcal{V}$ such that $\mathcal{R}(i) \subset \mathcal{R}(j)$ (properly). Let $\mathcal{R}_1, \ldots, \mathcal{R}_d$ denote all reaches of the graph $\mathcal{G}$. We associate a set of reaching nodes $\mathcal{U}_k$ with each reach set $\mathcal{R}_k$ and it is defined as $\mathcal{U}_k = \{i \in \mathcal{V} \mid \mathcal{R}(i) = \mathcal{R}_k\}$. For each set $\mathcal{R}_k$, the exclusive set $\mathcal{X}_k$ and the common set $\mathcal{C}_k$ are defined as $\mathcal{X}_k = \mathcal{R}_k \setminus \cup_{i \neq k} \mathcal{R}_i$ and $\mathcal{C}_k = \mathcal{R}_k \setminus \mathcal{X}_k$, respectively.*

Remark 4.1. *The description of the sets in Definition 4.1 differs from [31, Definition 2.6] as we use the sensing convention rather the information flow one. For a given graph with sensing convention, the same results can be obtained by using the information flow convention if the direction of each edge is reversed.*

To obtain an intuition behind the concepts in Definition 4.1, we see the weight $a_{ij} \neq 0$ as an influence weight from j to i. In this case, a reach set $\mathcal{R}_k$ is a set in which at least one of nodes influences all others directly or indirectly, and this set cannot be included in a bigger such set. Set $\mathcal{U}_k$ is the set of nodes in $\mathcal{R}_k$ which influences all others in $\mathcal{R}_k$. Set $\mathcal{X}_k$ is the set of nodes in $\mathcal{R}_k$ which are in no other reach set $\mathcal{R}_q$ with $q \neq k$. Set $\mathcal{C}_k$ is the set of nodes in $\mathcal{R}_k$ which are also in some other reach set $\mathcal{R}_q$ with $q \neq k$. The following example shows how these sets are defined for a given graph.

Example 1. The graph shown in Figure 4.2 has three reach sets $\mathcal{R}_1 = \{1, 2, 8, 9, 10, 11, 12\}$, $\mathcal{R}_2 = \{3, 4, 5, 8, 9, 10, 11, 12\}$ and $\mathcal{R}_3 = \{6, 7\}$. By using the definitions of $\mathcal{X}_k$ and $\mathcal{C}_k$ for $k =$

1,2,3, the exclusive sets and common sets includes $\mathcal{X}_1 = \{1,2\}$, $\mathcal{X}_2 = \{3,4,5\}$, $\mathcal{X}_3 = \{6,7\}$, $\mathcal{C}_1 = \mathcal{C}_2 = \{8,9,10,11,12\}$ and $\mathcal{C}_3 = \varnothing$. The reaching sets are described by $\mathcal{U}_1 = \{1,2\}$, $\mathcal{U}_2 = \{3\}$ and $\mathcal{U}_3 = \{7\}$.

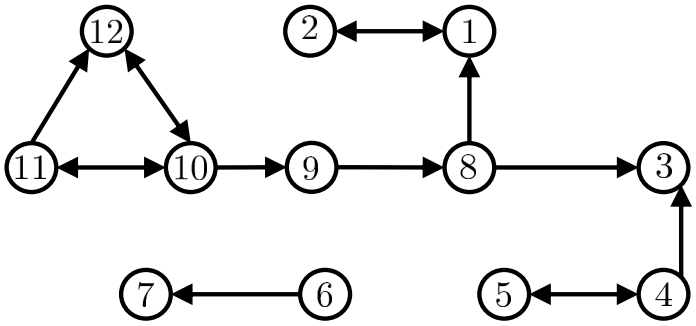

Figure 4.1: A directed graph with 12 nodes in Example 1.

In the following lemma, some properties of these sets are presented.

Lemma 4.1. *Given a graph $\mathcal{G}(\mathcal{V},\mathcal{E},\mathcal{W})$ and the corresponding sets in Definition 4.1, the following properties hold for every $k = 1,\ldots,d$.*

1. $\mathcal{X}_k \cap \mathcal{C}_k = \varnothing$.
2. $\mathcal{U}_k \subseteq \mathcal{X}_k$.
3. *For every $i \in \mathcal{U}_k$, $j \in \mathcal{X}_k \backslash \mathcal{U}_k$, $p \in \mathcal{X}_k$, and $m \in \mathcal{C}_k$, we have*
   (a) $(i,j) \notin \mathcal{E}$.
   (b) $(p,m) \notin \mathcal{E}$.
4. *For every $\mathcal{U}_k$, the corresponding induced subgraph $\mathcal{G}(\mathcal{U}_k, \mathcal{E}_{\mathcal{U}_k}, \mathcal{W}_{\mathcal{U}_k})$ is strongly connected.*
5. *If $\mathcal{C}_k = \varnothing$ for some k, then $\mathcal{R}_k = \mathcal{X}_k$ which means that induced subgraph $\mathcal{G}(\mathcal{R}_k, \mathcal{E}_{\mathcal{R}_k}, \mathcal{W}_{\mathcal{R}_k})$ is disconnected from the rest of the graph.*

Proof.

Proof of 1. This property is a direct consequence of how the sets $\mathcal{C}_k$, $\mathcal{X}_k$ are defined.

Proof of 2. Choose an arbitrary node $i \in \mathcal{U}_k$. From the definition of $\mathcal{U}_k$ it follows that $\mathcal{R}(i) = \mathcal{R}_k$ and by definition of $\mathcal{R}(i)$ we have that $i \in \mathcal{R}_k$. We complete the proof by

contradiction. Assume $i \in \mathcal{C}_k$ which means there exists at least one $q \neq k$ such that $i \in \mathcal{C}_q$ and subsequently $i \in \mathcal{R}_q$. This means $\mathcal{R}_k \subset \mathcal{R}_q$ which contradicts maximality of $\mathcal{R}_k$. Hence $i \notin \mathcal{C}_k$.

Proof of 3(a). Since $i \in \mathcal{U}_k$, then $\forall u \in \mathcal{R}_k, u \nrightarrow i$. For the purpose of showing contradiction, suppose that $(i,j) \in \mathcal{E}$. Then $i \nrightarrow j$ and subsequently $\forall u \in \mathcal{R}_k, u \nrightarrow j$ which is equivalent to $j \in \mathcal{U}_k$. This contradicts $j \in \mathcal{X}_k \backslash \mathcal{U}_k$.

Proof of 3(b). Assume that $p \in \mathcal{X}_k$ and $m \in \mathcal{C}_k$. For the purpose of showing contradiction, assume $(p,m) \in \mathcal{E}$ which is equivalent to $j \nrightarrow m$. Since $m \in \mathcal{C}_k$, there exists at least q such that $m \in \mathcal{R}_q$ which along with the existence of $j \nrightarrow m$ implies $j \in \mathcal{R}_q$. This concludes $\mathcal{X}_k \cap \mathcal{R}_q \neq \varnothing$ which is in contradiction with the definition of $\mathcal{X}_k$.

Proof of 4. We prove the fourth property by contradiction. Since a graph with single node is strongly connected, without loss of generality, we assume $|\mathcal{U}_k| > 1$. Assume that $\mathcal{G}_k$ is not strongly connected. Hence, there exists at least two nodes $i,\ j \in \mathcal{U}_k$ such that $i \nrightarrow j$. This means $i \notin \mathcal{R}(j)$ and since by definition of $\mathcal{R}(i)$, $i \in \mathcal{R}(i)$, we have $\mathcal{R}(i) \neq \mathcal{R}(j)$. This contradicts the assumption $\mathcal{R}(i) = \mathcal{R}(j) = \mathcal{R}_k$. Hence, $\mathcal{G}_k$ is strongly connected.

Proof of 5. If $\mathcal{C}_k = \varnothing$, from Definition 4.1, we then obtain $\mathcal{R}_k \backslash \mathcal{X}_k = \varnothing \iff \mathcal{R}_k = \mathcal{X}_k$. Furthermore, $\mathcal{R}_k \cap \mathcal{R}_i = \varnothing$ for all $i \neq k$ which means

$$\forall u \in \mathcal{R}_k, \forall v \in \mathcal{R}_i \implies (u,v) \notin \mathcal{E} \text{ and } (v,u) \notin \mathcal{E}.$$

This completes the proof of the fifth property. □

We now turn to Example 1 to illustrate that Lemma 4.1 holds in this example.

Example 1 (Continued). It is straightforward to check that the properties 1 and 2 in Lemma 4.1 hold. To check the third property, it is observed that $(3,4) \notin \mathcal{E}$ as $3 \in \mathcal{U}_2$ and $4 \in \mathcal{X}_2 \backslash \mathcal{U}_2$. Note that the node 4 cannot be in the set $\mathcal{U}_2$ as $\mathcal{R}(4) = \{3,4,5\} \subset \mathcal{R}_2$. It is observed that all subgraphs induced by $\mathcal{U}_k,\ k = 1,2,3$ are strongly connected. We note that $\mathcal{C}_3$ is empty which means the original graph has a disconnected subgraph.

For a graph with non-negative weights, we list the properties of its Laplacian matrix and its eigenvectors in the following lemma.

Lemma 4.2. *Consider a graph $\mathcal{G}(\mathcal{V},\mathcal{E},\mathcal{W})$ with non-negative weights and Laplacian matrix L.*

Assume that the graph has d^* reach sets $\mathcal{R}_k$ with the corresponding sets $\mathcal{X}_k, \mathcal{U}_k$, and $\mathcal{R}_k$ according to Definition 4.1. Then, zero is a semisimple eigenvalue of L with multiplicity d. Denote the right and the left eigenvectors associated with the zero eigenvalue of L that form the orthogonal bases for its eigenspace by $\gamma_1, \ldots, \gamma_d \in \mathbb{R}^N$ and $\mu_1, \ldots, \mu_d \in \mathbb{R}^N$, respectively. Each γ_k, $k = 1, \ldots, d$ can be chosen to satisfy the following conditions:

1. $[\gamma_k]_i = 1$ *for* $i \in \mathcal{X}_k$;
2. $[\gamma_k]_i = 0$ *for* $i \in \mathcal{V} \backslash \mathcal{R}_k$;
3. $[\gamma_k]_i \in (0, 1)$ *for* $i \in \mathcal{C}_k$;
4. $\sum_{k=1}^{d} \gamma_k = \mathbf{1}_N$.

Furthermore, each μ_k can be chosen such that their entries satisfy the following conditions:

1. $[\mu_k]_i \in (0, 1)$ *for* $i \in \mathcal{U}_k$;
2. $[\mu_k]_i = 0$ *for* $i \in \mathcal{V} \backslash \mathcal{U}_k$;
3. $\sum_{i \in \mathcal{U}_k} [\mu_k]_i = 1$

Proof. By taking into account Remark 4.1, the fact that the eigenvalue is semisimple and the results regarding γ_k correspond to [31, Corollary 4.1]. Denote A the adjacency matrix of $\mathcal{G}$. By relabeling the nodes, they can be partitioned such that the first $|\mathcal{X}_1|$ nodes in the first partition belong to the set $\mathcal{X}_1$, the second $|\mathcal{X}_2|$ nodes in the second partition belong to the set $\mathcal{X}_2$, and so on, and the remaining nodes belong to the set $\mathcal{C} = \bigcup_{k=1}^{d} \mathcal{C}_k$. This means that there exist maps $\Pi_{\mathcal{V}} : \mathcal{V} \to \widetilde{\mathcal{V}}$, $\Pi_{\mathcal{E}} : \mathcal{E} \to \widetilde{\mathcal{E}}$ such that the new graph $\widetilde{\mathcal{G}}(\widetilde{\mathcal{V}}, \widetilde{\mathcal{E}}, \widetilde{\mathcal{W}})$ has d reach sets $\widetilde{\mathcal{R}}_k = \Pi_{\mathcal{V}} \circ \mathcal{R}_k$, exclusive sets $\widetilde{\mathcal{X}}_k = \Pi_{\mathcal{V}} \circ \mathcal{X}_k$, and reaching nodes sets $\widetilde{\mathcal{U}}_k = \Pi_{\mathcal{V}} \circ \mathcal{U}_k$, where $\circ$ denotes the element-wise operation on the set. There is also a permutation matrix $P \in \mathbb{R}^{N \times N}$ that relates the adjacency and Laplacian matrices of $\widetilde{\mathcal{G}}$ to the ones of $\mathcal{G}$ via $\tilde{A} = PAP^{-1}$ and $\tilde{L} = PLP^{-1}$.

*The number of reach sets d can be found by identifying the reachable set of each node and then checking conditions (a) and (b) in Definition 4.1.

By employing Properties 1 – 3 in Lemma 4.1, $\tilde{A}$ can be written as

$$\left[\begin{array}{cccc|c} \tilde{A}_{\widetilde{\mathcal{X}}_1\widetilde{\mathcal{X}}_1} & \mathbf{0} & \cdots & \cdots & \mathbf{0} \\ \mathbf{0} & \tilde{A}_{\widetilde{\mathcal{X}}_2\widetilde{\mathcal{X}}_2} & \cdots & \cdots & \mathbf{0} \\ \vdots & \ddots & \ddots & \cdots & \vdots \\ \mathbf{0} & \mathbf{0} & \cdots & \tilde{A}_{\widetilde{\mathcal{X}}_d\widetilde{\mathcal{X}}_d} & \mathbf{0} \\ \hline \tilde{A}_{\widetilde{\mathcal{C}}\widetilde{\mathcal{X}}_1} & \tilde{A}_{\widetilde{\mathcal{C}}\widetilde{\mathcal{X}}_2} & \cdots & \tilde{A}_{\widetilde{\mathcal{C}}\widetilde{\mathcal{X}}_d} & \tilde{A}_{\widetilde{\mathcal{C}}\widetilde{\mathcal{C}}} \end{array}\right], \tag{4.1}$$

where $\tilde{A}_{SS'}$ means the matrix of weights induced by set S and S'. Due to the property 3(a) in Lemma 4.1, each block $\tilde{A}_{\widetilde{\mathcal{X}}_k\widetilde{\mathcal{X}}_k}$ is decomposed to

$$\left[\begin{array}{cc} \tilde{A}_{\widetilde{\mathcal{U}}_i\widetilde{\mathcal{U}}_i} & \mathbf{0} \\ \tilde{A}_{\widetilde{\mathcal{M}}_i\widetilde{\mathcal{U}}_i} & \tilde{A}_{\widetilde{\mathcal{M}}_i\widetilde{\mathcal{M}}_i} \end{array}\right], \tag{4.2}$$

with $\widetilde{\mathcal{M}}_i = \widetilde{\mathcal{X}}_i \backslash \widetilde{\mathcal{U}}_i$. Consequently, the Laplacian matrix $\tilde{L}$ is represented by

$$\left[\begin{array}{cccc|c} \tilde{L}_{\widetilde{\mathcal{X}}_1\widetilde{\mathcal{X}}_1} & \mathbf{0} & \cdots & \cdots & \mathbf{0} \\ \mathbf{0} & \tilde{L}_{\widetilde{\mathcal{X}}_2\widetilde{\mathcal{X}}_2} & \cdots & \cdots & \mathbf{0} \\ \vdots & \ddots & \ddots & \cdots & \vdots \\ \mathbf{0} & \mathbf{0} & \cdots & \tilde{L}_{\widetilde{\mathcal{X}}_d\widetilde{\mathcal{X}}_d} & \mathbf{0} \\ \hline \tilde{L}_{\widetilde{\mathcal{C}}\widetilde{\mathcal{X}}_1} & \tilde{L}_{\widetilde{\mathcal{C}}\widetilde{\mathcal{X}}_2} & \cdots & \tilde{L}_{\widetilde{\mathcal{C}}\widetilde{\mathcal{X}}_d} & \tilde{L}_{\widetilde{\mathcal{C}}\widetilde{\mathcal{C}}} \end{array}\right], \tag{4.3}$$

where the block diagonal terms are

$$\left[\begin{array}{cc} \tilde{L}_{\widetilde{\mathcal{U}}_k\widetilde{\mathcal{U}}_k} & \mathbf{0} \\ \tilde{L}_{\widetilde{\mathcal{M}}_k\widetilde{\mathcal{U}}_k} & \tilde{L}_{\widetilde{\mathcal{M}}_k\widetilde{\mathcal{M}}_k} \end{array}\right], \tag{4.4}$$

and $\tilde{L}_{\widetilde{\mathcal{U}}_k\widetilde{\mathcal{U}}_k} \in \mathbb{R}^{|\widetilde{\mathcal{U}}_k|\times|\widetilde{\mathcal{U}}_k|}$ is the Laplacian matrix of the induced subgraph $\widetilde{\mathcal{G}}_k(\widetilde{\mathcal{U}}_k, \widetilde{\mathcal{E}}_{\widetilde{\mathcal{U}}_k}, \widetilde{\mathcal{W}}_{\widetilde{\mathcal{U}}_k})$ which is strongly connected (property 4 in Lemma 4.1). Hence, there exists a left eigenvector $\tilde{v}_k \in \mathbb{R}^{|\widetilde{\mathcal{U}}_k|}$ that corresponds to the unique zero eigenvalue of $\tilde{L}_{\widetilde{\mathcal{U}}_k\widetilde{\mathcal{U}}_k}$, i.e. $\tilde{v}_k^T \tilde{L}_{\widetilde{\mathcal{U}}_k\widetilde{\mathcal{U}}_k} = \mathbf{0}^T$, with the following properties [26],

1. $[\tilde{v}_k]_j \in (0,1)$ for $i = 1, \ldots, |\widetilde{\mathcal{U}}_k|$.

2. $\sum_{i=1}^{|\widetilde{\mathcal{U}}_k|} [\tilde{v}_k]_i = 1$

In light of the discussion above, it is observed that

$$\tilde{\mu}_k = [\mathbf{0}^T_{|\widetilde{\mathcal{X}}_1|} \; \mathbf{0}^T_{|\widetilde{\mathcal{X}}_2|} \; \dots \; \tilde{v}_k^T \mathbf{0}^T_{|\widetilde{\mathcal{M}}_k|} \; \dots \; \mathbf{0}^T_{|\widetilde{\mathcal{X}}_d|} \; \mathbf{0}^T_{|\widetilde{\mathcal{C}}|}]^T, \tag{4.5}$$

is a left eigenvector for $\tilde{L}$ corresponding to the zero eigenvalue. Since $\widetilde{\mathcal{U}}_i \cap \widetilde{\mathcal{U}}_j = \varnothing$ for $i \neq j$, $\tilde{\mu}_j^T \tilde{\mu}_i = 0$ which means $\tilde{\mu}_1, \dots, \tilde{\mu}_d$ are orthogonal bases for the eigenspace of zero eigenvalues. As $\tilde{L} = PLP^{-1}$, we have $\mu_k = P^T \tilde{\mu}_k$ which along with (4.5) and the properties of $\tilde{v}_k$ lead to Properties 1 – 3 of μ_k. This completes the proof. □

Example 1 (Continued). Now, we illustrate the results of Lemma 4.2 by assigning the following weights to the edges of the graph in Figure 4.2: $a_{12} = 2$, $a_{21} = 1$, $a_{43} = 3$, $a_{45} = 5$, $a_{54} = 4$, $a_{67} = 7$, $a_{81} = 1$, $a_{83} = 3$, $a_{98} = 8$, $a_{10,9} = 9$, $a_{10,11} = 11$, $a_{10,12} = 12$, $a_{11,10} = 10$, $a_{11,12} = 12$, $a_{12,10} = 10$. The eigenvalues of the Laplacian matrix L are $\lambda_1 = \lambda_2 = \lambda_3 = 0$, $\lambda_4 = 1.101$, $\lambda_5 = 2.265$, $\lambda_6 = 3$, $\lambda_{7,8} = 4 + 4i$, $\lambda_9 = 7$, $\lambda_{10} = 10.899$, $\lambda_{11} = 22$, $\lambda_{12} = 39.735$. It is observed that the Laplacian matrix has three zero eigenvalues that is consistent with the point that the underlying graph has three reach sets. Denote the right and the left eigenvectors associated with the zero eigenvalue of L by $\gamma_1, \gamma_2, \gamma_3 \in \mathbb{R}^{12}$ and $\mu_1, \mu_2, \mu_3 \in \mathbb{R}^{12}$, respectively. In order to choose γ_1, we follow the properties 1 and 2 in Lemma 4.2, leading to $[\gamma_1]_1 = [\gamma_1]_2 = 1$ and $[\gamma_1]_6 = [\gamma_1]_7 = 0$. The remaining entries of γ_1 are then obtained by solving $L\gamma_1 = \mathbf{0}_{12}$ that results in $\gamma_1 = [1 \; 1 \; \mathbf{0}_5^T \; \frac{1}{4} \; \frac{1}{4} \; \frac{1}{4} \; \frac{1}{4} \; \frac{1}{4}]^T$. It can be seen that $[\gamma_1]_i \in (0,1)$ for $i \in \mathcal{C}_1$ (properties 3 in Lemma 4.2). Similarly, we have $\gamma_2 = [\mathbf{0}_2^T \; 1 \; 1 \; 1 \; \mathbf{0}_2^T \; \frac{3}{4} \; \frac{3}{4} \; \frac{3}{4} \; \frac{3}{4} \; \frac{3}{4}]^T$ and $\gamma_3 = [\mathbf{0}_5^T \; 1 \; 1 \; \mathbf{0}_5^T]^T$. It is now straightforward to check the property 4 in Lemma 4.2, i.e. $\gamma_1 + \gamma_2 + \gamma_3 = \mathbf{1}_{12}$. Turning into the construction of μ_1, we use the second property in Lemma 4.2 that leads to $[\mu_1]_i = 0$ for $i \in \mathcal{V} \backslash \mathcal{R}_1 = \{3, \dots, 12\}$. The remaining entries of μ_1 are obtained by solving $\mu_1^T L = \mathbf{0}_{12}^T$ that results in $\mu_1 = [\frac{1}{3} \; \frac{2}{3} \; \mathbf{0}_{10}^T]^T$. It can be observed that $[\mu_1]_i \in (0,1)$ for $i \in \mathcal{U}_1$ (properties 1 in Lemma 4.2), and $[\mu_1]_1 + [\mu_1]_2 = 1$ (properties 3 in Lemma 4.2). Following the same approach, we have $\mu_2 = [\mathbf{0}_2^T \; 1 \; \mathbf{0}_9^T]^T$ and $\mu_2 = [\mathbf{0}_6^T \; 1 \; \mathbf{0}_5^T]^T$.

4.3 Problem Formulation and Results

Motivated by the applications stated in Section 4.1, we investigate the effect of negative weights on the eigenvalues of the Laplacian matrix. Subsection 4.3.1 is mainly concerned with finding an upper bound on the magnitude of negative weights for added edges such that the eigenvalues of the Laplacian matrix have a specific property. We also present a discussion on the applicability of the notion of effective resistance for directed graphs. In Subsection 4.3.2, we analyse the eigenvalues of Laplacian matrix for a graph with multiple negative weights whose magnitudes are infinitesimal.

4.3.1 Adding a (un)directed negative edge to directed signed graphs

In this subsection, we proceed to answering the following question:

Question 1. *Consider a signed graph $\mathcal{G}_1(\mathcal{V},\mathcal{E}_1,\mathcal{W}_1)$ with the Laplacian matrix L_1. Construct a new graph $\mathcal{G}(\mathcal{V},\mathcal{E},\mathcal{W}) = \mathcal{G}_1(\mathcal{V},\mathcal{E}_1,\mathcal{W}_1)\oplus\mathcal{G}_2(\mathcal{V},\mathcal{E}_2,\mathcal{W}_2)$, where $\mathcal{E}_2 = \{(u,v),(v,u)\}$ and $\mathcal{W}_2(u,v) = -\delta_{uv} \leq 0$ and $\mathcal{W}_2(v,u) = -\delta_{vu} \leq 0$. Denote L the Laplacian matrix of $\mathcal{G}$. Find conditions on $\mathcal{G}_1$ and a bound on δ_{uv} and δ_{vu} such that*

$$0 = \lambda_1(L) < \Re(\lambda_2(L)) \leq \cdots \leq \Re(\lambda_N(L)). \tag{4.6}$$

We first state the following definition and lemma that are used to prove the main results of this subsection.

Definition 4.2. *Consider a signed graph $\mathcal{G}(\mathcal{V},\mathcal{E},\mathcal{W})$ with the Laplacian matrix L. For given two arbitrary nodes u and v, and variables $\delta_{uv},\delta_{vu},\omega \geq 0$, we define $r(\omega,\delta_{uv},\delta_{vu})$ as follows*

$$r(\omega,\delta_{uv},\delta_{vu}) := (\mathbf{e}_u-\mathbf{e}_v)^T Q^T(\bar{L}-j\omega I)^{-1}Q(\delta_{uv}\mathbf{e}_u-\delta_{vu}\mathbf{e}_v), \tag{4.7}$$

where $\bar{L} = QLQ^T$ is the reduced Laplacian matrix.

Lemma 4.3. *Assume for a given directed graph $\mathcal{G}(\mathcal{V},\mathcal{E},\mathcal{W})$ with Laplacian matrix L,*

$$spec\{L\} = \{\underbrace{0,\ldots,0}_{d},\Lambda\},$$

where the set Λ contains the non-zero eigenvalues of L. Then,

1. *spec$\{\bar{L}\} = \{\underbrace{0,\ldots,0}_{d-1},\Lambda\}$. Furthermore, if $d = 1$, then $\bar{L}$ is invertible.*
2. *Suppose further that all weights are non-negative. $\bar{L}$ is invertible and $\Re\{\lambda_i(\bar{L})\} > 0$ for $i = 1,\ldots,N-1$ if and only if $\mathcal{G}$ is connected* [†].

Proof. The proof of the first part can be found in [138, Lemma1]. Even though the lemma deals with directed graphs with non-negative weights, the same arguments are applicable to directed signed graphs, since $L\mathbf{1}_N = \mathbf{0}$. If $\mathcal{G}$ is connected with non-negative weights, then $\mathrm{Spec}(L) = \{0,\lambda_2,\ldots,\lambda_N\}$ with $\Re\{\lambda_2\} > 0$ [3]. Taking into account this point along with the first part of the lemma proves the second part. □

We now present a necessity result for the non-zero eigenvalues of Laplacian matrix to have positive real parts in the presence of a negative weight.

Theorem 4.1. *Consider a signed graph $\mathcal{G}_1(\mathcal{V},\mathcal{E}_1,\mathcal{W}_1)$ with the Laplacian matrix L_1. Assume that L_1 has only one zero eigenvalue and the rest of its eigenvalues have positive real parts. Construct a new graph $\mathcal{G}(\mathcal{V},\mathcal{E},\mathcal{W}) = \mathcal{G}_1(\mathcal{V},\mathcal{E}_1,\mathcal{W}_1)\oplus\mathcal{G}_2(\mathcal{V},\mathcal{E}_2,\mathcal{W}_2)$, where $\mathcal{E}_2 = \{(u,v),(v,u)\}$ and $\mathcal{W}_2(u,v) = -\delta_{uv}$, $\mathcal{W}_2(v,u) = -\delta_{vu}$ with $\delta_{uv} \geq 0$, $\delta_{vu} \geq 0$. Denote L the Laplacian matrix of $\mathcal{G}$. If the eigenvalues of L satisfy (4.6), then*

$$r(0,\delta_{uv},\delta_{vu}) < 1. \tag{4.8}$$

Proof. Define $\bar{L} = QLQ^T$ and suppose that the eigenvalues of L satisfy (4.6). We show the condition (4.8) holds. In view of the first part of Lemma C.2 in Appendix C.1, if $r(0,\delta_{uv},\delta_{vu}) > 1$, then $\det\left(\bar{L}_1^{-1}\bar{L}\right) = \det\left(\bar{L}_1^{-1}\right)\det\left(\bar{L}\right) < 0$. Hence $\bar{L}$ has at least one non-positive eigenvalue. If $r(0,\delta_{uv},\delta_{vu}) = 1$, then $\det\left(\bar{L}_1^{-1}\bar{L}\right) = 0$. Thus, $\bar{L}$ has at least one zero eigenvalue. This means that the condition (4.8) is necessary for the eigenvalues of L satisfy (4.6). □

We now present a sufficiency theorem for the non-zero eigenvalues of Laplacian matrix to have positive real parts in the presence of a negative weight.

[†]For a graph with non-negative weights, the definition of connectivity, falls somewhere between the definitions of strong and weak connectivity [3,137].

Theorem 4.2. *Consider a signed graph $\mathcal{G}_1(\mathcal{V}, \mathcal{E}_1, \mathcal{W}_1)$ with the Laplacian matrix L_1. Assume that L_1 has only one zero eigenvalue and the rest of its eigenvalues have positive real parts. Construct a new graph $\mathcal{G}(\mathcal{V}, \mathcal{E}, \mathcal{W}) = \mathcal{G}_1(\mathcal{V}, \mathcal{E}_1, \mathcal{W}_1) \oplus \mathcal{G}_2(\mathcal{V}, \mathcal{E}_2, \mathcal{W}_2)$, where $\mathcal{E}_2 = \{(u,v),(v,u)\}$ and $\mathcal{W}_2(u,v) = -\delta q_{uv} \leq 0$, $\mathcal{W}_2(v,u) = -\delta q_{vu} \leq 0$ with $\delta > 0$ and given $q_{uv}, q_{vu} \geq 0$. Denote L the Laplacian matrix of $\mathcal{G}$. Let δ^* be obtained by,*

$$\begin{aligned} \min_{\delta_1 \in \mathbb{R}_{>0}, \omega \in \mathbb{R}_{\geq 0}} \quad & \delta_1 \\ \textit{subject to} \quad & r(\omega, \delta_1 q_{uv}, \delta_1 q_{vu}) = 1. \end{aligned} \tag{4.9}$$

Then, the eigenvalues of L satisfy (4.6) for all $\delta \in [0, \delta^*)$.

Proof. Denote L_2 the Laplacian matrix of $\mathcal{G}_2$. Since $\mathcal{E}_2 = \{(u,v),(v,u)\}$, L_2 can be expressed as $L_2 = -(\delta_{uv}\mathbf{e}_u - \delta_{vu}\mathbf{e}_v)(\mathbf{e}_u - \mathbf{e}_v)^T$ with $\delta_{uv} = \delta q_{uv}$ and $\delta_{vu} = \delta q_{vu}$. Under conditions of the theorem, L can be written as $L = L_1 + L_2$, leading to the following expression for $\bar{L}$,

$$\bar{L} = \underbrace{QL_1Q^T}_{\bar{L}_1} - Q(\delta_{uv}\mathbf{e}_u - \delta_{vu}\mathbf{e}_v)(\mathbf{e}_u - \mathbf{e}_v)^T Q^T. \tag{4.10}$$

Since L_1 has only one zero eigenvalue and the rest of its eigenvalues have positive real parts, all eigenvalues of $\bar{L}_1 - j\omega I$ have positive real parts according to Property 1 in Lemma 4.3.

We now prove the theorem for the case with $q_{uv}, q_{vu} > 0$. The proof of theorem for the cases with $q_{uv} > 0$, $q_{vu} = 0$ or $q_{uv} = 0$, $q_{vu} > 0$ follows the same lines. Since $q_{uv}, q_{vu} > 0$, we have $\delta_{uv} = \delta q_{uv}$ and $\delta_{vu} = \delta q_{vu}$. Note that for $\delta = 0$, $\bar{L} = \bar{L}_1$ and for sufficiently large δ, i.e. $\delta > \sum_{i=1}^{N} [L_1]_{ii}$, the sum of the diagonal entries of L becomes negative. This leads L to have at least one eigenvalue with a negative real part, and consequently, in view of Property 1 in Lemma 4.3, $\bar{L}$ has that eigenvalue with negative real part. Hence, the continuity of eigenvalues of $\bar{L}$ with respect to δ states that

$$\exists\, \delta^* > 0 \text{ such that } \forall\ \delta \in [0, \delta^*),\ \Re\{\lambda_i(\bar{L})\}_{i=1}^{N-1} > 0, \tag{4.11}$$

and also with $\delta = \delta^*$, $\Re\{\lambda_i(\bar{L})\} = 0$ for some i. This means there exists at least one $\omega \in \mathbb{R}_{\geq 0}$ such that $\lambda_i(\bar{L}) = j\omega$ for $\delta = \delta^*$, or equivalently $\det\left(\bar{L} - j\omega I\right) = 0$. Using the expression of

$\bar{L}$ in (4.10) and taking into account that $\bar{L}_1 - j\omega I$ is invertible, we have

$$\begin{aligned}
\det\left(\bar{L} - j\omega I\right) &= \det\left(\bar{L}_1 - j\omega I - Q(\delta_{uv}\mathbf{e}_u - \delta_{vu}\mathbf{e}_v)(\mathbf{e}_u - \mathbf{e}_v)^T Q^T\right) \\
&= \det\left(\bar{L}_1 - j\omega I\right)\left(1 - (\mathbf{e}_u - \mathbf{e}_v)^T Q^T (\bar{L}_1 - j\omega I)^{-1} Q(\delta_{uv}\mathbf{e}_u - \delta_{vu}\mathbf{e}_v)\right) \\
&= \det\left(\bar{L}_1 - j\omega I\right)\left(1 - \delta^*(\mathbf{e}_u - \mathbf{e}_v)^T Q^T (\bar{L}_1 - j\omega I)^{-1} Q(q_{uv}\mathbf{e}_u - q_{vu}\mathbf{e}_v)\right) \\
&= 0,
\end{aligned} \tag{4.12}$$

where the last two equalities are obtained by applying Lemma C.1 and taking into account $\delta_{uv} = \delta q_{uv}$ and $\delta_{vu} = \delta q_{vu}$. Since $\bar{L}_1 - j\omega I$ is invertible, we observe that $\det\left(\bar{L} - j\omega I\right) = 0$ if and only if $\delta^*(\mathbf{e}_u - \mathbf{e}_v)^T Q^T (\bar{L}_1 - j\omega I)^{-1} Q(q_{uv}\mathbf{e}_u - q_{vu}\mathbf{e}_v) = 1$. By solving (4.9), we find the minimum value of δ^* such that the eigenvalues of L satisfy (4.6) for all $\delta \in (0, \delta^*)$. The optimisation problem (4.9) always has a solution since the continuity argument above guarantees that the eigenvalues of $\bar{L}$ cross the imaginary axis for some $\delta \in (0, \delta_1]$. This completes the proof of the case $q_{uv}, q_{vu} > 0$. □

Remark 4.2. *Theorem 4.2 includes three different cases that correspond to perturbing the edge (u,v) ($q_{uv} > 0, q_{vu} = 0$), the edge (v,u) ($q_{uv} = 0, q_{vu} > 0$), or both edges (u,v) and (v,u) ($q_{uv} > 0, q_{vu} > 0$). The variables q_{uv}, q_{vu} allow to incorporate all these cases in only one optimisation problem as stated in (4.9).*

The sufficiency condition (4.9) in Theorem 4.2 correspond to the minimum value of δ^* such that the eigenvalues of L satisfy (4.6) for all $\delta \in (0, \delta^*)$. One of the following statements holds for δ^* obtained from solving (4.9):

1. δ^* is obtained with $\omega_1, \ldots, \omega_k$ where $\omega_i \neq 0$ for $i = 1, \ldots, k$ and k is the number of solutions for (4.9) which is finite since the constraint is a non trivial polynomial equation in ω by definition of $r(\omega, \delta_{uv}, \delta_{vu})$;

2. or, there exists at least one zero ω_i.

In the second case, the matrix $\bar{L}$ has at least one zero eigenvalue with $\delta = \delta^*$ (in the view of (4.11)) which means that $\det\left(\bar{L}_1^{-1}\bar{L}\right) = 0$ for $\delta = \delta^*$. In this case, the condition (4.8) becomes necessary and sufficient for the non-zero eigenvalues of Laplacian matrix have

positive real parts in the presence of a negative weight according to the following theorem.

Theorem 4.3. *Consider a signed graph $\mathcal{G}_1(\mathcal{V}, \mathcal{E}_1, \mathcal{W}_1)$ with the Laplacian matrix L_1. Assume that L_1 has only one zero eigenvalue and the rest of its eigenvalues have positive real parts. Construct a new graph $\mathcal{G}(\mathcal{V}, \mathcal{E}, \mathcal{W}) = \mathcal{G}_1(\mathcal{V}, \mathcal{E}_1, \mathcal{W}_1) \oplus \mathcal{G}_2(\mathcal{V}, \mathcal{E}_2, \mathcal{W}_2)$, where $\mathcal{E}_2 = \{(u,v),(v,u)\}$ and $\mathcal{W}_2(u,v) = -\delta q_{uv} \leq 0$, $\mathcal{W}_2(v,u) = -\delta q_{vu} \leq 0$ with $\delta > 0$ and given $q_{uv}, q_{vu} \geq 0$. Denote L the Laplacian matrix of $\mathcal{G}$. Let δ^* be obtained from (4.9) with $\omega_1, \ldots, \omega_k$ being the roots of the equality constraint. Assume further that there exists at least one zero ω_i. The eigenvalues of L satisfy (4.6) if and only if*

$$\underbrace{\delta \left(\mathbf{e}_u - \mathbf{e}_v\right)^T Q^T \bar{L}_1^{-1} Q \left(q_{uv}\mathbf{e}_u - q_{vu}\mathbf{e}_v\right)}_{r(0,\delta q_{uv},\delta q_{vu})} < 1. \tag{4.13}$$

Furthermore, $\delta^* \left(\mathbf{e}_u - \mathbf{e}_v\right)^T Q^T \bar{L}_1^{-1} Q \left(q_{uv}\mathbf{e}_u - q_{vu}\mathbf{e}_v\right) = 1$ and $\left(\mathbf{e}_u - \mathbf{e}_v\right)^T Q^T \bar{L}_1^{-1} Q \left(q_{uv}\mathbf{e}_u - q_{vu}\mathbf{e}_v\right) > 0$.

Proof. The necessity part results from Theorem 4.1, i.e. if the eigenvalues of L satisfy (4.6), then (4.13) holds. We now show that the condition (4.13) is sufficient for the case with $q_{uv}, q_{vu} > 0$. The cases with $q_{uv} > 0$, $q_{vu} = 0$ or $q_{uv} = 0$, $q_{vu} > 0$ can be proven by using the same arguments.
In the proof of Theorem 4.2, it is observed from the continuity of eigenvalues of $\bar{L}$ with respect to δ that

$$\exists\ \delta^* > 0 \text{ such that } \forall\ \delta \in [0, \delta^*),\ \Re\{\lambda_i(\bar{L})\}_{i=1}^{N-1} > 0, \tag{4.14}$$

and also with $\delta = \delta^*$, $\Re\{\lambda_i(\bar{L})\} = 0$ for some i. Since δ^* is obtained from (4.9) with at least one zero ω_i, then there exists at least one zero eigenvalue $\lambda_i(\bar{L}) = 0$ for $\delta = \delta^*$, meaning that $\det\left(\bar{L}_1^{-1}\bar{L}\right) = 0$. From the definition of $r(0, \delta q_{uv}, \delta q_{vu})$ in (4.13), we have

$$r_\delta := r(0, \delta q_{uv}, \delta q_{vu}) = \alpha\delta, \tag{4.15}$$

where $\alpha = \left(\mathbf{e}_u - \mathbf{e}_v\right)^T Q^T \bar{L}_1^{-1} Q \left(q_{uv}\mathbf{e}_u - q_{vu}\mathbf{e}_v\right)$.

Let assume $\alpha > 0$. Using this assumption, (4.14) can be rewritten as

$$\exists\, r^* > 0 \text{ such that } \forall\ r_\delta \in [0, r^*),\ \Re\{\lambda_i(\bar{L})\}_{i=1}^{N-1} > 0. \tag{4.16}$$

We now need to show $r^* = 1$. If $r^* < 1$, according to (4.16), the real part of at least one eigenvalue of $\bar{L}$ is negative for $r_\delta > r^*$ and the real part becomes zero at $r_\delta = r^*$; however, from Lemma C.2 in Appendix C.1, it is observed that $\bar{L}$ can have zero eigenvalue(s) if and only if $r_\delta = 1$. This contradicts the assumption $r^* < 1$. Hence, $r^* = 1$

To complete the proof, we should show the assumption $\alpha > 0$. To do so, we show α cannot be zero or strictly negative by considering two cases.

Case 1: To obtain a contradiction, assume $\alpha = 0$. Then $r_\delta = 0$, and according to (C.2), $\det\left(\bar{L}_1^{-1}\bar{L}\right)$ cannot be zero which means $\bar{L}$ has no zero eigenvalue. This means that $\delta^* = +\infty$ or equivalently all eigenvalues of $\bar{L}$ have positive real parts. However, this is not true, since for sufficiently large δ, i.e. $\delta > \sum_{i=1}^{N} [L_1]_{ii}$, the sum of the diagonal entries of L becomes negative. This leads L to have at least one eigenvalue with a negative real part. Hence, in view of Property 1 in Lemma 4.3, $\bar{L}$ has the same eigenvalue with negative real part. This is in contradiction with $\delta^* = +\infty$. Therefore, $\alpha \neq 0$.

Case 2: To obtain a contradiction, assume $\alpha < 0$. Thus (4.14) and (4.15) imply

$$\exists\, r^* > 0 \text{ such that } \forall\ r_\delta \in (-r^*, 0],\ \Re\{\lambda_i(\bar{L})\}_{i=1}^{N-1} > 0. \tag{4.17}$$

Furthermore, letting $r_\delta = -r^*$ yields $\Re\{\lambda_i(\bar{L})\} = 0$ for some i as r^* is taken as the maximum value satisfying (4.17). This means that $\det\left(\bar{L}_1^{-1}\bar{L}\right) = 0$ for $r_\delta = -r^* < 0$. However, according to (C.2), $\det\left(\bar{L}_1^{-1}\bar{L}\right) = 0$ if and only if $r_\delta = 1$. This contradicts $r_\delta < 0$. Hence, α cannot be negative. This completes the proof. □

The key step to apply Theorems 4.2 and 4.3 is to numerically solve the optimisation problem (4.9), which has at least one solution as explained in the proof of Theorem 4.2. The feasible set of this optimisation problem can be interpreted in terms of the Nyquist

plots of the following system Σ_{uv},

$$\Sigma_{uv} := \begin{cases} \frac{d}{dt}x_{uv} &= \bar{L}_1 x_{uv} + Q(q_{uv}\mathbf{e}_u - q_{vu}\mathbf{e}_v)u_{uv} \\ y_{uv} &= (\mathbf{e}_u - \mathbf{e}_v)^T Q^T x_{uv} \end{cases} \tag{4.18}$$

where $x_{uv} \in \mathbb{R}^{N-1}$, $u_{uv} \in \mathbb{R}$ and $y_{uv} \in \mathbb{R}$ denote the state, the input and the output of the system Σ_{uv}. Consider the optimisation problem (4.9) and the system Σ_{uv} in a negative feedback structure with a proportional controller δ_1. The optimisation problem (4.9) yields the minimum value of the gain for which the Nyquist diagram of $\delta_1 G_{uv}(s)$ crosses the critical point -1 where $G_{uv}(s)$ is the transfer function from u_{uv} to y_{uv}. Hence, to attain δ^*, one can plot the Nyquist diagram of Σ_{uv} and find frequencies ω_i, $i = 1, \ldots, k$, at which it crosses the real axis. Then, $\delta^* = \frac{1}{|G_{uv}(j\omega^*)|}$ where $G_{uv}(j\omega^*) \leq G_{uv}(j\omega_i)$ for $i = 1, \ldots, k$. If $\omega^* = 0$, then we can use the results of Theorem 4.3; otherwise we should use the results of Theorem 4.2. In the following examples, we illustrate how to apply the results of Theorems 4.2 and 4.3.

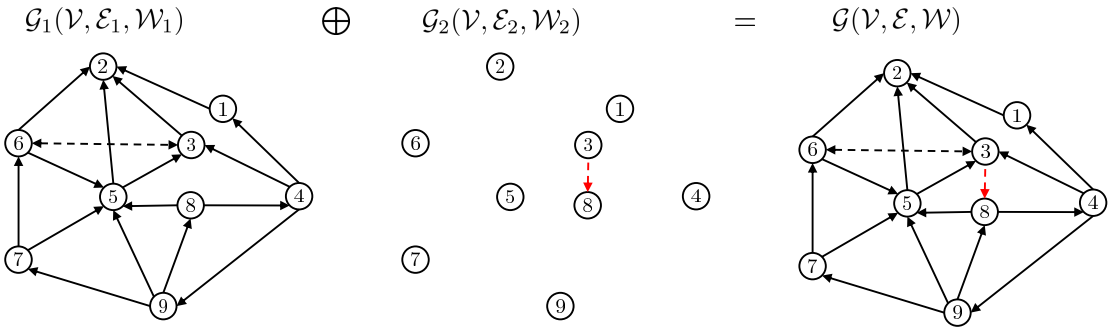

Figure 4.2: A directed graph studied in Example 2. The solid arrows represent the positive weight edges while the dashed arrows show the edges with negative weights. All positive and negative weights are set equal to 2 and -1, respectively.

Example 2. Consider the graphs $\mathcal{G}_1(\mathcal{V}, \mathcal{E}_1, \mathcal{W}_1)$, $\mathcal{G}_2(\mathcal{V}, \mathcal{E}_2, \mathcal{W}_2)$ and $\mathcal{G}(\mathcal{V}, \mathcal{E}, \mathcal{W})$ depicted in Figure 4.2 with the Laplacian matrices L_1, L_2, L respectively. In this figure, the solid arrows represent the positive weights which are set equal to 2, and the dashed arrows represent the negative weights with $a_{36} = a_{63} = a_{38} = -1$. The graph $\mathcal{G}$ is constructed from the graphs $\mathcal{G}_1$ and $\mathcal{G}_2$ by adding negative weights between two pairs of nodes, i.e. $\mathcal{G} = \mathcal{G}_1 \oplus \mathcal{G}_2$.

We now add the negative directed edge $a_{38} = -\delta$. The Nyquist diagram plotted in Figure 4.3 crosses the real axis at $\omega_1 = 0$ and $\omega_2 = \infty$. Furthermore, the magnitude of the Nyquist diagram at ω_1 is smaller than of that at ω_2. Hence, in view of Theorem 4.3, the condition (4.13) is necessary and sufficient condition, leading to $\delta^* = 1.94285$. This means that the eigenvalues of L satisfy (4.6) if and only if $\delta < 1.94285$.

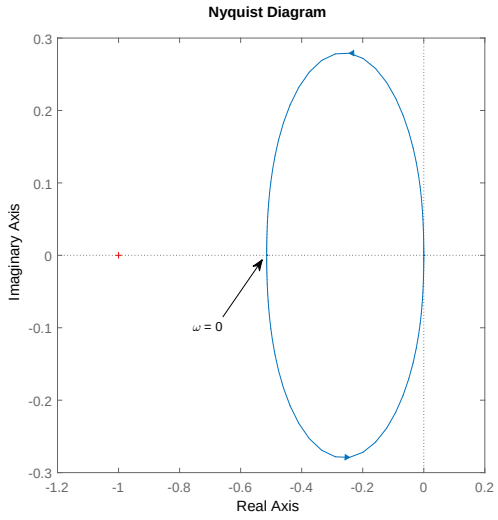

Figure 4.3: The Nyquist diagram in Example 2.

Example 3. Consider the graphs $\mathcal{G}_1(\mathcal{V}, \mathcal{E}_1, \mathcal{W}_1)$, $\mathcal{G}_2(\mathcal{V}, \mathcal{E}_2, \mathcal{W}_2)$ and $\mathcal{G}(\mathcal{V}, \mathcal{E}, \mathcal{W})$ depicted in Figure 4.4 with the Laplacian matrices L_1, L_2, L respectively. In this figure, the solid black arrows, the dashed red arrow and the solid read arrows represent the positive weights, the negative weight and the perturbed edges, respectively. We assign the following weights to the edges of the graph $\mathcal{G}_1$: $a_{12} = 1$, $a_{14} = 1$, $a_{15} = 1$, $a_{21} = 1$, $a_{23} = 1$, $a_{24} = 1$, $a_{31} = -1$, $a_{32} = 1$, $a_{35} = -0.8$, $a_{42} = -0.3$, $a_{43} = 1.5$, $a_{45} = -2$, $a_{51} = 2$, $a_{52} = 1$, $a_{53} = 2$, $a_{54} = 1$.

In the first scenario, the graph $\mathcal{G}$ is constructed from the graphs $\mathcal{G}_1$ and $\mathcal{G}_2$ by perturbing positive weights between two pairs of nodes 1 and 2. According to the left Nyquist diagram plotted in Figure 4.5, the Nyquist diagram crosses the real axis at $\omega_1 = 0$, $\omega_{2,3} = \pm 0.6$ and $\omega_{4,5} = \pm\infty$. Furthermore, the magnitude of the Nyquist diagram at $\omega_{2,3}$ is smaller than others. Hence, in view of Theorem 4.3, the condition (4.13) is sufficient, leading to

$\delta^* = 0.52$. This means that if $\delta < 0.52$ the eigenvalues of L meet (4.6). On the other hand, the necessary condition (4.8) holds for $\delta < 1.8$.

In the second scenario, the graph $\mathcal{G}$ is constructed from the graphs $\mathcal{G}_1$ and $\mathcal{G}_2$ by perturbing positive weights between two pairs of nodes 2 and 5. According to the right Nyquist diagram plotted in Figure 4.5, the Nyquist diagram crosses the real axis at $\omega_1 = 0$, $\omega_{2,3} = \pm 0.63$, $\omega_{4,5} = \pm 0.8$ and $\omega_{6,7} = \pm\infty$. Furthermore, the magnitude of the Nyquist diagram at ω_1 is smaller than others. Hence, in view of Theorem 4.3, the condition (4.13) is necessary and sufficient condition, leading to $\delta^* = 2.3239$. This means that the eigenvalues of L meet (4.6) if and only if $\delta < 2.3239$.

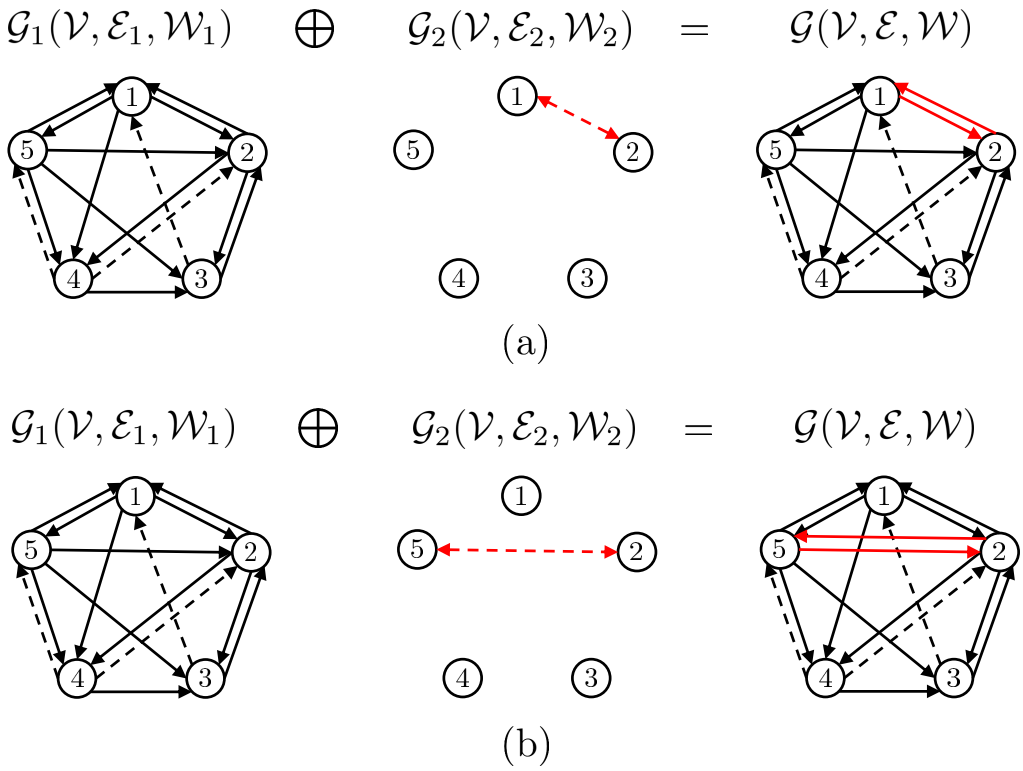

Figure 4.4: A directed graph studied in Example 3. The solid arrows represent the positive weight edges while the dashed arrows show the edges with negative weights. All positive and negative weights are set equal to 2 and −1, respectively.

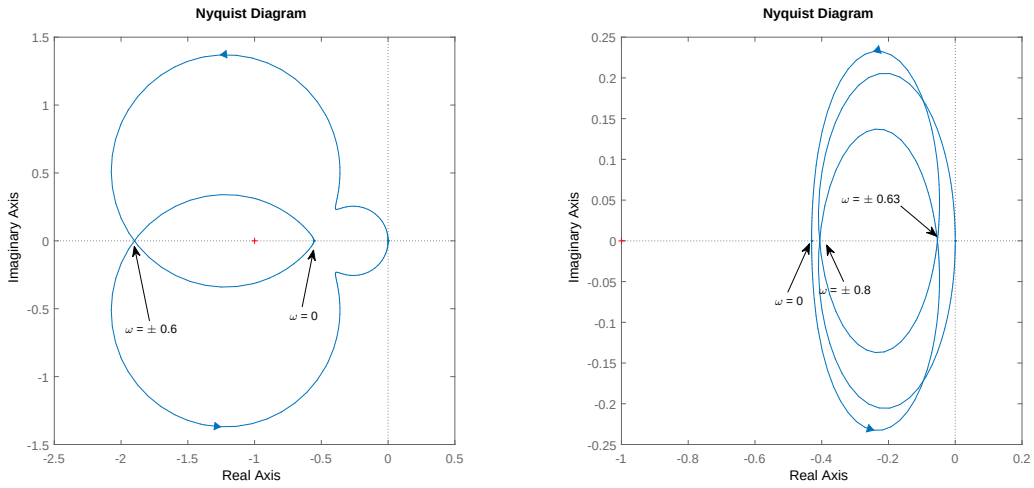

Figure 4.5: The Nyquist diagrams in Example 3. The left Nyquist diagram corresponds to the first scenario with the graph in Figure 4.4(a), while the right Nyquist diagram corresponds to the second scenario with the graph in Figure 4.4(b).

Remark 4.3. *The results of this subsection are different from those in [95] where sufficient conditions for the upper bound δ has been derived via Nyquist stability criteria. First, we provide the necessary result which considers the case in which both edges between any arbitrary pairs of nodes are perturbed with negative weights. Secondly, our sufficiency result is more general than the main result of [95] since we also allow perturbing two edges between two nodes with the same negative weight. Our results cover a more general set of graphs as a graph with multiple negative edges might satisfy the assumption of the theorem, while [95, Theorem 1] only is applied to graphs with no negative edges. Even though the results of this paper are interpreted via Nyquist criteria, the definitions of systems are different from [95]. Finally, we highlight the case where the condition becomes necessary and sufficient.*

In all theorems above, it is assumed that the original graph $\mathcal{G}_1$ satisfy (4.6). If $\mathcal{G}_1$ is connected and all of its weight are non-negative, the second part of Lemma 4.3 provides the necessary and sufficient conditions for $\mathcal{G}_1$ to satisfy (4.6). In this case, the following corollaries are obtained.

Corollary 4.1. *Consider a signed graph $\mathcal{G}(\mathcal{V}, \mathcal{E}, \mathcal{W})$ with the Laplacian matrix L where it is decomposed into two subgraphs $\mathcal{G}(\mathcal{V}, \mathcal{E}^+, \mathcal{W}^+)$ and $\mathcal{G}(\mathcal{V}, \mathcal{E}^-, \mathcal{W}^-)$ with the corresponding Laplacian*

matrices L^+ and L^-, respectively. Assume $\mathcal{E}^- = \{(u,v),(v,u)\}$ with $\mathcal{W}^-(u,v) = -\delta q_{uv} \leq 0$ and $\mathcal{W}^-(v,u) = -\delta q_{vu} \leq 0$ with $\delta > 0$ and given $q_{uv}, q_{vu} \geq 0$. Assume also $\mathcal{G}(\mathcal{V},\mathcal{E}^+,\mathcal{W}^+)$ is connected, and define $\bar{L}^+ = QL^+Q^T$. Let δ^* be obtained by,

$$\begin{aligned} \min_{\omega \in \mathbb{R}_{\geq 0}} \quad & \delta_1 \\ \text{subject to} \quad & \delta_1 (\mathbf{e}_u - \mathbf{e}_v)^T Q^T (\bar{L}^+ - j\omega I)^{-1} Q (q_{uv}\mathbf{e}_u - q_{vu}\mathbf{e}_v) = 1, \quad \delta_1 > 0. \end{aligned} \tag{4.19}$$

Then, the eigenvalues of L satisfy (4.6) for all $\delta \in [0, \delta^*)$.

Corollary 4.2. *Consider a signed graph $\mathcal{G}(\mathcal{V},\mathcal{E},\mathcal{W})$ with the Laplacian matrix L where it is decomposed into two subgraphs $\mathcal{G}(\mathcal{V},\mathcal{E}^+,\mathcal{W}^+)$ and $\mathcal{G}(\mathcal{V},\mathcal{E}^-,\mathcal{W}^-)$ with the corresponding Laplacian matrices L^+ and L^-, respectively. Assume $\mathcal{E}^- = \{(u,v),(v,u)\}$ with $\mathcal{W}^-(u,v) = -\delta q_{uv} \leq 0$ and $\mathcal{W}^-(v,u) = -\delta q_{vu} \leq 0$ with $\delta > 0$ and given $q_{uv}, q_{vu} \geq 0$. Assume also $\mathcal{G}(\mathcal{V},\mathcal{E}^+,\mathcal{W}^+)$ is connected, and define $\bar{L}^+ = QL^+Q^T$. Let δ^* be obtained from (4.9) with $\omega_1, \ldots, \omega_k$ for $i = 1, \ldots, k$. Assume further that there exists at least one zero ω_i. The eigenvalues of L satisfy (4.6) if and only if*

$$\underbrace{\delta \, (\mathbf{e}_u - \mathbf{e}_v)^T \, Q^T \left(\bar{L}^+\right)^{-1} Q \, (q_{uv}\mathbf{e}_u - q_{vu}\mathbf{e}_v)}_{r(0, q_{uv}, q_{vu})} < 1. \tag{4.20}$$

Furthermore, $\delta^* \, (\mathbf{e}_u - \mathbf{e}_v)^T \, Q^T \left(\bar{L}^+\right)^{-1} Q \, (\mathbf{e}_u - \mathbf{e}_v) = 1$ and $(\mathbf{e}_u - \mathbf{e}_v)^T \, Q^T \left(\bar{L}^+\right)^{-1} Q \, (\mathbf{e}_u - \mathbf{e}_v) > 0$.

We end this subsection by commenting on the relationship between the aforementioned results and the concept of effective resistance introduced in the literature e.g. see [140] and references there in. First, consider an undirected graph $\mathcal{G}(\mathcal{V},\mathcal{E}^+,\mathcal{W}^+)$ with non-negative weights and the Laplacian matrix $\bar{L}^+$. Assume that the graph is connected. We construct an electrical network from the graph $\mathcal{G}(\mathcal{V},\mathcal{E}^+,\mathcal{W}^+)$ by replacing each weighted edge (i,j) with a resistor $R_{ij} = a_{ij}^{-1}$ as shown in Figure 4.6. Then, a constant current source I is connected between nodes u and v, and the voltage at its terminal is calculated. The effective resistance between nodes u and v is computed by $r_{uv} = \frac{V}{I}$. Using electrical circuit theory, it was shown that r_{uv} can be obtained by [82]

$$r_{uv} = (\mathbf{e}_u - \mathbf{e}_v)^T \, Q^T \left(\bar{L}^+\right)^{-1} Q \, (\mathbf{e}_u - \mathbf{e}_v), \tag{4.21}$$

which has the same expression as (4.20) with $q_{uv} = q_{vu} = 1$.
Now consider the case where a negative undirected edge is added between the nodes u and v to construct the undirected graph $\mathcal{G}(\mathcal{V}, \mathcal{E}, \mathcal{W})$ with the Laplacian matrix L. The corresponding equivalent electrical circuit contains two parallel resistors r_{uv} and $R_- = -\delta^{-1}$‡, which correspond to the aforementioned effective resistance and the added negative edge, respectively (Figure 4.7). In this case, the equivalent resistance between nodes u and v is calculated by

$$R_{th} = \frac{-\delta^{-1} r_{uv}}{r_{uv} - \delta^{-1}}.$$

The interpretation of the inequality (4.20)§ from the electrical circuit perspective is as follows: the equivalent resistance R_{th} is positive as long as (4.20) holds. Otherwise, R_{th} is either short circuit (if $\delta^{-1} = r_{uv}$) or negative (if $\delta^{-1} < r_{uv}$). By taking into account this point and Corollary 4.1, it is concluded that the Laplacian matrix L satisfies the condition (4.6) if and only if the equivalent resistance R_{th} of the corresponding equivalent electrical circuit is positive.

For directed graphs satisfying in the conditions of Corollary 4.2, one may be interested in interpreting the condition (4.20) using the concept of effective resistance similar to undirected graphs if directed graph satisfy assumptions of Corollary 4.2. However, this is not directly possible. Indeed, the notion of effective resistance has been recently introduced for both directed and undirected graphs as [137],

$$r_{uv} = 2 \left(\mathbf{e}_u - \mathbf{e}_v \right)^T Q^T \Sigma \, Q \left(\mathbf{e}_u - \mathbf{e}_v \right), \tag{4.22}$$

where Σ is a symmetric matrix obtained from the Lyapunov equation

$$\bar{L}\Sigma + \Sigma \left(\bar{L} \right)^T = I_{N-1}. \tag{4.23}$$

For a connected undirected graph $\mathcal{G}(\mathcal{V}, \mathcal{E}^+, \mathcal{W}^+)$, $\frac{1}{2} \left(\bar{L}^+ \right)^{-1} = \frac{1}{2} \left(\bar{L}^+ \right)^{-T}$ is a unique solution of (4.23) and r_{uv} has the same expression as (4.21). Unlike the case of undirected graphs,

‡Negative resistance has a practical meaning in electrical circuit theory as there exist electrical components with this property (see [84]).

§Note that inequality (4.20) is necessary and sufficient for this case as the underlying graph is undirected.

the expression of r_{uv} in (4.20) (even with $q_{uv} = q_{vu} = 1$) cannot be obtained from (4.22) and (4.23), since $\left(\bar{L}^{+}\right)^{-1} \neq \left(\bar{L}^{+}\right)^{-T}$. This reveals that, unlike undirected graph, the upper bound of δ cannot be interpreted by effective resistance defined in (4.22). As a result, it is not clear how to generalise the notion of effective resistance for directed graphs with non-negative weights by using electrical circuit theory.

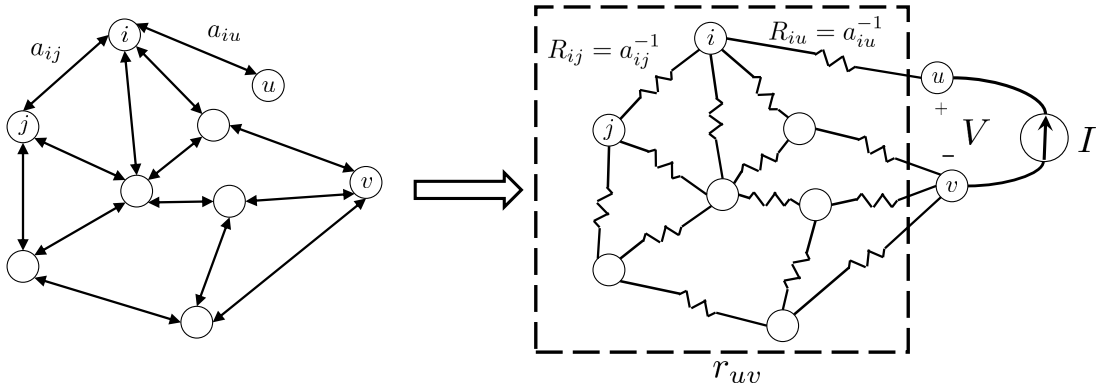

Figure 4.6: An equivalent electrical circuit for a connected undirected graph $\mathcal{G}(\mathcal{V}, \mathcal{E}^{+}, \mathcal{W}^{+})$ with non-negative weights to measure the effective resistance between two nodes u and v.

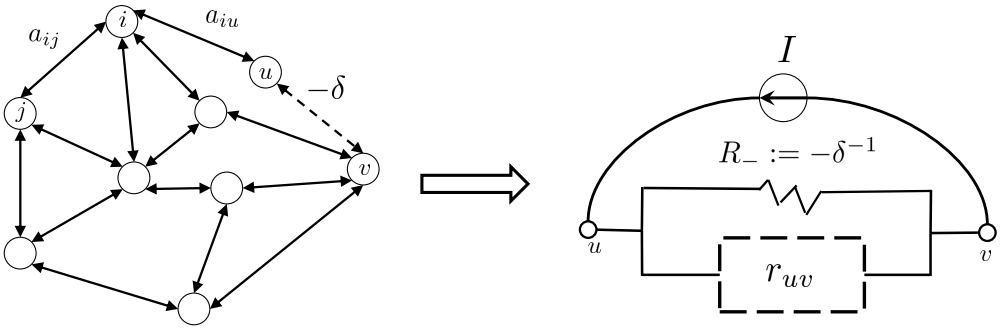

Figure 4.7: An equivalent electrical circuit for $\mathcal{G}(\mathcal{V}, \mathcal{E}, \mathcal{W})$ which is obtained by adding a negative edge to $\mathcal{G}(\mathcal{V}, \mathcal{E}^{+}, \mathcal{W}^{+})$.

4.3.2 Directed graphs with multiple negative weights

In this subsection, we examine the eigenvalues of the Laplacian matrix for graphs with multiple negative weights by stating the following question.

Question 2. *Given a graph $\mathcal{G}_1(\mathcal{V}, \mathcal{E}_1, \mathcal{W}_1)$ with non-negative edge weights, identify a set of pairs*

of nodes $\mathcal{E}_2 \subseteq \{\mathcal{V} \times \mathcal{V}\} \backslash \mathcal{E}_1$, $\mathcal{E}_2 = \{(u_1, v_1), \ldots, (u_l, v_l)\}$, *called sensitive pairs of nodes such that if a new graph is constructed from* $\mathcal{G}_1$ *by connecting those pairs of nodes with negative weights whose magnitudes are infinitesimal, the Laplacian matrix of the new graph has at least one eigenvalue with negative real part.*

The following theorem is aimed at answering the aforementioned question. Figure 4.8 shows a schematic diagram of a graph in which the negative edge weights connect those pairs of the nodes.

Theorem 4.4. *Consider a graph* $\mathcal{G}_1(\mathcal{V}, \mathcal{E}_1, \mathcal{W}_1)$ *with non-negative edge weights and its Laplacian matrix* L_1. *Assume that* $\mathcal{G}_1$ *consists of* $d \neq 1$ *reach sets* $\mathcal{R}_k$, $k = 1, \ldots, d$ *with corresponding reaching nodes sets* $\mathcal{U}_k$, *exclusive sets* $\mathcal{X}_k$ *and common sets* $\mathcal{C}_k$ *according to Definition 4.1. Let* $\mathcal{G}(\mathcal{V}, \mathcal{E}, \mathcal{W}) = \mathcal{G}_1(\mathcal{V}, \mathcal{E}_1, \mathcal{W}_1) \oplus \mathcal{G}_2(\mathcal{V}, \mathcal{E}_2, \mathcal{W}_2)$ *where* $\mathcal{E}_2 \subseteq \{\mathcal{V} \times \mathcal{V}\} \backslash \mathcal{E}_1$, $\mathcal{E}_2 = \{(u_1, v_1), \ldots, (u_l, v_l)\}$, $\mathcal{W}_2(u_k, v_k) = -\epsilon a_{u_k v_k}$ *for every* $(u_k, v_k) \in \mathcal{E}_2$ *with* ϵ *being a sufficiently small positive scalar and* $a_{u_k v_k} > 0$, *and* $\mathcal{W}_2(u_k, v_k) = 0$ *for every* $(u_k, v_k) \in \{\mathcal{V} \times \mathcal{V}\} \backslash \mathcal{E}_2$. *If there exists at least one negative edge weight* $(u_k, v_k) \in \mathcal{E}_2$ *such that*

1. *either* $u_k \in \mathcal{U}_i$ *and* $v_k \in \mathcal{X}_j$ *for some* $j \neq i$,

2. *or* $u_k \in \mathcal{U}_i$ *and* $v_k \in \mathcal{C}_j$ *for some* j *(including* $j = i$*),*

then the Laplacian matrix of $\mathcal{G}$ *has at least one eigenvalue with non-positive real part.*

Proof. Suppose all conditions of Theorem 4.4 hold. The Laplacian matrix of $\mathcal{G}$ can be expressed as

$$L = L_1 + L_2 = L_1 + \epsilon \tilde{L}_2, \tag{4.24}$$

where L_2 is the Laplacian matrix of $\mathcal{G}_2$, and $\tilde{L}_2$ is the Laplacian matrix for a graph $\widetilde{\mathcal{G}} = (\mathcal{V}, \mathcal{E}_2, \widetilde{\mathcal{W}}_2)$ with $\widetilde{\mathcal{W}}_2(u_k, v_k) = -a_{u_k v_k}$ for every $(u_k, v_k) \in \mathcal{E}_2$, and $\widetilde{\mathcal{W}}_2(u_k, v_k) = 0$ for every $(u_k, v_k) \in \{\mathcal{V} \times \mathcal{V}\} \backslash \mathcal{E}_2$.

Without loss of generality, we suppose the nodes of $\mathcal{G}_1$ are labelled such that the structure of the adjacency matrix of $\mathcal{G}_1$ is consistent with the structure of (4.1). Since zero is a semisimple eigenvalue of L with multiplicity d, in view of Lemmas C.3 and C.4, it is enough show that at least the real part of one of the eigenvalues of $\Theta := \Upsilon \tilde{L}_2 \Gamma$ becomes

negative (see Lemma C.4 for definitions of Υ and Γ). Conditions 1 and 2 in the theorem statement are equivalent to statements 3 and 4 of Lemma C.4. Hence, if there exists at least one negative edge (u, v) satisfying one of conditions 1 and 2, then according to Lemma C.4, Θ has at least a negative diagonal term which means $\text{trace}(\Theta) < 0$ or equivalently $\sum_{i=1}^{d} \lambda_i(\Theta) < 0$. This implies that there exists at least one eigenvalue $\lambda_i(\Theta)$ with $\Re\{\lambda_i(\Theta)\} < 0$. □

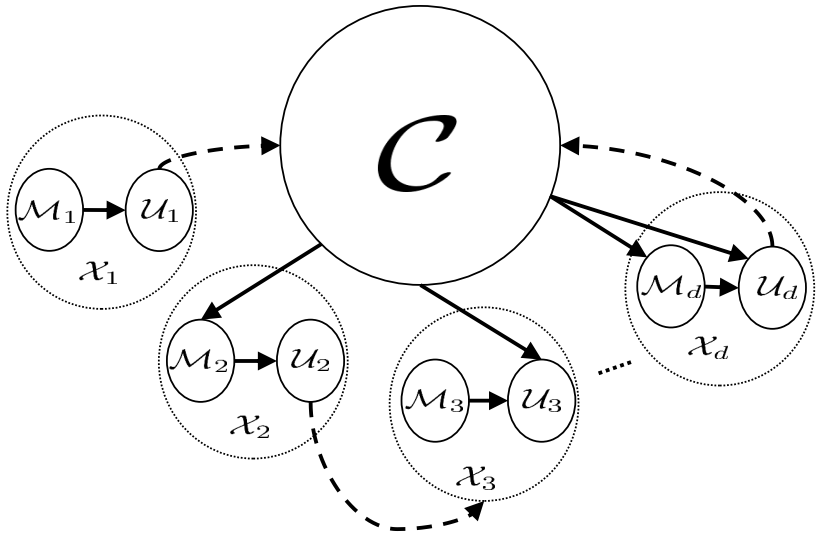

Figure 4.8: A schematic diagram of the connections between the nodes in a graph whose negative edges meet conditions 1 and 2 in Theorem 4.4. The solid arrows represent the positive weight edges while the dashed arrows show the edges with negative weights.

Remark 4.4. *For undirected graphs, it is straightforward to see that $\mathcal{R}_i = \mathcal{U}_i$. In view of Theorem 4.4, if $\mathcal{G}$ is connected while $\mathcal{G}_1$ is not, then $\mathcal{G}_2$ contains negative weight edges which satisfy the first condition of Theorem 4.4, and connect disconnected components of $\mathcal{G}_1$. In this case, Theorem 4.4 ensures that the Laplacian matrix of $\mathcal{G}$ is indefinite as it is symmetric and also has negative eigenvalue(s). This result is consistent with the result of Theorem IV.3 in [140].*

Remark 4.5. *In Theorem 4.4, we have characterised a class of sensitive pairs of nodes. However, there are other classes of sensitive pairs of nodes that we have not considered. As an example, $(u_k, v_k) \in \mathcal{E}_-$ such that:*

1. *either $u \in \mathcal{U}_i$ and $v \in \mathcal{X}_i$,*

2. *or* $u \in \mathcal{R}_i \backslash \mathcal{U}_i$ *and* $v \in \mathcal{R}_j$ *for some* $i \neq j$.

In this case, it can be shown that the corresponding diagonal term of the matrix Θ *in the proof of Theorem 4.4 is zero. Hence, the same argument in Theorem 4.4 cannot be followed to achieve similar results.*

Example 4. We illustrate the results of Theorem 4.4 and the point mentioned in Remark 4.5 using the graphs depicted in Figure 4.9. All positive weights are assigned to be 2. We have observed in Example 1 that the graph $\mathcal{G}_1$ has three reaching nodes sets $\mathcal{U}_1 = \{1,2\}, \mathcal{U}_2 = \{3\}, \mathcal{U}_3 = \{7\}$, three exclusive sets $\mathcal{X}_1 = \{1,2\}, \mathcal{X}_2 = \{3,4,5\}, \mathcal{X}_3 = \{6,7\}$, and three common sets $\mathcal{C}_1 = \mathcal{C}_2 = \{8,9,10,11,12\}$ and $\mathcal{C}_3 = \varnothing$.

In what follow, we demonstrate the application of Theorem 4.4. To this end, let $\epsilon_1 = 0.0001$ and $\epsilon_2 = 0$. In this case, $\mathcal{E}_2 = \{(7,9),(1,4)\}$. Note that

(i) the nodes 1 and 4 belong to the sets $\mathcal{U}_1$ and $\mathcal{X}_2$ (Condition 1 in Theorem 4.4);

(ii) the nodes 7 and 9 belong to the sets $\mathcal{U}_3$ and $\mathcal{C}_1$(or $\mathcal{C}_2$) (Condition 2 in Theorem 4.4),

which means that the negative edge satisfies the conditions of Theorem 4.4. By computing the eigenvalues of the Laplacian matrix of $\mathcal{G}$, it is observed that it has two eigenvalues with negative real parts, while the remaining eigenvalues have positive real parts.

Next, we investigate the statement of Remark 4.5 via choosing $\epsilon_1 = 0$, $\epsilon_2 = 0.0001$ and $\mathcal{E}_2 = \{(3,4),(7,6),(6,5),(4,8)\}$. Note that

(i) the nodes 3 and 4 belong to the sets $\mathcal{U}_2$ and $\mathcal{X}_2$ (Condition 1 in Remark 4.5);

(ii) the nodes 7 and 6 belong to the sets $\mathcal{U}_3$ and $\mathcal{X}_3$ (Condition 1 in Remark 4.5);

(iii) the nodes 6 and 5 belong to the sets $\mathcal{X}_3 \subset \mathcal{R}_3 \backslash \mathcal{U}_3$ and $\mathcal{X}_2 \subset \mathcal{R}_2$ (Condition 2 in Remark 4.5);

(iv) the nodes 4 and 8 belong to the sets $\mathcal{X}_2 \subset \mathcal{R}_2 \backslash \mathcal{U}_2$ and $\mathcal{C}_1 \subset \mathcal{R}_1$ (Condition 2 in Remark 4.5),

which means that the negative edges of the graph depicted in Figure 4.9 meet the conditions outlined in Remark 4.5. By computing the eigenvalues of the Laplacian matrix,

we noticed that all eigenvalues of the Laplacian matrix (excluding the single zero one) have positive real parts, however, their real parts become negative if the absolute values of negative weights are not small. This shows that for these negative edges, knowing that they are negative is not enough to conclude about the sign of real parts of eigenvalues, but their weights also play a role, unlike the one in the first case.

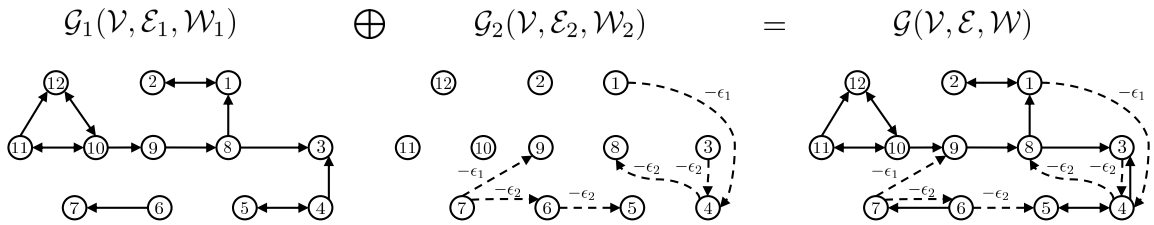

Figure 4.9: A directed signed graph studied in Example 4. The solid arrows represent the positive weight edges while the dashed arrows show the edges with negative weights. For the first case and second case $\epsilon_1 = 0.001, \epsilon_2 = 0$ and $\epsilon_1 = 0, \epsilon_2 = 0.001$, respectively.

4.4 Application in Consensus Protocol

In this section, we elucidate the application of our results to the consensus problem in social networks with antagonistic interactions. The dynamic of the whole network with N node is written as

$$\dot{\mathbf{x}} = -L\mathbf{x}, \tag{4.25}$$

where $\mathbf{x} \in \mathbb{R}^N$, $\mathbf{x} = [x_1 x_2 \dots x_N]^T$ is the stack vector consisting of the state of each node in the network. L is the Laplacian matrix of the network graph. The network achieves consensus, i.e. $\lim_{t\to\infty} \|x_i(t) - x_j(t)\| = 0$ for all $i, j = 1, \dots, N$ and $\mathbf{x}(0) \in \mathbb{R}^N$, if and only if the condition (4.6) holds [97, Lemma 2].

Consider a network with a graph network $\mathcal{G}_1(\mathcal{V},\mathcal{E}_1,\mathcal{W}_1)$ in Example 2. In Example 2, we have shown that the Laplacian matrix L_1 with these values for weights satisfies (4.6), and consequently, the network achieves consensus. We have perturbed the network with negative directed edge $a_{38} = -\delta$. We have pointed out that the eigenvalues of L meet (4.6) if and only if $\delta < 1.94285$.

With the choice of $\delta = 1.5$, the eigenvalues of L satisfy (4.6) and network achieves consensus as shown in Figure 4.10. However, with $\delta = 1.95$, the eigenvalues of L no

longer satisfy (4.6) and network does not achieve consensus as shown in Figure 4.11.

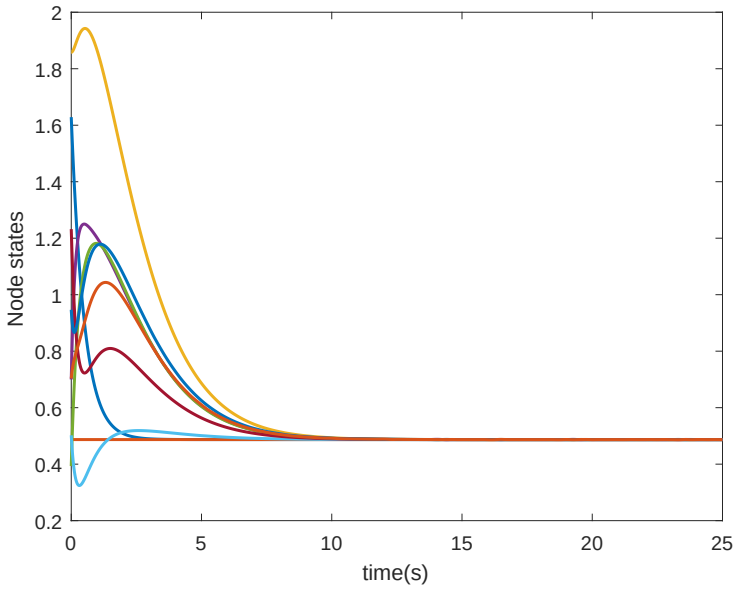

Figure 4.10: Evolution of node states over time for a network with the graph in Example 1. The perturbation between two nodes 3 and 8 set equal to $\delta_{38} = 1.5$.

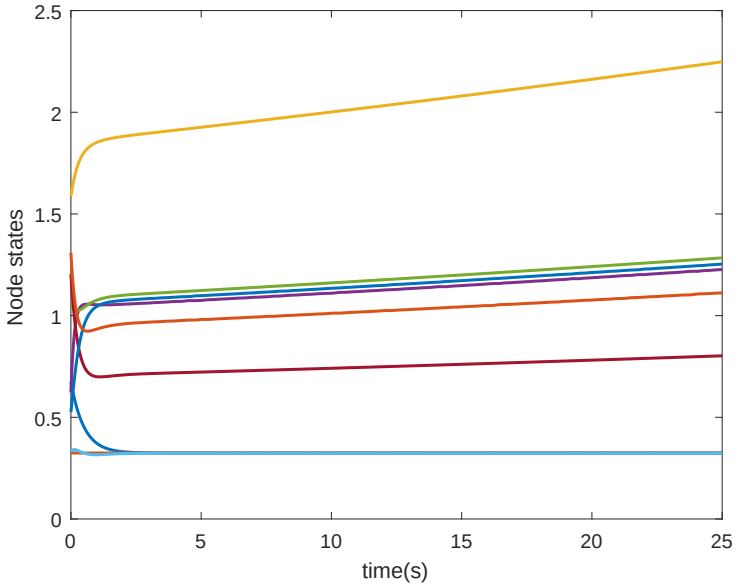

Figure 4.11: Evolution of node states over time for a network with the graph in Example 1. The perturbation between two nodes 3 and 8 set equal to $\delta_{38} = 1.95$.

4.5 Conclusion and Remark on applicability of results on Synchronisation

We analysed the eigenvalues of the Laplacian matrix for a class of directed graphs with positive and negative weights. The first part of this chapter dealt with directed signed graphs where arbitrary negative edges were added between any arbitrary pairs of nodes in the original graphs. Under certain condition, we showed that if the magnitude of that added negative weight violates a computable upper bound, all eigenvalues of the Laplacian matrix (except the single zero eigenvalue) of the original graph have positive real parts (condition (4.6)). We pointed out that, unlike undirected graphs, it appears that effective resistance definition does not apply directly to this case. In the second part, we showed that if the graph is perturbed by adding edge(s) with negative weight(s) to certain nodes, the Laplacian matrix of the perturbed graph has at least one eigenvalue with negative real part.

There are some applications, such as consensus in social network [97] and synchronisation in network of linear oscillators [110], in which condition (4.6) ensures that synchronisation is achieved in the network. Furthermore, the synchronisation disappears if there is at least one eigenvalue of the Laplacian matrix with a negative real part. There are many networks (including networks of neural population) in which the presence/absence of synchronisation are not determined by only the condition (4.6). Our motivation initially was to obtain results that are applicable to a network of neural mass models. However, we were not able find a reasonable neural mass model to which our results can be directly applied. It is still an open problem to analyse these networks with both positive and negative edges.

Chapter 5
Summary and Future Work

5.1 Summary of Thesis

In Chapter 2, we investigated how changes in network structure can lead to pathologic oscillations that occur in the epileptic brain. Specifically, we conducted a bifurcation analysis of a network of two neural mass models, representing two cortical regions, to investigate different aspects of its behaviour with respect to changes in the input and interconnection gains. The bifurcation diagrams, along with simulated EEG time series, exhibited many behaviours in both regions when varying the input, coupling terms, and network structure. We showed that this simple network can generate various oscillatory activities including delta wave activity, which has not been previously reported. Our analysis showed that spike-wave discharges can occur in a cortical region as a result of input changes in the other region, which can have important implications for epilepsy treatment. The bifurcation analysis was related to clinical data in two case studies.

In Chapter 3, we investigated the problem of synchronisation in a network of homogeneous Wilson-Cowan oscillators with diffusive coupling. Such networks can be used to model the behaviour of populations of neurons in cortical tissue, referred to as neural mass models. A new approach was proposed to address conditions for local synchronisation for this type of neural mass models. By analysing the linearised model around a limit cycle, we studied synchronisation within a network with direct coupling. We used both analytical and numerical approaches to link the presence or absence of synchronised behaviour to the location of eigenvalues of the Laplacian matrix. For the analytical part, we applied two-time scale averaging and the Chetaev theorem, while, for the remaining

part, we used a recently proposed numerical approach. Sufficient conditions were established to highlight the effect of network topology on synchronous behaviour when the interconnection is undirected. These conditions were utilised to address points that have been previously reported in the literature through simulations: synchronisation might persist or vanish in the presence of perturbation in the interconnection gains. Simulation results confirmed and illustrated our results.

In Chapter 4, the eigenvalues of the Laplacian matrix for a class of directed graphs with both positive and negative weights were studied. The Laplacian matrix naturally arises in a wide range of applications involving networks. First, a class of directed signed graphs was investigated in which one pair of nodes (either connected or not) is perturbed with negative weights. A necessary condition was proposed to attain the following objective for the perturbed graph: the real parts of the non-zero eigenvalues of its Laplacian matrix are positive. A sufficient condition was also presented that ensures the aforementioned objective for unperturbed graph. It was then highlighted the case where the condition becomes necessary and sufficient. Secondly, for directed graphs, a subset of pairs of nodes was identified where if any of the pairs is connected by an edge with infinitesimal negative weight, the resulting Laplacian matrix will have at least one eigenvalue with negative real part. Illustrative examples were presented to show the applicability of the results.

5.2 Future Work

There are several future directions outlined in the sequel.

Co-dimension 2 Bifurcation Analysis for Heterogeneous Networks

In Chapter 2, the outstanding assumption is that the neural populations are homogeneous. However, the brain can be seen as a network of heterogeneous neural populations. It would be interesting to conduct bifurcation analysis for the case in which one region has seizure-like related parameters (instead of standard values). This analysis would be helpful to understand the mechanism of the seizure propagation between two

regions that could be in different areas. Furthermore, the results can be extended by doing bifurcation analysis with respect to changes in two parameters of the underlying network (co-dimension 2 bifurcation). This may lead new behaviours which were not revealed by our analysis in Chapter 2.

As mentioned in Section 2.8, our estimation approach was conservative, as we estimated the input with other parameters fixed. By estimating more parameters, it may be possible to obtain a more realistic approximation of the true behaviour. However, with more free parameters, it becomes difficult or impossible to relate the estimated parameter trajectories to a bifurcation analysis. Therefore, such an extension can be a potential direction of research for future.

Synchronisation in a Network of Diffusive Wilson-Cowan

As future work, one can study global synchronisation in the network of diffusive Wilson-Cowan using the Lipschitz property of the sigmoid function that converts the average membrane potential into an average pulse density of action potentials. Since the Lipschitz function is also QUAD, it is worthwhile to investigate if the results of [44, 44, 45] could be applied the the synchronisation problem.

Another interesting approach is to extend the method in Chapter 3 to a non-identical network of Wilson-Cowan where the heterogeneity results from variations of parameters in the model; for instance in matrices Y_i, Ξ_i defined by (3.4). It is also worthwhile to follow the same method to study local synchronisation in a network of Jansen and Rit models [76, 133]. This model fits the general model considered in [113], however, the interconnections between nodes in the network of Jansen and Rit models are not diffusive. Developing results for this class of network will be a challenging question.

Eigenvalues of Laplacian Matrix for Directed Signed Graphs

The first part of the results in Chapter 4 considers the situation in which a single pair of nodes is perturbed. However, the perturbation can be applied to multiple pairs of nodes

in general. Recently, the problem has been solved for undirected graphs with an additional assumption restricting the original graph to have only positive weights [34]. This was done using a notion of effective resistance and the methodology was borrowed from electrical circuits. Currently, it is not clear how the problem for directed graphs can be linked to electrical circuits. Either extending the proof technique of Chapter 4 or finding a corresponding electrical circuit for directed graphs are interesting future directions, yet extremely challenging.

Another possible extension of our result is to investigate the case mentioned in 4.5. Through many examples, it was observed that the Laplacian matrix of perturbed graph has no eigenvalue with non-positive real part for sufficiently small ϵ. However, this is not the situation for the case in Theorem 4.4. We also observed that for both cases the Laplacian matrix of perturbed graph has at least an eigenvalue with non-positive real part if ϵ is increased. These observations are worthwhile to be explored further.

Synchronisation in Networks with Positive and negative Feedbacks

It is mentioned in Chapter 1 that passivity and counterclockwise property are used for systems with negative and positive feedback, respectively. There are mathematical models such as Janesn-Rit model that have both positive and negative interconnections in their dynamic. Hence, it is worthwhile to find a concept which can be used to analyse these systems (perhaps by combining these two concepts). Then, it may be possible to start analysing synchronisation in networks which have both positive and negative feedbacks.

Appendix A

Supplementary Materials For Chapter 2

A.1 Jacobian matrix of the network of Jansen-Rit in (2.4)

The jacobian matrix of the network of Jansen-Rit with two regions (2.4) is as follows:

$$J = \begin{bmatrix} J_{11} & J_{12} \\ J_{21} & J_{22} \end{bmatrix} \tag{A.1}$$

where

$$J_{jj} = \begin{bmatrix} 0 & 1 & 0 & 0 & 0 & 0 & 0 & 0 \\ -\zeta_e^{j\,2} & -2\zeta_e^j & \alpha_e^j\zeta_e^j h(v_1^j - v_2^j) & 0 & -\alpha_e^j\zeta_e^j h(v_1^j - v_2^j) & 0 & 0 & 0 \\ 0 & 0 & 0 & 1 & 0 & 0 & 0 & 0 \\ \alpha_e^j\zeta_e^j c_{ep}^j c_{pe}^j h(c_{pe}^j v_0^j) & 0 & -\zeta_e^{j\,2} & -2\zeta_e^j & 0 & 0 & 0 & 0 \\ 0 & 0 & 0 & 0 & 0 & 1 & 0 & 0 \\ \alpha_i^j\zeta_i^j c_{ip}^j c_{pi}^j h(c_{pi}^j v_0^j) & 0 & 0 & 0 & -\zeta_i^{j\,2} & -2\zeta_i^j & 0 & 0 \\ 0 & 0 & 0 & 0 & 0 & 0 & 0 & 1 \\ 0 & 0 & \alpha_e^j\zeta_d^j h(v_1^j - v_2^j) & 0 & -\alpha_e^j\zeta_d^j h(v_1^j - v_2^j) & 0 & -\zeta_d^{j\,2} & -2\zeta_d^j \end{bmatrix}, \tag{A.2}$$

and $h(v) = \frac{2e_0 r\ exp(r(v_{th}-v))}{(1+\exp(r(v_{th}-v)))^2}$ for j=1,2. Furthermore, the matrices J_{jl} for $j \neq l$ are defined as

$$J_{jl} = \begin{bmatrix} 0 & 0 & 0 & 0 & 0 & 0 & 0 & 0 \\ 0 & 0 & 0 & 0 & 0 & 0 & 0 & 0 \\ 0 & 0 & 0 & 0 & 0 & 0 & 0 & 0 \\ 0 & 0 & 0 & 0 & 0 & 0 & \alpha_e^j \zeta_e^j K^{j,l} & 0 \\ 0 & 0 & 0 & 0 & 0 & 0 & 0 & 0 \\ 0 & 0 & 0 & 0 & 0 & 0 & 0 & 0 \\ 0 & 0 & 0 & 0 & 0 & 0 & 0 & 0 \\ 0 & 0 & 0 & 0 & 0 & 0 & 0 & 0 \end{bmatrix}. \tag{A.3}$$

A.2 Detection of a saddle-node homoclinic bifurcation

A homoclinic orbit is a trajectory connecting a hyperbolic equilibrium (saddle node) to itself. There is no general method to find and identify a limit cycle; however, it is possible to compute it using the continuation procedure provided in the MATCONT package [64]. In order to check if the bifurcation is saddle-node homoclinic, the period of oscillation versus the bifurcation parameters is usually plotted (it is depicted for case I with connection gain 25 in Figure A.1). As the bifurcation parameter p approaches the bifurcation point, the period of oscillation is eventually increased which means that the cycle is born from this point.

A.3 Notes on Equilibria for Case II

As pointed out in Sections 2.3 and 2.5, the equilibria for the second case are obtained from (2.5), (2.6), and (2.7) with $u^b = 0$. In this case, (2.7) can be written as follows ($K^{ab} = K^{ba} = K$):

$$\begin{aligned} y^a &= \frac{\alpha_e}{\zeta_e} c_{ep} g\left(\frac{\alpha_e}{\zeta_e} c_{pe} g\left(y^a\right)\right) - \frac{\alpha_i}{\zeta_i} c_{ip} g\left(\frac{\alpha_e}{\zeta_e} c_{pi} g\left(y^a\right)\right) + \tilde{P}^a \\ y^b &= \frac{\alpha_e}{\zeta_e} c_{ep} g\left(\frac{\alpha_e}{\zeta_e} c_{pe} g\left(y^b\right)\right) - \frac{\alpha_i}{\zeta_i} c_{ip} g\left(\frac{\alpha_e}{\zeta_e} c_{pi} g\left(y^b\right)\right) + \tilde{P}^b, \end{aligned} \tag{A.4}$$

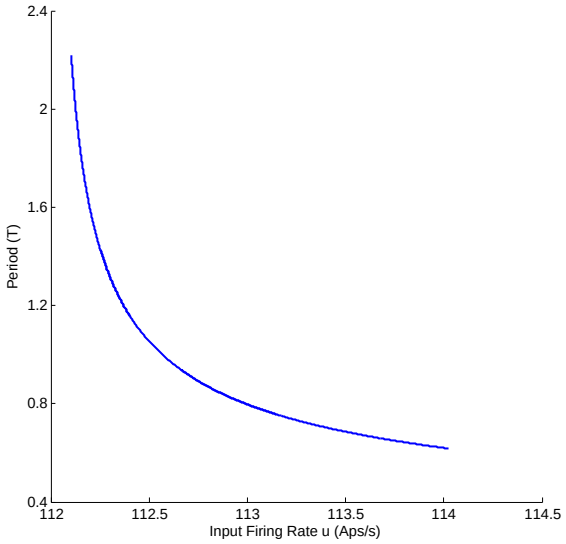

Figure A.1: Detecting a saddle-node homoclinic bifurcation. The period of oscillation versus the bifurcation parameter p. The period eventually increases when the value of p approaches to the point at which saddle-node bifurcation occurs.

where

$$\begin{aligned} \tilde{u}^a &= \frac{\alpha_e}{\zeta_e} u^a + \frac{\alpha_e^2}{\zeta_e \zeta_d} K g(y^b) \\ \tilde{u}^b &= \frac{\alpha_e^2}{\zeta_e \zeta_d} K g(y^a). \end{aligned} \tag{A.5}$$

This implies that finding the equilibria of the whole network is equivalent to finding the equilibria of each single region when the input of each region are defined by (A.5).

We first claim that, the equilibria of region a are affected significantly by changing u^a rather than changing the values of K while the equilibria of region b are affected significantly by variations of K. Since the sigmoid function satisfies $g(\cdot) \leq 2e_0$, the following inequalities are obtained from (A.5):

$$\begin{aligned} \tilde{u}^a &\leq \frac{\alpha_e}{\zeta_e} u^a + \frac{2e_0 \alpha_e^2}{\zeta_a \zeta_d} K \\ \tilde{u}^b &\leq \frac{2e_0 \alpha_e^2}{\zeta_a \zeta_d} K. \end{aligned} \tag{A.6}$$

For typical values of e_0, α_e, ζ_a, and ζ_d (see Table 2.1), the value of $\frac{2e_0\alpha_e^2}{\zeta_a\zeta_d}$ is on the order of 10^{-2} and, consequently, the variation of $\frac{2e_0\alpha_e^2}{\zeta_a\zeta_d}K$ is much smaller than the variation of

u even for large values of k. Hence, y^a and, consequently, the equilibria of region a are not affected significantly by feedback from region b due to the small interaction term $\frac{\alpha_e^2}{\zeta_e\zeta_d}Kg(y^b)$; however, the equilibria of region b are significantly affected by the output of region a.

In order to find the equilibria, we used a numerical approach to find all values for y^a and y^b which satisfy (A.4) and (A.5) for different values of u^a and K. To do so, we varied the value of $y^b \in (-20, 20)$ and calculated the value of y^a from the second equation in (A.4), i.e. from solving the equation,

$$g\left(y^a\right) = \underbrace{\frac{\zeta_e\zeta_d}{K\alpha_e^2}\left(y^b - \frac{\alpha_e}{\zeta_e}c_{ep}g\left(\frac{\alpha_e}{\zeta_e}c_{pe}g\left(y^b\right)\right) + \frac{\alpha_i}{\zeta_i}c_{ip}g\left(\frac{\alpha_e}{\zeta_e}c_{pi}g\left(y^b\right)\right)\right)}_{\Upsilon(y^b,K)}. \tag{A.7}$$

By knowing the value of y^a and y^b, the associated value u^a was obtained from the first equation in (A.4), which can be rewritten as,

$$u^a = \frac{\zeta_e}{\alpha_e}\left(\frac{\alpha_e}{\zeta_e}c_{ep}g\left(\frac{\alpha_e}{\zeta_e}c_{pe}g\left(y^a\right)\right) - \frac{\alpha_i}{\zeta_i}c_{ip}g\left(\frac{\alpha_e}{\zeta_e}c_{pi}g\left(y^a\right)\right) + \frac{\alpha_e^2}{\zeta_e\zeta_d}Kg(y^b) - y^a\right). \tag{A.8}$$

Since $g(v)$ is an strictly increasing function and $0 \le g(v) \le 2e_0$, (A.7) has a solution if and only if

$$0 \le \Upsilon(y^b, K) \le 2e_0. \tag{A.9}$$

Among all values of $y^b \in (-20, 20)$, the acceptable ones are those that satisfy (A.9). As a consequence, some values in the interval $y_b \in (-20, 20)$ may not be equilibria. For typical values of e_0, α_e, ζ_a, and ζ_d (see Table 2.1), we plotted $\Upsilon(y^b, K)$ for $y^b \in (-30, 30)$ and different values of K in Figure A.2. This figure indicate that the inequality (A.9) cannot be satisfied fur sufficiently large and small values of y^b that means that there exist no equilibria for those values of y^b. From the magnified part of the figure, it is observed that, for all values of K, there is no equilibrium point for $y^b \in (4.57, 6.07)$. Furthermore, the underlying network has equilibria for all values for $y^b \in (-1.9, 4.57)$ if $K = 250, 300$. However, this is not the case for other values of K. This indicates that the second region

has three branches of equilibria that do not intersect for $K = 50, 100, 150, 200$. This point can be seen from Figure A.3. The lower and middle branches join up as the coupling gain is increased (for $K = 250, 300$), which leads to the appearance of a saddle-node in the bifurcation diagram of the system. Hence, for the second case, we studied the bifurcation diagram for interconnection gains $K = 50, 250$.

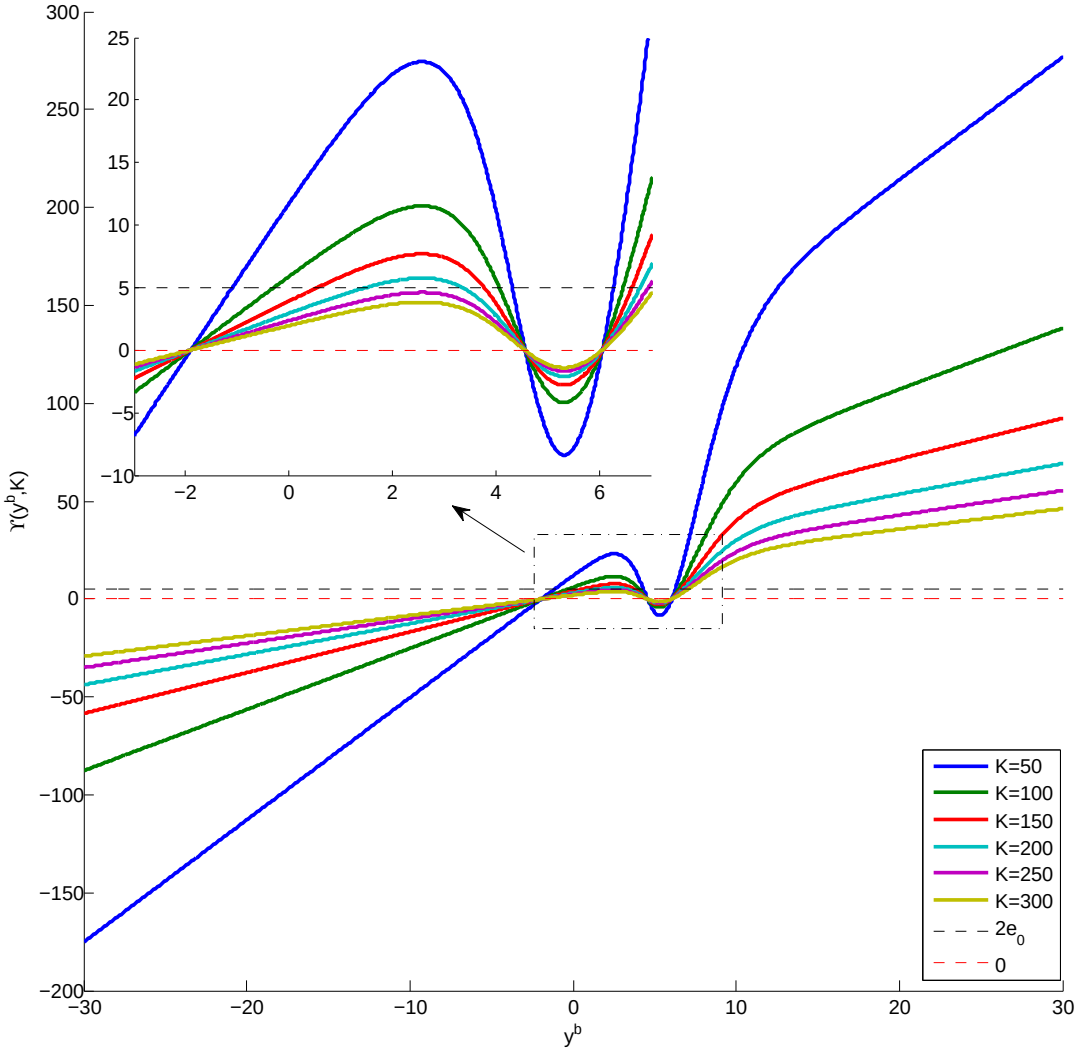

Figure A.2: The values of $\Upsilon(y^b, K)$ defined in A.7 for different values of coupling gain K.

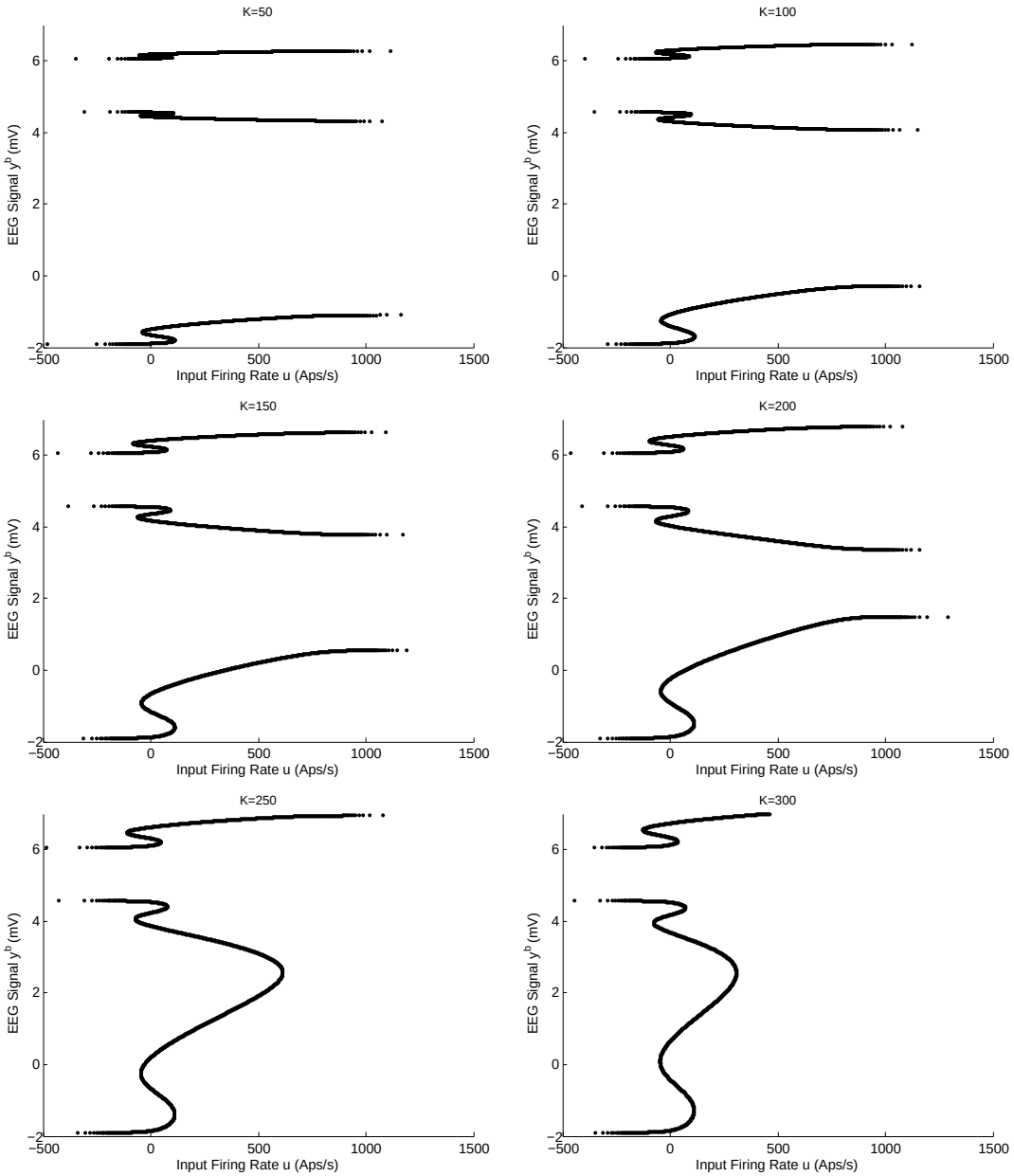

Figure A.3: Equilibria of second region for case II and for different values of coupling gain K.

A.4 Estimation Method

A.4.1 Augmented Model of a Cortical Region

The model of a cortical region Eq. (2.1) can be written in the form

$$\dot{\mathbf{x}} = \mathbf{A}\mathbf{x} + \mathbf{B}\vec{\phi}\,(\mathbf{C}\mathbf{x})\,, \tag{A.10}$$

where $\mathbf{x} \in \mathbb{R}^{N_x}$ is a state vector representing the postsynaptic membrane potentials generated by each population synapse and their time derivatives. There are two states per synapse and $N_x = 2N_s$ is the total number of states, where for N_s synaptic connections in the models the state vector is of the form

$$\mathbf{x} = \begin{bmatrix} v_1 & z_1 & \cdots & v_{N_s} & z_{N_s} \end{bmatrix}^\mathsf{T}.$$

The matrix $\mathbf{A}$ encodes the dynamics induced by the membrane time constants. For N synapses, $\mathbf{A}$ has the block diagonal structure

$$\mathbf{A} = \operatorname{diag}\begin{pmatrix} \boldsymbol{\Psi}_1 & \cdots & \boldsymbol{\Psi}_N \end{pmatrix},$$

where

$$\boldsymbol{\Psi}_n = \begin{bmatrix} 0 & 1 \\ -\zeta_n^2 & -2\zeta_n \end{bmatrix}.$$

The matrix of synaptic gains from internal inputs, $\mathbf{B}$, has the diagonal form

$$\mathbf{B} = \operatorname{diag}\begin{pmatrix} 0 & \alpha_1 & \cdots & 0 & \alpha_{N_s} \end{pmatrix}.$$

The vector function $\phi(\cdot)$ has the following form

$$\vec{\phi}\,(\mathbf{C}\mathbf{x}) = \begin{bmatrix} 0 & g\,(\mathbf{c}_{2,:}\mathbf{x}) & \cdots & 0 & g\,(\mathbf{c}_{N_x-2,:}\mathbf{x}) & 0 & u \end{bmatrix}^\mathsf{T}. \tag{A.11}$$

The adjacency matrix, $\mathbf{C}$, defines the connectivity structure of the model. It is a ma-

trix of zeros or ones that specifies all the connections between the cell population types (excluding external inputs) that has the block structure

$$\mathbf{C} = \begin{bmatrix} 0 & 0 & \cdots & 0 & 0 \\ \mathbf{c}_{2,1} & 0 & & \mathbf{c}_{2,N_x-1} & 0 \\ \vdots & & \ddots & & \vdots \\ 0 & 0 & & 0 & 0 \\ \mathbf{c}_{N_x,1} & 0 & & \mathbf{c}_{N_x,N_x-1} & 0 \end{bmatrix}.$$

For example, if the PSPs from synapses 1 and 2 are summed and transformed by the sigmoid to give the input firing rate to synapse n, then row $2n$ of $\mathbf{C}$ with have the form

$$\mathbf{c}_{2n,:} = \begin{bmatrix} 1 & 0 & 1 & 0 & 0 & 0 & \cdots & 0 & 0 \end{bmatrix}.$$

It is necessary to discretise the model to numerically integrate the equations and run simulations. The discrete time version of the model is

$$\mathbf{x}_{t+1} = \mathbf{A}^{\delta}\mathbf{x}_t + \mathbf{B}^{\delta}\vec{\phi}\left(\mathbf{C}\mathbf{x}_t\right) + \mathbf{w}_t. \tag{A.12}$$

The matrices $\mathbf{A}^{\delta}$ and $\mathbf{B}^{\delta}$ are discrete time versions of $\mathbf{A}$ and $\mathbf{B}$, respectively, and are defined in [58]. For ease of notation, we shall abbreviate increments or decrements in time (by the integration time step) by $t+1$ or $t-1$, respectively. The additional term $\mathbf{w}_t$ models uncertainty in the system for estimation purposes.

The neural mass model is mapped to electrophysiological measurements by the observation equation

$$\mathbf{y}_t = \mathbf{H}\mathbf{x}_t + \mathbf{v}_t, \tag{A.13}$$

where $\mathbf{H} \in \mathbb{R}^{N_x \times N_y}$ is the observation matrix, $\mathbf{v} \sim \mathcal{N}(0, \mathbf{R}) \in \mathbb{R}^{N_y}$ is the observation noise, and N_y is the number of observations.

A.4.2 Re-parametrization for Model for Inversion

To estimate the input within our framework, we assume that it is varying on a time scale much slower than the state variables (v and z). Following this assumption we can reduce the model dimension since

$$v_{p3} = \text{constant} = \tilde{u} \approx \alpha_{xu} c_{xu} \zeta_{xu}^2 \frac{u}{\zeta_{xu}^2}, \tag{A.14}$$

in the steady state limit. A further modification for model inversion induces a new parameter, λ, to deal with DC offsets on the EEG signals due to electrode-tissue interactions. The offset parameter is added to the post-synaptic potential at the excitatory to pyramidal connection Eq. (2.1),

$$v_{p1} = z_{p1} + \lambda, \tag{A.15}$$

but removed from it where it feeds back to the system in the sigmoidal activation function. This way the system dynamics are unaffected by this addition, but the observation is offset by λ (since v_{p1} contributes to the EEG). The additional parameter enables us to estimate a slowly (with respect to the sate variables) changing DC offset in real data. We also modify the form of the activation function $g(\cdot)$ to

$$g(v) \approx \tilde{g}(v) = \frac{1}{2}\left(\text{erf}\left(\frac{v - v_0}{\varsigma}\right) + 1\right), \tag{A.16}$$

where $\varsigma = 1.699/r$. The function $\tilde{g}(\cdot)$ enables exact propagation of Gaussian variables through time in the estimation method. It only differs from $g(\cdot)$ slightly at the turning points of the sigmoid and does not change the dynamics of the system significantly.

The modified vectorized activation function has the following form

$$\tilde{\vec{\phi}}(\mathbf{Cx}) = \left[0 \quad \tilde{g}(\mathbf{c}_{2,:}\mathbf{x} + \tilde{u} - \lambda) \quad 0 \quad \tilde{g}(\mathbf{c}_{4,:}\mathbf{x} + \tilde{u} - \lambda) \quad \cdots \quad 0 \quad \tilde{g}\left(\mathbf{c}_{\tilde{N}_x - 2,:}\mathbf{x}\right)\right]^\top, \tag{A.17}$$

where $\tilde{N}_x = N_x - 2$ (from the input modification).

Any neural mass model with an arbitrary number of populations can be written in the

form described above, including the model of the two coupled regions that we employ in Chapter 2. It is straight forward to construct the matrices **A**, **B** and **C**, therefore for the sake of conciseness, we leave the basic form of the state-space model here.

A.4.3 Augmentation for Model for Inversion

In order to perform online joint state and parameter estimation we augment the model and concatenate the inputs and measurement offsets to the state vector. To define to the augmented model we first define a vector of parameters as

$$\boldsymbol{\theta} = \begin{bmatrix} u^a & u^b & \lambda^a & \lambda^b \end{bmatrix}^\top.$$

The trivial dynamics for the parameter are model as

$$\dot{\boldsymbol{\theta}} = 0, \tag{A.18}$$

or in discrete time as

$$\boldsymbol{\theta}_{t+1} = \boldsymbol{\theta}_t. \tag{A.19}$$

The state vector $\mathbf{x}$ and the parameter vector $\boldsymbol{\theta}$ are concatenated to form the augmented state vector

$$\boldsymbol{\xi} = \begin{bmatrix} \mathbf{x}^T & \boldsymbol{\theta}^T \end{bmatrix}^\top. \tag{A.20}$$

Our augmented state-space model is

$$\boldsymbol{\xi}_t = \mathbf{A}_\theta \boldsymbol{\xi}_{t-1} + \mathbf{B}_\theta \phi(\mathbf{C}_\theta \boldsymbol{\xi}_{t-1}) + \mathbf{w}_{t-1}, \tag{A.21}$$

where $\mathbf{w}_t \sim \mathcal{N}(0, \mathbf{Q})$. The state vector $\boldsymbol{\xi} \in \mathbb{R}^{N_\xi \times 1}$ and matrices $\mathbf{A}_\theta$, $\mathbf{B}_\theta$, and $\mathbf{C}_\theta$ are $\in \mathbb{R}^{N_\xi \times N_\xi}$

and have the form

$$\mathbf{A}_\theta = \begin{bmatrix} \mathbf{A}_\delta & \mathbf{0} \\ \mathbf{0} & \mathbf{I} \end{bmatrix}, \mathbf{B}_\theta = \begin{bmatrix} \mathbf{B} & \mathbf{0} \\ \mathbf{0} & \mathbf{0} \end{bmatrix}, \mathbf{C}_\theta = \begin{bmatrix} \mathbf{C} & \mathbf{0} \\ \mathbf{0} & \mathbf{0} \end{bmatrix}. \tag{A.22}$$

To make the next step a little easier we will simplify the notation by dropping the subscript θ on the system matrices and abbreviate the activation function giving

$$\boldsymbol{\xi}_t = \mathbf{A}\boldsymbol{\xi}_{t-1} + \mathbf{B}\phi(\mathbf{C}\boldsymbol{\xi}_{t-1}) + \mathbf{w}_{t-1}. \tag{A.23}$$

A.4.4 A Filter for the Population Model

The filter provides an estimate of the most likely sequences of states, $\hat{\boldsymbol{\xi}}_t^+$, and the associated error covariances, $\hat{\mathbf{P}}_t^+$, given (uncertain) knowledge of the biophysics and anatomy of the brain regions of interest combined with the noisy EEG measurements, $\mathbf{y}_t$. The method is based on the Kalman filter [80], but falls in the category of an assumed density filter (using a Gaussian prior). The optimal state estimates can be formally stated using the expectations

$$\hat{\boldsymbol{\xi}}_t^+ = \mathbb{E}\left[\boldsymbol{\xi}_t | \mathbf{y}_1, \mathbf{y}_2, \cdots, \mathbf{y}_t\right], \tag{A.24}$$

$$\hat{\mathbf{P}}_t^+ = \mathbb{E}\left[\left(\boldsymbol{\xi}_t - \hat{\boldsymbol{\xi}}_t^+\right)\left(\boldsymbol{\xi}_t - \hat{\boldsymbol{\xi}}_t^+\right)^\top\right], \tag{A.25}$$

which are known as the a posteriori state estimate and state estimate covariance, respectively. The a posteriori state estimate is computed by correcting the a priori state estimate, which is a prediction though our model and defined as [58]

$$\begin{aligned} \hat{\boldsymbol{\xi}}_t^- &= \mathbb{E}\left[\boldsymbol{\xi}_t | \mathbf{y}_1, \mathbf{y}_2, \cdots, \mathbf{y}_{t-1}\right] \\ &= \mathbb{E}\left[\mathbf{A}\boldsymbol{\xi}_{t-1} + \mathbf{B}\phi(\boldsymbol{\xi}_{t-1}) + \mathbf{w}_t\right] \\ &= \mathbf{A}\hat{\boldsymbol{\xi}}_{t-1}^+ + \mathbf{B}\hat{\boldsymbol{\phi}}_{t-1}, \end{aligned} \tag{A.26}$$

where the vectors (note the square root is element-wise and $\circ$ is the Hadamard product)

$$\begin{aligned}\hat{\boldsymbol{\phi}}_{t-1} =& \frac{1}{2}\left(\operatorname{erf}\left(\boldsymbol{\beta} \circ \boldsymbol{\sigma}^{-1/2}\right) + 1\right),\\ \boldsymbol{\beta}_t =& \mathbf{C}\hat{\boldsymbol{\xi}}_{t-1}^{+} - v_0,\\ \boldsymbol{\sigma}_t =& 2\left(\operatorname{diag}\left(\mathbf{C}\mathbf{P}_{t-1}^{+}\mathbf{C}^{\top}\right) + \varsigma^2\right).\end{aligned} \tag{A.27}$$

The a posteriori state estimate is calculated using a weighted difference between an uncertain prediction of the observations (EEG) and the actual noisy measurements

$$\hat{\boldsymbol{\xi}}_t^{+} = \hat{\boldsymbol{\xi}}_t^{-} + \mathcal{K}_t \underbrace{\left(\mathbf{y}_t - \mathbf{H}\hat{\boldsymbol{\xi}}_t^{-}\right)}_{\text{EEG prediction error}}. \tag{A.28}$$

The weighting to correct the a priori augmented state estimate, $\mathcal{K}_t$, is known as the Kalman gain. The Kalman gain is computed from the confidence in a prediction of the augmented state and the noisy measurement model by

$$\mathcal{K}_t = \hat{\mathbf{P}}_t^{-}\mathbf{H}^{\top}\left(\mathbf{H}\hat{\mathbf{P}}_t^{-}\mathbf{H}^{\top} + \kappa_t\mathbf{R}\right)^{-1}, \tag{A.29}$$

where κ_t is an annealing parameter. The annealing schedule is

$$\kappa_t = \kappa_0^{\frac{t_a - t}{t_a - 1}}, \tag{A.30}$$

and κ_0 is a larger number. Following this schedule the annealing parameter will decrease from κ_0 to 1 following a geometric series. When the annealing parameter is high, the Kalman gain is small and the measurements are not full utilized. The annealing has the effect of slowly introducing corrections from the measurements on initialization, avoiding taking large steps towards local minima when our initial uncertainty is high. The a priori state estimate error covariance is

$$\begin{aligned}\hat{\mathbf{P}}_t^{-} =& \mathbb{E}\left[\left(\boldsymbol{\xi}_t - \hat{\boldsymbol{\xi}}_t^{-}\right)\left(\boldsymbol{\xi}_t - \hat{\boldsymbol{\xi}}_t^{-}\right)^{\top}\right]\\ =& \mathbb{E}\left[\left(\mathbf{A}\boldsymbol{\xi}_{t-1} + \mathbf{B}\phi(\mathbf{C}\boldsymbol{\xi}_{t-1}) + \mathbf{w}_{t-1} - \left(\mathbf{A}\hat{\boldsymbol{\xi}}_{t-1}^{+} + \mathbf{B}\hat{\boldsymbol{\phi}}_{t-1}\right)\right)(\cdot)^{\top}\right]\end{aligned}$$

$$= \mathbf{A}\hat{\mathbf{P}}_{t-1}^{+}\mathbf{A}^{\top} + \mathbf{B}\mathbb{E}\left[\phi(\boldsymbol{\xi}_{t-1})\phi^{\top}(\boldsymbol{\xi}_{t-1})\right]\mathbf{B}^{\top} + \mathbf{Q} - \mathbf{B}\hat{\boldsymbol{\phi}}_{t-1}\hat{\boldsymbol{\phi}}_{t-1}^{\top}\mathbf{B}^{\top} + \boldsymbol{\Phi}_{t-1} + \boldsymbol{\Phi}_{t-1}^{\top}, \tag{A.31}$$

where

$$\begin{aligned}\boldsymbol{\Phi}_{t-1} =& \mathbf{A}\mathbb{E}\left[\boldsymbol{\xi}_{t-1}\phi^{\top}(\mathbf{C}\boldsymbol{\xi}_{t-1})\right]\mathbf{B}^{\top} - \mathbf{A}\hat{\boldsymbol{\xi}}_{t-1}^{+}\mathbb{E}\left[\boldsymbol{\phi}^{\top}(\mathbf{C}\boldsymbol{\xi}_{t-1})\right]\mathbf{B}^{\top} \\ =& \mathbf{A}\left(\mathbf{P}_{t-1}^{+}\mathbf{C}^{\top} \circ \mathbf{1} \times \boldsymbol{\Lambda}^{\top}\right)\mathbf{B}^{\top},\end{aligned} \tag{A.32}$$

with $\boldsymbol{\Lambda} = (\pi\boldsymbol{\sigma})^{-1/2}\exp\left(-\boldsymbol{\beta} \circ \boldsymbol{\beta} \circ \boldsymbol{\sigma}^{-1}\right)$. We can analytically calculate all the elements of $\hat{\mathbf{P}}_{t}^{-}$ except for $\mathbb{E}\left[\phi(\boldsymbol{\xi}_{t-1})\phi^{\top}(\boldsymbol{\xi}_{t-1})\right]$, which is known to have no analytic solution. Nevertheless, we can compute a precise solution (to error of 10^{-14}) as explained in [61]. The elements, indexed by i and j, of the matrix resulting from evaluating the expectation are equivalent to the probabilities of the bivariate Gaussians

$$\mathbb{E}\left[\boldsymbol{\phi}\left(\mathbf{C}\boldsymbol{\xi}_{t-1}\right)\boldsymbol{\phi}^{\top}\left(\mathbf{C}\boldsymbol{\xi}_{t-1}\right)\right]_{ij} = P\left(x > 0, y > 0\right), \tag{A.33}$$

where $(x, y)^{\top} \sim \mathcal{N}(\boldsymbol{\mu}, \boldsymbol{\Sigma})$ and

$$\begin{aligned}\boldsymbol{\mu} &= -\left[\left(\mathbf{C}\hat{\boldsymbol{\xi}}_{t-1}^{+}\right)_{i}, \left(\mathbf{C}\hat{\boldsymbol{\xi}}_{t-1}^{+}\right)_{j}\right]^{\top}, \\ \boldsymbol{\Sigma} &= \begin{bmatrix}\left(\operatorname{diag}\left(\mathbf{C}\hat{\mathbf{P}}_{t-1}^{+}\mathbf{C}^{\top}\right) + \varsigma^{2}\right)_{i} & \left(\mathbf{C}\hat{\mathbf{P}}_{t-1}^{+}\mathbf{C}^{\top}\right)_{ij} \\ \left(\mathbf{C}\hat{\mathbf{P}}_{t-1}^{+}\mathbf{C}^{\top}\right)_{ij} & \left(\operatorname{diag}\left(\mathbf{C}\hat{\mathbf{P}}_{t-1}^{+}\mathbf{C}^{\top}\right) + \varsigma^{2}\right)_{j}\end{bmatrix}.\end{aligned}$$

These probabilities can be computed easily in Matlab using `mvncdf`, where each element is `mvncdf` $(\mathbf{0}, \boldsymbol{\mu}, \boldsymbol{\Sigma})$. For a linear observation function, the a posteriori covariance is then updated by using the Kalman gain to provide the correction

$$\hat{\mathbf{P}}_{t}^{+} = \left(\mathbf{I} - \mathcal{K}_{t}\mathbf{H}\right)\hat{\mathbf{P}}_{t}^{-}. \tag{A.34}$$

Practically, the actual state is not known so the Kalman filter must be initialised with the best guess for $\hat{\boldsymbol{\xi}}_{0}^{+}$ and $\hat{\mathbf{P}}_{0}^{+}$, which provides the posteriori state estimate and state estimate covariance for time $t = 0$. The other parameters that must be initialised are $\mathbf{Q}$ and $\mathbf{R}$.

Appendix B

Instability Lemma in the Proof of Proposition 3.1

B.1 Instability Using Two-Time Averaging

Lemma B.1. *(Instability Using Two-Time Averaging). Consider the linear time-varying system described by the state space model*

$$\begin{bmatrix} \dot{\hat{s}}_i \\ \dot{\hat{r}}_i \end{bmatrix} = \left(\begin{bmatrix} \mathbf{0} & \mathbf{0} \\ \mathbf{0} & H \end{bmatrix} - \epsilon \begin{bmatrix} \top_{11}(t) & \top_{12}(t) \\ \top_{21}(t) & \top_{22}(t) \end{bmatrix} \right) \begin{bmatrix} \hat{s}_i \\ \hat{r}_i \end{bmatrix} - (-1)^i \beta \begin{bmatrix} \top_{11}(t) & \top_{12}(t) \\ \top_{21}(t) & \top_{22}(t) \end{bmatrix} \begin{bmatrix} \hat{s}_{3-i} \\ \hat{r}_{3-i} \end{bmatrix}, \tag{B.1}$$

where $\hat{s} \in \mathbb{R}^p$ and $\hat{r} \in \mathbb{R}^q$. Assume that $\top_{ij}(t)$, $i,j = 1,2$ are T-periodic, piecewise, continuous functions bounded by the scalar $\iota_{ij} > 0$, i.e. $|\top_{ij}(t)| \leq \iota_{ij}$ for all $t \geq 0$. Now consider the average system described by

$$\dot{\hat{s}} = -\epsilon \bar{\top}_{11} \hat{s} \ , \ \ \bar{\top}_{11} = \frac{1}{T} \int_0^T \top_{11}(\tau) d\tau. \tag{B.2}$$

If $\bar{\top}_{11}$ and H are Hurwitz, then there exists ϵ^* and $\psi : [0, \epsilon^*] \to \mathbb{R}_{\geq 0}$ such that for every $\epsilon \in (0, \epsilon^*)$ and a corresponding $\beta \in [0, \psi(\epsilon)]$, the origin of system (B.1) is unstable.

Proof. Similar to [108,113], we change the coordinate of the system by defining a new state $\check{s}$ as

$$\hat{s} \triangleq \mathfrak{H} \check{s} = \left[I - \epsilon \int_0^t (\top_{11}(\tau) - \bar{\top}_{11}) d\tau \right] \check{s}. \tag{B.3}$$

Note that since $|\int_0^T (\top_{11}(\tau) - \bar{\top}_{11}) d\tau| \leq 2T\iota_{11}$, if $\epsilon < \epsilon_1 \triangleq \frac{1}{2T\iota_{11}}$, then the inverse of $\mathfrak{H}$ exists and, therefore, $|\mathfrak{H}^{-1}| \leq \gamma = \frac{1}{1-2\epsilon_1 T\iota_{11}}$. In this case, the original system (B.1) is

represented in the new coordinates as

$$\begin{bmatrix} \check{s}_i \\ \hat{r}_i \end{bmatrix} = \left(\begin{bmatrix} \mathbf{0} & \mathbf{0} \\ \mathbf{0} & H \end{bmatrix} - \alpha \begin{bmatrix} \mathfrak{M}_{11}(t) & \mathfrak{M}_{12}(t) \\ \mathfrak{M}_{21}(t) & \mathfrak{M}_{22}(t) \end{bmatrix} \right) \begin{bmatrix} \check{s}_i \\ \hat{r}_i \end{bmatrix} - (-1)^i \beta \begin{bmatrix} \mathfrak{Q}_{11}(t) & \mathfrak{Q}_{12}(t) \\ \mathfrak{Q}_{21}(t) & \mathfrak{Q}_{22}(t) \end{bmatrix} \begin{bmatrix} \hat{s}_{3-i} \\ \hat{r}_{3-i} \end{bmatrix}, \tag{B.4}$$

where

$$\begin{aligned} \mathfrak{M}_{11} &= \mathfrak{H}^{-1} \urcorner_{11}(t) \mathfrak{H} + \mathfrak{H}^{-1} (\bar{\urcorner}_{11} - \urcorner_{11}(t)) \\ \mathfrak{Q}_{11} &= \mathfrak{H}^{-1} \urcorner_{11}(t) \mathfrak{H} \ , \ \mathfrak{M}_{12} = \mathfrak{Q}_{12} = \mathfrak{H}^{-1} \urcorner_{12}(t) \\ \mathfrak{M}_{21} &= \mathfrak{Q}_{21} = \urcorner_{21}(t) \mathfrak{H} \ , \ \mathfrak{M}_{22} = \mathfrak{Q}_{22} = \urcorner_{22}(t), \end{aligned} \tag{B.5}$$

Since the matrices $\bar{\urcorner}_{11}$ and H are Hurwitz, there exist positive definite matrices P_s and P_r such that $P_s \bar{\urcorner}_{11} + \bar{\urcorner}_{11}^T P_s = -I$ and $P_r H + H^T P_r = -I$. Now, define the Lyapunov function as $V = \sum_{i=1}^{2} \check{s}_i^T P_s \check{s}_i - \hat{r}_i^T P_r \hat{r}_i$. Taking the derivative of the Lyapunov function leads to

$$\begin{aligned} \dot{V} \geq & (\epsilon\gamma - 4T\epsilon^2 \gamma \iota_{11}^2 |P_s|) |\check{s}_1|^2 - 4\epsilon\gamma\iota_{12} |P_r| |\check{s}_1| |\hat{r}_1| \\ & + (1 - 2\epsilon\iota_{22} |P_r|) |\hat{r}_1|^2 - 2\epsilon\iota_{21} (1 + 2\epsilon T \iota_{11}) |P_r| |\hat{r}_1| |\check{s}_1| \\ & + (\epsilon\gamma - 4T\epsilon^2 \gamma \iota_{11}^2 |P_s|) |\check{s}_2|^2 - 4\epsilon\gamma\iota_{12} |P_r| |\check{s}_2| |\hat{r}_2| \\ & + (1 - 2\epsilon\iota_{22} |P_r|) |\hat{r}_2|^2 - 2\epsilon\iota_{21} (1 + 2\epsilon T \iota_{11}) |P_r| |\hat{r}_2| |\check{s}_2| \\ & + \beta \left(2\check{s}_1^T P_s (\mathfrak{Q}_{11} \check{s}_2 + \mathfrak{Q}_{12} \hat{r}_2) - 2\hat{r}_1^T P_r (\mathfrak{Q}_{21} \check{s}_2 + \mathfrak{Q}_{22} \hat{r}_2) \right) \\ & + \beta \left(- 2\check{s}_2^T P_s (\mathfrak{Q}_{11} \check{s}_1 + \mathfrak{Q}_{12} \hat{r}_1) + 2\hat{r}_2^T P_r (\mathfrak{Q}_{21} \check{s}_1 + \mathfrak{Q}_{22} \hat{r}_1) \right). \end{aligned} \tag{B.6}$$

If $\epsilon \leq \frac{\epsilon_1}{2|P_s|}$ and $\epsilon \leq \epsilon_2 \triangleq \frac{1}{\iota_{22}|P_r|}$, the first, third, fifth, and seventh terms of (B.6) are positive, and, hence there exists ϵ such that the derivative of the Lyapunov function is positive when $\beta = 0$. Indeed, using the Schur complement, the positiveness of the right hand side of (B.6) in the case of $\beta = 0$ is equivalent to existence of positive value ϵ_3 such that $\mathcal{F} = \begin{bmatrix} \Psi_{11} & \Psi_{12} \\ \Psi_{12} & \Psi_{22} \end{bmatrix} > 0$ with $\Psi_{11} = \epsilon_3\gamma - 4T\epsilon_3^2\gamma\iota_{11}^2|P_w|$, $\Psi_{22} = 1 - 2\epsilon_3\iota_{22}|P_r|$, and $\Psi_{12} = -\left(\epsilon_3\gamma\iota_{12}|P_s| + \epsilon_3\iota_{21}(1 + 2\epsilon T\iota_{11})|P_r|\right)$. Now, let us define $\epsilon^* \triangleq \min(\epsilon_1, \frac{\epsilon_1}{2|P_s|}, \epsilon_2, \epsilon_3)$. Then, for every $\epsilon \in (0, \epsilon^*)$, the inverse of the coordinate change exists and the derivative of the Lyapunov function is positive when $\beta = 0$. Now, pick any $\bar{\epsilon} \in (0, \epsilon^*)$ and denote the evaluated matrix $\mathcal{F}$ at $\bar{\epsilon}$ by $\bar{\mathcal{F}}$. We obtain the associated $\psi(\bar{\epsilon})$ by solving the following

optimization problem:

$$\psi(\bar{\epsilon}) = \max_{\bar{\beta}>0} \bar{\beta} \qquad s.t. \quad \begin{bmatrix} \bar{\mathcal{F}} & \bar{\beta}\bar{\mathcal{Z}} \\ \bar{\beta}\bar{\mathcal{Z}} & \bar{\mathcal{F}} \end{bmatrix} > 0, \tag{B.7}$$

where $\bar{\mathcal{Z}} = \begin{bmatrix} -2|P_s|\gamma\iota_{11}(1+2T\bar{\epsilon}\iota_{11}) & -2|P_s|\gamma\iota_{12} \\ -2|P_r|(1+2T\bar{\epsilon}\iota_{11})\iota_{21} & -2|P_r|\iota_{22} \end{bmatrix}$. Under this set up, $\dot{V} > 0$ for $\bar{\epsilon}$ and $\beta \in [0, \psi(\bar{\epsilon})]$. Note that the set $\Omega \triangleq \left\{(\check{s}_1, \hat{r}_1, \check{s}_2, \hat{r}_2) \in \mathbb{R}^{2(p+q)} \mid V \geq 0\right\}$ is nonempty, since the candidate Lyapunov function is quadratic type. Hence, according to Chetaev's theorem for time-varying systems [67], the origin of (B.1) is unstable. This completes the proof. □

Remark B.1. *In the proof of Lemma B.1, it is straightforward to check that if $P_s\mathfrak{Q}_{11} = \mathfrak{Q}_{11}^T P_s$ and $P_r\mathfrak{Q}_{22} = \mathfrak{Q}_{22}^T P_r$, then the matrix $\bar{\mathcal{Z}}$ is simplified to*

$$\bar{\mathcal{Z}} = \begin{bmatrix} 0 & 2|P_s|\gamma\iota_{12} \\ 2|P_r|(1+2T\bar{\epsilon}\iota_{11})\iota_{21} & 0 \end{bmatrix},$$

which leads to a less conservative result.

Lemma B.2. *(Stability Using Two-Time Averaging). Consider the linear time-varying system described by the state space model (B.1). Assume that $\beth_{ij}(t)$, $i, j = 1, 2$ are T-periodic, piecewise, continuous functions bounded by the scalar $\iota_{ij} > 0$, i.e. $|\beth_{ij}(t)| \leq \iota_{ij}$ for all $t \geq 0$. Now consider the average system described by*

$$\dot{\hat{s}} = -\epsilon\bar{\beth}_{11}\hat{s} \ , \ \bar{\beth}_{11} = \frac{1}{T}\int_0^T \beth_{11}(\tau)d\tau. \tag{B.8}$$

If $-\bar{\beth}_{11}$ and H are Hurwitz, then there exists ϵ^* and $\psi : [0, \epsilon^*] \to \mathbb{R}_{\geq 0}$ such that for every $\epsilon \in (0, \epsilon^*)$ and a corresponding $\beta \in [0, \psi(\epsilon)]$, the origin of system (B.1) is stable.

Proof. Similar to the proof of Lemma B.1, we change the coordinate of the system by defining a new state $\check{s}$ as (B.3), and obtain the system (B.4) in the new coordinate. Since the matrices $-\bar{\beth}_{11}$ and H are Hurwitz, there exist positive definite matrices P_s and P_r such that $P_s\bar{\beth}_{11} + \bar{\beth}_{11}^T P_s = I$ and $P_r H + H^T P_r = -I$. Now, define the Lyapunov function as

$V = \sum_{i=1}^{2} \check{s}_i^T P_s \check{s}_i + \hat{r}_i^T P_r \hat{r}_i$. Taking the derivative of the Lyapunov function leads to

$$\begin{aligned}
\dot{V} \leq & -(\epsilon\gamma - 2\epsilon^2\gamma T\iota_{11})|\check{s}_1|^2 + \epsilon\gamma\iota_{12}|\check{s}_1||\hat{r}_1| \\
& -(1-\epsilon\iota_{22})|\hat{r}_1|^2 + \epsilon\iota_{21}(1+2\epsilon T\iota_{11})|\hat{r}_1||\check{s}_1| \\
& -(\epsilon\gamma - 2\epsilon^2\gamma T\iota_{11})|\check{s}_2|^2 + \epsilon\gamma\iota_{12}|\check{s}_2||\hat{r}_2| \\
& -(1-\epsilon\iota_{22})|\hat{r}_2|^2 + \epsilon\iota_{21}(1+2\epsilon T\iota_{11})|\hat{r}_2||\check{s}_2| \\
& +\beta\left(2\check{s}_1^T P_s(\mathfrak{Q}_{11}\check{s}_2 + \mathfrak{Q}_{12}\hat{r}_2) - 2\hat{r}_1^T P_r(\mathfrak{Q}_{21}\check{s}_2 + \mathfrak{Q}_{22}\hat{r}_2)\right) \\
& +\beta\left(-2\check{s}_2^T P_s(\mathfrak{Q}_{11}\check{s}_1 + \mathfrak{Q}_{12}\hat{r}_1) + 2\hat{r}_2^T P_r(\mathfrak{Q}_{21}\check{s}_1 + \mathfrak{Q}_{22}\hat{r}_1)\right).
\end{aligned} \tag{B.9}$$

If $\epsilon \leq \frac{1}{2T\iota_{11}}$ and $\epsilon \leq \epsilon_2 \triangleq \frac{1}{\iota_{22}}$, the first, third, fifth, and seventh terms of (B.9) are negative, and, hence there exists ϵ such that the derivative of the Lyapunov function is positive when $\beta = 0$. Indeed, using the Schur complement, the positiveness of the right hand side of (B.9) in the case of $\beta = 0$ is equivalent to existence of positive value ϵ_3 such that $\mathcal{X} = \begin{bmatrix} \mathcal{X}_{11} & \mathcal{X}_{12} \\ \mathcal{X}_{12} & \mathcal{X}_{22} \end{bmatrix} < 0$ with $\mathcal{X}_{11} = -(\epsilon_3\gamma - 2\epsilon_3^2\gamma T\iota_{11})$, $\mathcal{X}_{22} = -(1-\epsilon_3\iota_{22})$, $\mathcal{X}_{12} = \frac{1}{2}\big(\epsilon_3\gamma\iota_{12} + \epsilon_3\iota_{21} + \epsilon_3^2(2T\iota_{21}\iota_{11})\big)$. Now, let us define $\epsilon^* \triangleq \min(\epsilon_1, \frac{1}{2T\iota_{11}}, \epsilon_2, \epsilon_3)$. Then, for every $\epsilon \in (0, \epsilon^*)$, the inverse of the coordinate change exists and the derivative of the Lyapunov function is negative when $\beta = 0$. Now, pick any $\bar{\epsilon} \in (0, \epsilon^*)$ and denote the evaluated matrix $\mathcal{X}$ at $\bar{\epsilon}$ by $\bar{\mathcal{X}}$. We obtain the associated $\psi(\bar{\epsilon})$ by solving the following optimization problem:

$$\psi(\bar{\epsilon}) = \max_{\bar{\beta}>0} \bar{\beta} \qquad s.t. \quad \begin{bmatrix} \bar{\mathcal{X}} & \bar{\beta}\bar{\mathcal{Z}} \\ \bar{\beta}\bar{\mathcal{Z}} & \bar{\mathcal{X}} \end{bmatrix} < 0, \tag{B.10}$$

where $\mathcal{Z} = \begin{bmatrix} \gamma\iota_{11}(1+2T\bar{\epsilon}\iota_{11}) & \gamma\iota_{12} \\ (1+2T\bar{\epsilon}\iota_{11})\iota_{21} & \iota_{22} \end{bmatrix}$. Under this set up, $\dot{V} < 0$ for $\bar{\epsilon}$ and $\beta \in [0, \psi(\bar{\epsilon})]$, meaning that the origin of system (B.1. This completes the proof. □

Remark B.2. *In the proof of Lemma B.2, it is straightforward to check that if* $P_s\mathfrak{Q}_{11} = \mathfrak{Q}_{11}^T P_s$ *and*

$P_r\mathfrak{Q}_{22} = \mathfrak{Q}_{22}^T P_r$, then the matrix $\bar{\mathcal{Z}}$ is simplified to

$$\mathcal{Z} = \begin{bmatrix} 1 & \gamma\iota_{12} \\ (1+2T\bar{\epsilon}\iota_{11})\iota_{21} & 0 \end{bmatrix},$$

which leads to a less conservative result.

Remark B.3. *Lemma B.2 is the generalisation of Lemma A.1 in [113] for directed networks.*

Appendix C
Supplementary Lemmas in Chapter 4.

C.1 Lemmas in Proof of Theorems 4.1 and 4.3

The following lemmas are used in the proofs of Theorems 4.1 and 4.3.

Lemma C.1 (Fact 2.16.3 in [19]). *Let $A \in \mathbb{C}^{n\times n}$, assume that A is nonsingular, and let $c, d \in \mathbb{R}^{n\times 1}$. Then*

$$\det(A + cd^T) = \det(A)(1 + d^T A^{-1} c). \tag{C.1}$$

Lemma C.2. *Consider a signed graph $\mathcal{G}_1(\mathcal{V}, \mathcal{E}_1, \mathcal{W}_1)$ with the Laplacian matrix L_1. Assume that L_1 has only one zero eigenvalue and the rest of its eigenvalues have positive real parts. Construct a new graph $\mathcal{G}(\mathcal{V}, \mathcal{E}, \mathcal{W}) = \mathcal{G}_1(\mathcal{V}, \mathcal{E}_1, \mathcal{W}_1) \oplus \mathcal{G}_2(\mathcal{V}, \mathcal{E}_2, \mathcal{W}_2)$, where $\mathcal{E}_2 = \{(u, v), (v, u)\}$ and $\mathcal{W}_2(u, v) = -\delta_{uv}$, $\mathcal{W}_2(v, u) = -\delta_{vu}$ with $\delta_{uv} \geq 0$, $\delta_{vu} \geq 0$. Denote L the Laplacian matrix of $\mathcal{G}$. Then,*

$$Spec\{\bar{L}_1^{-1}\bar{L}\} = \{\underbrace{1, \ldots, 1}_{N-2}, 1 - r(\omega, \delta_{uv}, \delta_{vu})\}, \tag{C.2}$$

where $r(\omega, \delta_{uv}, \delta_{vu}) = (\mathbf{e}_u - \mathbf{e}_v)^T Q^T \bar{L}_1^{-1} Q(\delta_{uv}\mathbf{e}_u - \delta_{vu}\mathbf{e}_v)$, and $\bar{L} = QLQ^T$ and $\bar{L}_1 = QL_1Q^T$ the reduced Laplacian matrices for $\mathcal{G}$ and $\mathcal{G}_1$, respectively.

Proof. Denote L_2 the Laplacian matrix of $\mathcal{G}_2$. Since $\mathcal{E}_2 = \{(u, v), (v, u)\}$, L_2 can be expressed as $L_2 = -(\delta_{uv}\mathbf{e}_u - \delta_{vu}\mathbf{e}_v)(\mathbf{e}_u - \mathbf{e}_v)^T$. Furthermore,

$$\mathrm{Spec}(L_2) = \{\underbrace{0, \ldots, 0}_{N-1}, -(\delta_{uv} + \delta_{vu})\}, \tag{C.3}$$

with the set of eigenvectors $\{\mathbf{1}_N, \mathbf{e}_1, \ldots, \mathbf{e}_N\} \backslash \{\mathbf{e}_u, \mathbf{e}_v\}$ that corresponds to the zero eigen-

values, and $\delta_{uv}\mathbf{e}_u - \delta_{vu}\mathbf{e}_v$ that corresponds to the eigenvalue $-(\delta_{uv} + \delta_{vu})$. Using the first property in Lemma 4.3 with (C.3), we have

$$\text{Spec}\left(\bar{L}_2\right) = \{\underbrace{0, \ldots, 0}_{N-2}, -(\delta_{uv} + \delta_{vu})\}, \tag{C.4}$$

where $\bar{L}_2 = QL_2Q^T$. The graphs $\mathcal{G}_1$ and $\mathcal{G}_2$ have the same set of nodes which means L can be written as $L = L_1 + L_2$ leading to the following expression for $\bar{L}$,

$$\bar{L} = \underbrace{QL_1Q^T}_{\bar{L}_1} - Q(\delta_{uv}\mathbf{e}_u - \delta_{vu}\mathbf{e}_v)(\mathbf{e}_u - \mathbf{e}_v)^TQ^T. \tag{C.5}$$

Since L_1 has only one zero eigenvalue, $\bar{L}_1$ is invertible according to Lemma 4.3. By multiplying both sides of (C.5) by $\bar{L}_1^{-1}$ and then $(\mathbf{e}_u - \mathbf{e}_v)^TQ^T$, we obtain

$$\begin{aligned}(\mathbf{e}_u - \mathbf{e}_v)^TQ^T\bar{L}_1^{-1}\bar{L} &= (\mathbf{e}_u - \mathbf{e}_v)^TQ^T - \underbrace{(\mathbf{e}_u - \mathbf{e}_v)^TQ^T\bar{L}_1^{-1}Q(\delta_{uv}\mathbf{e}_u - \delta_{vu}\mathbf{e}_v)}_{r_\delta := r(\omega, \delta_{uv}, \delta_{vu})}(\mathbf{e}_u - \mathbf{e}_v)^TQ^T \\ &= (\mathbf{e}_u - \mathbf{e}_v)^TQ^T(1 - r_\delta),\end{aligned} \tag{C.6}$$

or equivalently,

$$(\mathbf{e}_u - \mathbf{e}_v)^TQ^T\left(\bar{L}_1^{-1}\bar{L} - (1 - r_\delta)I_{N-1}\right) = \mathbf{0}_{N-1}^T. \tag{C.7}$$

Since Q^T is a full column rank matrix, (C.7) implies that the vector $QE_2 \in \mathbb{R}^{N-1}$ is a left eigenvector of matrix $\bar{L}_1^{-1}\bar{L} \in \mathbb{R}^{(N-1)\times(N-1)}$ that corresponds to the eigenvalue $1 - r_\delta$. Showing (C.2) is equivalent to showing that $X = I_{N-1} - \bar{L}_1^{-1}\bar{L}$ has $N-2$ zero eigenvalues. From (C.5), we obtain

$$\bar{L}_1X = \bar{L}_1 - \bar{L} = -\bar{L}_2, \tag{C.8}$$

which means $\text{spec}\{\bar{L}_1X\} = \text{spec}\{-\bar{L}_2\}$. Using (C.4) and noting that $\bar{L}_1$ is non-singular, we conclude X has $N-2$ zero eigenvalues. This completes the proof. □

C.2 Lemmas in Proof of Theorem 4.4

We recall particular case of Theorem 2.1 in [94] and present Lemma C.4 that are used in proof of Theorem 4.4.

Lemma C.3 ([94]). *Assume $\lambda \in \mathbb{C}$ is semisimple eigenvalue of a square matrix $A \in \mathbb{R}^{N\times N}$ with multiplicity d. Consider a perturbed matrix $A + \epsilon B$ where B is an arbitrary matrix and ϵ introduces a small perturbation parameter. Then, there are d eigenvalues of the perturbed matrix which are described by a first-order expansion*

$$\lambda_i = \lambda + \xi_i \epsilon + o(\epsilon),\ i = 1, \dots, d \tag{C.9}$$

where ξ_i are the eigenvalues of the $d \times d$ matrix $\Upsilon B \Gamma$ and $o(\epsilon)$ contains remaining terms such that $\lim_{\epsilon\to 0} \frac{o(\epsilon)}{\epsilon} = 0$. The j^{th} row and column of Υ and Γ are respectively, the left and right eigenvectors of A corresponding to λ which are orthonormal, i.e. $\Upsilon\Gamma = I_d$.

Lemma C.4. *Consider a graph $\mathcal{G}_1(\mathcal{V}, \mathcal{E}_1, \mathcal{W}_1)$ with non-negative edge weights and its Laplacian matrix L_1. Assume,*

1. *$\mathcal{G}_1$ consists of $d \neq 1$ reach sets $\mathcal{R}_k,\ k = 1, \dots, d$.*
2. *All nodes of $\mathcal{G}_1$ are labeled such that the structure of the adjacency matrix of $\mathcal{G}_1$ has the structure in (4.1).*

Denote γ_k and μ_k the right and left eigenvectors associated with the zero eigenvalue of L_1, respectively. Construct a new graph $\mathcal{G}(\mathcal{V}, \mathcal{E}, \mathcal{W}) = \mathcal{G}_1(\mathcal{V}, \mathcal{E}_1, \mathcal{W}_1) \oplus \mathcal{G}_2(\mathcal{V}, \mathcal{E}_2, \mathcal{W}_2)$ with $\mathcal{E}_2 \subseteq \{\mathcal{V} \times \mathcal{V}\} \backslash \mathcal{E}_1$, and $\mathcal{W}_2(u, v) < 0$ for every $(u, v) \in \mathcal{E}_2$. Define $\Theta \in \mathbb{R}^{d\times d}$ as

$$\Theta = \Upsilon L_2 \Gamma, \tag{C.10}$$

where $\Upsilon = \left[\frac{\mu_1}{\|\mu_1\|} \dots \frac{\mu_d}{\|\mu_d\|}\right]^T$, $\Gamma = \left[\frac{\gamma_1}{\|\gamma_1\|} \dots \frac{\gamma_d}{\|\gamma_d\|}\right]$, and L_2 is the Laplacian matrix of $\mathcal{G}_2$. If $|\mathcal{E}_1| = 1$, the following statements are true for $i = 1, \dots, d$.

1. *If $u \notin \mathcal{U}_i$, then $[\Theta]_{ii} = 0$;*
2. *if $u \in \mathcal{U}_i$ and $v \in \mathcal{X}_i$, then $[\Theta]_{ii} = 0$;*

3. *if* $u \in \mathcal{U}_i$ *and* $v \in \mathcal{X}_j$ *or* $v \in \mathcal{C}_j$ *for* $j \neq i$, *then* $[\Theta]_{ii} < 0$;

4. *if* $u \in \mathcal{U}_i$ *and* $v \in \mathcal{C}_i$, *then* $[\Theta]_{ii} < 0$,

where the reaching nodes sets $\mathcal{U}_k$, *the exclusive sets* $\mathcal{X}_k$ *and the common sets* $\mathcal{C}_k$ *are described according to Definition 4.1.*

Furthermore, if $|\mathcal{E}_2| > 1$, *then* $[\Theta]_{ii} \leq 0$. *In this case,* $[\Theta]_{ii} < 0$ *if and only if there exists at least one edge* $(u, v) \in \mathcal{E}_2$ *which satisfies either of the conditions given in statements* 3 *or* 4.

Proof. Suppose all conditions of Lemma C.4 hold. Partition the matrix L_2 in the same way as the adjacency matrix of $\mathcal{G}_1$. Since all weights of $\mathcal{G}_1$ are non-negative, γ_k and μ_k are characterised according to Lemma 4.2. Taking into account the structure of μ_i, we achieve

$$[\Theta]_{ii} = \tilde{\mu}_i^T \underbrace{\begin{bmatrix} L_{2_{\mathcal{U}_i x_1}} & L_{2_{\mathcal{U}_i x_2}} & \cdots & L_{2_{\mathcal{U}_i x_d}} & L_{2_{\mathcal{U}_i c}} \end{bmatrix}}_{L_{2_{\mathcal{U}_i}}} \frac{\gamma_i}{\|\gamma_i\|},$$

where $L_{2_{\mathcal{U}_i x_j}} = \begin{bmatrix} L_{2_{\mathcal{U}_i \mathcal{U}_j}} & L_{2_{\mathcal{U}_i \mathcal{M}_j}} \end{bmatrix}$, and $\tilde{\mu}_i \in \mathbb{R}^{|\mathcal{U}_i|}$ contains the non-zero terms of the vector $\frac{\mu_i}{\|\mu_i\|}$. First, assume there is only a single negative edge $\mathcal{E}_2 = \{(u, v)\}$ with $\mathcal{W}_2(u, v) = -\delta < 0$.

Proof of Statement 1: If $u \notin \mathcal{U}_i$, then $L_{2_{\mathcal{U}_i}} = \mathbf{0}$ leading to $[\Theta]_{ii} = 0$.

Proof of Statement 2: If $u \in \mathcal{U}_i$, the expression $[\Theta]_{ii}$ in above can be expanded as,

$$\begin{aligned} [\Theta]_{ii} &= -\frac{\delta}{\|\mu_i\|\|\gamma_i\|}[\mu_i]_u[\gamma_i]_u + \frac{\delta}{\|\mu_i\|\|\gamma_i\|}[\mu_i]_u[\gamma_i]_v \\ &= -\frac{\delta}{\|\mu_i\|\|\gamma_i\|}[\mu_i]_u\left(1 - [\gamma_i]_v\right). \end{aligned} \tag{C.11}$$

According to Lemma 4.2, $[\mu_i]_u > 0$ and $[\gamma_i]_v = 1$ for $v \in \mathcal{X}_i$ which along with (C.11) concludes $[\Theta_{ii}] = 0$.

Proof of Statements 3 and 4: For v given in statement 3 or statement 4, $[\gamma_i]_v = 0$ or $[\gamma_i]_v < 1$ which using (C.11) show $[\Theta]_{ii} < 0$.

To deal with multiple negative edge weights, i.e. $|\mathcal{E}_2| > 1$, it should be noted that the Laplacian matrix L_2 can be written as a sum of Laplacian matrices each of which corresponding to one negative edge weight. As adding a negative edge weight does not contribute to any positive value for $[\Theta]_{ii}$, we conclude that the diagonal terms of

Θ are non-positive, i.e. $[\Theta]_{ii} \leq 0$ for $i = 1, \ldots, d$. In addition, from our discussion for a single negative edge weight, it is observed that $[\Theta]_{ii}$ becomes negative if and only if there exists at least one edge $(u, v) \in \mathcal{E}_2$ that meets the one of the conditions mentioned in the statements 3 and 4. This completes the proof. □

Bibliography

[1] S. Achuthan and C. C. Canavier, "Phase-resetting curves determine synchronization, phase locking, and clustering in networks of neural oscillators," *Journal of Neuroscience*, vol. 29, no. 16, pp. 5218–5233, 2009.

[2] H. Adeli, Z. Zhou, and N. Dadmehr, "Analysis of EEG records in an epileptic patient using wavelet transform," *Journal of neuroscience methods*, vol. 123, no. 1, pp. 69–87, 2003.

[3] R. Agaev and P. Chebotarev, "On the spectra of nonsymmetric Laplacian matrices," *Linear Algebra and its Applications*, vol. 399, pp. 157–168, 2005.

[4] S. Ahmadizadeh, D. Nešić, D. B. Grayden, and D. R. Freestone, "Analytic synchronization conditions for a network of Wilson and Cowan oscillators," in *54th IEEE Conference on Decision and Control (CDC)*, 2015, pp. 3104–3109.

[5] S. Ahmadizadeh, D. Nešić, D. R. Freestone, and D. B. Grayden, "On synchronization of networks of Wilson–Cowan oscillators with diffusive coupling," *Automatica*, vol. 71, pp. 169–178, 2016.

[6] C. Altafini, "Consensus problems on networks with antagonistic interactions," *IEEE Transactions on Automatic Control*, vol. 58, no. 4, pp. 935–946, 2013.

[7] D. Angeli, "A Lyapunov approach to incremental stability properties," *IEEE Transactions on Automatic Control*, vol. 47, no. 3, pp. 410–421, 2002.

[8] ——, "Systems with counterclockwise input-output dynamics," *IEEE Transactions on Automatic Control*, vol. 51, no. 7, pp. 1130–1143, 2006.

[9] ——, "Multistability in systems with counter-clockwise input–output dynamics," *IEEE Transactions on Automatic Control*, vol. 52, no. 4, pp. 596–609, 2007.

[10] ——, "Convergence in networks with counterclockwise neural dynamics," *IEEE Transactions on Neural Networks*, vol. 20, no. 5, pp. 794–804, 2009.

[11] M. Arcak, "Passivity as a design tool for group coordination," *IEEE Transactions on Automatic Control*, vol. 52, no. 8, pp. 1380–1390, 2007.

[12] ——, *Passivity Approach to Network Stability Analysis and Distributed Control Synthesis*. The Control Systems Handbook, Second Edition, 2010.

[13] ——, "Diagonal stability on cactus graphs and application to network stability analysis," *IEEE Transactions on Automatic Control*, vol. 56, no. 12, pp. 2766–2777, 2011.

[14] M. Arcak and E. D. Sontag, "Diagonal stability of a class of cyclic systems and its connection with the secant criterion," *Automatica*, vol. 42, no. 9, pp. 1531 – 1537, 2006.

[15] ——, "A passivity-based stability criterion for a class of biochemical reaction networks," *Mathematical Biosciences and Engineering*, vol. 5, no. 1, p. 1, 2008.

[16] R. A. Badawy and G. D. Jackson, "Cortical excitability in migraine and epilepsy: a common feature?" *Journal of Clinical Neurophysiology*, vol. 29, no. 3, pp. 244–249, 2012.

[17] F. Bauer, "Normalized graph Laplacians for directed graphs," *Linear Algebra and its Applications*, vol. 436, no. 11, pp. 4193–4222, 2012.

[18] I. Belykh, V. Belykh, and M. Hasler, "Generalized connection graph method for synchronization in asymmetrical networks," *Physica D: Nonlinear Phenomena*, vol. 224, no. 1, pp. 42–51, 2006.

[19] D. S. Bernstein, *Matrix Mathematics: Theory, Facts, and Formulas*. Princeton University Press, 2009.

[20] G. Bettus, F. Wendling, M. Guye, L. Valton, J. Régis, P. Chauvel, and F. Bartolomei, "Enhanced EEG functional connectivity in mesial temporal lobe epilepsy," *Epilepsy Research*, vol. 81, no. 1, pp. 58–68, 2008.

[21] R. L. Beurle, "Properties of a mass of cells capable of regenerating pulses," *Philosophical Transactions of the Royal Society of London. Series B, Biological Sciences*, vol. 240, no. 669, pp. 55–94, 1956.

[22] J. Bronski, L. DeVille, and K. P. Koutsaki, "The spectral index of signed Laplacians and their structural stability," *arXiv preprint arXiv:1503.01069*, 2015.

[23] J. C. Bronski and L. DeVille, "Spectral theory for dynamics on graphs containing attractive and repulsive interactions," *SIAM Journal on Applied Mathematics*, vol. 74, no. 1, pp. 83–105, 2014.

[24] J. C. Bronski, L. DeVille, and T. Ferguson, "Graph homology and stability of coupled oscillator networks," *SIAM Journal on Applied Mathematics*, vol. 76, no. 3, pp. 1126–1151, 2016.

[25] E. Brown, J. Moehlis, and P. Holmes, "On the phase reduction and response dynamics of neural oscillator populations," *Neural Computation*, vol. 16, no. 4, pp. 673–715, 2004.

[26] R. A. Brualdi, "Spectra of digraphs," *Linear Algebra and its Applications*, vol. 432, no. 9, pp. 2181–2213, 2010.

[27] N. Brunel and X.-J. Wang, "Effects of neuromodulation in a cortical network model of object working memory dominated by recurrent inhibition," *Journal of Computational Neuroscience*, vol. 11, no. 1, pp. 63–85, 2001.

[28] J. B. Buck, "Synchronous rhythmic flashing of fireflies," *The Quarterly Review of Biology*, vol. 13, no. 3, pp. 301–314, 1938.

[29] C. Cai and G. Chen, "Synchronization of complex dynamical networks by the incremental ISS approach," *Physica A: Statistical Mechanics and its Applications*, vol. 371, no. 2, pp. 754–766, 2006.

[30] S. Campbell and D. Wang, "Synchronization and desynchronization in a network of locally coupled Wilson-Cowan oscillators," *IEEE Transactions on Neural Networks*, vol. 7, no. 3, pp. 541–554, 1996.

[31] J. S. Caughman and J. Veerman, "Kernels of directed graph Laplacians," *The Electronic Journal of Combinatorics*, vol. 13, no. 1, p. R39, 2006.

[32] B. Cessac, "A view of neural networks as dynamical systems," *International Journal of Bifurcation and Chaos*, vol. 20, no. 06, pp. 1585–1629, 2010.

[33] A. Chaillet, A. Y. Pogromsky, and B. S. Ruffer, "A Razumikhin approach for the incremental stability of delayed nonlinear systems," in *52nd IEEE Conference on Decision and Control (CDC)*. IEEE, 2013, pp. 1596–1601.

[34] W. Chen, J. Liu, Y. Chen, S. Z. Khong, D. Wang, T. Başar, L. Qiu, and K. H. Johansson, "Characterizing the positive semidefiniteness of signed laplacians via effective resistances," in *55th IEEE Conference on Decision and Control (CDC),*, 2016, pp. 985–990.

[35] M. Chong, R. Postoyan, D. Nešić, L. Kuhlmann, and A. Varsavsky, "A robust circle criterion observer with application to neural mass models," *Automatica*, vol. 48, no. 11, pp. 2986–2989, 2012.

[36] F. R. Chung, *Spectral Graph Theory*. American Mathematical Society., 1997, vol. 92.

[37] M. J. Cook, T. J. O'Brien, S. F. Berkovic, M. Murphy, A. Morokoff, G. Fabinyi, W. D'Souza, R. Yerra, J. Archer, L. Litewka *et al.*, "Prediction of seizure likelihood with a long-term, implanted seizure advisory system in patients with drug-resistant epilepsy: a first-in-man study," *The Lancet Neurology*, vol. 12, no. 6, pp. 563–571, 2013.

[38] D. Cumin and C. Unsworth, "Generalising the Kuramoto model for the study of neuronal synchronisation in the brain," *Physica D: Nonlinear Phenomena*, vol. 226, no. 2, pp. 181–196, 2007.

[39] F. L. Da Silva, A. Hoeks, H. Smits, and L. H. Zetterberg, "Model of brain rhythmic activity," *Kybernetik*, vol. 15, no. 1, pp. 27–37, 1974.

[40] A. Daffertshofer and B. C. van Wijk, "On the influence of amplitude on the connectivity between phases," *Frontiers in Neuroinformatics*, vol. 5, 2011.

[41] O. David, S. J. Kiebel, L. M. Harrison, J. Mattout, J. M. Kilner, and K. J. Friston, "Dynamic causal modeling of evoked responses in EEG and MEG," *NeuroImage*, vol. 30, no. 4, pp. 1255–1272, 2006.

[42] O. David and K. J. Friston, "A neural mass model for MEG/EEG: coupling and neuronal dynamics," *NeuroImage*, vol. 20, no. 3, pp. 1743–1755, 2003.

[43] F. De Smet and D. Aeyels, "Clustering in a network of non-identical and mutually interacting agents," *Proceedings of the Royal Society A: Mathematical, Physical and Engineering Science*, vol. 465, no. 2103, pp. 745–768, 2009.

[44] P. DeLellis, M. di Bernardo, and G. Russo, "On QUAD, Lipschitz, and contracting vector fields for consensus and synchronization of networks," *IEEE Transactions on Circuits and Systems I: Regular Papers*, vol. 58, no. 3, pp. 576–583, 2011.

[45] P. DeLellis, F. Garofalo *et al.*, "Novel decentralized adaptive strategies for the synchronization of complex networks," *Automatica*, vol. 45, no. 5, pp. 1312–1318, 2009.

[46] A. Demir, A. Mehrotra, and J. Roychowdhury, "Phase noise in oscillators: a unifying theory and numerical methods for characterization," *IEEE Transactions on Circuits and Systems I: Fundamental Theory and Applications*, vol. 47, no. 5, pp. 655–674, 2000.

[47] M. Di Bernardo, G. Russo, and J.-J. Slotine, "An algorithm to prove contraction, consensus and network synchronization," in *Proceedings of the 1st IFAC Workshop on Networked Control Systems (NECSYS 09), Venice (Italy)*, 2009.

[48] Z. Ding, "Consensus output regulation of a class of heterogeneous nonlinear systems," *IEEE Transactions on Automatic Control*, vol. 58, no. 10, pp. 2648–2653, 2013.

[49] A. S. Dolby and T. C. Grubb Jr, "Benefits to satellite members in mixed-species foraging groups: an experimental analysis," *Animal Behaviour*, vol. 56, no. 2, pp. 501–509, 1998.

[50] L. G. Dominguez, R. A. Wennberg, W. Gaetz, D. Cheyne, O. . C. Snead, and J. Velazquez, "Enhanced synchrony in epileptiform activity? local versus distant phase synchronization in generalized seizures," *The Journal of Neuroscience*, vol. 25, no. 35, pp. 8077–8084, 2005.

[51] F. Dörfler and F. Bullo, "Synchronization and transient stability in power networks and nonuniform Kuramoto oscillators," *SIAM Journal on Control and Optimization*, vol. 50, no. 3, pp. 1616–1642, 2012.

[52] ——, "Synchronization in complex oscillator networks: A survey," *Automatica*, 2013.

[53] D. Efimov, P. Sacré, and R. Sepulchre, "Controlling the phase of an oscillator: a phase response curve approach," in *48th IEEE Conference on Decision and Control (CDC), held jointly with the 28th Chinese Control Conference (CCC)*. IEEE, 2009, pp. 7692–7697.

[54] M. Farkas, *Periodic Motions*. Springer-Verlag, 1994.

[55] J. A. Fax and R. M. Murray, "Information flow and cooperative control of vehicle formations," *IEEE transactions on Automatic Control*, vol. 49, no. 9, pp. 1465–1476, 2004.

[56] R. FitzHugh, "Mathematical models of threshold phenomena in the nerve membrane," *The Bulletin of Mathematical Biophysics*, vol. 17, no. 4, pp. 257–278, 1955.

[57] A. Franci, L. Scardovi, and A. Chaillet, "An Input-Output approach to the robust synchronization of dynamical systems with an application to the Hindmarsh-Rose neuronal model," in *50th IEEE Conference on Decision and Control and European Control Conference (CDC-ECC)*, 2011, pp. 6504–6509.

[58] D. R. Freestone, P. J. Karoly, D. Nešić, P. Aram, M. J. Cook, and D. B. Grayden, "Estimation of effective connectivity via data-driven neural modeling," *Frontiers in Neuroscience*, vol. 8, p. 383, 2014.

[59] F. Freyer, J. A. Roberts, R. Becker, P. A. Robinson, P. Ritter, and M. Breakspear, "Biophysical mechanisms of multistability in resting-state cortical rhythms," *The Journal of Neuroscience*, vol. 31, no. 17, pp. 6353–6361, 2011.

[60] S. Geng, W. Zhou, X. Zhao, Q. Yuan, Z. Ma, and J. Wang, "Bifurcation and oscillation in a time-delay neural mass model," *Biological Cybernetics*, pp. 1–10, 2014.

[61] A. Genz, "Numerical computation of rectangular bivariate and trivariate normal and t probabilities," *Statistics and Computing*, vol. 14, no. 3, pp. 251–260, 2004.

[62] P. Gerrard and R. Malcolm, "Mechanisms of modafinil: a review of current research," *Neuropsychiatric disease and treatment*, vol. 3, no. 3, p. 349, 2007.

[63] W. Gerstner and W. M. Kistler, *Spiking Neuron Models: Single Neurons, Populations, Plasticity*. Cambridge university press, 2002.

[64] W. Govaerts, Y. A. Kuznetsov, V. De Witte, A. Dhooge, H. G. E. Meijer, W. Mestrom, A. M. Riet, and B. Sautois, "MATCONT and CL-MATCONT: Continuation toolboxes in MATLAB," *Gent University and Utrech University, Tech. Rep*, 2011.

[65] F. Grimbert and O. Faugeras, "Bifurcation analysis of Jansen's neural mass model," *Neural Computation*, vol. 18, no. 12, pp. 3052–3068, 2006.

[66] S. Y. Ha, C. Lattanzio, B. Rubino, and M. Slemrod, "Flocking and synchronization of particle models," *Quarterly of Applied Mathematics*, vol. 69, no. 1, pp. 91–103, 2011.

[67] W. M. Haddad and V. Chellaboina, *Nonlinear Dynamical Systems and Control: a Lyapunov-based Approach*. Princeton University Press, 2008.

[68] J. K. Hale, "Diffusive coupling, dissipation, and synchronization," *Journal of Dynamics and Differential Equations*, vol. 9, no. 1, pp. 1–52, 1997.

[69] A. Hamadeh, G.-B. Stan, R. Sepulchre, and J. Gonçalves, "Global state synchronization in networks of cyclic feedback systems," *IEEE Transactions on Automatic Control*, vol. 57, no. 2, pp. 478–483, 2012.

[70] R. Hegselmann and U. Krause, "Opinion dynamics and bounded confidence models, analysis, and simulation," *Journal of Artificial Societies and Social Simulation*, vol. 5, no. 3, 2002.

[71] D. J. Hill and P. J. Moylan, "Dissipative dynamical systems: basic input-output and state properties," *Journal of the Franklin Institute*, vol. 309, no. 5, pp. 327–357, 1980.

[72] J. Hindmarsh and R. Rose, "A model of neuronal bursting using three coupled first order differential equations," *Proceedings of the Royal society of London. Series B. Biological sciences*, vol. 221, no. 1222, pp. 87–102, 1984.

[73] A. L. Hodgkin and A. F. Huxley, "A quantitative description of membrane current and its application to conduction and excitation in nerve," *The Journal of Physiology*, vol. 117, no. 4, p. 500, 1952.

[74] S. L. Holliday and R. L. Brey, "Memory problems after epilepsy surgery," *Neurology*, vol. 60, no. 6, pp. E3–E5, 2003.

[75] F. C. Hoppensteadt and E. M. Izhikevich, *Weakly Connected Neural Networks*. Springer Science & Business Media, 2012, vol. 126.

[76] B. H. Jansen and V. G. Rit, "Electroencephalogram and visual evoked potential generation in a mathematical model of coupled cortical columns," *Biological Cybernetics*, vol. 73, no. 4, pp. 357–366, 1995.

[77] Z. P. Jiang, I. Mareels, and Y. Wang, "A Lyapunov formulation of the nonlinear small-gain theorem for interconnected iss systems," *Automatica*, vol. 32, no. 8, pp. 1211–1215, 1996.

[78] V. K. Jirsa, W. C. Stacey, P. P. Quilichini, A. I. Ivanov, and C. Bernard, "On the nature of seizure dynamics," *Brain*, vol. 137, no. 8, pp. 2210–2230, 2014.

[79] J. Juang and Y.-H. Liang, "Cluster synchronization in networks of neurons with chemical synapses," *Chaos: An Interdisciplinary Journal of Nonlinear Science*, vol. 24, no. 1, p. 013110, 2014.

[80] R. E. Kalman, "A new approach to linear filtering and prediction problems," *Journal of Basic Engineering*, vol. 82, no. 1, pp. 35–45, 1960.

[81] H. K. Khalil, *Nonlinear Systems*, 3rd ed., 2002.

[82] D. J. Klein and M. Randić, "Resistance distance," *Journal of Mathematical Chemistry*, vol. 12, no. 1, pp. 81–95, 1993.

[83] N. Komin, A. C. Murza, E. Hernández-García, and R. Toral, "Synchronization and entrainment of coupled circadian oscillators," *Interface Focus*, vol. 1, no. 1, pp. 167–176, 2011.

[84] F. Kouřil and K. Vrba, *Non-linear and Parametric Circuits: Principles, Theory and Applications*. Ellis Horwood, 1988.

[85] Y. A. Kuznetsov, *Elements of Applied Bifurcation Theory*. Springer, 2004.

[86] F. Lopes da Silva, A. Van Rotterdam, P. Barts, E. Van Heusden, and W. Burr, "Models of neuronal populations: the basic mechanisms of rhythmicity," *Progress in Brain Research*, vol. 45, pp. 281–308, 1976.

[87] W. Lu and T. Chen, "Synchronization of coupled connected neural networks with delays," *IEEE Transactions on Circuits and Systems Part 1: Regular Papers*, vol. 51, no. 12, pp. 2491–2503, 2004.

[88] J. L. Massera, "Contributions to stability theory," *Annals of Mathematics*, pp. 182–206, 1956.

[89] A. Mauroy, P. Sacré, and R. Sepulchre, "Kick synchronization versus diffusive synchronization," in *51st IEEE Conference on Decision and Control (CDC)*. IEEE, 2012, pp. 7171–7183.

[90] R. Merrison-Hort, N. Yousif, F. Njap, U. G. Hofmann, O. Burylko, and R. Borisyuk, "An interactive channel model of the basal ganglia: bifurcation analysis under healthy and parkinsonian conditions," *The Journal of Mathematical Neuroscience*, vol. 3, no. 1, p. 14, 2013.

[91] A. Mirtabatabaei and F. Bullo, "Opinion dynamics in heterogeneous networks: convergence conjectures and theorems," *SIAM Journal on Control and Optimization*, vol. 50, no. 5, pp. 2763–2785, 2012.

[92] J. M. Montenbruck, M. Burger, and F. Allgower, "Practical cluster synchronization of heterogeneous sytems on graphs with acyclic topology," in *52nd IEEE Conference on Decision and Control (CDC)*, 2013, pp. 692–697.

[93] J. M. Montenbruck, M. Bürger, and F. Allgöwer, "Practical synchronization with diffusive couplings," *Automatica*, vol. 53, pp. 235–243, 2015.

[94] J. Moro, J. V. Burke, and M. L. Overton, "On the Lidskii–Vishik–Lyusternik perturbation theory for eigenvalues of matrices with arbitrary Jordan structure," *SIAM Journal on Matrix Analysis and Applications*, vol. 18, no. 4, pp. 793–817, 1997.

[95] D. Mukherjee and D. Zelazo, "Consensus over weighted digraphs: a robustness perspective," in *55th IEEE Conference on Decision and Control (CDC)*, 2016.

[96] F. Núñez, Y. Wang, and F. J. Doyle, "Synchronization of pulse-coupled oscillators on (strongly) connected graphs," *IEEE Transactions on Automatic Control*, vol. 60, no. 6, pp. 1710–1715, 2015.

[97] R. Olfati-Saber, J. A. Fax, and R. M. Murray, "Consensus and cooperation in networked multi-agent systems," *Proceedings of the IEEE*, vol. 95, no. 1, pp. 215–233, 2007.

[98] R. Olfati-Saber and R. M. Murray, "Consensus problems in networks of agents with switching topology and time-delays," *IEEE Transactions on Automatic Control*, vol. 49, no. 9, pp. 1520–1533, 2004.

[99] A. Palmigiano, J. Pastor, R. G. de Sola, and G. J. Ortega, "Stability of synchronization clusters and seizurability in temporal lobe epilepsy," *PLoS One*, vol. 7, no. 7, p. e41799, 2012.

[100] E. Panteley and A. Loria, "Synchronization and dynamic consensus of heterogeneous networked systems," *IEEE Transactions on Automatic Control*, 2017.

[101] A. Pavlov, A. Pogromsky, N. van de Wouw, and H. Nijmeijer, "Convergent dynamics, a tribute to Boris Pavlovich Demidovich," *Systems & Control Letters*, vol. 52, no. 3, pp. 257–261, 2004.

[102] L. M. Pecora and T. L. Carroll, "Master stability functions for synchronized coupled systems," *Physical Review Letters*, vol. 80, no. 10, p. 2109, 1998.

[103] M. Porfiri and M. Di Bernardo, "Criteria for global pinning-controllability of complex networks," *Automatica*, vol. 44, no. 12, pp. 3100–3106, 2008.

[104] W. Ren and R. W. Beard, "Consensus seeking in multiagent systems under dynamically changing interaction topologies," *IEEE Transactions on Automatic Control*, vol. 50, no. 5, pp. 655–661, 2005.

[105] E. Rodriguez, N. George, J.-P. Lachaux, J. Martinerie, B. Renault, and F. J. Varela, "Perception's shadow: long-distance synchronization of human brain activity," *Nature*, vol. 397, no. 6718, pp. 430–433, 1999.

[106] B. S. Rüffer, N. van de Wouw, and M. Mueller, "Convergent systems vs. incremental stability," *Systems & Control Letters*, vol. 62, no. 3, pp. 277–285, 2013.

[107] H. Sandberg, E. Mollerstedt, and B. Bernhardsson, "Frequency-domain analysis of linear time-periodic systems," *IEEE Transactions on Automatic Control*, vol. 50, no. 12, pp. 1971–1983, 2005.

[108] S. Sastry and M. Bodson, *Adaptive Control: Stability, Convergence and Robustness*. Courier Corporation, 2011.

[109] L. Scardovi, M. Arcak, and E. Sontag, "Synchronization of interconnected systems with applications to biochemical networks: An Input-Output approach," *IEEE Transactions on Automatic Control*, vol. 55, no. 6, pp. 1367–1379, 2010.

[110] L. Scardovi and R. Sepulchre, "Synchronization in networks of identical linear systems," *Automatica*, vol. 45, no. 11, pp. 2557–2562, 2009.

[111] E. Seneta, "Coefficients of ergodicity: structure and applications," *Advances in Applied Probability*, pp. 576–590, 1979.

[112] R. Sepulchre, "Consensus on nonlinear spaces," *Annual reviews in control*, vol. 35, no. 1, pp. 56–64, 2011.

[113] S. Y. Shafi, M. Arcak, M. Jovanović, and A. K. Packard, "Synchronization of diffusively-coupled limit cycle oscillators," *Automatica*, vol. 49, no. 12, pp. 3613–3622, 2013.

[114] I. Shames, T. Summers, and M. Cantoni, "Manipulating factions evolved in signed networks," in *Proceedings of the 21st International Symposium on Mathematical Theory of Networks and Systems (MTNS)*, 2014.

[115] A. L. Shil'nikov, "On bifurcations of the Lorenz attractor in the Shimizu-Morioka model," *Physica D: Nonlinear Phenomena*, vol. 62, no. 1-4, pp. 338–346, 1993.

[116] J.-J. E. Slotine and W. Wang, "A study of synchronization and group cooperation using partial contraction theory," in *Cooperative Control*. Springer, 2005, pp. 207–228.

[117] E. D. Sontag, "Smooth stabilization implies coprime factorization," *IEEE Transactions on Automatic Control*, vol. 34, no. 4, pp. 435–443, 1989.

[118] ——, "Passivity gains and the "secant condition" for stability," *Systems & Control Letters*, vol. 55, no. 3, pp. 177 – 183, 2006.

[119] E. D. Sontag and M. Arcak, "Passivity-based stability of interconnection structures," in *Recent Advances in Learning and Control*. Springer, 2008, pp. 195–204.

[120] A. Spiegler, S. J. Kiebel, F. M. Atay, and T. R. Knösche, "Bifurcation analysis of neural mass models: Impact of extrinsic inputs and dendritic time constants," *NeuroImage*, vol. 52, no. 3, pp. 1041–1058, 2010.

[121] G.-B. Stan and R. Sepulchre, "Analysis of interconnected oscillators by dissipativity theory," *IEEE Transactions on Automatic Control*, vol. 52, no. 2, pp. 256–270, 2007.

[122] R. A. Stefanescu and V. K. Jirsa, "A low dimensional description of globally coupled heterogeneous neural networks of excitatory and inhibitory neurons," *PLoS Computational Biology*, vol. 4, no. 11, p. e1000219, 2008.

[123] E. Steur, I. Tyukin, and H. Nijmeijer, "Semi-passivity and synchronization of diffusively coupled neuronal oscillators," *Physica D: Nonlinear Phenomena*, vol. 238, no. 21, pp. 2119–2128, 2009.

[124] J. Sun, E. M. Bollt, and T. Nishikawa, "Constructing generalized synchronization manifolds by manifold equation," *SIAM Journal on Applied Dynamical Systems*, vol. 8, no. 1, pp. 202–221, 2009.

[125] J. R. Terry, O. Benjamin, and M. P. Richardson, "Seizure generation: the role of nodes and networks," *Epilepsia*, vol. 53, no. 9, pp. e166–e169, 2012.

[126] M. S. Titcombe, L. Glass, D. Guehl, and A. Beuter, "Dynamics of Parkinsonian tremor during deep brain stimulation," *Chaos: An Interdisciplinary Journal of Nonlinear Science*, vol. 11, no. 4, pp. 766–773, 2001.

[127] J. Touboul, F. Wendling, P. Chauvel, and O. Faugeras, "Neural mass activity, bifurcations, and epilepsy," *Neural Computation*, vol. 23, no. 12, pp. 3232–3286, 2011.

[128] H. L. Trentelman, K. Takaba, and N. Monshizadeh, "Robust synchronization of uncertain linear multi-agent systems," *IEEE Transactions on Automatic Control*, vol. 58, no. 6, pp. 1511–1523, 2013.

[129] T. Ueta and G. Chen, "On synchronization and control of coupled Wilson-Cowan neural oscillators," *International Journal of Bifurcation and Chaos*, vol. 13, no. 01, pp. 163–175, 2003.

[130] A. Von Stein and J. Sarnthein, "Different frequencies for different scales of cortical integration: from local Gamma to long range Alpha/Theta synchronization," *International journal of psychophysiology*, vol. 38, no. 3, pp. 301–313, 2000.

[131] W. Wang and D. Nesic, "Diagonal stability for a class of graphs with connected circle," in *Proceedings of the 2012 Australian Control Conference*. Engineers Australia, 2012, p. 168.

[132] W. Wang and J.-J. E. Slotine, "On partial contraction analysis for coupled nonlinear oscillators," *Biological Cybernetics*, vol. 92, no. 1, pp. 38–53, 2005.

[133] F. Wendling, J. Bellanger, F. Bartolomei, and P. Chauvel, "Relevance of nonlinear lumped-parameter models in the analysis of depth-EEG epileptic signals," *Biological Cybernetics*, vol. 83, no. 4, pp. 367–378, 2000.

[134] J. C. Willems, "Dissipative dynamical systems part i: General theory," *Archive for Rational Mechanics and Analysis*, vol. 45, no. 5, pp. 321–351, 1972.

[135] H. R. Wilson and J. D. Cowan, "Excitatory and inhibitory interactions in localized populations of model neurons," *Biophysical Journal*, vol. 12, no. 1, pp. 1–24, 1972.

[136] W. Xia and M. Cao, "Clustering in diffusively coupled networks," *Automatica*, vol. 47, no. 11, pp. 2395–2405, 2011.

[137] G. Young, L. Scardovi, and N. Leonard, "A new notion of effective resistance for directed graphs—Part I: Definition and properties," *IEEE Transactions on Automatic Control*, vol. PP, no. 99, pp. 1–1, 2015.

[138] G. F. Young, L. Scardovi, and N. E. Leonard, "Robustness of noisy consensus dynamics with directed communication," in *American Control Conference (ACC)*, 2010, pp. 6312–6317.

[139] W. Yu, G. Chen, and M. Cao, "Consensus in directed networks of agents with nonlinear dynamics," *IEEE Transactions on Automatic Control*, vol. 56, no. 6, pp. 1436–1441, 2011.

[140] D. Zelazo and M. Burger, "On the robustness of uncertain consensus networks," *IEEE Transactions on Control of Network Systems*, vol. PP, no. 99, pp. 1–1, 2015.

[141] J. Zhao, D. J. Hill, and T. Liu, "Synchronization of dynamical networks with non-identical nodes: Criteria and control," *IEEE Transactions on Circuits and Systems I: Regular Papers*, vol. 58, no. 3, pp. 584–594, 2011.

[142] ——, "Global bounded synchronization of general dynamical networks with non-identical nodes," *IEEE Transactions on Automatic Control*, vol. 57, no. 10, pp. 2656–2662, 2012.

[143] Y. Zheng, G. Wang, K. Li, G. Bao, and J. Wang, "Epileptic seizure prediction using phase synchronization based on bivariate empirical mode decomposition," *Clinical Neurophysiology*, vol. 125, no. 6, pp. 1104–1111, 2014.

[144] J. Zhou and T. Hagiwara, "2-regularized Nyquist criterion in linear continuous-time periodic systems and its implementation," *SIAM Journal on Control and Optimization*, vol. 44, no. 2, pp. 618–645, 2005.